Search for solar axions with the CCD detector at CAST (CERN Axion Solar Telescope)

Donghwa Kang

FAKULTÄT FÜR MATHEMATIK UND PHYSIK
ALBERT-LUDWIGS-UNIVERSITÄT FREIBURG

Search for solar axions with the CCD detector at CAST (CERN Axion Solar Telescope)

Dissertation
zur
Erlangung des Doktorgrades
der
Fakultät für Mathematik und Physik
der
Albert-Ludwigs-Universität
Freiburg im Breisgau

vorgelegt von
Donghwa Kang
aus Südkorea

Januar 2007

Dekan:	**Prof. Dr. Jörg Flum**
Leiter der Arbeit:	**Prof. Dr. Kay Königsmann**
Referent:	**Prof. Dr. Kay Königsmann**
Koreferent:	**Prof. Dr. Karl Jakobs**
Tag der Verkündung des Prüfungsergebnisses:	**26. Februar 2007**

Contents

Chapter 1

Introduction

The standard model of elementary particle physics is the gauge theory which gives a successful description of strong, weak and electromagnetic interactions. However, it has a small blemish: we have not explained why the predicted violation of charge conjugation times parity (CP) symmetry in the strong interactions is not observed in experiments. This unsolved question is known as the strong CP problem. An elegant explanation of CP conservation in the strong interaction was proposed by Roberto Peccei and Helen Quinn in 1977 by introducing an additional Peccei-Quinn (PQ) symmetry in quantum chromodynamics (QCD). This symmetry is spontaneously broken at an unknown symmetry breaking scale f_a. A new, light, and neutral pseudoscalar particle could thus arise, namely an axion associated with the spontaneous symmetry breaking. The original axion with a mass of about 100 keV was quickly ruled out by several laboratory experiments. New models were thus considered with very light axions having very weak couplings with matter and a long lifetime, so-called invisible axions. If axions exist, they could be formed in the early universe, thereby playing a significant role in astrophysics and cosmology. Astrophysical considerations can give a bound on the properties of axions. In addition, axions with a small mass are an excellent candidate for cold dark matter and could constitute some of the cosmic dark matter.

Axions would be produced in the core of stars like our sun by interacting with thermal photons in the Coulomb field of electric charges by Primakoff conversion. In an external transverse magnetic field, the axions can be reconverted to X-ray photons which have the energy and momentum of the original axions. The sun is preferred for axion searches because of its closeness compared with other stellar objects.

The CERN Axion Solar Telescope (CAST) experiment searches for solar axions with energies in the keV range. The axions from the sun could convert back into photons in a 9 Tesla Large Hadron Collider (LHC) prototype superconducting magnet, where the two beam pipes inside the magnet are straight. The magnet can be moved automatically to follow the sun. The data are taken every morning and evening for approximately 1.5 hours by three different independent detectors installed at both ends of the 9.26 m long dipole magnet. They are sensitive in the energy range up to 10 keV. A Time Projection Chamber (TPC) covering both beam bores is looking for photons coming from the magnet after axion to photon conversion during sunset, while at the other end of the magnet a MICROMesh GAseous Structure (MicroMegas) and a Charge Coupled Device (CCD) are detecting the photons during sunrise.

An X-ray focusing mirror telescope designed for the German X-ray satellite mission ABRIXAS is mounted between the magnet and the CCD. The mirror telescope focuses the photons from the magnet bore of 14.5 cm^2 aperture to a spot size of about 6 mm^2 on the CCD, therefore the signal to background ratio improves by a factor of about 200 and hence it improves the sensitivity of the experiment significantly.

The experiment operated successfully for about 6 months from May to November in 2003 as well as during 2004 with improved conditions in all detectors. First results of the 2003 data taking were published showing no significant signal above background. These results constrain the upper limit of the axion-photon coupling constant by a factor 5 compared to previous axion search experiments. Moreover, results from the data taken in 2004 are better than the astrophysical bound from globular cluster.

This thesis is devoted to the determination of the upper limit on the axion-photon coupling constant $g_{a\gamma}$. In particular, the data which were taken with the CCD detector located in the focal plane of the X-ray mirror telescope will be discussed here. In Chapter 2 an overview of the general axion physics including the theoretical motivation in particle physics, axion properties, limits on its mass and coupling constant by astrophysics is given. In addition, several experimental methods for axion detection are briefly reviewed. In Chapter 3 the experimental setup is described in detail. The basic principle and performance of the CCD detector as well as the X-ray telescope are discussed in Chapter 4. The analysis of the 2003 data and experimental results are discussed in Chapter 5, Chapter 6 gives the results of the 2004 data analysis in detail. Finally, the combined result of $g_{a\gamma}$ and future prospects are presented in Chapter 7.

Chapter 2

Axion Physics

2.1 Theoretical motivation

The axion has been proposed as an explanation of the strong CP problem in quantum chromodynamics. It is a hypothetical neutral pseudoscalar particle, which has no spin and very feebly interacts with ordinary particles like photons and quarks. In this Section, starting with the strong CP problem, the theoretical origin of the axion and its properties are briefly reviewed.

2.1.1 The U(1)$_A$ problem

QCD describes the theory of the color symmetry of strong interactions between colored quarks and vector gluons. Calculations in QCD are typically perturbative, which means that particles and interactions are characterized by expanding the field around the ground state or vacuum. The typical perturbative QCD Lagrangian L_{pert} is described by the standard form

$$L_{pert} = \sum_f \overline{q}_f (i\gamma^\mu D_\mu - m_f) q_f - \frac{1}{4} G^a_{\mu\nu} G^{\mu\nu}_a, \tag{2.1}$$

where f denotes all flavors of quarks, q are the quark fields with constituent quark masses m_f and $G^a_{\mu\nu}$ are the eight vector gluon fields with $a = 1, \ldots, 8$. The covariant derivative D_μ is

$$D_\mu \equiv \partial_\mu + i\mathrm{g} T_a G^a_\mu, \tag{2.2}$$

where T_a are the generators which commute with each other. The gauge invariant gluon field strength tensor $G^a_{\mu\nu}$ with coupling g between quarks and gluons is

$$G^a_{\mu\nu} = \partial_\mu G^a_\nu - \partial_\nu G^a_\mu - \mathrm{g} f_{abc} G^b_\mu G^c_\nu. \tag{2.3}$$

The first term of Eq. (2.1) is the kinetic energy and mass term of q, and the second shows that gluons themselves carry color charge. They arise due to the non-Abelian[1] character of the gauge group. The derivation of Eq. (2.1) can be found in Ref. [1].

In the chiral limit $m_f \to 0$, the QCD Lagrangian L_{pert} is invariant under a global axial vector transformation, i.e. the axial current is conserved. If it is true, there would be a symmetry between left- and right-handed quarks, leading to parity degeneracy of the hadron spectrum. The u and d quark masses are so small compared with the scale of QCD, so that the chiral symmetry is a reasonable approximation. However, this symmetry is not observed experimentally in the spectrum of hadrons, implying that the chiral symmetry is broken spontaneously. As a consequence, there should exist a zero mass pseudoscalar Goldstone boson. Its mass would be zero in the limit $m_f = 0$ but would be expected to be non-zero yet very small in the realistic case of small quark masses [2].

Since L_{pert} is invariant under chiral transformations, with three massless quarks there should be nine light pseudoscalars. The obvious pseudoscalar particles are π, K, η and η' whose masses would be zero if $m_f = 0$. The η is the eighth of a pure SU(3) octet state and the $\eta'(J^{PC} = 0^{-+})$ is a fairly pure SU(3) singlet state[2] [3]. However, the mass of η' is heavier ($m_{\eta'}$ = 958 MeV) than predicted since the mass of a flavor singlet pseudoscalar particle should be

$$m_{\eta'} \leq m_{\pi}\sqrt{3}. \tag{2.4}$$

This inconsistency is known as the U(1)$_A$ problem [4].

2.1.2 The θ-vacuum

A solution to the U(1)$_A$ problem was given by 't Hooft [5]. Due to instanton effects, so-called topological vacua, the U(1)$_A$ axial current has an anomaly that leads to the physical nonconservation of the ninth axial charge, so that the U(1)$_A$ symmetry is broken by the Adler-Bell-Jackiw (ABJ) anomaly [6]. Anomalies occur in field theories usually when classical symmetries are broken by quantum effects. Consequently, this anomaly gives rise to an additional term, the so-called θ term, to the QCD Lagrangian Eq. (2.1)

$$L_{\theta} = \theta \frac{g^2}{32\pi^2} G^a_{\mu\nu} \widetilde{G}^{\mu\nu}_a, \tag{2.5}$$

---

[1] Non-Abelian means that not all the generators commute with each other. The commutator of any two is a linear combination of all generators: $[T_a, T_b] = i f_{abc} T_c$. If the structure constants of the group f_{abc} is not equal to zero, then the group is non-Abelian.

[2] $|\eta'> = \frac{1}{\sqrt{3}}(u\overline{u} + d\overline{d} + s\overline{s})$

where g is the strong coupling constant, $G^a_{\mu\nu}$ is the color field strength tensor and $\widetilde{G}^{\mu\nu}_a$ denotes its dual tensor given by

$$\widetilde{G}^{\mu\nu}_a = -\frac{1}{2}\varepsilon^{\mu\nu\alpha\beta}G^a_{\alpha\beta}. \tag{2.6}$$

The ε tensor that occurs in the definition of $\widetilde{G}$ implies that L_θ is not invariant under parity and thus odd under CP.

One question is then why a CP violating L_θ term is allowed in the QCD Lagrangian. Here the up and down (light) quarks are only treated, so the quark fields and the quark mass matrix are

$$q = \begin{pmatrix} u \\ d \end{pmatrix}, \quad M_q = \begin{pmatrix} m_u & 0 \\ 0 & m_d \end{pmatrix}. \tag{2.7}$$

Let us make a U(1)$_A$ rotation on the up quark field $u \rightarrow e^{i\alpha\gamma^5}u$ and this rotation is truly chiral because right and left handed fields transform in different ways:

$$u_R \rightarrow e^{i\alpha}u_R, \quad u_L \rightarrow e^{-i\alpha}u_L. \tag{2.8}$$

Under a U(1)$_A$ rotation, the mass term of the up quark is not invariant, however if $m_u = 0$, this axial symmetry would be restored. In general, the mass of the up quark is not zero, therefore the additional L_θ term should be present in the QCD Lagrangian.

Considering the additional term in Eq. (2.5) with the form

$$L_\theta = constant \times tr(G_{\mu\nu}\widetilde{G}^{\mu\nu}), \tag{2.9}$$

where the corresponding dual of the field strength tensor is given in Eq. (2.6). In electromagnetism, an analogous term would be formed by

$$tr(F_{\mu\nu}\widetilde{F}^{\mu\nu}) = 4\vec{E}\cdot\vec{B}. \tag{2.10}$$

This term clearly violates the parity (P) but is conserved under charge conjugation (C), since [7]

$$\begin{aligned} P\vec{E} &= -\vec{E}, \quad P\vec{B} = \vec{B} \\ C\vec{E} &= -\vec{E}, \quad C\vec{B} = -\vec{B}. \end{aligned} \tag{2.11}$$

Subsequently, the presence of the term Eq. (2.5) in QCD will give rise to a violation of CP and P invariance, since it is proportional to $\vec{E}\cdot\vec{B}$.

The chiral transformations change the vacuum angle [8, 9], i.e. a chiral U$(1)_A$ rotation on the θ-vacuum[3] shifts the vacuum angle by the value of the phase of the determinant of the quark mass matrix. There is thus an additional contribution to the θ term as given by

$$\overline{\theta} = \theta + arg(detM_q), \tag{2.12}$$

where M_q is the diagonal quark mass matrix obtained by the symmetry breaking. Therefore, the effect of the vacuum may be represented by a new term in the QCD Lagrangian

$$L_{QCD} = L_{pert} + L_{\overline{\theta}} = L_{pert} + \overline{\theta}\frac{g^2}{32\pi^2} G^a_{\mu\nu}\widetilde{G}^{\mu\nu}_a, \tag{2.13}$$

where $\overline{\theta}$ is the effective vacuum angle in the basis where all quark masses are real and diagonal.

2.1.3 The strong CP problem

As we have seen in Section 2.1.2, the U$(1)_A$ problem is solved with $L_{\overline{\theta}}$, however another problem takes its place, i.e. the strong CP problem was born after the solution of the U$(1)_A$ problem by instantons. $L_{\overline{\theta}}$ violates charge conjugation (C), charge conjugation times parity (CP) and time reversal (T) symmetries. P violation is a well-known feature in the weak interaction, but CP and hence T violation has so far been found only in the neutral kaon system. Since a CP violation, assuming validity of the CPT theorem, implies a violation of T, the observed violation of CP provoked both experimental and theoretical studies of electric dipole moments of neutral particles, in particular that of the neutron.

An investigable consequence of CP violation is an electric dipole moment (EDM) of the neutron d_n, which is theoretically estimated to be $d_n = 8.2 \times 10^{-16}\,\overline{\theta}$ e·cm. Baluni calculated this neutron electric dipole moment within the MIT bag model[4] and details can be found in Ref. [10]. The current experimental upper limit of neutron EDM [11, 12] is found to be

$$|d_n| < 2.9 \times 10^{-26}\ \mathrm{e \cdot cm} \quad (90\%\ \mathrm{C.L.}). \tag{2.14}$$

It indicates that $\overline{\theta}$ cannot be much greater than 10^{-10}. Little is known of how large $\overline{\theta}$ should be. The parameter $\overline{\theta}$ can basically possess any value between 0 and 2π. However, why should the $\overline{\theta}$ parameter be so close to zero. The smallness of $\overline{\theta}$ is referred to as the strong CP problem.

---

[3] The superposition of the degenerate vacua is called the θ-vacuum: $|\theta> \equiv \sum_{n=-\infty}^{\infty} e^{-in\theta}|n>$.

[4] The bag model describes that quarks are confined within a hadron or meson. It is assumed to be static with spherically symmetric boundaries and the interaction between quarks can be ignored.

2.1.4 The Peccei-Quinn solution

The strong CP problem is a small blemish on the successful standard model of particle physics. Many physicists have suggested to evade this problem. The most attractive solution to the strong CP problem was proposed by Peccei and Quinn in 1977 [13, 14]. The idea is based on making $\overline{\theta}$ a dynamical field. They explained the small value of $\overline{\theta}$ by introducing a new global $U(1)_{PQ}$ symmetry, namely Peccei-Quinn (PQ) symmetry. The PQ mechanism involves a pseudoscalar boson, called axion, which arises by spontaneous symmetry breaking (SSB) at an energy scale f_a.

Due to the chiral anomaly of the PQ symmetry, this new field gives an additional term L_a to the QCD Lagrangian L_{QCD}

$$L_{QCD} = L_{pert} + \overline{\theta}\frac{g^2}{32\pi^2} G^a_{\mu\nu}\widetilde{G}^{\mu\nu}_a + L_a, \tag{2.15}$$

$$L_a = -\frac{1}{2}(\partial_\mu a)^2 + C_a \frac{a}{f_a}\frac{g^2}{32\pi^2} G^a_{\mu\nu}\widetilde{G}^{\mu\nu}_a, \tag{2.16}$$

where a is the axion field, f_a is the scale of the spontaneous PQ symmetry breaking and C_a is a model dependent constant which will be discussed later in detail. The first term of Eq. (2.16) is the kinetic energy of the axion field and the second term represents the interaction of the axion with gluons. This term is similar to the CP violating term of Eq. (2.5) and provides an effective potential $V_{eff}(a)$ for the axion field a. The minimum of this potential determines the vacuum expectation value (VEV) of the axion field $< a >$:

$$\left\langle \frac{\partial V_{eff}}{\partial a} \right\rangle = -\frac{C_a}{f_a}\frac{g^2}{32\pi^2}\langle G^a_{\mu\nu}\widetilde{G}^{\mu\nu}_a\rangle|_{<a>} = 0. \tag{2.17}$$

It forces the VEV of the axion field to have the value

$$< a >= -\frac{f_a}{C_a}\overline{\theta} \tag{2.18}$$

for which the $G\widetilde{G}$ term vanishes. To make $\overline{\theta}$ a dynamical field, the true vacuum is chosen as $\overline{\theta} = 0$. The minimum of the potential energy is at $\overline{\theta} = 0$ because of the periodicity of the axion potential [15]. The $\overline{\theta}$ parameter has been effectively replaced by the dynamical axion field and its mass arises because of the non perturbative $G\widetilde{G}$ term.

Thus the dynamical relaxation of $\overline{\theta}$ solves the strong CP problem. The neutron electric dipole moment does not depend on f_a. For unrestricted values of f_a, the strong CP problem is solved. The standard axion corresponds to $f_a \approx 250$ GeV, and the invisible axion corresponds to $f_a \gg 250$ GeV, which is actually restricted by astrophysics and cosmology.

2.1.5 The standard axion

As given above in Section 2.1.4, introducing an axion with appropriate properties can solve the strong CP problem. This Section gives an outline of the standard Peccei-Quinn-Weinberg-Wilczek (PQWW) axion.

In the original PQWW axion models [13, 16] one needs to introduce two Higgs fields, in this case two Higgs doublets. The global PQ symmetry is introduced in the standard model by having two Higgs doublets with degenerate vacua. Quarks, leptons and the intermediate bosons of this theory get a mass because the Higgs doublets are assumed to have nonzero vacuum expectation value $\lambda_{i=1,2}$. The symmetry must be spontaneously broken at an energy scale f_a which is equal to the electroweak scale [17]

$$f_a = (\lambda_1^2 + \lambda_2^2)^{1/2} = (\sqrt{2}\mathrm{G_F})^{-1/2} \approx 250 \text{ GeV} = f_{weak}, \tag{2.19}$$

where $\mathrm{G_F}$ is the Fermi coupling constant. The ratio of the expectation values of the Higgs fields is denoted by $x = \lambda_1/\lambda_2$. The x is a positive number by definition and there is no special reason to have an arbitrary value. Thus the original axion was characterized by a SSB scale of order the weak scale and a mass of order about 100 keV.

Bardeen and Tye [18] estimated the mass of the PQWW axion using current algebra methods. The PQ current is constructed from the axion, quark and lepton transformations under the PQ symmetry. The axion gets a mass because the PQ current has the color anomaly. The U(1)$_{PQ}$ symmetry is associated with the U(1) axial vector current constructed from the axion, quark and lepton transformation under PQ symmetry:

$$J^{\mu}_{PQ} = f_a \partial^{\mu} a + \frac{x}{2} \sum \bar{u}\gamma^{\mu}\gamma_5 u + \frac{1}{2x} \sum \bar{d}\gamma^{\mu}\gamma_5 d + (\text{lepton currents}), \tag{2.20}$$

where a is the axion field, u is the charge +2/3 quark and d is the charge -1/3 quark. The lepton current can be neglected for the axion mass. This current is conserved except for the strong interaction anomaly, i.e. it is not stable because of an anomaly. Thus the anomaly free chiral current denoted by $\tilde{J}^{\mu}_{PQ}$ can be constructed by subtracting a proper fraction from J^{μ}_{PQ}

$$\tilde{J}^{\mu}_{PQ} = J^{\mu}_{PQ} - N(x + \frac{1}{x})(\frac{1}{1+Z})(\bar{u}\frac{\gamma^{\mu}\gamma_5}{2}u + \bar{d}\frac{\gamma^{\mu}\gamma_5}{2}d), \tag{2.21}$$

where u and d are the usual light quarks, $Z \equiv m_u/m_d \approx 0.56$ is the ratio of the light quark masses and N is the number of quark doublets. The current is conserved in the limit of vanishing quark masses. The anomalous divergence of this current depends on the total number of quark doublets N and is given by

$$\partial_{\mu}\tilde{J}^{\mu}_{PQ} = N(x + \frac{1}{x}) \frac{m_u}{m_u + m_d} (\bar{u}\gamma^{\mu}\gamma_5 u + \bar{d}\gamma^{\mu}\gamma_5 d). \tag{2.22}$$

Using standard current algebra methods, the axion mass is related to the divergence of $\tilde{J}_a^\mu$

$$\begin{aligned} m_a^2 f_a^2 &= N^2(x+\frac{1}{x})^2 \frac{Z}{(1+Z)^2}(-m_d < \bar{u}u > -m_u < \bar{d}d >) && (2.23) \\ &= N^2(x+\frac{1}{x})^2 \frac{Z}{(1+Z)^2} m_{\pi^0}^2 f_\pi^2, && (2.24) \end{aligned}$$

where m_{π^0} = 135 MeV and f_π = 93 MeV are the pion mass and decay constant[5]. We obtain then the axion mass

$$m_a = N(x+\frac{1}{x})\frac{\sqrt{Z}}{1+Z}\frac{f_\pi m_{\pi^0}}{f_a} \cong 25N(x+\frac{1}{x}) \text{ keV}, \tag{2.25}$$

with $N = 2$, $x \approx 1$ and $Z \approx 0.56$, the axion mass m_a is at least 100 keV.

However, this axion was quickly ruled out by several laboratory experiments. One of those experiments as an example will be shortly summarized. If $f_a = f_{weak}$, then the axion mass is quite light ($\mathcal{O}$(100 keV)) and it has a long decay time ($\mathcal{O}(10^{-1}$ sec)). Therefore, in the Crystal Ball experiment the direct coupling of the axion with heavy quarks was measured by determining the branching ratios in a parallel search for both J/ψ and Υ decays to $\gamma + a$ [19]. The decay rate of the J/ψ to a photon plus an axion is given by

$$B(J/\psi \rightarrow \gamma a) \propto x^2, \tag{2.26}$$

where the free parameter x is the ratio of the vacuum expectation values of the two Higgs fields. The corresponding formula for Υ decay is given by

$$B(\Upsilon \rightarrow \gamma a) \propto \frac{1}{x^2}. \tag{2.27}$$

Due to couplings of the axion to charge +2/3 and -1/3 quarks, each rate is proportional to x^2 and $1/x^2$, respectively. In order to eliminate the free parameter x, Eq. (2.26) and (2.27) can be combined by

$$\begin{aligned} B(J/\psi \rightarrow \gamma a)\cdot B(\Upsilon \rightarrow \gamma a) &= B(J/\psi \rightarrow \mu^+\mu^-)\cdot B(\Upsilon \rightarrow \mu^+\mu^-)\frac{(\mathrm{G_F} m_c m_b)^2}{2\pi^2\alpha^2} \\ &= (1.4 \pm 0.3)\times 10^{-8}, && (2.28) \end{aligned}$$

where $\mathrm{G_F}$ is the Fermi coupling constant, m_c = 1.4 GeV is the mass of the charmed quark, m_b = 4.9 GeV is the mass of the bottom quark, and α is the fine structure constant. The error

---

[5] The pion decay constant f_π is the same for charged and neutral pions.

arises from the experimental uncertainty in the $\mu^+\mu^-$ branching ratios[6] and the quark masses. The Crystal Ball experiment [20] has obtained an upper limit of

$$B(J/\psi \to \gamma a) \cdot B(Y \to \gamma a) < 5.6 \times 10^{-10}. \tag{2.29}$$

Based on the search just mentioned above, one can carefully conclude that

$$f_a > 10^3 \text{ GeV} \quad \text{or} \quad m_a < 6 \text{ keV}. \tag{2.30}$$

Hence the search proved that the original axion was ruled out within the standard model.

2.1.6 The invisible axion

In order to keep the PQ solution of the strong CP problem, the invisible axion was invented. The main problem of the PQWW axion was that the U(1)$_{PQ}$ symmetry breaking scale f_a is related to the electroweak symmetry breaking scale f_{weak}. Practically, it is not necessary that the PQ symmetry breaking scale is the same as the weak scale. Hence the symmetry scale is an arbitrary parameter in invisible axion models, implying that the couplings of axions are not fixed. The dynamical adjustment of the strong CP parameter $\overline{\theta} = 0$ works therefore for any scale of f_a. The invisible axion model assumes that the symmetry breaking scale is much larger than the electroweak symmetry breaking scale. If $f_a \gg f_{weak}$, then the axions are very light, very feebly coupled and very long lived. For these reasons, they were originally called the invisible axion.

In invisible axion models, one introduces a new complex scalar field σ which does not take part in the weak interactions [15]. Due to the assumption of $f_a \gg f_{weak}$, in all these models the U(1)$_{PQ}$ symmetry should be broken by the vacuum expectation value of the new scalar field, so that the axion field can be simply interpreted as the phase of the singlet complex scalar field. The complex scalar field σ possesses a U(1)$_{PQ}$ global symmetry described by the Lagrangian

$$\begin{aligned} L &= (\partial_\mu \sigma)^* (\partial^\mu \sigma) - \mathrm{V}(\sigma) \\ &= (\partial_\mu \sigma)^* (\partial^\mu \sigma) + \mu^2 \sigma^* \sigma - \lambda (\sigma^* \sigma)^2 \end{aligned} \tag{2.31}$$

with mass μ and coupling λ. This Lagrangian is invariant under a chiral phase transformation, which is usually referred to as the PQ symmetry, of form

$$\sigma \quad \to \quad e^{i\alpha} \sigma, \tag{2.32}$$

where α is a constant. The potential V(σ) is then chosen to be a Mexican hat with an absolute minimum at $\sigma = f_a/\sqrt{2}$. The ground state is characterized by a nonvanishing vacuum

---

[6] $B(J/\psi \to \mu^+\mu^-) = 0.069 \pm 0.009$ and $B(Y \to \mu^+\mu^-) = 0.033 \pm 0.005$ [20]

expectation value $<\sigma>=(f_a/\sqrt{2})e^{i\varphi}$ with an arbitrary phase φ. The minimum breaks spontaneously the PQ symmetry because it is not invariant under the transformation of Eq. (2.32). Then we may write

$$\sigma = \frac{1}{\sqrt{2}}(f_a+\rho)e^{ia/f_a} \tag{2.33}$$

in terms of new fields a and ρ corresponding to angular and radial excitations around the ground state. The potential V(σ) provides a large mass for ρ, so that the massless mode a is linked with the axion [21].

The invisible axion models can be classified into two types according to direct coupling to leptons. One is the Kim-Shifman-Vainshtein-Zakharov (KSVZ) axion, so-called hadronic axion or heavy quark axion, which has to introduce heavy quarks [15, 22]. Another is the Dine-Fischler-Srednicki-Zhitnitskii (DFSZ) axion, so-called GUT axion, where one introduces additional Higgs doublets so that both light quarks and Higgs doublets carry non-vanishing PQ charges [23]. The main difference between KSVZ and DFSZ models is that in the latter model it is possible to have a very small coupling with leptons and both light quarks.

KSVZ axion

In the hadronic axion model, one introduces a new heavy quark Q [22]. The SU(2)×U(1) singlet field σ interacts with Q which carries U(1)$_{PQ}$ charge by the Yukawa interaction. The relevant Yukawa coupling and Higgs potential consistent with the PQ symmetry are

$$\begin{aligned} L_{KSVZ} &= -f\overline{Q}_L\sigma Q_R - f^*\overline{Q}_R\sigma^* Q_L && (2.34)\\ V[\varphi,\sigma] &= -\mu_\varphi^2\varphi^\dagger\varphi - \mu_\sigma^2\sigma^*\sigma + \lambda_\varphi(\varphi^\dagger\varphi)^2 + \lambda_\sigma(\sigma^*\sigma)^2 + \lambda_{\varphi\sigma}\varphi^\dagger\varphi\sigma^*\sigma, && (2.35)\end{aligned}$$

where φ is the Higgs doublet in the standard model [15]. The Lagrangian is invariant under the PQ transformation,

$$Q_L \to e^{i\alpha/2}Q_L\ , \quad Q_R \to e^{-i\alpha/2}Q_R. \tag{2.36}$$

The associated PQ current due to the Noether theorem is

$$J^\mu_{PQ} = f_a\partial^\mu a - \frac{1}{2}\overline{Q}\gamma^\mu\gamma_5 Q. \tag{2.37}$$

However, the axial current has an ABJ anomaly and hence, as we have seen in Section 2.1.5, the appropriate axion current was constructed from the divergence of the current

$$J^\mu_a = f_a\partial^\mu a - \frac{1}{2}\overline{Q}\gamma^\mu\gamma_5 Q + \frac{1}{2(1+Z)}(\overline{u}\gamma_\mu\gamma_5 u + \overline{d}\gamma_\mu\gamma_5 d). \tag{2.38}$$

The axion mass is estimated as

$$m_a^2 f_a^2 = (\frac{1}{1+Z})^2 Z(-m_d < \bar{u}u > -m_u < \bar{d}d >) = (\frac{\sqrt{Z}}{1+Z} f_\pi m_{\pi^0})^2, \tag{2.39}$$

where $Z \equiv m_u/m_d \approx 0.56$. Therefore, the axion mass of KSVZ model is given by

$$m_a = \frac{f_\pi m_{\pi^0}}{f_a} \frac{\sqrt{Z}}{1+Z} \cong 0.61\text{eV} \frac{10^7\text{GeV}}{f_a}, \tag{2.40}$$

where f_a is the symmetry breaking scale. The coupling with ordinary matters is discussed in detail in Section 2.1.7.

DFSZ axion

Since σ is a singlet, a direct coupling of σ to light quarks is not possible. The conventional way is to couple σ to the Higgs doublets which then couple to the light quarks. Therefore, the DFSZ axion introduced an additional Higgs doublet. In this model, the expected strength of the coupling of axion to leptons and quarks is straightforward to compute. This is reviewed in detail in Ref. [23]. Moreover, using current algebra methods give the same expression for the axion mass as the KSVZ model.

2.1.7 Axion properties and couplings

In this Section the properties of the axion and its couplings with ordinary matter, i.e. photons, electrons and nucleons are described. An important point is that the axion properties depend on the PQ symmetry breaking scale f_a, i.e. the axion coupling constant is proportional to the axion mass m_a, or equivalently to the inverse of the PQ scale $1/f_a$:

$$\text{coupling} \propto m_a \propto \frac{1}{f_a}. \tag{2.41}$$

Axion mass

As discussed above in Section 2.1.4, the axion is a Goldstone boson associated with the spontaneously broken chiral $\mathrm{U}(1)_{PQ}$ symmetry. Although axions are massless, they obtain an effective mass by interaction with gluons as given in Eq. (2.16). This induces transitions to $q\bar{q}$ states and hence to neutral pions as shown in Fig. 2.1, which means physically that a and π^0 are mixing with each other. Subsequently, the axion acquires a small mass which is approximately given by $m_a f_a \sim m_{\pi^0} f_\pi$ [24]. The mass is estimated following as above current algebra methods and is given by in Eq. (2.40) which is related to the unknown symmetry breaking scale f_a.

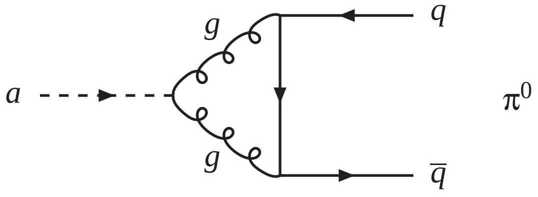

Figure 2.1: Axion mixing with $q\overline{q}$ states and thus with π^0.

The axion-photon coupling

The most important interaction is the effective axion coupling to two photons as shown in Fig. 2.2 which arises because of the axion-pion mixing. The pion couples to two photons due to the electromagnetic anomaly and this results in an axion-photon coupling. In general, the effective Lagrangian for the interaction of axions with photons is written as [21]

$$L_{int} = -\frac{1}{4} g_{a\gamma} F_{\mu\nu} \widetilde{F}^{\mu\nu} a = g_{a\gamma} \vec{E} \cdot \vec{B} a, \tag{2.42}$$

where F is the electromagnetic field strength tensor, $\widetilde{F}$ its dual and a the axion field. The axion-photon coupling strength $g_{a\gamma}$ with the dimension (energy)$^{-1}$ is given by

$$g_{a\gamma} = \frac{\alpha}{2\pi f_a} \left[\frac{E}{N} - \frac{2(4+z+w)}{3(1+z+w)} \right], \tag{2.43}$$

where $\alpha = 1/137$ is the fine structure constant and z and w are the mass ratio of the u to the d quark and the u to the s quark, respectively, given by [25]

$$\begin{aligned} z \equiv \quad & m_u/m_d & \cong 0.553 \pm 0.043, \\ w \equiv \quad & m_u/m_s & \cong 0.029 \pm 0.004. \end{aligned} \tag{2.44}$$

Using Eq. (2.44), the coupling strength can be rewritten by

$$g_{a\gamma} = \frac{\alpha}{2\pi f_a} \left(\frac{E}{N} - 1.95 \pm 0.08 \right) = \frac{\alpha}{2\pi f_a} C_{a\gamma}. \tag{2.45}$$

The ratio of the electromagnetic to the color anomaly of the PQ symmetry E/N is defined by

$$\frac{E}{N} \equiv \sum_{i=fermions} Q^i_{PQ} (Q^{em}_i)^2, \tag{2.46}$$

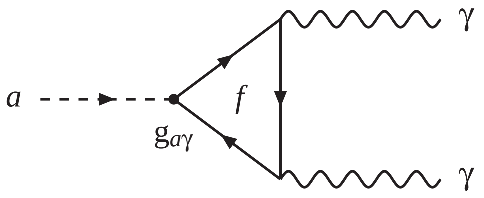

Figure 2.2: Diagram for the interaction of an axion with two photons via a fermion triangle loop.

where Q_{PQ} is 1 for color singlets (charged lepton) and 3 for color triplets (quarks), and Q^{em} is the electric charge of fermions.

In the DFSZ model,

$$\frac{E}{N} = \left[1 \cdot (-1)^2 + 3 \cdot \left(\frac{2}{3}\right)^2 + 3 \cdot \left(-\frac{1}{3}\right)^2\right] = \frac{8}{3}, \tag{2.47}$$

which leads to $C_{a\gamma} \approx 0.72$ [15]. In the KSVZ models, however, axions couple only to light quarks

$$\frac{E}{N} = \left[3 \cdot \left(\frac{2}{3}\right)^2 + 3 \cdot \left(-\frac{1}{3}\right)^2 + 3 \cdot \left(-\frac{1}{3}\right)^2\right] = 2. \tag{2.48}$$

The hadronic axion has $E/N = 2$, so that it leads to a small $C_{a\gamma} \approx 0.05$, i.e. the axion-photon coupling is strongly suppressed and may actually vanish.

Axion-electron interaction

Axions interact with fermions according to a pseudo-scalar or a derivative axial vector interaction. The effective Lagrangian for the interactions of axions with electrons is [26]

$$L_{int} = i\frac{g_{ae}}{2m_e}\partial_\mu a(\bar{e}\gamma^\mu\gamma_5 e) \tag{2.49}$$

with the associated Feynman diagram as shown in Fig. 2.3. The pseudo-vector coupling may be written instead as a pseudo-scalar coupling, e.g. $ig_{ae}a(\bar{e}\gamma_5 e)$, by means of a suitable phase

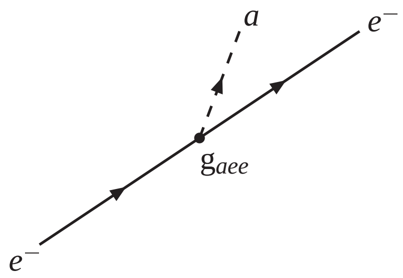

Figure 2.3: Direct coupling of axion with electron. This Feynman diagram is only for DFSZ axions.

rotation of the fermion fields. The axion coupling for electrons in terms of the axion mass is given by

$$g_{ae} = C_{ae}\frac{m_e}{f_a} = C_{ae} 0.85 \times 10^{-10}\, \frac{m_a}{\mathrm{eV}}. \tag{2.50}$$

In the KSVZ model $C_{ae} = 0$ at tree level, even if there are small radiatively induced couplings [27]. In the DFSZ model

$$C_{ae} = \cos^2\beta / N_f, \tag{2.51}$$

where $\cos^2\beta$ is the ratio of vacuum expectation values x and N_f is the number of families, which is 3.

Axion-nucleon interaction

When two nucleons collide, one of the axion emission processes in a hot dense star, e.g. in a supernova, is nucleon bremsstrahlung as shown in Fig. 2.4. This process is related to the axion coupling to nucleons. The nucleon interaction in general axion models were investigated by Kaplan [28]. The axion nucleon coupling [26] is given by

$$L_{int} = i\frac{g_{aN}}{2m_N}\partial_\mu a(\overline{N}\gamma^\mu\gamma_5 N) \tag{2.52}$$

with an axion coupling to nucleons

$$g_{aN} = C_{aN}\frac{m_N}{f_a} = C_{aN} 1.56 \times 10^{-7}\, \frac{m_a}{\mathrm{eV}}, \tag{2.53}$$

where C_{aN} is the effective PQ charge of the nucleon. In the axion nucleon coupling the PQ charge for nucleons is given by roughly 30% of protons and 70% of neutrons in the relevant

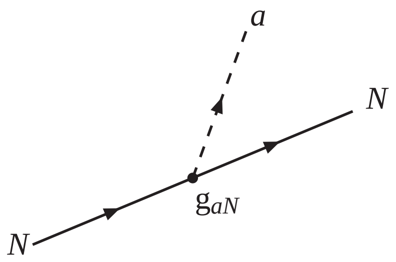

Figure 2.4: Coupling of axion with nucleon.

region of a supernova core[7],

$$C_{aN} \equiv \sqrt{0.3C_{ap}^2 + 0.7C_{an}^2}. \tag{2.54}$$

The charges for proton and neutron are [21]

$$\begin{aligned} C_{ap} &= (C_u - \eta)\Delta u + (C_d - \eta z)\Delta d + (C_s - \eta w)\Delta s, \\ C_{an} &= (C_u - \eta)\Delta d + (C_d - \eta z)\Delta u + (C_s - \eta w)\Delta s, \end{aligned} \tag{2.55}$$

where $\eta \equiv (1+z+w)^{-1}$ and the quark fraction of nucleons are

$$\Delta u = +0.85, \quad \Delta d = -0.41, \quad \Delta s = -0.08 \tag{2.56}$$

with uncertainties of ±0.03 each [29]. The axion couples to the axial vector current of the fundamental fermions, i.e. to the particle's spin, so that the interaction strength with protons depends on the proton spin.

In the DFSZ model,

$$C_u = \frac{\sin^2\beta}{N_f} \quad \text{and} \quad C_d = C_s = \frac{\cos^2\beta}{N_f}. \tag{2.57}$$

Using

$$\begin{aligned} C_u + C_d &= 1/N_f, \\ C_u - C_d &= -\cos 2\beta/N_f, \\ C_d = C_s &= C_{ae}, \end{aligned} \tag{2.58}$$

---

[7] When the iron core of the supernova star begins to collapse, it consists of almost equal numbers of protons to neutrons ($N_p/N_n \sim 0.4$). However N_p drops somewhat during the infall phase because ν_e escape before all neutrinos are trapped.

we obtain then with $N_f = 3$

$$\begin{aligned} C_{ap} &= -0.10 - 0.45\cos^2\beta, \\ C_{an} &= -0.18 + 0.39\cos^2\beta. \end{aligned} \tag{2.59}$$

On the other hand, in the KSVZ model, $C_u = C_d = C_s = 0$ which gives

$$\begin{aligned} C_{ap} &= -0.39, \\ C_{an} &= -0.04. \end{aligned} \tag{2.60}$$

Therefore, the effective nucleon coupling is

$$C_{aN} \equiv \sqrt{0.3C_{ap}^2 + 0.7C_{an}^2} \approx 0.2. \tag{2.61}$$

Axion couplings to photons, electrons and nucleons yield bounds on the axion mass, or equivalently on the PQ symmetry breaking scale. This is discussed in Section 2.2.

The lifetime of the axion

All axion couplings are proportional to $1/f_a$, or equivalently to m_a. This means that the smaller the axion mass, or the larger the PQ symmetry breaking scale, the more weakly the axion couples. The coupling of the axion to two photons arises through the electromagnetic anomaly of the PQ symmetry and the axion decay into two photons is allowed with a lifetime [30, 31]

$$\tau_{a\gamma\gamma} = 6.8 \times 10^{24}\text{sec}\frac{(m_a/\text{eV})^{-5}}{[(E/N - 1.95)/0.72]^2}. \tag{2.62}$$

The axion lifetime to two photons depends on the 5th power of the axion mass and the ratio of the electromagnetic to the color anomaly[8]. For axions with masses $m_a = \mathcal{O}(1\text{ eV})$ the lifetime $\tau_{a\gamma\gamma}$ is $\mathcal{O}(10^{24}\text{ sec})$. The age of the universe is about 10^{18} sec, so that the light axions are very stable.

---

[8] For the DFSZ axions, $E/N = 8/3$ and $(E/N - 1.95) \simeq 0.72$.

2.2 Astrophysical bounds

While the properties of axion are well known in terms of the PQ symmetry breaking scale f_a, its quantity has no preferred value. It might lie anywhere in the range of 10^2 to 10^{19} GeV, corresponding to axion masses between 10^{-12} eV and 100 keV. Bounds on the axion mass m_a or PQ scale f_a are usually based on limits on the coupling strength with photons, electrons and nucleons. Those limits are constrained from astrophysical objects like the sun or horizontal branch stars where axion production would increase the stellar energy loss, the so-called energy loss argument. Very weakly interacting and small mass particles contribute to the energy loss in stars. This additional energy loss rate accelerates the cooling of the stars. Therefore, the observable cooling speed allows one to constrain the process or to detect new particles. The most relevant astrophysical objects, which are mainly globular cluster and the supernova 1987A, are described in this Section.

Stellar evolution

First of all, the stages of stellar evolution are shortly reviewed to understand how stars live and die. The Hertzsprung-Russell diagram illustrates the stellar luminosity on the vertical axis versus surface temperature on the horizontal axis as shown in Fig. 2.5. Red colours and cooler surface temperatures are to the right direction, and higher luminosities or lower magnitudes toward the top.

A hydrogen burning star is located in a single point on a curve called the main sequence. After central hydrogen exhaustion the helium ashes have accumulated at the center in a dense core surrounded by a hydrogen burning shell. The stellar surface becomes larger i.e. the luminosity increases and the surface temperature decreases, so that the star moves eventually over to a red giant branch. As the hydrogen burning continues, the helium in the core supports itself by thermal pressure. Soon it becomes so dense that the electrons become degenerate. The core of a red giant reaches its limiting mass when it becomes so hot and dense that helium ignites. Since the nucleus ^{8}Be, which consists of two α particles is unstable, He burning proceeds directly to carbon via the so-called triple α reaction ($3\alpha \rightarrow {}^{12}$C). In a red giant, core helium ignites when its mass is approximately $0.5M_\odot$[9] with central conditions of density of 10^6 g cm^{-3} and temperature of 10^8 K. Ultimately, the helium core ignites and the star moves over to horizontal branch. The final configuration with a helium burning core and a hydrogen burning shell is known as a horizontal branch star.

---

[9] Solar mass $M_\odot = 1.988 \times 10^{30}$ kg

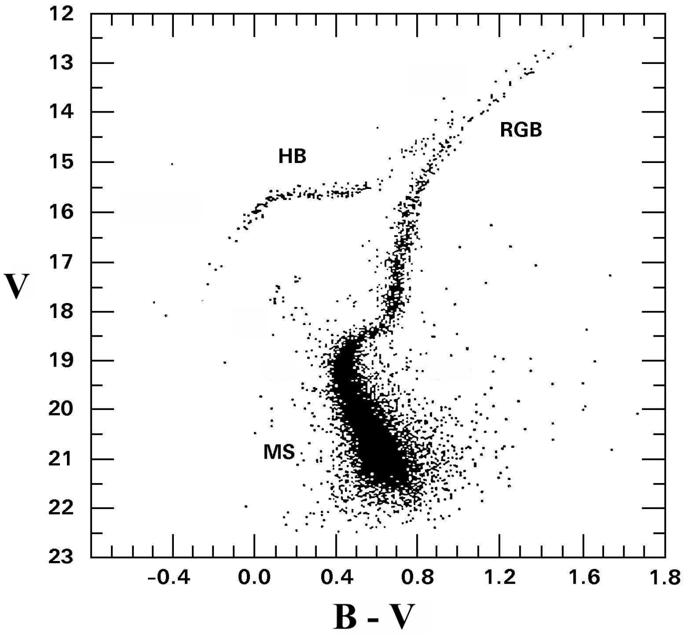

Figure 2.5: Hertzsprung-Russell diagram of stellar luminosity (V) versus surface temperature (B-V). The magnitude observed with a V filter (λ = 540 nm) is plotted vertically and the difference in magnitudes with a B filter (λ = 440 nm) and a V filter is plotted horizontally. Main sequence (MS): core hydrogen burning, Red giant branch (RGB): hydrogen burning in a thin shell with a growing core until the helium ignites, Horizontal branch (HB): helium burning in the core and hydrogen burning in a shell [32].

2.2.1 Axions and horizontal branch

Globular clusters are gravitationally bound concentrations of approximately ten thousands to one million stars, spread over a volume of several tens to about 200 light years in diameter. Stars in the globular cluster were all formed at essentially the same time and equal chemical properties. Particularly, two different kinds of stars are interesting for axions, namely the red giant branch (RGB) and the horizontal branch (HB).

A red giant is a star with a compact energy source at the center and a large gaseous body. The main characteristic of RGB stars is thus a degenerate helium core with shell hydrogen burning, while the horizontal branch star is characterized by a helium burning core with a hydrogen burning shell. HB stars are found on the horizontal part of the Hertzsprung-Russell diagram (Fig. 2.5). In the globular cluster, photons can be converted into axions via the axion-photon interaction, so-called Primakoff conversion [33], in both RGB and HB star cores. The Primakoff conversion is however much more effective in HB stars because of the different core densities.

Thus, the most limiting constraint on axion-photon coupling comes from HB stars in globular clusters. Axion production in these stars occurs via the Primakoff process $\gamma\gamma^* \to a$ where γ^* corresponds to the electromagnetic field induced by protons and electrons in the star plasma (Fig. 2.6).

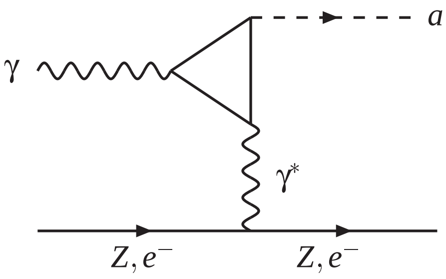

Figure 2.6: Primakoff conversion of axions in the Coulomb fields of charged particles.

Energy loss rate

The axionic energy loss rate of a non-degenerate plasma by the Primakoff effect was calculated in Ref. [34] and is given by

$$\varepsilon = \frac{g_{a\gamma}^2}{4\pi}\frac{T^7}{\rho}F(\kappa^2), \tag{2.63}$$

where the Debye-Hückel effect[10] is described by the dimensionless function

$$F(\kappa^2) = \frac{\kappa^2}{2\pi^2}\int_0^\infty dx \frac{x}{e^x-1}[(x^2+\kappa^2)\ln(1+\frac{x^2}{\kappa^2})-x^2], \tag{2.64}$$

where the dimensionless axion energy $x = \omega/T$. In the standard solar model, $\kappa^2 \approx 12$ throughout the sun with a variation of less than 15%. In the core of an HB star with $\rho = 10^4$ g cm^{-3} and $T = 10^8$ K, it is $\kappa^2 \approx 2.5$. One finds $F = 0.98$ and 1.84 for $\kappa^2 \approx 2.5$ and 12, respectively [35].

An argument to constrain the properties of new particles arises from the observed duration of helium burning of low mass stars, i.e. from the lifetime of the horizontal branch stars.

---

[10] The Debye-Hückel effect is a screening effect, i.e. the Primakoff effect involves the Coulomb fields of the target particles, and such electric fields will be screened in an environment of freely moving electric charges like a stellar plasma (screening effect). Thus the cross section of the relevant reaction of axion production will be reduced.

The measured HB/RGB number ratio in the globular clusters indicates that the duration of helium burning agrees with stellar evolution theory to within about 10%. It implies that the nonstandard energy loss of the helium core should not exceed about 10% of its standard energy production rate via triple α reaction, as given by

$$L_x < 0.1 L_{3\alpha}, \tag{2.65}$$

where $L_{3\alpha}$ is the standard helium burning luminosity of a HB star core and L_x is the nonstandard energy loss rate integrated over the core. The standard value of $L_{3\alpha}$ is about $20L_\odot$[11] and the core averaged energy rate is $\varepsilon_{3\alpha} \approx 80$ erg $\mathrm{g}^{-1}\mathrm{s}^{-1}$. Thus, the nonstandard energy loss rate is bound by

$$\varepsilon_x \lesssim 10 \text{ erg g}^{-1}\text{s}^{-1}. \tag{2.66}$$

With the Primakoff emission rate of Eq. (2.63), a bound on $\mathrm{g}_{a\gamma}$ can be derived from the energy loss argument applied to the globular cluster stars. It follows that at $\mathrm{T} \approx 10^8$ K the axionic energy loss rate is below 10 erg $\mathrm{g}^{-1}\mathrm{s}^{-1}$ for a density of about 0.6×10^4 g cm^{-3} corresponding to a classic plasma and for about 2×10^5 g cm^{-3} corresponding to degeneracy. For a typical HB star model one finds $\mathrm{T}_8^7/\rho_4 \approx 0.3$ where $\mathrm{T}_8 = \mathrm{T}/10^8$ K and $\rho_4 = \rho/10^4$ g cm^{-3}. Hence,

$$\varepsilon_a \approx \mathrm{g}_{10}^2 30 \text{ erg g}^{-1}\text{s}^{-1}, \tag{2.67}$$

where $\mathrm{g}_{10} \equiv \mathrm{g}_{a\gamma}/10^{-10}$ GeV^{-1}. The axionic energy loss rate should be smaller than the nonstandard energy loss of HB star core, so that we obtain a limit on the axion-photon coupling constant [21]

$$\mathrm{g}_{a\gamma} \lesssim 0.6 \times 10^{-10} \text{ GeV}^{-1} \quad \text{or} \quad f_a/C_{a\gamma} \gtrsim 4 \times 10^7 \text{ GeV}. \tag{2.68}$$

This constraint from HB stars, which is often referred to as the globular cluster limit, has an uncertainty in its estimation by a factor of 2. Therefore, the limit of the globular cluster $\mathrm{g}_{a\gamma} \lesssim 1.0 \times 10^{-10}$ GeV^{-1} is used in general to compare with experimental results of axion searches. Recalling that $\mathrm{g}_{a\gamma} = (\alpha/2\pi f_a) C_{a\gamma}$ with $C_{a\gamma} = E/N - 1.92$, in terms of corresponding axion mass is

$$m_a C_{a\gamma} < 0.3 \text{ eV}, \tag{2.69}$$

where $C_{a\gamma} \approx 0.05$ for KSVZ model and 0.75 for DFSZ model.

---

[11] Solar luminosity $L_\odot$ = 3.85 $\times 10^{33}$ erg/s, 1 erg $\equiv 10^{-7}$ J

2.2.2 Axions and low-mass red giants

In low-mass red giants, the primary axion emission processes are: the Compton like process $\gamma + e^- \to a + e^-$ and axion bremsstrahlung $e^- + Z \to e^- + Z + a$. A red giant core is nearly two orders of magnitudes denser than the core of an HB star, so that the main production is from the Bremsstrahlung process, as given in Fig. 2.7. Bremsstrahlung is a particularly important effect under the degeneracy conditions. In this case, one neglects e^-e^- collisions entirely which are suppressed by degeneracy relative to the electron nucleus process. If the electrons are strongly degenerated, the energy integrals can be done analytically.

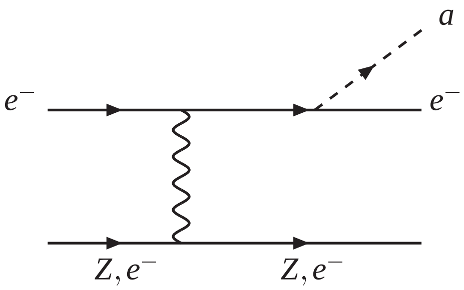

Figure 2.7: Electron bremsstrahlung emission of axions.

Therefore, the energy loss rate per unit volume is a simple integral over the initial state photon phase space weighted with the Bose Einstein occupation numbers. Details are found in Ref. [24]. For a single species of nuclei with charge Ze and atomic weight A, the energy loss rate per unit mass is

$$\varepsilon \approx \frac{\pi\alpha^2 g_{ae}^2}{60}\frac{Z^2}{A}\frac{\mathrm{T}^4}{m_u m_e^2}, \tag{2.70}$$

where α is fine structure constant and T a temperature. With T = 10^8K and $\rho = 10^6$g cm^{-3} in a degenerate helium core of red giants the axionic energy loss rate is

$$\varepsilon_a \approx g_{10}^2 1.6 \times 10^{26} \mathrm{erg\ g^{-1} s^{-1}}. \tag{2.71}$$

As mentioned above, one requirement is that a nonstandard energy loss must not exceed 10 erg g^{-1} s^{-1} for the typical conditions encountered in the core of a horizontal branch star and in the core of red giant just before helium ignition which both have T $\approx 10^8$ K. The stellar energy loss argument leads then to a limit on the axion-electron couplings

$$g_{ae} < 2.5 \times 10^{-13}\ \mathrm{GeV}^{-1}. \tag{2.72}$$

In terms of the coupling

$$g_{ae} \equiv C_{ae}\frac{m_e}{f_a} = C_{ae} 0.85 \times 10^{-10} m_a, \tag{2.73}$$

the resulting bound

$$f_a/C_{ae} > 2 \times 10^9 \text{ GeV} \quad \text{or} \quad m_a C_{ae} < 0.003 \text{ eV} \tag{2.74}$$

is currently the best limit on the axion-electron coupling only for DFSZ axion model, where $C_{ae} = \cos^2\beta/N_f$ with β an arbitrary angle and $N_f = 3$.

2.2.3 Axions and supernova 1987A

The most restrictive astrophysical limit on the axion nucleon coupling comes from the neutrino signal of the supernova (SN) 1987A. At first the observations of neutrino signal are shortly reviewed and then the interaction of axions with nucleons in a nuclear medium, i.e. supernova core, is discussed.

Supernova 1987A A massive star, which is larger than $8M_\odot$, with several burning shells surrounding a degenerate iron core inevitably becomes unstable at the end of its life. It collapses and ejects its outer mantle in a supernova (SN) explosion. When the explosion of the supergiant Sanduleak in the Large Magellanic Cloud, which is a satellite galaxy of our Milky Way at a distance of about 50 kpc[12], was detected on 23 February 1987. It was possible for the first time to measure the neutrino emission from a primary neutron star known as SN 1987A. Shortly after the gravitational collapse, the central temperature of the early formed neutron star was about 30 MeV and the central density was around 3×10^{14} g cm^{-3}, corresponding to a core size of a few tens of kilometers. During the collapse of the iron core the gravitational binding energy of about 3×10^{53} erg was liberated, and thus this energy is radiated over several seconds in thermal neutrinos [30].

Anomalies in the neutrino observations The neutrino signal from SN 1987A was observed by the $\overline{\nu}_e p \to n e^+$ reaction in several detectors. The events are shown in the time-energy plane in Fig. 2.8. The distribution of the Kamiokande and IMB events shows a number of puzzling features. The average $\overline{\nu}_e$ energies inferred from the Kamiokande and IMB observations are quite different. An outstanding anomaly is the large time gap of 7.3 s between the first 8 and the last 3 Kamiokande events. Ideas were proposed to explain the pulsed structure of the signal from the occurrence of a phase transition in the nuclear medium (pions or quarks) to a secondary collapse to a black hole. However, that gap is partially filled in by the IMB and Baksan data. The most significant anomaly is the remarkable deviation from isotropy of the events in both detectors, actually in conflict with the expected signature from $\overline{\nu}_e p \to n e^+$. The expected signal agrees only at the 0.8% level with the measured angular distribution. The combined set of IMB and Kamiokande data for high energy events is

---

[12] 1 pc = 3×10^{16} m = 3.262 ly

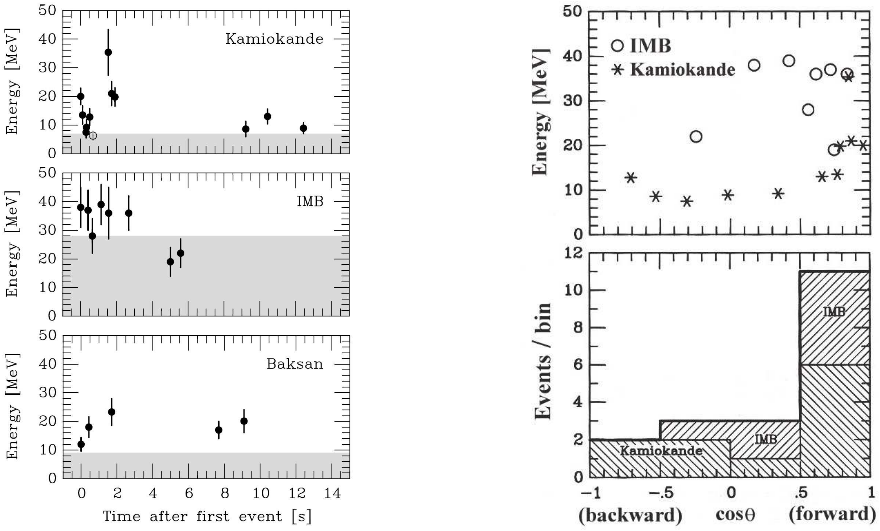

Figure 2.8: Left: The measured events of the SN 1987A neutrino at Kamiokande, IMB and Baksan. The energy refers to the detected secondary positrons from the $\overline{\nu}_e p \to ne^+$ reaction, not the primary neutrinos. In the shaded area the trigger efficiency is less than 30%. The time is relative to the first event. The event marked with open circle in Kamiokande is usually persumed to be background. Right: Angular distribution of SN 1987A neutrinos for the Cherenkov detectors where θ is the angle relative to the opposite direction of the SN, i.e. relative to the direction of the neutrino flux [21].

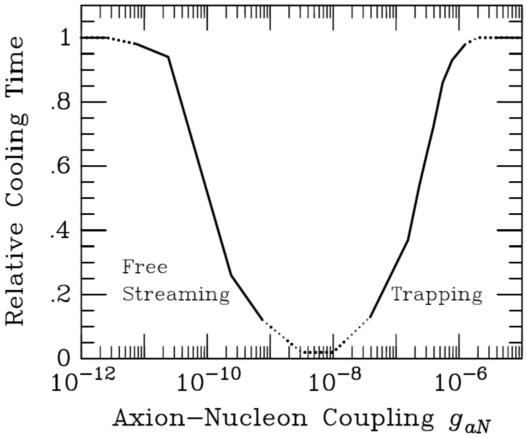

Figure 2.9: Neutrino cooling time of a SN core as a function of the axion-nucleon coupling [21]. In the free streaming region, axions are emitted from the entire volume of the core, and from the axion sphere at about unit optical depth in the trapping region. The solid line is from a numerical calculation. The dotted line is an arbitrary completion of the two curves.

consistent with isotropy only at the 0.07% level, so that the relevant events at Kamiokande are all forward. A forward peaked distribution would be expected from $\overline{\nu}_e e^- \to e^- \overline{\nu}_e$ elastic scattering, however this process has a much lower cross section than the $\overline{\nu}_e p$ process. For the interpretation of these apparent anomalies of the observed neutrino events, a very speculative idea was proposed. The existence of a new neutral boson such as the axion which could produce photons when interacting with nucleons.

Duration of neutrino emission Figure 2.9 shows the expected duration of SN neutrino cooling time as a function of the axion-nucleon coupling. With increasing g_{aN}, corresponding to an increasing energy loss rate, the signal duration drops sharply. For a sufficiently large coupling, however, axions no longer escape freely. They are trapped and thermally emitted from the axion sphere at unit optical depth.

In the SN core, the dominant process for axion production is axion Bremsstrahlung in the nucleon-nucleon processes, $NN \to Na$, as shown in Fig. 2.10. Thus, the emission rate is computed on the basis of a bremsstrahlung amplitude with the nucleons interacting by pion exchange, i.e. the energy loss rate depends on the axion-nucleon Yukawa coupling g_{aN}.

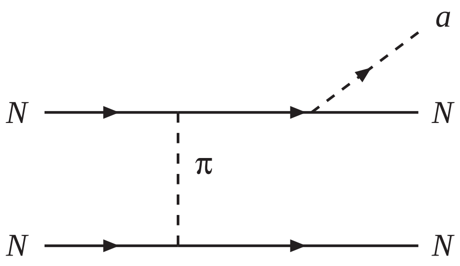

Figure 2.10: Nucleon nucleon bremsstrahlung emission of axions.

At about 1 sec after core collapse the neutrino luminosity is about 3×10^{52} erg s^{-1}. The mass of the object is about $1.5 M_\odot = 3 \times 10^{33}$ g, so that its average energy loss rate is $L_\nu / M \approx 1 \times 10^{19}$ erg g^{-1}s^{-1}. Therefore, one can estimate a limit on the energy loss rate on the free streaming region by the simple criterion that the new channel should be less effective than the standard neutrino losses, corresponding to

$$\varepsilon_x < 10^{19} \text{ erg g}^{-1}\text{s}^{-1}. \tag{2.75}$$

It was evaluated with typical core conditions, i.e. at a temperature of about 30 MeV and a density of around 3×10^{14} g cm^{-3}.

For the emission of axions, the total energy loss rate [21] is given by

$$Q_a = \frac{128 g_{aN}^2 \alpha_\pi^2}{140\pi^{3/2}} \frac{n_b^2 T^{3.5}}{m_N^{9/2}}, \tag{2.76}$$

where α_π is the pionic fine structure constant[13], m_N = 938 MeV the nucleon mass and n_b the baryon density summed over initial state nucleon numbers which are given by the Maxwell-Boltzmann distribution. Thus, the bremsstrahlung energy loss rate for the emission of an axion with a coupling g_{aN} is

$$\varepsilon_a = g_{aN}^2 2 \times 10^{39} \text{ erg g}^{-1}\text{s}^{-1} \rho_{15} T_{30}^{3.5}, \tag{2.77}$$

where $T_{30} = T/30$ MeV, $\rho_{15} = \rho/10^{15}$ g cm^{-3} and $\varepsilon_a = Q_a/\rho$ is the energy loss rate per unit mass.

Using Eq. (2.75) and the observed duration of the neutrino signal, the constraints on the coupling constant of axion to nucleons can be obtained. Therefore, the excluded range is

$$1 \times 10^{-10}\ \text{GeV}^{-1} \lesssim \quad g_{aN} \quad \lesssim 3 \times 10^{-7}\ \text{GeV}^{-1}, \tag{2.78}$$

where $g_{aN} \equiv C_{aN} m_N / f_a$ with $C_{aN} \equiv \sqrt{0.3C_{ap}^2 + 0.7C_{an}^2} \approx 0.2$ assuming a proton fraction of 0.3 inside the SN core. The upper limit in Eq. (2.78) is equivalent to axion trapping in the supernova. In terms of axion mass, ultimately the corresponding range on the axion mass

$$\begin{aligned} 0.6 \times 10^6\ \text{GeV} \lesssim \quad & f_a \quad \lesssim 0.6 \times 10^9\ \text{GeV} \\ 0.01\ \text{eV} \lesssim \quad & m_a \quad \lesssim 10\ \text{eV} \end{aligned} \tag{2.79}$$

is excluded for invisible axions.

---

[13] $\alpha_\pi \equiv \frac{1}{4\pi}(f 2m_N/m_\pi)^2 \approx 15$ with $f \approx 1.0$ GeV

2.3 Cosmological constraints

Besides astrophysical considerations cosmology also provides an upper bound on f_a, or equivalently a lower bound for the axion mass. Axions, if they exist within the allowed mass region, may be a fair amount of dark matter of the universe and will have potentially detectable relic abundances. If $f_a \lesssim 10^8$ GeV axions are produced thermally in the early universe. For $f_a \gtrsim 10^8$ GeV cosmic axions are produced nonthermally by misalignment mechanisms. In this Section the axion production in cosmology by misalignment mechanism is described.

In cosmology, relic axions arise at temperature T $\sim f_a$, where the $U(1)_{PQ}$ symmetry is broken. Above a temperature T $> f_a$, the axion is in thermal equilibrium. However, when the universe goes through the PQ symmetry phase transition at a temperature T $\sim f_a$, the axion field develops a vacuum expectation value. It is naturally expected that the vacuum expectation value $\bar{\theta}$ of the axion field is likely on the order of the PQ scale, i.e. an initial value of $\bar{\theta}$, denoted by $\bar{\theta}_1 \sim \bar{\theta}/f_a \sim 1$. With the temperature of the universe T $\sim \Lambda_{QCD}$, the axion acquires a mass of order $m_a \sim \Lambda_{QCD}^2$ and the vacuum expectation value $\bar{\theta}$ of the axion field is dynamically forced to zero. Hence the $\bar{\theta}$ angle will relax to $\bar{\theta} \to 0$, which is the CP conserving value. It means that the axion field is misaligned with the minimum of its potential. Then the vacuum value $\bar{\theta}$ will oscillate around $\bar{\theta} = 0$. This oscillating vacuum corresponds to a coherent motion of axions. The oscillation of the axion field contributes to the energy density of universe in the shape of relic axions. The larger f_a is, the weaker the axion interacts and more early the PQ phase transition occurs in the universe, so that the axion density ρ_a increases with f_a. This contribution cannot exceed the closure density of the universe, thus it gives an upper limit for f_a.

The equation of motion of the axion field in an homogeneous and isotropic universe is [36]

$$\ddot{\bar{\theta}} + 3H\dot{\bar{\theta}} + m_a^2\bar{\theta} = 0, \tag{2.80}$$

where an overdot denotes d/dt and $H = \dot{R}/R$ is the Hubble constant with the expansion parameter R. At early times, when the axion mass is much less than the Hubble parameter, corresponding to temperatures much greater than Λ_{QCD}, the solution of Eq. (2.80) is $\bar{\theta} \simeq \bar{\theta}_1 = const$, so that the axion field stays constant, i.e. there is no oscillation. At a temperature T $\sim \Lambda_{QCD}$, the axion mass becomes comparable to the expansion rate, so that we have

$$m_a \sim H(T) \sim \frac{\Lambda_{QCD}^2}{M_{Planck}} \tag{2.81}$$

and the axion density [37] is

$$\rho_a \equiv \frac{1}{2} f_a^2 (m_a^2 \bar{\theta}^2 + \dot{\bar{\theta}}^2) \approx m_a^2 f_a^2. \tag{2.82}$$

After this moment, the axion field starts to oscillate around $\overline{\theta} = 0$. At T $\ll \Lambda_{QCD}$, the axion mass is slowly varying and the axion energy density varies as R^{-3}:

$$\rho_a = const \frac{m_a}{R^3}. \tag{2.83}$$

The axion number density is then $n_a = \rho_a / m_a$. Thus the present axion density is of order

$$\rho_a \sim \frac{\Lambda^3_{QCD} \mathrm{T}^3}{m_a M_{Planck}}, \tag{2.84}$$

where T = 2.7 K is the present temperature of the universe. Therefore, the contribution of axions to the present energy density is

$$\Omega_a h^2 \approx 2 \times 10^{\pm 0.4} (\frac{10^{-6}\ \mathrm{eV}}{m_a})^{1.18}, \tag{2.85}$$

where Ω is the density normalized to the critical density[14] and h is the Hubble parameter today in unit of 100 km/s/Mpc. Detail estimations can be found in Ref. [30]. If the universe is flat, then $\Omega_a h^2 = 1$. This requires that the axion energy density should be smaller than the closure density of the universe. Comparing this with Eq. (2.85) gives the lower limit on the axion mass

$$m_a \geq (10^{-5} - 10^{-6})\ \mathrm{eV}. \tag{2.86}$$

Consequently, the astrophysical and cosmological constrains on invisible axions allow only a small window for the axion mass, roughly

$$10^{-6}\ \mathrm{eV} \lesssim m_a \lesssim 10^{-3}\ \mathrm{eV}. \tag{2.87}$$

All constraints are summarized in Fig. 2.11. Even though the allowed window for axion masses is very narrow, axions could still exist and also these astrophysical and cosmological bounds are not utterly restricted. Therefore, experiments are going on searching for axions even in the excluded regions.

---

[14] The critical density is the mass density of the universe which just stops the expansion of space at infinite cosmic time. It is the boundary value between open model and closure model and defined by $\rho_c = \frac{3H^2}{8\pi G}$.

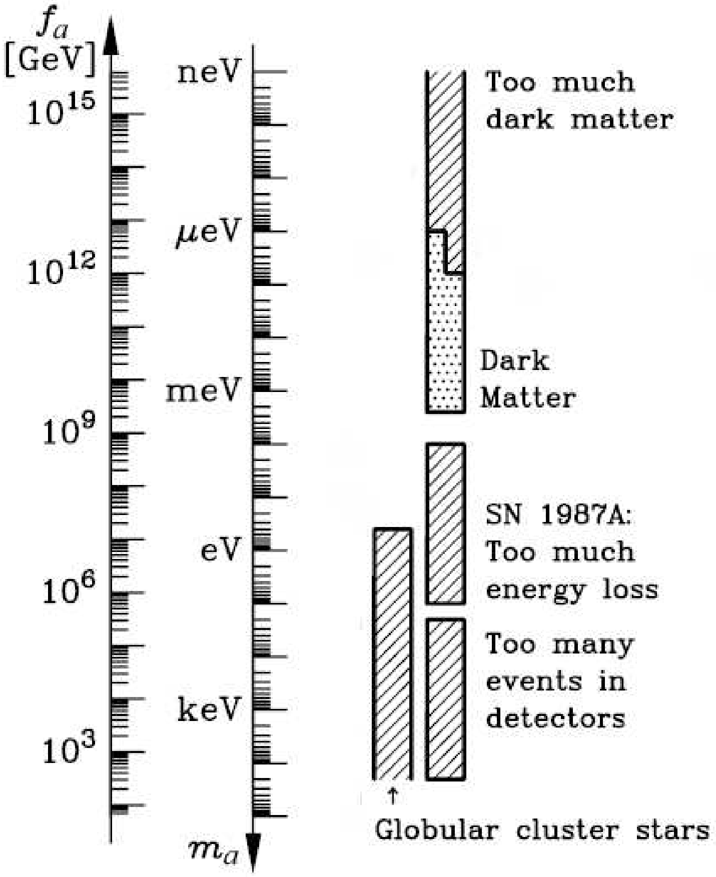

Figure 2.11: Exclusion regions with dashed lines from astrophysical and cosmological constraints on the axion mass and correspondingly to the PQ scale. An open end of an exclusion bar means a rough estimate, i.e. its exact location has not been established or it depends on detailed model assumptions. The axion photon coupling depends on the globular cluster bounds and the axion nucleon coupling depends on the SN 1987A limits. The inside the region marked with dots indicates that axions would be a feasibly dark matter candidate [38].

2.4 Detection of invisible axions

In this Section several laboratory experiments to detect invisible axions coupled to two photons with very tiny coupling constant and their results are discussed. The decay constant of invisible axions is in the range 10^8 GeV $\lesssim f_a \lesssim 10^{12}$ GeV by astrophysical and cosmological constraints. In 1983 Pierre Sikivie [39] devised laboratory experiments to detect invisible axions which convert into photons using a strong magnetic field as in the Primakoff effect. There are three different kinds of searches: axion haloscopes, axion helioscopes and laser experiments. The axion haloscopes, e.g. cavity detectors, are designed to search for galactic halo axions for f_a near 10^{12} GeV, while the axion helioscopes are intended to detect axions from the solar interior for f_a down to 10^8 GeV. The laser experiments are designed to detect laboratory axions generated by a laser beam.

2.4.1 Microwave cavity experiments

The axion is a well-known cold dark matter (CDM)[15] candidate, so that it constitutes a significant fraction of the dark matter halo of our galaxy. A microwave cavity experiment looks for dark matter axions to measure the full energy of an axion, i.e. the sum of its rest mass plus kinetic energy. As implied in Section 2.3, axions fill the missing mass of the universe for $f_a \approx 10^{11}$ GeV. If these masses are gathered in the halos of galaxies, then the halo axion density would be expected to be in the order of $\rho_{halo} \equiv 10^{-24}$ g/cm^3. Galactic objects have velocities in the order of $\beta \approx 10^{-3}$, in other words, the velocity of axions relative to earth is expected to be of order $(v/c) \equiv \beta \approx 10^{-3}$. Thus the kinetic energy of the axions is very small and hence the signal is corresponding to the energy of the photon that equals the converted axion energy [40]. The signal is maximal when the frequency $\nu = \mathrm{E}_\gamma = \mathrm{E}_a = \mathrm{m}_a + \mathrm{m}_a\, \beta^2/2 = \mathrm{m}_a(1 + \mathcal{O}(10^{-6}))$. The principle of detecting dark matter axions based on the Primakoff effect [33] as shown by Pierre Sikivie [39] is that galactic axions convert to photons as a microwave signal in a cavity resonator with a high quality factor in a strong magnetic field. Due to the small velocity spread of axions, the converted photons in the microwave region are monochromatic with a relative spread of order 10^{-6}. This narrow spread is an experimental sign of galactic axions. The cavity has to be tunable because the cavity resonant frequency should correspond to the unknown axion mass. The conversion power $\mathrm{P}_{a\to\gamma}$ is proportional to the square of couplings $\mathrm{g}^2_{a\gamma}$.

Pioneering experiments with a small sensitivity volume $\sim$ 1 liter (Rochester-BNL-Fermilab [41] and University of Florida [42]) were performed and limits were set on the mass range of axions

$$4.5\ \mu\mathrm{eV} < \mathrm{m}_a < 16.3\ \mu\mathrm{eV}.$$

---

[15] CDM is composed of particles moving at non-relativistic velocities.

Recent experiments [40] with a higher sensitivity (volume of cavity $\sim$ 200 liters and magnetic field $\sim$ 7.5 T) have excluded KSVZ axions in the mass range

$$2.9\ \mu\mathrm{eV} < \mathrm{m}_a < 3.3\ \mu\mathrm{eV}.$$

In addition, the Axion Dark Matter eXperiment (ADMX) [43], using the cavity concept, has excluded the mass range $1.9\ \mu\mathrm{eV} < \mathrm{m}_a < 2.3\ \mu\mathrm{eV}$. Further developments in SQUID[16] amplifier and magnet technologies may improve the sensitivity of experiments to cover the axion mass range down to the theoretical limit. Other experiments for the dark matter axion search are CARRACK[17] I and CARRACK II in Japan using a Rydberg-atom-cavity detector [44]. CARRACK I has been carried out to search for axions in the mass range around 10 μeV and CARRACK II expects to cover the broad range of

$$2\ \mu\mathrm{eV} < \mathrm{m}_a < 50\ \mu\mathrm{eV}.$$

2.4.2 Telescope searches

Telescope experiments look for axions of mass 3 - 8 eV dominated by thermal production in the early universe. Even though their contribution to the critical density is very small, $\Omega \sim 0.01\ (\mathrm{m}_a/\mathrm{eV})$, the axions have large relic abundance and lifetime $\tau_{a\rightarrow\gamma\gamma} \approx 10^{25}$ s $(\mathrm{m}_a/\mathrm{eV})^{-5}$ which are well matched cosmologically. One might thus constrain thermally produced axions by searching for a quasi monochromatic photon line from galactic clusters. An axion decaying into 2 photons will produce an emission line at a wavelength $\lambda_a = 2hc/\mathrm{m}_a \simeq 24800(\mathrm{Å}) / \mathrm{m}_a(\mathrm{eV})$. This line would be at half the axion mass. The line has an expected intensity of roughly $\mathrm{I}_a \approx 10^{-17}\ (\mathrm{m}_a/3\ \mathrm{eV})^7$ erg cm^{-2} arcsec^{-2} Å^{-1} s^{-1} [45].

At the Kitt Peak National Observatory (KPNO) [46] a search for thermal axions in three rich Abell clusters was carried out. The line intensity of axions should decrease from the center of the cluster outward. The observing strategy is to record a spectrum from near the cluster center and subtract the spectrum of the outer part of the cluster. However, no axion decay line was detected, thus the mass range

$$3\ \mathrm{eV} < \mathrm{m}_a < 8\ \mathrm{eV}$$

is efficiently excluded. The radio telescope made at Haystack Observatory [47] searches for axions decaying into photons of mass range of $298\ \mu\mathrm{eV} < \mathrm{m}_a < 363\ \mu\mathrm{eV}$ in dwarf galaxies. This observation excluded the axion-photon coupling constant

$$\mathrm{g}_{a\gamma} > 1.0 \times 10^{-9}\ \mathrm{GeV}^{-1}.$$

---

[16] Superconducting QUantum Interference Devices

[17] Cosmic Axion Research using Rydberg Atoms in a resonant Cavity in Kyoto

2.4.3 Search for solar axions

Solar axions could be abundantly produced at the core of the sun by interaction of thermal photons in the Coulomb field with electric charges by the Primakoff conversion. The expected solar axion flux at earth is $\Phi_a \approx 10^{11}$ cm^{-2} s^{-1} $(g_{a\gamma}/10^{-10}\ \mathrm{GeV}^{-1})^2$ and the average energy is about 4 keV. In a transverse magnetic field, the axions can be reconverted to X-ray photons which have the energy and momentum of the original axions. Thus the basic concept of a search for solar axions is to look for their conversion to X-rays in a strong magnetic field. The conversion efficiency of an axion to a photon in a strong magnetic field increases with $(B{\cdot}L)^2$ where B and L are the magnetic field strength and the magnet length, respectively.

The first search [48] with this idea was carried out using a large dipole magnet with helium gas. A magnet of 1.8 m length, 15 cm bore diameter and 2.2 T field was fixed in orientation to take data when the sun crossed the horizon at sunset for approximately 15 min every day. Axions were bounded by

$$g_{a\gamma} < 3.6 \times 10^{-9}\ \mathrm{GeV}^{-1}$$

for $m_a < 0.03$ eV and

$$g_{a\gamma} < 7.7 \times 10^{-9}\ \mathrm{GeV}^{-1}$$

for 0.03 eV $< m_a <$ 0.11 eV. Another helioscope experiment [49] used a rotatable superconducting magnet with a length of 2.3 m and a magnetic field of 3.93 T to track the sun. Limits were set on the axion coupling to two photons

$$g_{a\gamma} < 6 \times 10^{-10}\ \mathrm{GeV}^{-1}$$

for axion masses $m_a < 0.03$ eV and

$$g_{a\gamma} < 6.8 \text{ - } 10.9 \times 10^{-10}\ \mathrm{GeV}^{-1}$$

for axion masses $m_a < 0.3$ eV. Currently, the CERN Axion Solar Telescope (CAST) experiment using the same principle is searching for solar axions. In this thesis, this ongoing search at CERN is described in detail in Chapter 3.

Another possibility to detect solar axions is to use a crystal germanium detector [50]. Solar axions can be detected through their coherent Primakoff reconversion into photons in a lattice of a germanium crystal when the incident angle satisfies the Bragg condition[18] with a crystalline plane. Results of SOLar AXion (SOLAX) [51] in Sierra Grande, Argentina, using a germanium detector give an upper bound of

---

[18] Bragg's law $n\lambda = 2d\sin\theta$ states, that crystals reflect X-rays only at certain incident angles θ, where d is the distance between atomic layers in a crystal and λ is the wavelength of the incident X-rays.

$$g_{a\gamma} < 2.7 \times 10^{-9}\ \mathrm{GeV}^{-1}$$

for axion masses up to $m_a \approx 1$ keV. The COSME [52] experiment with a similar germanium detector at the Canfranc Underground Laboratory obtained an upper limit of

$$g_{a\gamma} < 2.78 \times 10^{-9}\ \mathrm{GeV}^{-1}$$

which is practically identical to SOLAX result. The DArk MAtter (DAMA) [53] experiment at the Gran Sasso also constrains

$$g_{a\gamma} < 1.7 \times 10^{-9}\ \mathrm{GeV}^{-1}\ (95\%\ \mathrm{C.L.})$$

for m_a in the eV range by using NaI crystals.

2.4.4 Photon regeneration

The idea of photon regeneration experiments is, that axions can be produced by photons propagating in a transverse magnetic field. Photons from a laser beam shine to the bore of a superconducting dipole magnet, where the photon beam interacts with a virtual photon from the static magnetic field, in order to produce a pseudoscalar axion. The conversion probability is proportional to $(g_{a\gamma}BL)^2$, where L is the length of magnetic field. Due to their very feeble interaction with ordinary matter, the axion penetrates a wall, which is an optical barrier interposed between two magnets, and then in the second magnet it interacts with another virtual photon (see Fig. 2.12). The regenerated photon can be detected in a photomultiplier tube [54].

An experiment [55] using two magnets of 4.4 m effective length and 3.7 T magnetic field has carried out a search of photon regeneration in a magnetic field and limited the coupling constant

$$g_{a\gamma} < 6.7 \times 10^{-7}\ \mathrm{GeV}^{-1}$$

for the mass $m_a < 0.001$ eV.

2.4.5 Polarization experiments

Using the same concept as in the previous experiment, the presence of axions could affect the polarization of a photon beam propagating through a transverse magnetic field. Thus the axions would change the polarization of the photon beam before and after the wall. Only the component of the electric field of an incident laser beam parallel ($E_{||}$) to the magnetic field will be attenuated by the production of axions, while the orthogonal component ($E_{\perp}$)

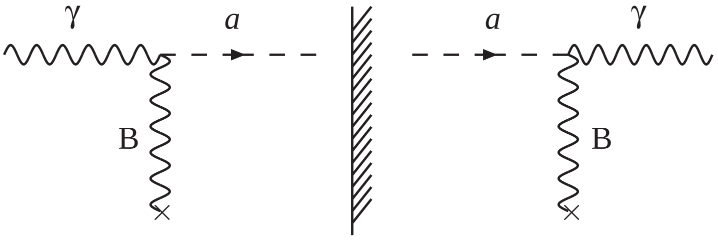

Figure 2.12: Principle of photon regeneration experiments. Real photons from a laser are incoming into the magnet bore and interact with the virtual photons from the magnetic field to produce axions. The axions penetrate the wall and then reconvert to photons in the second magnet.

is unaffected. Hence the incident light polarized at 45° to the direction of the magnetic field will show a small rotation of the polarization vector, the so-called dichroism effect. The other effect is the birefringence of the vacuum. When axions pass through the magnetic field, light which is linearly polarized becomes elliptically polarized and an ellipticity of the passing beam is measurable.

A search [56] using the above principle has put a limit on the coupling constant

$$g_{a\gamma} < 2.5 \times 10^{-6}\ \mathrm{GeV}^{-1}$$

for $m_a < 7 \times 10^{-4}$ eV. More recently, the PVLAS[19] experiment [57] carried out a search of rotations and ellipticities induced by a transverse magnetic field onto a linearly polarized laser beam and observed an unexpected large rotation effect. One explanation might be the existence of an oscillation between a photon and a light spin zero boson, and their interpretation deduced a coupling constant of about $10^{-6}\mathrm{GeV}^{-1}$ and an axion mass of about meV. However, this limit is far larger than current experimental limits published in Ref. [58]. This result therefore will have to be confirmed by a large scale laboratory experiment such as a photon regeneration experiment [59].

---

[19] Polarizzazione del Vuoto con Laser (Vacuum polarization with laser)

Chapter 3

Detection of Solar Axions

Even though there are many kinds of axion sources, the sun due to its closeness to the earth would be the most intense. Solar axion production proceeds via the Primakoff conversion of photons into axions in the presence of external electromagnetic fields of the sun's interior. Based on solar models, the solar axion flux is estimated to be detectable on earth. The CAST[1] helioscope is used to detect the solar axions which can reconvert to photons in a transverse laboratory magnetic field. In this Chapter, the detection principle of axions from the sun, particularly, the axion flux on earth and the conversion probability of axions to photons, are discussed at first. Moreover, the CAST experiment searching for solar axions is described in detail.

3.1 Solar axion flux on earth

In the self-luminous core of the sun, which is extremely hot and dense, thermal blackbody photons with energies of several keV interact with virtual photons from the strong electromagnetic field of the charged particles in the hot plasma [33]. In the Primakoff reaction both photons are then converted into an axion as given by the diagram in Fig. 3.1:

$$\gamma + Ze \rightarrow Ze + a.$$

The differential cross section for the Primakoff reaction on a target with charge Ze in a plasma is found as [34]

$$\frac{d\sigma_{\gamma\rightarrow a}}{d\Omega} = \frac{g_{a\gamma}^{2} Z^{2}\alpha}{8\pi} \frac{|\mathbf{k}_{\gamma} \times \mathbf{k}_{\mathbf{a}}|^{\mathbf{2}}}{\mathbf{q}^{\mathbf{4}}} \frac{\mathbf{q}^{\mathbf{2}}}{\kappa^{\mathbf{2}} + \mathbf{q}^{\mathbf{2}}}, \tag{3.1}$$

---

[1] **C**ERN **A**xion **S**olar **T**elescope

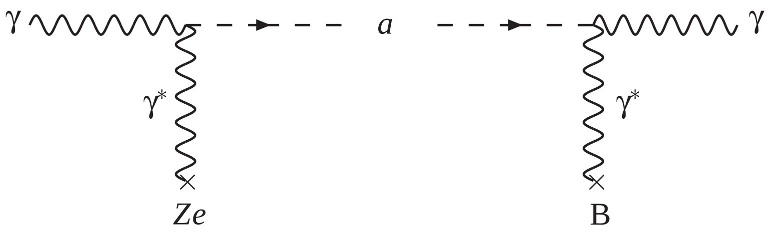

Figure 3.1: Feynman diagram of Primakoff conversion for solar axions. Left: Primakoff production of axions by the interaction of a photon with nucleus. Right: Axion conversion to photon in the presence of the transverse magnetic field.

where $g_{a\gamma}$ is the axion photon coupling constant and $\mathbf{q} = \mathbf{k}_\gamma - \mathbf{k_a}$ is the momentum transfer between photon and axion. In general, the Debye-Hückel scale κ accounts for the screening effect in a plasma and is given by

$$\kappa^2 = \left(\frac{4\pi\alpha}{T}\right)\sum_j Z_j^2 N_j, \tag{3.2}$$

where T is the temperature of the plasma and N_j is the number density of charged particle with charges $Z_j e$. Most photons transform to axions in the electric field of charged particles without changing their direction of motion and the momentum is transferred since the photon mass and the axion mass are different. The energy of the axion is close to the energy of the original photon because the photon energies are small compared to nuclear masses, i.e. the photon energy is about equal to the plasma frequency.

The medium is assumed to be non-relativistic, and recoil effects by the targets can be neglected because photon energies of a few keV are much smaller than the electron mass. Integrating over all targets of the medium, the transition rate of a photon into an axion of the same energy reads [60]

$$\Gamma_{\gamma\to a} = \frac{T\kappa^2 g_{a\gamma}^2}{32\pi}\frac{|\mathbf{k}_\gamma|}{\omega}\int d\Omega \frac{|\mathbf{k}_\gamma \times \mathbf{k_a}|^2}{\mathbf{q}^2(\mathbf{q}^2+\kappa^2)}, \tag{3.3}$$

where ω is the energy of photons. Integrating over the whole phase space, Eq. (3.3) can be written as

$$\begin{aligned}\Gamma_{\gamma\to a} &= \frac{\mathrm{T}\kappa^2 \mathrm{g}_{a\gamma}^2}{32\pi}\frac{\mathrm{k}_\gamma}{\omega}\left(\frac{[(\mathrm{k}_\gamma+\mathrm{k}_a)^2+\kappa^2][(\mathrm{k}_\gamma-\mathrm{k}_a)^2+\kappa^2]}{4\mathrm{k}_\gamma\mathrm{k}_a\kappa^2}\right.\\ &\left.\times\ln\left[\frac{(\mathrm{k}_\gamma+\mathrm{k}_a)^2+\kappa^2}{(\mathrm{k}_\gamma-\mathrm{k}_a)^2+\kappa^2}\right]-\frac{(\mathrm{k}_\gamma^2-\mathrm{k}_a^2)^2}{4\mathrm{k}_\gamma\mathrm{k}_a\kappa^2}\ln\left[\frac{(\mathrm{k}_\gamma+\mathrm{k}_a)^2}{(\mathrm{k}_\gamma-\mathrm{k}_a)^2}\right]-1\right)\end{aligned}\tag{3.4}$$

with the photon momentum $\mathrm{k}_\gamma = |\mathbf{k}_\gamma|$ and the axion momentum $\mathrm{k}_a = |\mathbf{k_a}|$. The photon mass in the medium corresponding to the plasma frequency ω_p is small in the sun, typically about 0.3 keV. The typical photon energies, which roughly correspond to the mean energies of axions, are around 3T $\approx$ 4 keV [61] because the temperature near the center of the sun is about T = 15.6 $\times 10^6$ K = 1.3 keV. Thus, the plasma frequency can be ignored and photons can be regarded as massless. In a photon-axion transition the energy is conserved since we ignore recoil effects. Therefore, in terms of $\mathrm{k}_\gamma = \mathrm{E}_a$ and $\mathrm{k}_a = \mathrm{p} = \sqrt{\mathrm{E}_a^2+m_a^2}$ the transition rate becomes

$$\begin{aligned}\Gamma_{\gamma\to a} &= \frac{\mathrm{T}\kappa^2 g_{a\gamma}^2}{32\pi}\left(\frac{(m_a^2-\kappa^2)^2+4\mathrm{E}_a^2\kappa^2}{4\mathrm{E}_a p\kappa^2}\ln\left[\frac{(\mathrm{E}_a+\mathrm{p})^2+\kappa^2}{(\mathrm{E}_a-\mathrm{p})^2+\kappa^2}\right]\right.\\ &\left.-\frac{m_a^4}{4\mathrm{E}_a\mathrm{p}\kappa^2}\ln\left[\frac{(\mathrm{E}_a+\mathrm{p})^2}{(\mathrm{E}_a-\mathrm{p})^2}\right]-1\right),\end{aligned}\tag{3.5}$$

where E_a and m_a are the axion energy and mass, respectively.

The solar axion flux on earth can be estimated by comparing the axion photon transition rate Eq. (3.3) with the blackbody photon distribution. By integrating the standard solar model [62], the axion flux at the earth can be found [61] to be:

$$\frac{d\Phi_a}{d\mathrm{E}_a} = \frac{1}{4\pi D_\odot^2}\int_0^{R_\odot} d^3\mathbf{r}\frac{1}{\pi^2}\frac{\mathrm{E}_a^2}{e^{\mathrm{E}_a/\mathrm{T}}-1}\Gamma_{\gamma\to a},\tag{3.6}$$

where $D_\odot = 1.5\times10^{13}$ cm is the distance from the sun and $R_\odot = 6.96\times10^8$ m is the solar radius. The term $1/(e^{\mathrm{E}_a/\mathrm{T}}-1)$ represents the Bose-Einstein distribution and T depends on the position inside the sun. Based on the standard model in 1982, van Bibber *et al.* [63] approximated the differential axion flux as

$$\frac{d\Phi_a}{d\mathrm{E}_a} = 4.02\times10^{10}\ \mathrm{cm}^{-2}\mathrm{s}^{-1}\mathrm{keV}^{-1}\left(\frac{\mathrm{g}_{a\gamma}}{10^{-10}\ \mathrm{GeV}^{-1}}\right)^2\frac{(\mathrm{E}_a/\mathrm{keV})^3}{e^{\mathrm{E}_a/1.08\mathrm{keV}}-1},\tag{3.7}$$

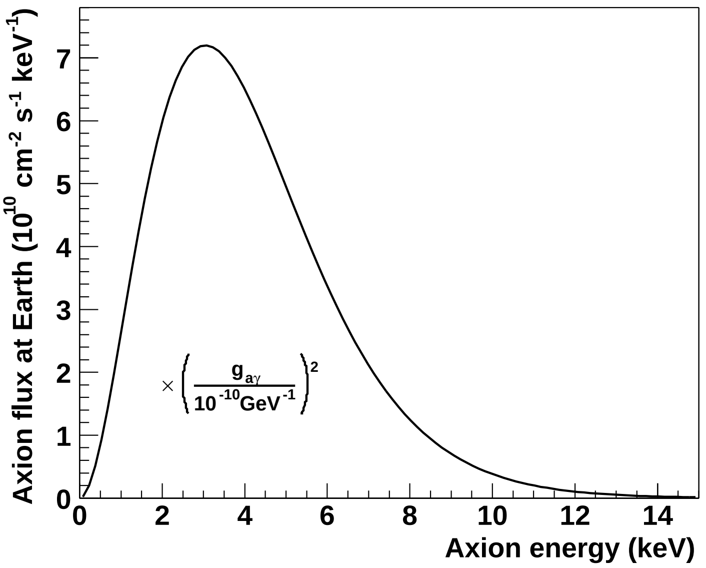

Figure 3.2: Solar axion flux on earth as a function of the axion energy based on the solar model 1982.

where E_a is the axion energy. Fig. 3.2 shows the differential solar axion flux at the earth assuming that axions are only produced by the Primakoff conversion of photons in the interior of the sun. The average axion energy is $< E_a >$ = 4.2 keV. The total axion flux on earth is

$$\Phi_a = 3.54 \times 10^{11}\ \mathrm{cm}^{-2}\mathrm{s}^{-1} \left(\frac{g_{a\gamma}}{10^{-10}\ \mathrm{GeV}^{-1}}\right)^2 . \tag{3.8}$$

As shown above, the solar axion flux is proportional to $g^2_{a\gamma}$ in the unit of 10^{-10} GeV^{-1} which is the sensitive range of the CAST experiment.

In the interior of the sun, it is possible that an axion can convert back into a photon due to the magnetic field of the sun's core. However, this process is highly suppressed. The reason is that axions are produced by incoherent process, i.e. a photon interacting with a single nucleus. In order to efficiently convert them back to photons by an external magnetic field would require that the field should be very strong and in a vacuum. The sun's core is extremely dense, so that in general the dispersion relation of the photon and axion state is not at all matched to allow the axion photon mixing. Therefore, this effect has been ignored so far for the center of the sun [64].

Modern solar model Since the solar model was updated recently, the solar axion flux on earth was evaluated with the most recent 2004 solar model by Bahcall and Pinsonneault [65]. The determination of the solar axion flux was based on the data of the modern solar model **solax1.dat**. This data is tabulated as the flux per unit surface area of the two dimensional solar disk as a function of the dimensionless radial coordinate r between 0 and 1 where r is normalized to the solar radius. The total axion flux can be calculated with the following formula

$$\Phi_a = 2\pi \int_0^1 \mathrm{d}r r \int_{\omega_p}^{\infty} \mathrm{dE}_a \varphi_a(\mathrm{E}_a, r), \tag{3.9}$$

where φ_a is the axion surface luminosity in units of $\mathrm{cm}^{-2}\mathrm{s}^{-1}\mathrm{keV}^{-1}$ per unit surface area. In order to calculate the new solar axion flux, Raffelt and Serpico [66] found an excellent fit function which is provided by three parameters:

$$\frac{\mathrm{d}\Phi_a}{\mathrm{dE}_a} = \mathrm{A}\left(\frac{\mathrm{E}_a}{\mathrm{E}_0}\right)^{\alpha} e^{-(\alpha+1)\mathrm{E}_a/\mathrm{E}_0}, \tag{3.10}$$

where A is a normalization constant and the fit parameter E_0 corresponds to the average energy <E> = E_0. Fitting the three parameters A, α, and E_0 is done by matching the axion number flux, the energy flux and the width of the distribution. From the analytical approximation with the improved fit function, the differential solar axion flux is obtained

$$\frac{\mathrm{d}\Phi_a}{\mathrm{dE}_a} = 6.02 \times 10^{10}\ \mathrm{cm}^{-2}\mathrm{s}^{-1}\mathrm{keV}^{-1} \left(\frac{g_{a\gamma}}{10^{-10}\ \mathrm{GeV}^{-1}}\right)^2 \frac{(\mathrm{E}_a/\mathrm{keV})^{2.481}}{e^{\mathrm{E}_a/1.205\ \mathrm{keV}}} \tag{3.11}$$

with a fit accuracy better than 1% in the range of 1 to 11 keV. Thus the total axion flux on earth by integrating over the energy range becomes

$$\Phi_a = 3.75 \times 10^{11}\ \mathrm{cm}^{-2}\mathrm{s}^{-1} \left(\frac{g_{a\gamma}}{10^{-10}\ \mathrm{GeV}^{-1}}\right)^2. \tag{3.12}$$

Fig. 3.3 shows the comparison of the differential axion spectra of the 1982 and 2004 solar models. Using the updated solar model, the amount of the total flux has changed only within a few percent. Hence one finds that the axion flux depends on the solar model quite mildly. However, in order to get the best and accurate experimental result, it is necessary to use the best estimation of the axion flux on earth.

The radial distribution of solar axions is shown in Fig. 3.4 where the radial coordinate r is in units of the solar radius $\mathrm{R}_\odot$. Fig. 3.5 represents the energy dependence of the solar axion flux with several values of the dimensionless radial coordinate r on the solar disk. As shown in Fig. 3.4 most axions come from a region within $0.2\mathrm{R}_\odot$. The integration of the axion flux up to $0.2\mathrm{R}_\odot$ yields 84.3% of the total number of axions emerging from the sun,

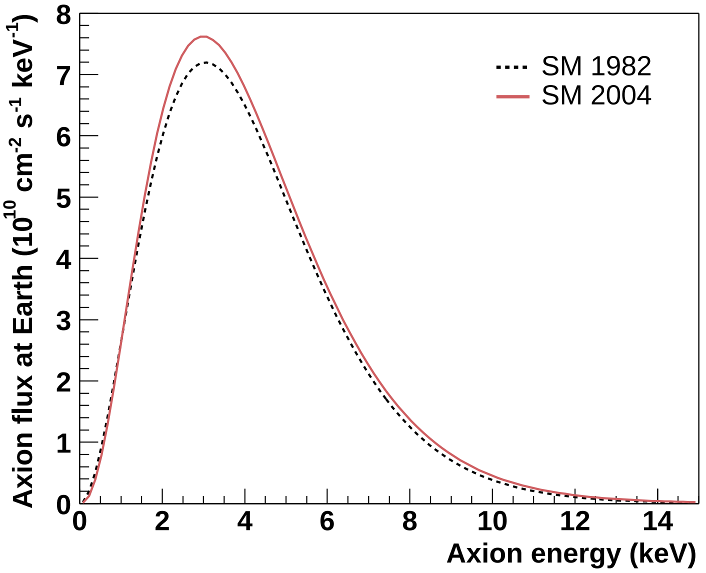

Figure 3.3: Solar axion flux from the modern solar model 2004 (red line) compared with the flux from the old solar model 1982 (dashed line).

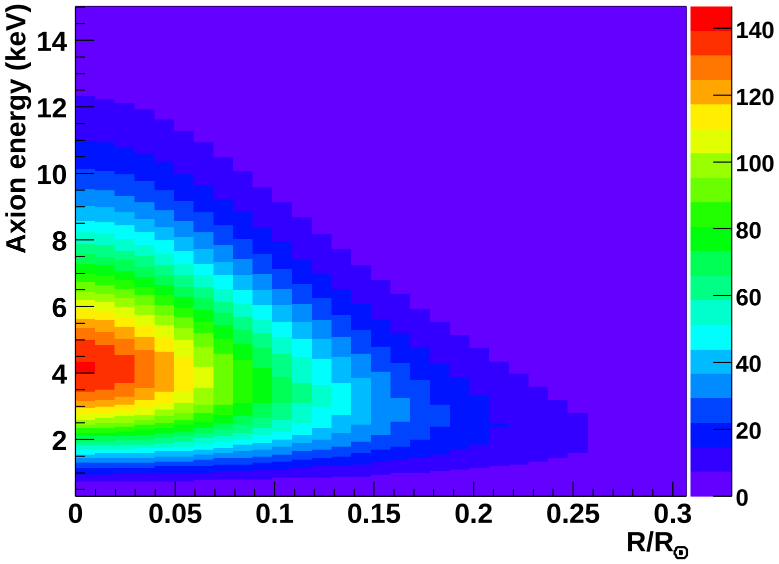

Figure 3.4: Solar axion flux as a function of axion energy vs the dimensionless radial coordinate *r* on the solar disk. The units are cm^{-1}s^{-1}keV^{-1} per unit surface of the solar disk.

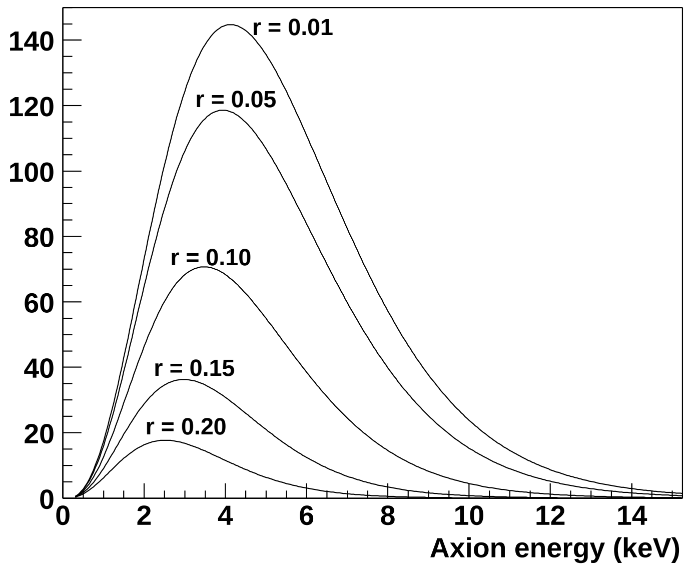

Figure 3.5: Axion surface luminosity of the solar disk as viewed from earth as a function of the axion energy with several values of the dimensionless radial coordinate $r = \mathrm{R}/\mathrm{R}_\odot$ on the solar disk. The units are the same as in Fig. 3.4.

and about 46.8% of the axions are expected from the more central region within $0.1\mathrm{R}_\odot$. The corresponding angles of the source regions as viewed from earth are roughly 0.10° and 0.05°, respectively. This is important for the experimental setup.

3.2 Axion to photon conversion in a magnetic field

The axions with few keV energies from the solar core can be reconverted by the same way via the Primakoff conversion into photons in the presence of a strong magnetic field and a refractive medium in the laboratory as shown in the right diagram of Fig. 3.1. In order to convert axions into photons we need a transverse magnetic field. The reason is that a free photon and an axion have spin-1 and spin-0, respectively, corresponding to the projections $J_z = \pm 1$ and $J_z = 0$. A longitudinal field cannot induce a change in J_z, so that will give no transitions. In principle, the two linear polarization states of the photon are parallel $||$ and perpendicular $\perp$ to the external magnetic field. Only the polarization component parallel to the magnetic field mixes with axions.

Raffelt and Stodolsky [67] have derived the wave equation for particles propagating along the z direction with a frequency ω in the presence of a transverse magnetic field B

$$\left[\begin{pmatrix} \omega - m_\gamma^2/2\omega - i\Gamma/2 & g_{a\gamma}B/2 \\ g_{a\gamma}B/2 & \omega - m_a^2/2\omega \end{pmatrix} - i\partial_z\right]\begin{bmatrix} A_{\|} \\ a \end{bmatrix} = 0, \tag{3.13}$$

where $A_{\|}$ and a denote the amplitudes of the parallel photon component to the magnetic field and the axion field, respectively. Here Γ is the damping coefficient, i.e. the inverse absorption length for photons. In general, from a first order solution of Eq. (3.13) the transition amplitude [63] can be found

$$\begin{aligned} < A_{\|}(z)|a > &= \frac{g_{a\gamma}}{2}\exp\left(-\int_0^z dz'\Gamma/2\right) \\ &\times \int_0^z dz' B \exp\left(i\int_0^{z'} dz''[(m_\gamma^2 - m_a^2)/2\omega - i\Gamma/2]\right). \end{aligned} \tag{3.14}$$

Here the momentum difference between photons in a medium and axions with $\omega = E_a$ is given by

$$q = |m_\gamma^2 - m_a^2|/2E_a. \tag{3.15}$$

From Eq. (3.14) we obtain then the probability of converting an axion to a photon in a magnetic field strength B at a length z = L

$$\begin{aligned} P_{a\to\gamma} &= |< A_{\|}(z)|a(0) >|^2 \\ &= \frac{g_{a\gamma}^2 B^2}{4}\frac{1}{q^2 + \Gamma^2/4}[1 + e^{-\Gamma L} - 2e^{-\Gamma L/2}\cos(qL)], \end{aligned} \tag{3.16}$$

where the path length L is much less than a photon absorption length and B is uniform. In vacuum, the damping coefficient Γ is zero, so that Eq. (3.16) can be written as

$$P_{a\to\gamma} = \frac{g_{a\gamma}^2}{4}(B \cdot L)^2 \frac{\sin^2(\frac{qL}{2})}{(\frac{qL}{2})^2}. \tag{3.17}$$

It has to be mentioned that the probability of axion to photon conversion is proportional to (B $\cdot$ L)^2 in case of coherent conversion. Due to $m_\gamma = 0$, the momentum transfer between axions and photons in vacuum can be also reduced by

$$q = m_a^2/2E_a. \tag{3.18}$$

To keep a constructive axion to photon interference over the whole magnetic length L, which means an axion photon oscillation wavelength larger than L, one needs the coherence condition $qL \ll 1$.

In this limit, the $\sin^2(\frac{qL}{2})/(\frac{qL}{2})^2$ term in Eq. (3.17) can be approximated by 1, so that the conversion probability from axion to photon in vacuum becomes

$$P_{a\rightarrow\gamma} \;=\; \frac{g_{a\gamma}^2}{4}(B\cdot L)^2, \tag{3.19}$$

assuming that the axion to photon conversion is fully coherent over the length of the magnetic field. If $qL \gg 1$, the axion photon dispersion relation does not match. Therefore, the coherence condition $qL \ll 1$ with L = 10 m in vacuum is satisfied only for axion masses $m_a \lesssim 0.02$ eV.

However, coherence can be restored for higher axion masses, if the conversion region inside the magnet bore is filled with a buffer gas with a low atomic number Z like Helium. The use of lower Z gas is just because the ionization energies of He in the relevant energy range roughly up to 10 keV are very low, so that the absorption can be achieved over the whole energy range. Photons in the presence of a buffer gas acquire an effective mass

$$m_\gamma^2 \equiv \omega_p^2 = 4\pi n_e r_e c^2, \tag{3.20}$$

where n_e is the electron density in the medium and r_e is the classical electron radius[2]. The photon mass then becomes equal to the plasma frequency of the gas which is the natural oscillation frequency of electrons in a plasma. Eq. (3.20) implies

$$m_\gamma(\mathrm{eV}) \approx \sqrt{\frac{P(\mathrm{atm})}{15}}. \tag{3.21}$$

Here P is the operating pressure at 300 K. With the momentum transfer of Eq. (3.15) the coherence limit becomes

$$\sqrt{m_\gamma^2 - \frac{2\pi E_a}{L}} \lesssim m_a \lesssim \sqrt{m_\gamma^2 + \frac{2\pi E_a}{L}}, \tag{3.22}$$

where the effective photon mass matches the axion mass. The coherence is restored again for a narrow mass range. The sensitivity is achieved up to axion masses of about 0.3 eV with a ^{4}He gas at 1 atm. The operating temperature of the superconducting magnet is usually 1.8 K, and 1 atm at 300 K corresponds to 6.08 mbar at 1.8 K. An example of two measurements in vacuum and in the presence of gas can be found in Fig. 3.6. Here the expected number of photons N_γ for the effective detector area S is given by

$$N_\gamma = \Phi_a \times P_{a\rightarrow\gamma} \times S \times t, \tag{3.23}$$

where t is the observation time in days and the detector efficiency is not included.

---

[2] $r_e = e^2/4\pi\varepsilon_\circ m_e c^2 = 2.817 \times 10^{-15}$ m

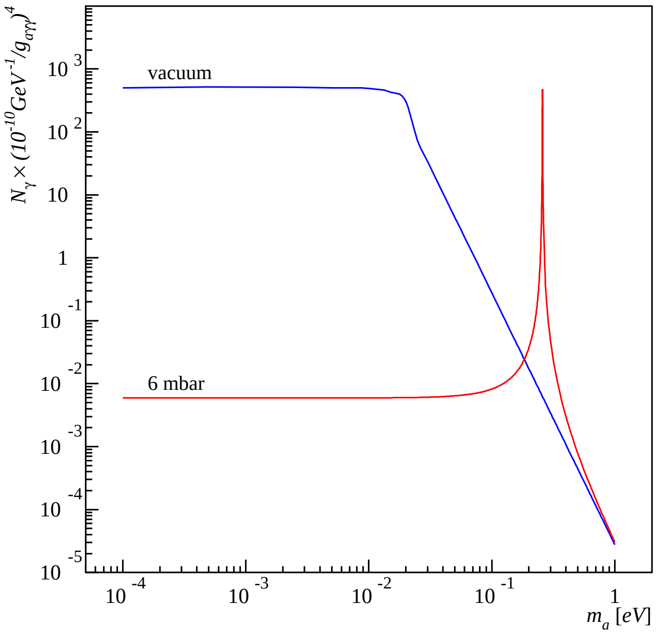

Figure 3.6: Comparison of two measurements in vacuum and in 6 mbar with a buffer gas [68]. The black line is the measurement in vacuum where coherence is fulfilled up to a certain point, and then the transition rate decreases rapidly due to the loss of coherence. The red line shows a very narrow mass window where coherence is restored with the help of a buffer gas. The mass depends on the pressure of the gas. The number of photons has been calculated using an exposure time of 33 days and a coupling constant of 1×10^{-10} GeV^{-1}.

Expected rate estimation According to Eq. (3.19), the conversion probability in vacuum can be approximated by

$$P_{a\to\gamma} \approx 1.7 \times 10^{-17} \left[\left(\frac{\mathrm{B} \cdot \mathrm{L}}{9.0\mathrm{T} \cdot 9.26\mathrm{m}} \right)^2 \cdot \left(\frac{g_{a\gamma}}{10^{-10}\mathrm{GeV}^{-1}} \right)^2 \right] \tag{3.24}$$

for a magnet with L = 9.26 m and B = 9.0 T in the CAST experiment. Using the cross section area of the magnet A = 2×14.5 cm^2, the solar axion flux through the magnet in Eq. (3.8) becomes

$$\Phi_a = 8.9 \times 10^{17} \mathrm{d}^{-1} \left(\frac{g_{a\gamma}}{10^{-10}\mathrm{GeV}^{-1}} \right)^2 . \tag{3.25}$$

Therefore, the number of expected photons N from the conversion of axions can be estimated

$$\begin{aligned} \mathrm{N} &\approx 1.7\times10^{-17}\times8.9\times10^{17}\left(\frac{\mathrm{g}_{a\gamma}}{10^{-10}\mathrm{GeV}^{-1}}\right)^{4} \\ &\approx 15\ events/d \end{aligned} \tag{3.26}$$

assuming 100% detection efficiency for the conversion photons.

3.3 The CAST experiment

In this Section, the general setup of the CAST experiment is explained. After a short overview of the CAST experiment, the magnet with its cryogenic system and the solar tracking system are discussed. After that, three different X-ray detectors are described.

The CERN Axion Solar Telescope (CAST) experiment at CERN[3] searches for solar axions with energies in the keV range. In this experiment [69], solar axions can be converted to photons in the field of a 9 Tesla LHC[4] prototype superconducting dipole magnet. The magnet is mounted on a movable platform in order to follow the sun $\pm8^\circ$ in vertical and $\pm40^\circ$ in horizontal direction, as shown in Fig. 3.7. At both ends of the 9.26 m long dipole magnet, three different X-ray detectors are installed, which are sensitive in the interesting photon energy range up to 10 keV. The photons from the axion to photon conversion in the magnetic field can be detected by these X-ray detectors. The reason for using three different detectors is that the three detectors with complementary designs ensure that systematic detector effects can be studied. On the left side of the magnet are a Charge Coupled Device (CCD) and a MICROMEsh GAseous Structure (Micromegas) mounted on each magnet bore looking for axions at sunrise. The CCD is located at the focal plane of an X-ray mirror telescope, so that the photons from the magnet bore are focused on the CCD plane to a millimeter spot by the telescope. Therefore, the signal to background ratio improves the sensitivity by two orders of magnitude. At the other end, a Time Projection Chamber (TPC) covering both magnet bores is installed to look for axions during sunset. All detectors are taking data every day for about 1.5 hours, the so-called tracking data, when the magnet is aligned with the sun either at sunrise or at sunset. During the other time, data taking is dedicated to background measurement. The exposure time of the background measurement is roughly 10 times larger than the one for tracking. The CAST experiment has two phases covering a broad range of axion masses:

---

[3] Conseil Europeen pour la Recherche Nucleaire (European organization for nuclear research)

[4] Large Hadron Collider

Phase I Phase I is the data taking period in which an axion mass range can be covered up to 0.02 eV by axion to photon conversion in vacuum. Phase I started data taking in 2003 and was finished at the end of 2004. The sensitivity of the axion to photon coupling constant has been improved significantly as compared to previous experiments and it is now for the first time comparable to constraints from astrophysical limit.

Phase II Phase II extends the mass range up to 0.82 eV by filling the magnet bore with a buffer gas using different pressure settings. Starting with ^{4}He inside the magnet at 1.8 K up to pressure settings of about 6 mbar with 74 steps of 0.08 mbar each, later ^{3}He will be used up to 60 mbar with 590 pressure settings in steps of 0.08 - 0.1 mbar. The measurements of the second phase have started at the end of 2005.

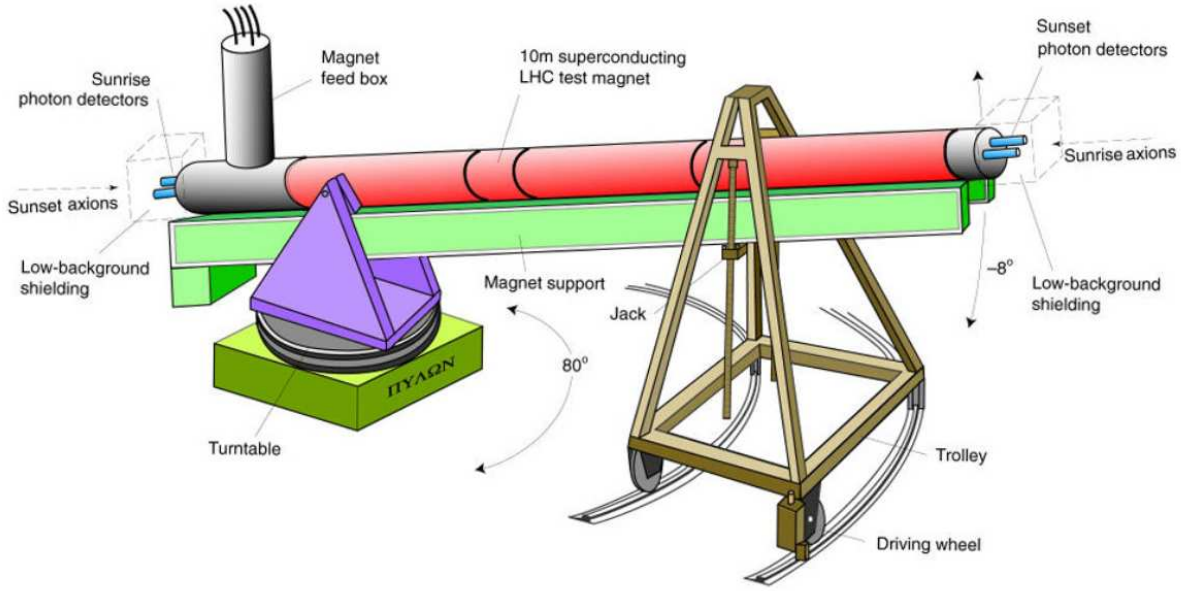

Figure 3.7: A schematic drawing of the CAST experiment at CERN. The movable magnet (red) is supported on a green girder. A turntable shown on the left end of the magnet allows the horizontal movement and the structure on the right end let the magnet move vertically.

3.3.1 The magnet

The first superconducting LHC dipole prototypes magnet [70] with twin apertures is used as a converter for axions to photons. The magnet shown in Fig. 3.8 consists of superconducting Niobium-Titanium (NbTi). The nominal magnetic field is 8.4 T, but the magnet reaches fields between 9 and 9.5 T inside of the two parallel beam pipes of an effective length L = 9.26 m. The aperture of the magnet beam pipes is 42.5 mm, thus the total cross section area A is 2×14.5 cm^2. Each aperture of the bores fully covers the potentially axion-emitting solar core (about 1/10th of the solar radius).

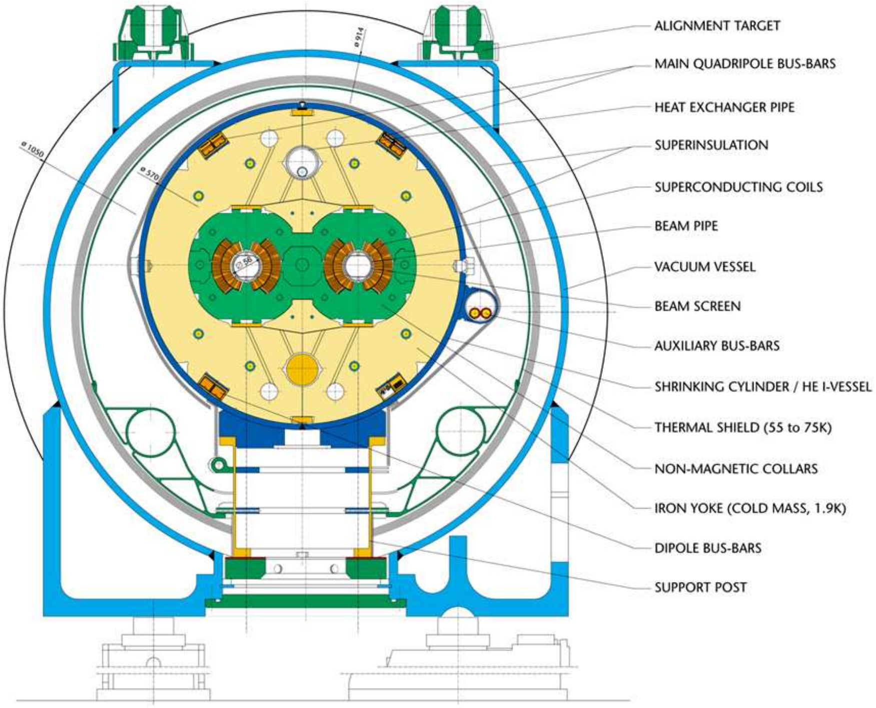

Figure 3.8: The standard cross section of LHC dipole magnet with a twin aperture [71].

To achieve the nominal field of 9 T, the evacuated magnet bore is completely immersed in superliquid helium and its temperature is maintained at 1.8 K. The magnet requires a temperature lower than the liquefaction temperature of helium, therefore the superfluid helium is used for a more efficient cooling and permits an operation on a variable slope of the magnet. The corresponding current of the magnetic field strength is I = 13000 A.

The entire cryogenic system to operate the magnet has been installed from the cryogenics of the previous DELPHI[5] experiment at the e^+e^- collider LEP[6]. To cool down the magnet to 1.8 K a new additional roots pumping group has been installed [72]. The Magnet Feed Box (MFB) providing all the cryogenic and electrical feeds to the magnet are located on top of the magnet's end. In total seven transfer lines mounted on the MFB are connected with the liquid helium supply, the gaseous helium pumping group and the quench recovery system. The lines are made flexible to allow a movement of the whole magnet platform without disturbing the cryogenic operation. Further details of the cryogenics can be found in Ref. [73].

Quench protection An important feature of a superconducting magnet is quenching. A quench in superconducting magnets typically occurs when any parameters of the magnet, e.g. temperature, magnetic field or current, changes from the superconductive state to the normal conductive state. After the sudden change, the cold helium is exhausted from the cryogenic system, thus the magnet is completely discharged. During a quench the magnet can be damaged by high temperature and pressure, therefore an appropriate protection system is required to protect the magnet and also the detectors. When a local resistance change on the superconductor occurs, a quench signal is detected by the quench protection system and the magnet is isolated from the MFB liquid helium by closing the quench protection valve. In general, the helium is safely recovered by an automatic cool down. Sometimes the protection system triggers a fake signal due to instabilities of the power supply. In any case, the data taking is interrupted by both real and fake quenches. However, the whole CAST cryogenic system is operating in quite stable conditions.

3.3.2 The vacuum system

Two interconnected beam bores of the magnet keep the vacuum at around 10^{-6} mbar during Phase I of the CAST experiment, while in Phase II of the experiment they will be filled with Helium gas at different pressures.

Valves On the both ends of the bores the three different detectors are mounted and four gate valves separate the magnet vacuum itself from the vacuum of the three different detectors: VT1 and VT2 on the TPC side, VT3 for the Micromegas, and VT4 for the telescope and CCD as shown in Fig. 3.9. In case of problems like a quench or a window breakdown of the detectors, those valves can be closed automatically under control of an Interlock system, in order to prevent damages of the detectors as well as the magnet. The CAST Interlock box controls the status of all valves and receives alarm signals like a vacuum alarm from

---

[5] DEtector with Lepton, Photon and Hadron Identification

[6] Large Electron Positron collider

the Pfeiffer boxes[7] and a quench alarm or compressed air shortage from the cryogenics system. As a result all valves are closed automatically. When the valves are closed there is no connection between each other detector so that also work on one detector can be performed without any effects on the others.

The valves V14 and V13 in Fig. 3.9 connect the X-ray telescope with the magnet and with the CCD detector, respectively. If the gate valve VT4 is closed due to some problems, then the V14 is also closed simultaneously with VT4 to put the telescope in safe condition. All valves should be open during data taking. The V13, V14 and VT4 are particularly important in the data analysis of the X-ray telescope and CCD detector. The reason is that data can be used only when those valves are open in data taking periods, so this is one of the essential cuts for the data selection.

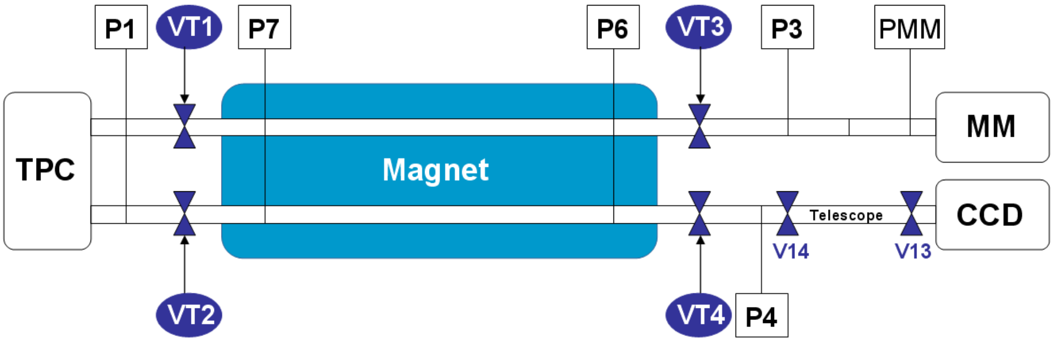

Figure 3.9: Scheme of the vacuum system of the CAST magnet.

Pressures All pressures of the beam pipes can be measured at various places as can be seen in Fig 3.9 as well as monitored by the Slow Control program. P1 close to the TPC windows shows the value of the vacuum pressure which is around 10^{-6} mbar when the gate valves VT1 and VT2 are open. P3 and PMM represent the pressure values for the Micromegas detector. If the corresponding gate valve VT3 is open, then P3 should be around 10^{-6} mbar. PMM is the pressure of an intermediate volume between the magnet vacuum and a thin window of the Micromegas chamber and is normally around 10^{-3} mbar. The volume is continuously

---

[7] The Pfeiffer boxes locate in different places under the magnet girder and monitor continuously the values of all pressures.

pumped to keep a low leakage rate of the detector into the magnet. The pressure P4 is related to the X-ray telescope and must be about 10^{-6} mbar when the gate valve VT4 opens. At both ends of the magnet the vacuum can be directly observed by P6 on the morning detector side and P7 on the TPC side. Those values should be roughly below 10^{-6} mbar as well.

3.3.3 Solar tracking system

In order to follow the sun with the magnet as well as to move the heavy magnet accurately, the hardware and the software systems for solar tracking are very important. The tracking system is therefore required to be very precise.

Platform and motors Here we go into details about the magnet movement and encoders. As shown in Fig. 3.7 the magnet is supported by a platform (girder) which consists of two metallic supports in order to allow a movement of the whole magnet structure horizontally and vertically. The platform was also made to allow an alignment of the magnet with the sun. Thus the time and statistics of data taking are maximized.

One of the supports is used to provide guidance for the platform as well as to move the magnet on rails from 0° close to the counting room up to almost 80° of a local system in the horizontal direction, where the corresponding azimuth is from 47° to 126°. The other support carrying two screws is used to allow a vertical motion at the same moment. A turntable on the opposite side of the magnet carries a great part of the weight of about 40 tons due to the cryogenic box and supports rotations of the magnet platform horizontally. The maximum vertical movement of the platform is ±8° with respect to the horizon. The moving limits are because of mechanical and cryogenic constraints from the internal setup of the superconducting magnet. Thus the magnet can be aligned with the sun every day about 1.5 h at sunrise and sunset. After all, it means that the total alignment time of the magnet with the sun is very roughly 1000 hours over one year.

Two motors can move the platform in vertical and horizontal direction to precalculated encoder values which come from a software program. Encoders allow the tracking software to know the actual position of the magnet. A correspondence between the encoder values and azimuth and altitude of the sun in degree [74] is shown in Table 3.1.

Tracking software The tracking software system controls the magnet movement and records all information about data taking to log files which are needed for data analysis later. Fig. 3.10 shows the working principle of the tracking software program [75]. For taking data the software program, which is written in the Laboratory Virtual Instrumentation Engineering Workbench (LabView) environment, calls an executable file based on the Noval Observatory

Ver. encoder	Altitude	Hor. encoder	Azimuth	Local system
51734	7.6°	184	47.19°	1°
45098	5.6°	3639	56.19°	10°
38463	3.6°	7477	66.19°	20°
31827	1.6°	11316	76.19°	30°
26492	0°	15155	86.19°	40°
21211	-1.6°	18994	96.19°	50°
14575	-3.6°	22833	106.19°	60°
7939	-5.6°	26672	116.19°	70°
1303	-7.6°	30511	126.19°	80°
		33199	133.19°	87°

Table 3.1: Correspondence between the encoder values and azimuth and altitude.

Vector Astrometry Subroutines (NOVAS) which contains the position of the sun and its corresponding time [76]. It reads out the time and date of the computer and calculates exactly the azimuth (AZ) and zenith distance (ZD) of the sun for the coordinates[8] of the CAST telescope every minute. Then the program takes the corresponding values of the encoders with the given values by looking in tables V_x(AZ,ZD) and V_y(AZ,ZD) and gives a signal to the motor in order to move the magnet to that point. These tables are prepared with the maximum possible accuracy.

The tracking system of both hardware and software has been accurately checked by geometric surveys with the help of the Engineering Support and Technology (EST) division at CERN and the magnet positions were calculated by a detailed description of the encoder values with an accuracy of 0.001°. Discrete data points from measurements were constructed by using the spline interpolation. The precision of pointing to the sun is always better than 0.01°, typically about 0.002° [77].

One more important thing is time synchronization. The system checks continuously the time with two CERN time server Network Time Protocol (NTP) which is synchronizing the clocks of the computer systems in the order of 1 ms. The Daylight Saving Time (DST) changes are taken into account. The overall possible sources for errors [78] in solar tracking are summarized in Table 3.2.

As given in Table 3.2 the total estimated precision of the CAST tracking system is better than 0.01°. In addition, the tracking system can be cross-checked independently twice a year

---

[8] 46° 15’ North and 6° 5’ East 330 m above sea level

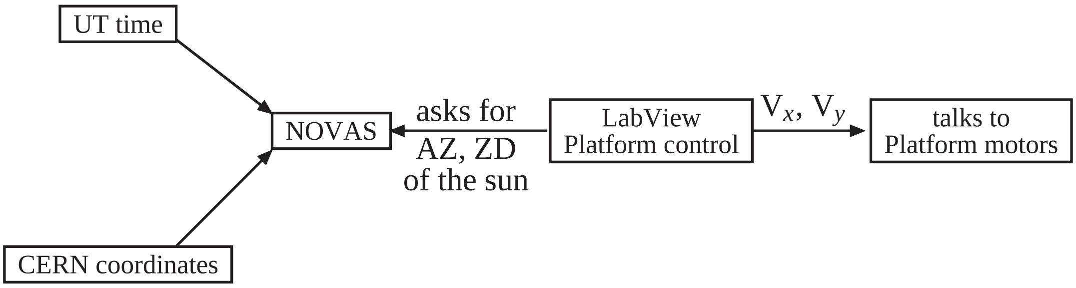

Figure 3.10: A scheme of the principle of the tracking program. NOVAS calculates the solar azimuthal angle (AZ) and the zenith distance (ZD) from the universal time and the experimental coordinates. The LabView platform control translates AZ and ZD to encoder values and then gives a signal to platform motors.

Error source	Typical value	Maximum value
Astronomical predictions	0.002°	0.006°
Uncertainty of CERN coordinates	$\sim 0.001^\circ$	
Grid measurements (0.02 mm precision)	0.001°	
Interpolation of grid measurements	0.002°	$< 0.01^\circ$
Horizontal encoder precision	$\sim 0.0014^\circ$	
Vertical encoder precision	$\sim 0.0003^\circ$	
Perfect linearity of motor speeds	$< 0.002^\circ$	
Clock time	$\sim 0^\circ$	
Total	$< 0.01^\circ$	

Table 3.2: All possible error sources for the solar tracking precision.

by filming the sun which will be described in the next Section. Furthermore, the tracking software records information about the temperatures in the experimental area, the pressure and the values of the magnetic field inside the magnet on log files. In order to record more information during data taking, a Slow Control data acquisition system was used.

Slow Control The slow control was used since late July 2003 in order to monitor the data taking system and record more information which are very useful for the data analysis. It is also written in LabView like the tracking software. The slow control contains the following specific implementations: pressures and temperatures inside the cryogenic system and in front of detectors, status (open or close) of the valves between the magnet and detectors, load on each of the two lifting screws, magnet position in motor encoder values and in angles from an independent position system, and permissions to open valves. Moreover, an alarm system was established to keep important informations for the operation of the experiment, like the vacuum level in front of the detectors, a check of the compressed air supply, a flammable gas supply, a quench signal, and a power failure.

3.3.4 Filming of the sun

Field of view The Field of View (FoV) represents the opening angle that can be viewed at a time through an optical device such as a telescope. If the magnet bore is regarded as an limited optical device, its FoV is quite useful to take a closer look at the detectors, particularly the CCD detector. It simply can be calculated by using the formula

$$\alpha = 2 \arctan \frac{d}{\mathrm{L}} \,,$$

where the opening angle α represents the field of view, d is the diameter of the magnet bore (d = 42.5 mm) and L is the effective length of the magnet (L = 9.26 m). A fully effective FoV is thus about 0.53° which corresponds to the entire sun. However, none of the detectors is directly mounted with its sensitive area to the magnet. The X-ray telescope separates the end of the magnet bore from the effective area of the CCD detector, while the Micromegas uses an extension pipe longer than 1 m. The TPC has a shorter extension but it is not directly installed at the magnet as well. The vignetting[9] effect appears because of these facts and the FoV of the detectors is not fully illuminated. If there is no telescope, then the FoV of the CCD detector is approximately 0.34° and it could cover about 64% of the whole sun. However, the telescope brings the converted photons from the magnet into focus with a diameter of 19 pixels (1 pixel $\approx$ 20 arcsec) on the CCD, corresponding to about 20% of the solar radius. As mentioned in Section 3.1 most axions are emitted from a region within 20% of the sun. To be able to look for these axions emitted from the interior of the sun, therefore

---

[9] Vignetting means that the image brightness in the edges fades away gradually compared to the image center.

a very high precision of the tracking system is required. Its accuracy should be at least 0.02°.

The aim of the solar filming is to cross-check the precision of the tracking software independently by directly observing of the sun. It has been performed regularly twice a year in March and September. It was done a total of six times up to now: September 2002, March and September 2003, September 2004 and March and September 2005.

The first filming of the sun was done with a webcam combined with a small optical telescope as well in 2003 as in 2004. A small PC controlled camera was installed on top of the magnet and aligned parallel to the sun. A window facing to the east on the wall of the experimental area was opened to view the sun through it for a few minutes just after sunrise during several days. The tracking for the filming is a little bit different from the tracking of the axion search due to the refraction of light in the atmosphere, thus a correction should be performed during filming. For axions it is not necessary to correct it because they do not interact significantly with the atmosphere.

The first filming presented quite an acceptable precision of 0.05°. In 2004 the solar filming was done with a webcam combined with a small optical telescope as well. In Spring 2005 the system was improved by using a CCD camera and a better optics with focal length of 200 mm. Fig. 3.11 shows an image taken on the 16th of March with the CCD camera. The new system verified the tracking precision with a remarkably better accuracy compared to old one. The precision of the magnet pointing to the solar center is of the order of 0.03°. This accuracy is limited by the optical alignment of the camera installed on the magnet. However, it confirmed that the magnet alignment is sufficiently precise within statistical and systematic errors for the desired tracking accuracy for CAST. Ref. [79] gives further details of the filming of the sun.

3.3.5 The Time Projection Chamber

The Time Projection Chamber (TPC) at CAST constructed with plexiglass is a conventional type of a three dimensional detector. The detection principle of a TPC is based on ideas from both Multi-Wire Proportional Chambers (MWPC) and drift chambers. Its center is a large gas filled volume, where incoming particles pass through the gas volume and produce free electrons. These free electrons drift toward a plane of wires and an avalanche process occurs near the anode due to the strong electric field. Thus signals can be amplified and detected by the anode wires.

Structure The conversion volume of the TPC is $10 \times 15 \times 30$ cm^3 with two thin entrance windows of diameter 6 cm. It covers both magnet beam bores having each a diameter of

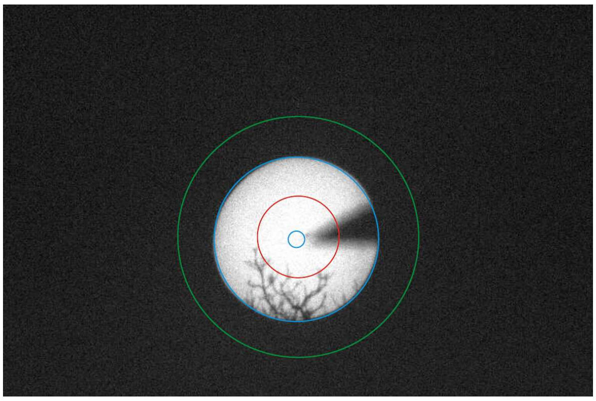

Figure 3.11: Picture taken on the 16th of March with the CCD camera with the optic being focused to 30 m [80]. The reference point is the center of the green circle with cross wires which were used to align the camera. The outer blue circle is the solar disk and the inner blue circle represents 10% region of the solar radius. The red circle is the acceptance region of the magnet bore which contains $\approx 1/2$ of the axion emission region.

42.5 mm with the centers of the two bores separated by 18 cm. The drift region of 10 cm is parallel to the magnet axis and the area of 15×30 cm^2 is oriented to this axis. The volume is filled with a mixture of 95% Argon (Ar) and 5% Methane (CH_4) at atmospheric pressure and allows a total conversion ($> 99\%$) of photons up to 6 keV at a drift field of 700 V/cm. The conversion efficiency decreases by about 50% at 11.5 keV. As can be seen in Fig. 3.12 basically the TPC consists of a drift electrode made of an aluminum layer which is located on the inside of the chamber close to the magnet and three planes which are arranged on the backside of the chamber: The anode plane at +1.8 kV between two grounded cathode planes contains 48 wires with 20 μm diameter and two cathode planes at ground with 96 wires of 100 μm diameter. The 48 anode wires and 96 cathode wires are placed perpendicular to each other at 3 mm wire spacing. The distance between the anode and the inner cathode plane closest to the drift region is 3 mm while the distance between the anode and the outer cathode plane is 6 mm. Each wire is read-out by a 10 MHz flash Analog to Digital Converter (ADC) so that a very good position resolution can be obtained. Thus the spatially localized X-ray events can be easily distinguished from the long tracks of cosmic rays. The whole chamber is constructed from plexiglass, due to the low level of radioactivity, except for the wires, the PCB[10] holding the wires and the screws keeping the chamber together. The thickness of the plexiglass is about 2 cm. A thin mylar foil is placed between the gas and the atmosphere to allow for a calibration with a low energy X-ray source.

---

[10] Printed Circuit Board

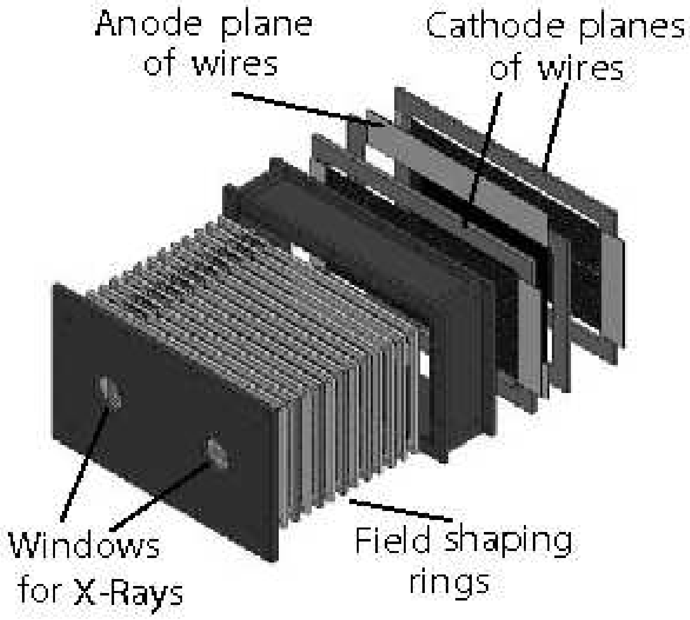

Figure 3.12: Layout of the time projection chamber. The two circular windows for X-ray photons coming from the magnet are connected with the two magnet bores. One anode plane at +1.8 kV between two grounded cathode planes is shown.

Windows The TPC is mounted on the two magnet bores by very thin aluminized 3 or 5 μm Mylar windows on a metallic strongback, in order to stand the difference of 1 atm pressure between the vacuum inside of the magnet and the gas volume in the detector. An additional continuous pumping system was accomplished in 2004 to decrease effectively the gas leaks through the windows of the detector towards the magnet and also to minimize the damage of the windows due to unexpected pressure changes or vacuum breakdown.

Shielding In order to reduce the background level, a passive shielding has been designed and installed around the TPC detector. It consists of an innermost copper cage of 5 mm thickness, surrounded by a lead layer of 2.5 cm, cadmium of 1 mm, and a 20 cm wall of polyethylene. The full setting is closed by a plastic cover which is pressurized in the interior by pure nitrogen (N_2) gas. It reduces the radon contamination from the air in the space close to the detector. Moreover, an active shielding is installed on top of the TPC to clearly identify and reject muons producing background. The full detector shielding on the TPC has reduced the average background level and the background counting rate is about 4.4×10^{-5} counts $\text{cm}^{-2}\ \text{sec}^{-1}\ \text{keV}^{-1}$ in the energy range between 1 and 10 keV.

Performance and data taking The TPC has an automatic calibration run four times per day with a low energy X-ray source ^{55}Fe. It gives an energy resolution of 12% (sigma) at 5.9 keV and the noise threshold is about 300 eV. The TPC was operated smoothly during the whole of 2003 and 2004 data taking periods and the total exposure time in 2003 (2004) was 62.7 h (203 h) for solar tracking data and 719.9 h (3408 h) for background data. The total amount of data in 2004 is roughly five times more compared to 2003. Details of the analysis of the TPC data are given in Ref. [81].

3.3.6 The MicroMegas

The MICROMEsh GAseous Structure (MicroMegas) detector is a novel gaseous X-ray detector based on a parallel plate electrode structure and microstrips for readout. It consists of a 25 mm conversion gap filled with gas and a narrow amplification gap separated by a conducting micromesh. Electrons created by an ionizing particle in the conversion region drift to the amplification region where they are multiplied by the avalanche process. Then charges are collected on the anode plane and can be detected.

Structure Figure 3.13 shows the schematic structure and the operation principle of the detector. The detector is made of plexiglass which is of low radioactivity material. It consists of a two-stage parallel-plate avalanche chamber of an amplification gap combined with a conversion gap. The conversion drift space is separated from the amplification gap by a micromesh. The space between two windows is filled with Helium gas to allow low energy X-ray conversions. The conversion region of 25 mm thickness is between an aluminized polypropylene window and the micromesh plane. The amplification gap of 50 μm is formed between the micromesh plane and the charge collection plane. The anode plane for charge collection consists of 192 X and 192 Y strips with a 50 μm pitch located on the same plane.

Operating principle The incoming particles passing through the drift electrode produce ion-electron pairs in the conversion gap and the ionization electrons released by an ionizing particle drift towards the multiplication region. They are transmitted by the cathode micromesh and multiplied up to 10^4 achieved by applying a very high uniform electric field of about 40 kV/cm in the amplification gap, while the drift region has a quite low electric field about 1 kV/cm. Therefore, the electron cloud is collected by the anode microstrips, while the ion cloud drifts to the opposite direction and is quickly collected on the micromesh plane. The collected charges on the anode plane can be read-out with a two dimensional X and Y strips structure by an ACD data acquisition system. The micromesh signal is used to trigger the acquisition of an event. A detailed description of the detector principle can be found in Ref. [82].

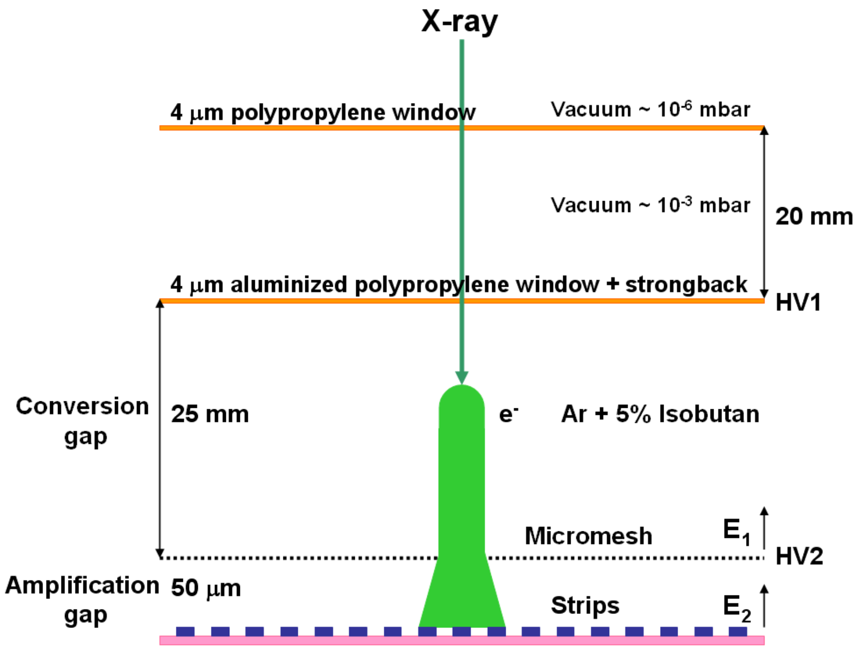

Figure 3.13: Schematic diagram of the Micromegas detector at the CAST experiment. A micromesh separates the conversion region from the amplification region. E_1 and E_2 are the electric fields in the conversion and amplification regions of the order of 1 kV/cm and 40 kV/cm, respectively.

Windows The MicroMegas detector [83] is operated with a standard gas mixture of 95% Argon and 5% Isobutan at atmospheric pressure and is interfaced with the magnet by two thin windows as can be seen in Fig. 3.13. Two thin windows working as a buffer for pressure changes are made of 4 μm thick aluminized polypropylene foils. The first window is located between the magnet and the buffer vacuum, and the second window with a stainless-steel strongback lies between the buffer vacuum and the detector. The volume between the magnet and the detector is continuously pumped. Using 2 windows with different vacuum level is to minimize the leak of the detector gas into the magnet, as well as to optimize the transmission of X-ray photons.

Performance and data taking The detector is sensitive to X-rays in the energy range 600 eV up to 10 keV. It has an excellent stability, a linear response, and a spatial resolution of better than 100 μm. The efficiency of the detector was measured to be about 50% at the PANTER X-ray facility at MPI Munich. Moreover, it has a good energy resolution of 14% FWHM at 5.9 keV obtained from the calibration with a ^{55}Fe source. The background rate is about 5×10^{-5} counts cm^{-1} sec^{-1} keV^{-1}. The MicroMegas has been operated stably since

October 2002 during the data taking periods in 2003 and 2004. The solar tracking data were taken at sunrise every morning, while the background data were recorded during the rest of the day. The calibration and pedestal[11] runs of the detector were done semiautomatically by shifters every morning. The total exposure time for both 2003 and 2004 is 273 h for tracking data and 2193 h for background data. Further details about the analysis of MicroMegas data can be found in Ref. [84].

3.3.7 The X-ray telescope and the CCD detector

The X-ray mirror telescope and the Charge Coupled Device (CCD) detector are described in the next Chapter.

---

[11] Charges are measured by the strips without real triggers

Chapter 4

The X-ray Telescope and CCD Detector

The most sensitive detector of CAST is an X-ray mirror telescope and a Charge-Coupled Device (CCD) detector as a focal plane detector. The telescope is assembled in front of one of the magnet bores on the end of the magnet. It is able to produce an axion image of the sun by focusing the photons emerging from the magnet bore of 14.5 cm^2 aperture to a spot size of about 6 mm^2 on the CCD. Thus an improvement by more than two orders of magnitude in the signal to background ratio is estimated. In this Chapter, the performance of the X-ray telescope and the CCD detector are discussed in detail.

4.1 The X-ray telescope

The X-ray mirror telescope of CAST is a prototype Wolter I type[1] telescope developed for the satellite mission ABRIXAS[2] [85]. The telescope consists of 27 gold-coated mirror shells with a focal length of 1600 mm. The mirror surfaces are polished with a resulting surface roughness of less than 5 Å. Coaxially incident X-ray photons are fully reflected on the smooth mirror surfaces twice if their incident angle is smaller than e.g. 1° for about 5 keV energy, i.e. reflection is achieved only with a shallow angle. Fig. 4.1 shows the principle of the telescope and the light path of the incoming X-rays in the telescope. X-rays are first reflected on the parabolic shaped mirror surface and then on the hyperbolic surface, and subsequently focused onto the focal point.

The aperture of the telescope has been subdivided into six sectors with a supporting spoke structure as shown in Fig. 4.2. The outermost mirror shell has the diameter of 163 mm while the diameter of the innermost is 76 mm. Since the opening of the CAST magnet bore

---

[1] In most descriptions a paraboloid-hyperboloid combination with two internal reflections is called Wolter I type and with one internal and one external reflection is called Wolter II type.

[2] A BRoad-band Imaging X-ray All-sky Survey

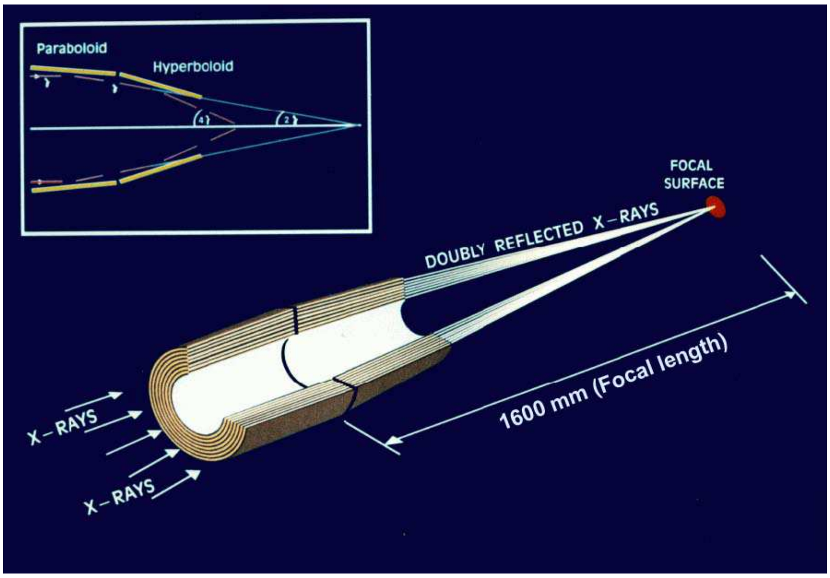

Figure 4.1: A schematic view of the X-ray mirror telescope. X-ray photons are reflected twice by a combination of parabolic and hyperbolic mirrors [86].

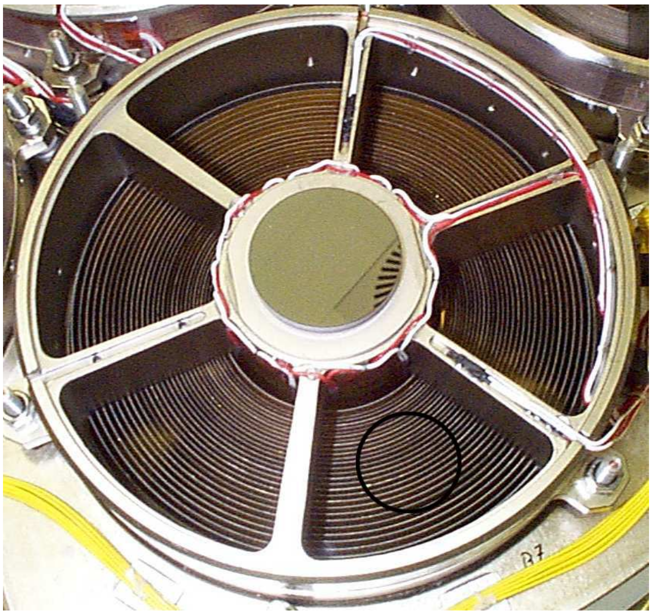

Figure 4.2: Front view of the X-ray mirror telescope for the CAST experiment. A spoke structure subdivided into six sectors supports the 27 mirror shells. One of these sectors is used to focus the X-rays into the focal plane detector (approximate size and location indicated by black circle) [87].

with a diameter of 43 mm is much smaller than the aperture of the telescope, only one part of the six sectors of the telescope is used. Hence the mirror system is mounted asymmetrically to the CAST magnet so that only one part of the full mirror aperture is illuminated by almost parallel X-ray beams and acceptance losses are minimized. The telescope is operated under vacuum condition with a pressure below 10^{-5} mbar to avoid contamination and absorption on the reflective mirror surfaces which would reduce the efficiency of the telescope.

4.1.1 Point spread function and effective area

The performance of an X-ray telescope can usually be specified by a Point Spread Function (PSF) which gives a spatial (or angular) resolution and an effective area[3]. Generally, the point spread function is an optical parameter and defines how a point source would be imaged with this instrument. A point source should ideally produce a sharp signal in one pixel on the image but this is not the case due to optical effects. The PSF then determines the spatial resolution of the instrument by the measured Full Width at Half Maximum (FWHM) of the point source.

In order to determine the PSF as well as the effective area for the CAST mirror system, calibration measurements of all six sectors of the X-ray telescope have been performed at the PANTER[4] facility in Munich using monoenergetic X-rays with various energies. The result is that the on-axis angular resolution of the telescope is 34 arcsec and 43 arcsec ($\sim 0.01^\circ$) Half Energy Width at 1.5 keV and 8.0 keV, respectively, which is nearly a factor 10 better than the expected axion spot size of the sun ($\sim 0.1^\circ$) as shown in Fig. 4.3.

Another important performance parameter of the mirror telescope is the effective area, which means the quality of the mirrors to collect radiation at different photon energies. In general, the effective area is a function of the off-axis angle, the micro roughness of the mirror surfaces and the photon energy. It is reduced by a larger surface roughness, larger photon incident angles, i.e. lower reflectivity, and geometric vignetting effects. The effective area of the telescope depends on the photon energy and measured for each sector of the telescope, the results are summarized in Table 4.1 [88]. The sector 4 of the telescope with the best effective area was selected to be used for CAST.

---

[3] An effective area of a telescope is defined as the product of the telescope mirror geometric area and the mirror reflectivity.

[4] The test facility PANTER operates for calibrations of X-ray telescopes and detectors. An X-ray source is installed at one end of the vacuum system and at the other end a test chamber is mounted. The test chamber has a diameter of 3.5 m and a length of 12 m. The distance of 130 m between X-ray source and telescope was chosen to approximate an infinite source distance of an X-ray object.

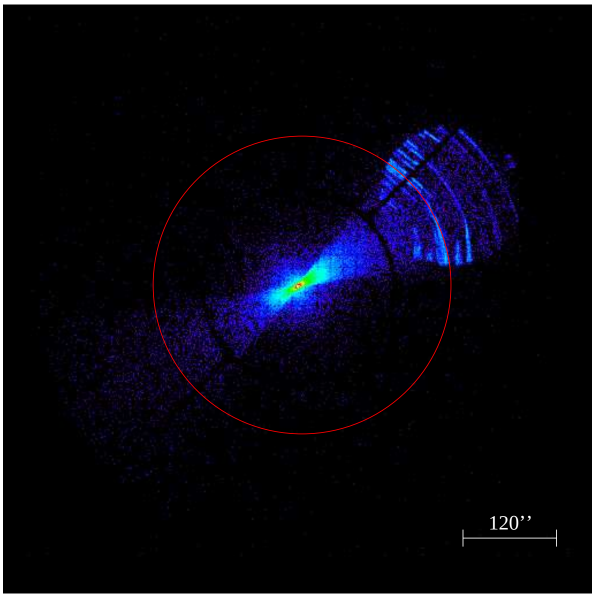

Figure 4.3: Intensity image of the point spread function of one mirror sector measured with a Position Sensitive Proportional Counter (PSPC) detector in the PANTER facility. The red circle indicates an expected spot size of a axion signal. Since the X-ray source is at a finite distance (d $\approx$ 130 m), photons reflected by only one of the parabolic or hyperbolic shaped mirror surface are apparent in the image [88].

Sector		effective	area (cm^2)	
	0.93 keV	1.49 keV	4.5 keV	8.04 keV
1	13.5	13.4	8.2	3.9
2	13.5	13.4	8.2	3.8
3	8.9	13.6	8.3	3.9
4	13.9	13.9	8.4	4.0
5	12.6	12.8	7.9	3.4
6	13.1	13.4	8.5	4.0

Table 4.1: Effective area of each mirror sector measured using X-rays with different energies at PANTER.

The on-axis effective area of this sector shown in Fig. 4.4 was measured at PANTER for a telescope aperture of 48 mm diameter, while the aperture diameter of the CAST magnet bore is 43 mm. Therefore, ray tracing simulations were done for both apertures, in order to translate the results from the PANTER aperture to the CAST aperture. These simulations included the mirror system with the mirror support structure and the magnet geometry assuming an almost straight beam bore. As a consequence, we obtain an energy dependent on-axis effective area and the vignetting function depending on the energy and the off-axis angle. The simulated on-axis effective area is shown as the blue line for a telescope aperture of 48 mm diameter. The effective area for the CAST aperture shown as red triangles is the result of the PANTER measurements scaled with the ratio of the simulated effective area for 48 mm and 43 mm diameter. The effective area for the 2003 data was simulated for a point source located at an infinite distance. However, to be more exact, for the data taking period in 2004, the on-axis effective area for the magnet bore aperture was newly simulated for a realistic axion energy and intensity distribution for the extended solar source. The results are shown in Fig. 4.5.

The point spread function (PSF) of the telescopes depends on the source size and thus on the off-axis angle could be as well. When increasing the off-axis angle, fewer photons entering the telescope reach the focal plane. This effect is called vignetting. The vignetting effect depends on the energy and radial off-axis angle. The influences of the off-axis angle of the telescope on the effective area can be seen in Fig. 4.6. The asymmetrical experimental setup with only one part of the six sectors, which breaks the radial symmetry of the mirror system, leads to a difference between the radial and the tangential off-axis angle. A slightly asymmetric point spread function and an asymmetry of the vignetting appear due to the magnet bore and the telescope structure. However, the asymmetry of the PSF can be ignored for CAST because the expected spot size of the axion signal is larger than the image of the PSF. The effects of the magnet bore and telescope geometry on the efficiency losses of the telescope are shown in Fig. 4.7. It can be clearly seen that for a slight misalignment, the telescope efficiency reduces, e.g. for an off-axis angle of above 2 acrmin the efficiency decreases by about 10%.

4.1.2 Efficiency

By combining the effective area, which was measured for different energies, with the results of the simulation, the on-axis effective area of the best sector for the interesting energy range of CAST was calculated by interpolation for the data collection period of 2003 and 2004. The overall X-ray detection efficiency used for data analysis later on is given by the mirror reflectivity of the telescope and the quantum efficiency of the CCD detector. The quantum efficiency of the CCD will be explained in more detail in Section 4.2.5. The reflectivity depends on the mounting of the telescope and the alignment of the telescope with respect to

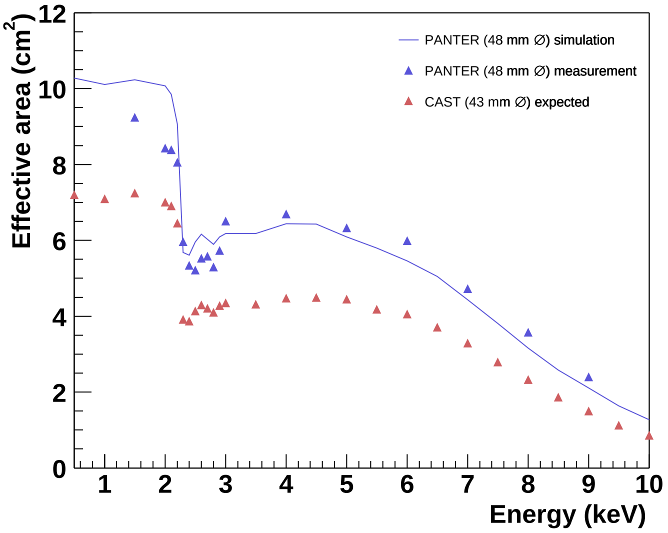

Figure 4.4: On-axis effective area of the X-ray mirror telescope. The blue triangles are the measured effective area at PANTER with an aperture of 48 mm diameter, the blue line shows the simulated effective area with the same aperture. The red triangles present the expected effective area for an aperture with 43 mm diameter for CAST, which is used for the 2003 data analysis [89].

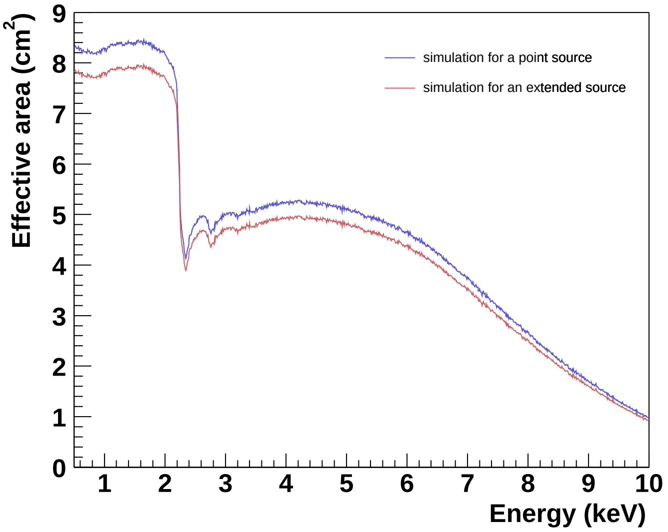

Figure 4.5: Simulated effective area for a point source and an extended source. The blue line shows the effective area of the telescope for the data taking period of 2003 for a point source located at infinite distance, whereas the red line is the effective area for the data taking period of 2004 for an extended source of the size of the axion emission region from the sun.

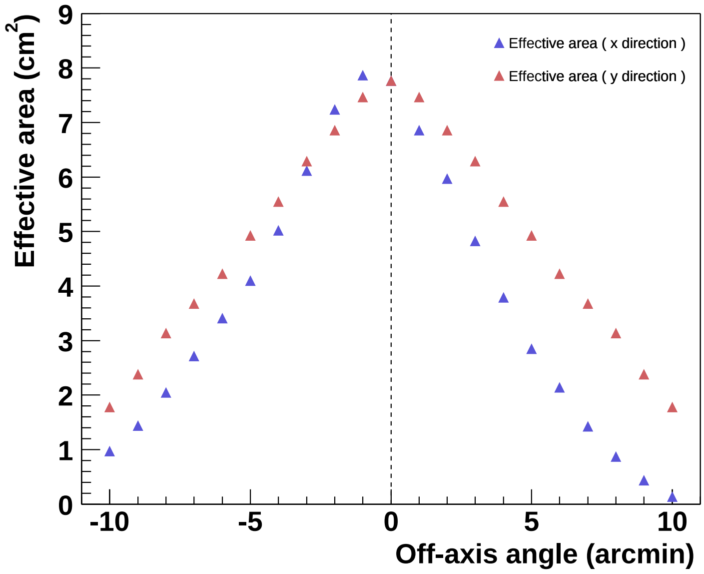

Figure 4.6: Vignetting effect on the effective area of the telescope at a photon energy 1.5 keV for radial (blue) and tangential (red) off-axis angles.

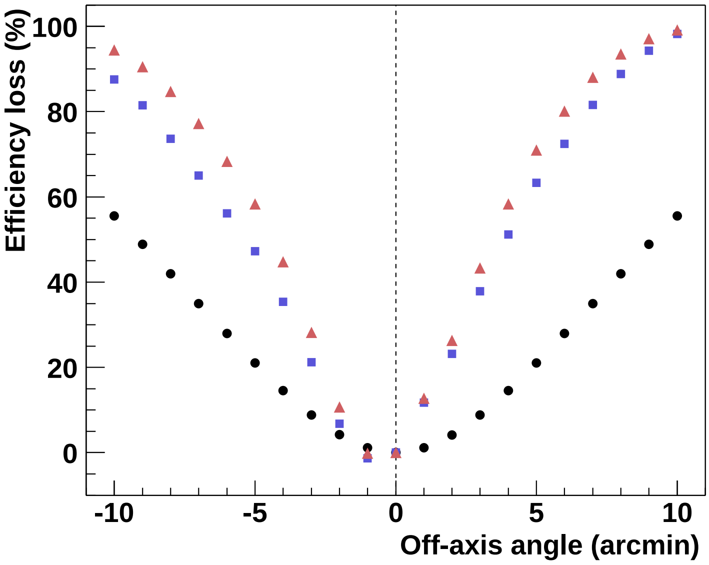

Figure 4.7: Efficiency loss due to vignetting effects at photon energy 1.5 keV. Closed circles are the vignetting effect due to the magnet pipe geometry with an assumption of an extended axion source, blue squares are vignettings due to the telescope geometry, and the total vignetting effect are given by red triangles.

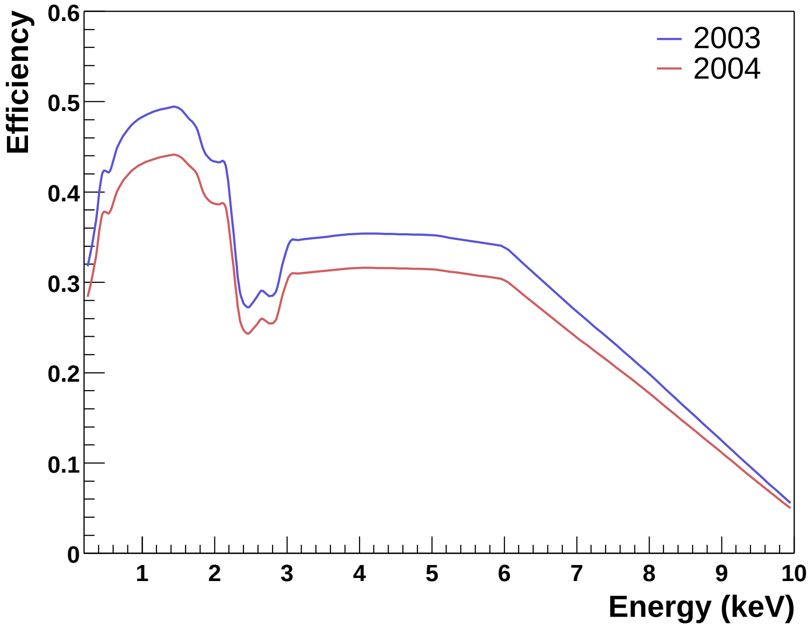

Figure 4.8: Efficiency of the X-ray telescope given by mirror reflection and the quantum efficiency of the CCD detector. The drop close to 2.2 keV is due to the gold absorption effects at the M edge of the gold coating of the mirror surface.

the axes of the magnet bore.

The efficiency curve in Fig. 4.8 shows the result of ray tracing simulations which were compared with transmission measurements at the PANTER facility before the installation of the telescope at CAST. The efficiency for the 2004 data collection period is reduced by about 10% compared to 2003 because the optical axis of the X-ray telescope is slightly tilted to the optical axis of the magnet bore. This small adjustment of the telescope axis was necessary for a better centering of the solar axion spot on the CCD sensitive area. The integrated detection efficiency of the X-ray mirror system is about 30 to 35% for the energy range from 1 to 7 keV.

4.2 The CCD detector

The focal plane detector of the CAST telescope is a Charge-Coupled Device (CCD) of the type used in XMM-Newton[5] [90] with high detection efficiency, low noise level, and an ultrafast read-out time. The X-ray photons emerging from the magnet bore can be focused by the optical telescope onto the pn-junction CCD with a sensitive thickness of 280 μm, a sensitive area of $1{\times}3$ cm^2 and a pixel size of $150{\times}150$ μm^2. The CCD detector is conceptually a derivative of the silicon drift detector proposed in 1983 by E. Gatti and P. Rehak. It has been developed at the Max Plank Institute Semiconductor Laboratory in Munich. In this Section, the basic concept, working principle, and performances of the CCD detector will be explained in detail.

4.2.1 Basic principle of semiconductors

In an intrinsic semiconductor crystal, the number of holes is equal to the number of electrons in the conduction band. Its balance can be altered by adding a small fraction of impurity atoms having one more or one less valence electron in their outer atomic shell. Silicon has four valence electrons so that four covalent bonds can be formed. In a silicon crystal, the atom can be replaced by either pentavalent atoms or trivalent atoms. This procedure is called doping. Depending on the type of doping material, one can classify n- and p-type semiconductors, respectively.

If the impurity atom is pentavalent with one more valence electron, there will be enough electrons to fill up the valence band and remains free for conduction. At room temperature, the extra electrons are excited into the conduction band and raise the conductivity of the semiconductor. Thus the electrons become the majority charge carriers, while the holes are the minority carriers. Such semiconductors with donor atoms and an excess of electrons in the conduction band are referred to as n-type semiconductors. Typical donor atoms are phosphorus, arsenic and antimony.

If the dopant is trivalent with only three valence electrons, one electron bounds in a covalent bond and a hole is created in the energy gap. The hole which is free for conduction can be filled by an electron from an adjacent atom which is equivalent to moving a hole. Electrons in the valence band are then easily excited into the extra level leaving extra holes behind. The excess of holes reduces the free electrons so that the holes are the majority charge carriers and the electrons are the minority carriers. Doped semiconductors with holes in the valence band are called p-type semiconductors. To make p-type semiconductors, the acceptor elements are usually boron, gallium and indium.

---

[5] The X-ray Multi-mirror Mission

For heavily doped semiconductors, impurity concentrations in these materials are very high so that they are highly conductive. To make a distinction between these materials and normally doped semiconductors, a + sign is put on after the material type. Thus a heavily doped n-type semiconductor is written as n^+ and a heavily doped p-types as p^+.

The pn-junction and depletion zone

The most important of the basic principle for the pn-CCD detector is the pn-junction which is formed by joining a p-type material with a n-type semiconductor. When the two volumes are put into contact, electrons diffuse into the p-region and holes into the n-region, and remainders will be created negative electric charge on the p-side and positive charge on the n-side. This creates an electric field gradient across the junction which halts the diffusion process. Due to this electric field, there is a potential difference across the junction which is known as a contact potential. The charge density and the corresponding electric field are shown in Fig. 4.9. In the energy band structure diagrammed in Fig. 4.9, the contact potential V_o, which is known as a diffusion voltage, is obtained from the fact that the Fermi levels have to line up in thermal equilibrium and are about the order of 1 eV [91].

The region of changing potential which is referred to as the depletion zone around the pn-junction boundary is almost free of all movable charge carriers, so that all entering electrons or holes into this region will pass by the electric field. Due to this special property of the depletion zone, ionizing radiation entering this zone will release electron-hole pairs which are swept away by the electric field. If electric contacts are placed on either end of the junction device, a current signal proportional to the ionization will be detected.

Interaction of radiation with semiconductors

The interaction of radiation with semiconductor materials creates electron-hole pairs which can be detected as electric signals. Photons have to interact with a target electron (photoelectric or Compton effect) or with the semiconductor nucleus (pair production). The occurrence of these effects and their ratios are strongly energy dependent. A part of the absorbed energy in the materials will be converted into ionization (i.e. creation of electron-hole pairs) and the rest into phonons (i.e. lattice vibrations) which means eventually into thermal energy. For a deposited energy, the signal will fluctuate around the mean value N given by

$$N = \frac{E}{\varepsilon} \tag{4.1}$$

with E is the absorbed energy in the detector and ε is the average energy spent for creating an electron-hole pair. The variance of the number of signal electrons or holes is given by

$$< \Delta N^2 >= F \cdot N = F \cdot \frac{E}{\varepsilon}, \tag{4.2}$$

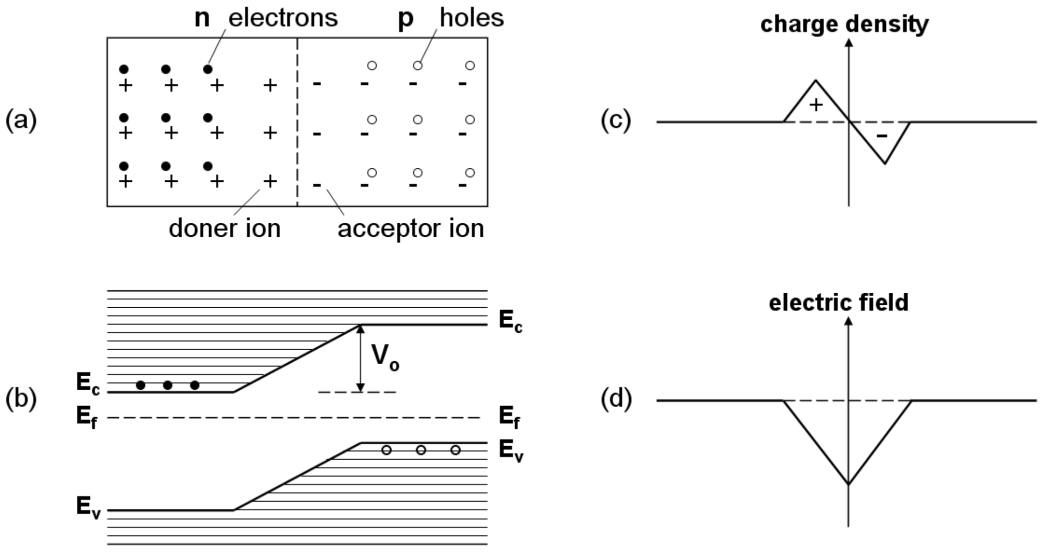

Figure 4.9: (a) A scheme of an pn-junction (closed circles are electrons, open circles are holes, - signs are negative ions from filled holes from p-type impurity, and + signs are positive ions from removed electrons from n-type impurity), (b) diagram of electron energy levels with a contact potential V_o, (c) charge density, and (d) electric field intensity.

where F is known as the Fano factor [92]. The factor F is a function of all various fundamental processes which can lead to an energy transfer in the detector. This includes all reactions which do not lead to ionization as well, e.g. phonon excitation. Thus it is an intrinsic constant of the detecting medium. The Fano factor for both silicon and germanium is still not accurately determined. However, it is clear that the factor F is small and on the order of 0.12. Therefore, the intrinsic energy resolution of detectors is dependent on the Fano factor.

Absorption coefficient

An important aspect in semiconductor materials is the penetration depth of charged particles and the absorption length of photons. A very small absorption length will lead to a very high probability of producing the signal close to the surface and a very high absorption length means that the radiation may leave the detector without interaction. X-rays of monoenergetic photons with an incident intensity I_o penetrating a material with mass thickness x and density $\rho(g/cm^3)$ emerges with intensity I given by the exponential attenuation law

$$I(x) = I_o e^{-\mu \rho d}, \tag{4.3}$$

where $\mu(\mathrm{cm}^2/\mathrm{g})$ is the mass absorption coefficient which is the inverse of the mean free path of photons. The mass thickness x is defined as the mass per unit area and can be obtained by multiplying the thickness d by the density ρ, i.e. $x = \rho d$. The absorption length of photons in silicon (Si) and silicon oxide (SiO_2) is plotted in Fig. 4.10 for the photon energy range of 1 eV to 20 keV. At this low energy range, the absorption coefficient is dominated by the photo effect. The range of photons in silicon varies from a few mm in the near infrared to several tens of Å for UV light and then increases again for higher energies to 1 mm for roughly 20 keV. The absorption is most efficient at the silicon M-, L- and K-absorption edges corresponding at roughly 20, 100-150 and 1830 eV, respectively.

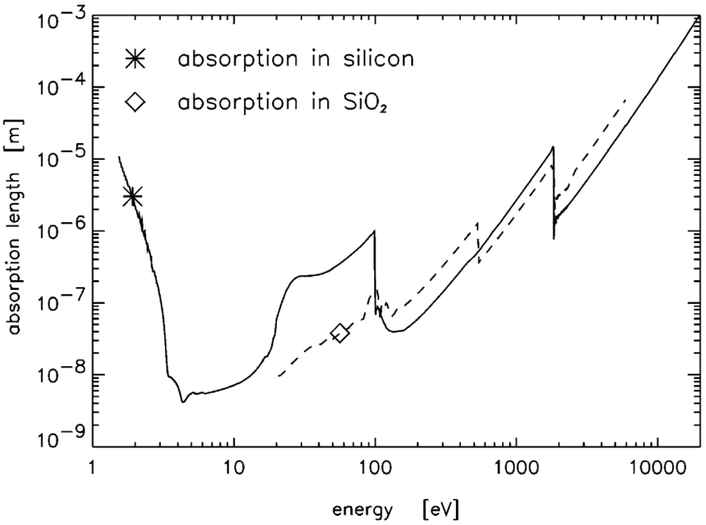

Figure 4.10: Energy dependence of the photon absorption length in Si and SiO_2 [86].

4.2.2 Structure and working principles

The basic concept and working principles of a fully depleted pn-CCD detector can be seen in Fig. 4.11 [93, 94]. A double-sided polished n-type silicon wafer with high resistivity has both surfaces covered with a p^+ boron implant. One edge of the device structure has a small (an essential condition for good noise performance) n^+ phosphorus implant for read-out which keeps an ohmic connection to the non-depleted silicon bulk. The silicon bulk is homogeneously doped with phosphorus with a concentration of 10^{12} per cm^3. A reverse bias is applied to both p^+ junctions, i.e. a negative voltage is applied with respect to the n^+ anode. The depletion in the high ohmic substrate with a resistivity of about 4 k Ωcm develops from both surfaces, until the depletion regions touch in the middle of the wafer. The potential minimum of electrons is then located in the middle of the wafer. An additional negative voltage on the p$^+$ back contact shifts the potential minimum for electrons from the center towards the surface having the pixel structure, i.e. a local potential minimum for electrons is created in a distance approximately 10 μm from the surface. Three p$^+$ strips with the three potentials (ϕ_1, ϕ_2, and ϕ_3) belong to one pixel. The depletion voltages on the backside are typically between -150 V and -200 V in the 280 μm thick fully depleted device.

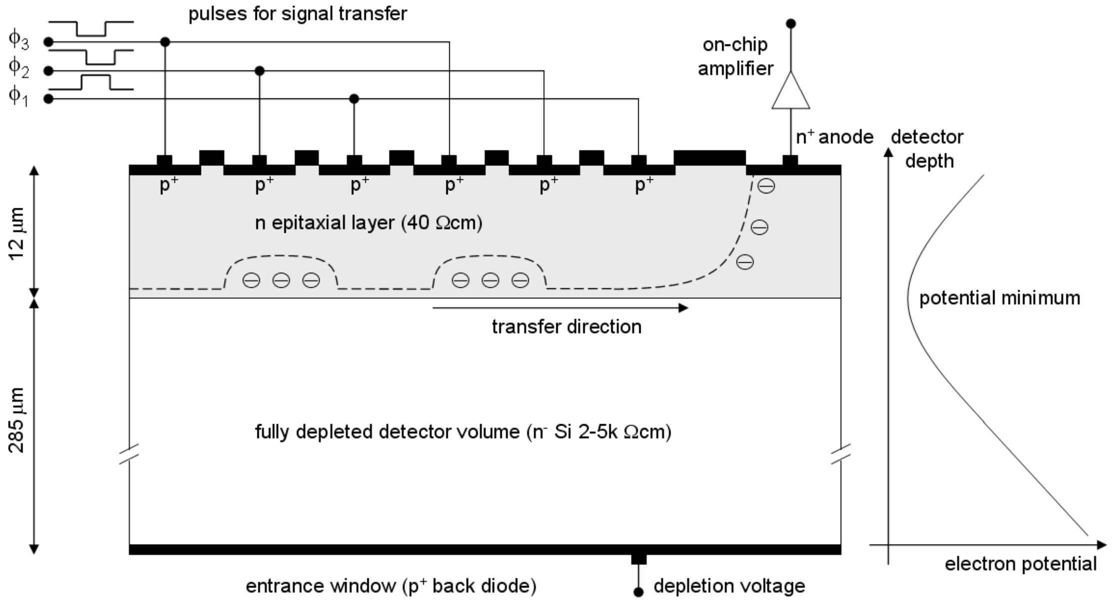

Figure 4.11: A schematic diagram of a fully depleted pn-CCD.

A periodic change of the applied voltages at the p$^+$ transfer registers ϕ_1, ϕ_2, and ϕ_3 allows a discrete transfers of the signal charges in the local potential minimum for electrons toward the read-out anode. The side having the p$^+$ transfer registers has an additional phosphorus doped epitaxial layer of a 12 μm thickness with a concentration of approximately 10^{14} donor atoms per cm^3. The interface of the epitaxial layer and the high resistivity bulk silicon acts as a potential barrier for electrons to a distance of roughly 10 μm below the top surface.

Figure 4.12 shows one pn-CCD unit consisted of 64×200 picture cells (pixels) with a total area 1×3 cm^2. The 64 individual transfer channels have its own read-out node designed for high speed read-out, so that parallel read-out is possible that requires only 70 ms for the complete device. The pixel size of 150×150 μm^2 is matched to the spatial resolution of the detector. A deep n-implantation below the p$^+$ transfer registers and below the SiO$_2$ is introduced to form a guiding channel for signal charges.

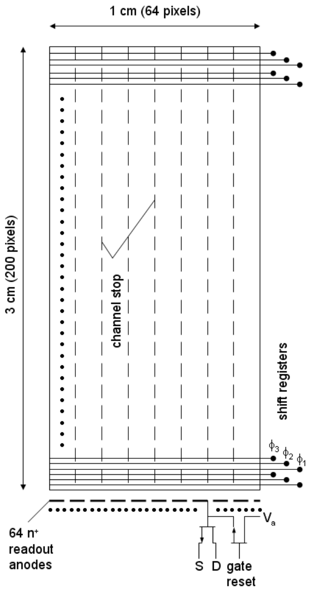

Figure 4.12: One pn-CCD subunit of a size 1×3 cm^2 with 64 on-chip preamplifiers.

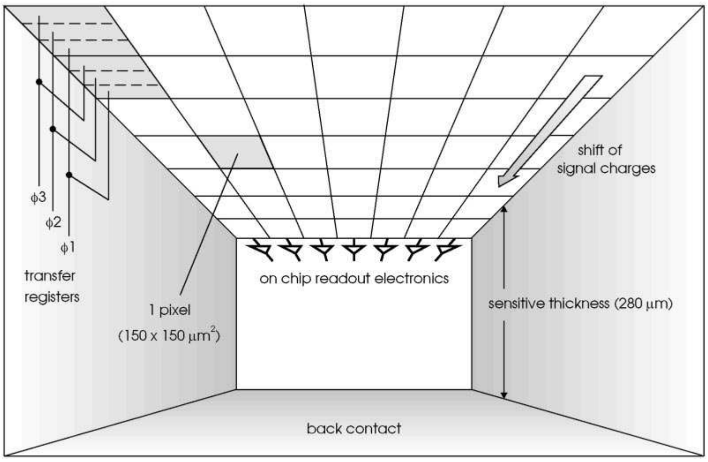

Figure 4.13: Inside of the pn-CCD. The photons enter the detector from the bottom. The charges are collected in the potential minima close to the surface having a pixel structure and shifted to the on-chip amplifier after integration.

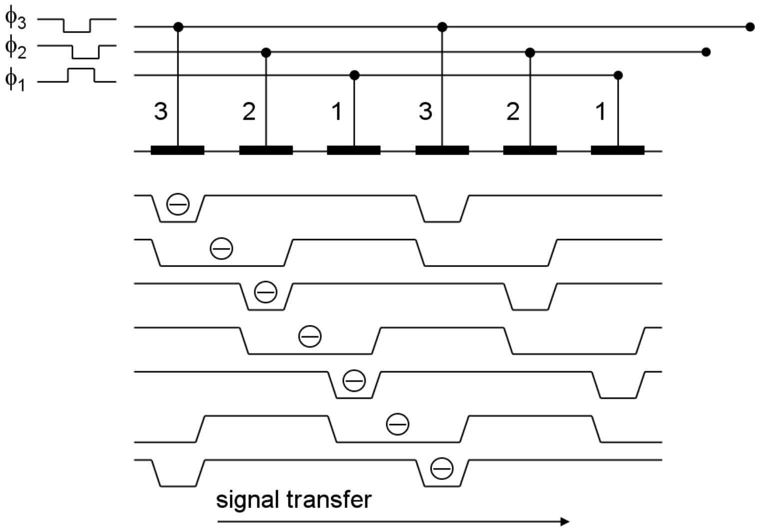

Figure 4.14: Signal transfer by three shift registers. Electrons collected in the potential minima can shifted toward the read-out anode by periodic change of the potentials.

A different view of the pn-CCD can be seen in Fig. 4.13. The X-ray photons hit the device from the backside illuminated window. The entrance window is made very thin in order to get a good response for short range radiation. The positively charged holes move to the negatively biased back side, electrons to their local potential minimum in the transfer channel, located about 10 μm below the surface having the pixel structure. Each CCD line in Fig. 4.13 is terminated by a read-out amplifier.

4.2.3 Read-Out concept

Electrons produced in the space-charge region by ionizing radiations will drift to the electron potential minima. The charge can be now shifted toward the read-out electronic by a periodic change of the voltage. The scheme of the charge transfer mechanism in a depth of roughly 10 μm below the shift registers can be seen in Fig. 4.14. First the signal charge is stored under the register ϕ_3 only. If ϕ_2 is now lowered to the same level as ϕ_3, the signal charge will spread between ϕ_2 and ϕ_3. Then ϕ_1 is increased, the signal charge will transfer below the electrode ϕ_3. If this sequence of suitably changing potentials is repeated, the signal will finally arrive at the read-out anode.

As shown in Fig. 4.15, the CCD chip has 200 pixels in the signal transfer direction and 64 pixels in the perpendicular direction. The entire sensitive area of the chip is 1×3 cm^2. The serial multiplexing CCD register is replaced by a total of 64 parallel output anodes which are

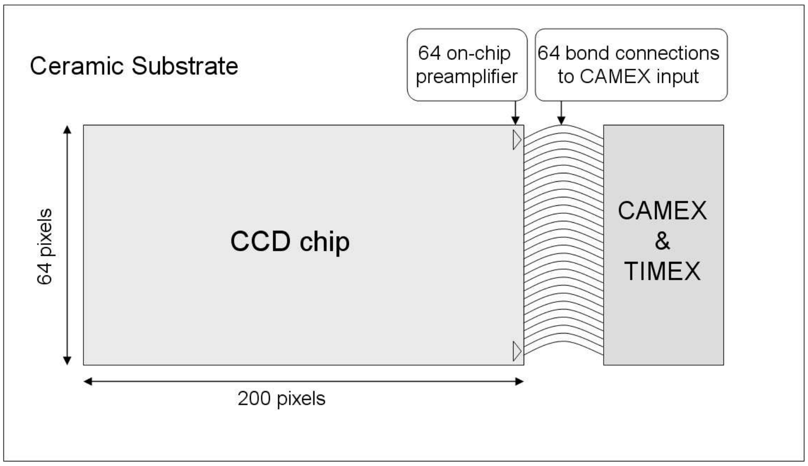

Figure 4.15: General layout of the CCD detector consisting of 64×200 pixels with a sensitive area 1×3 cm^2.

on-chip connected with 64 on-chip preamplifiers each consisting of one input Junction Field Effect Transistor (JFET) for low noise read-out. Those identical 64 CCD output channels are bonded to a 64 channel CMOS[6] amplifier chip (CAMEX64). Thus the 64 signals of each row are fed in parallel to the CAMEX64. CAMEX stands for CMOS Multichannel Analog MultiplEXer for the read-out of silicon strip detectors. It is a 64 channel amplifier chip developed at the Max Plank Institute Munich for amplification, shaping and multiplexing. The chip provides mainly signal amplification, noise filtering, parallel storage, and serial read-out of the analog signals. The output of the CAMEX chip is connected to the ADC, so that read-out and digitalization can take place in parallel. The digitalization of the 64 amplified output signals is very fast due to a 10 MHz 12 bit flash ADC. If the entire sensitive area is used, the complete read-out time needed is about 70 ms. The TIme MultiplEXer (TIMEX) is the digital control unit of the CAMEX. Further details can be found in Refs. [95, 96].

4.2.4 Properties of CCD signals

In order to better understand the images recorded with the CCD, we need to know the intrinsic properties of the CCD detector. Here the characterizations of the CCD in terms of noise, offset, partial events, split events, out of time events, gain, charge transfer efficiency, common mode, and pile up are described.

---

[6] Complementary Metal-Oxide-Semiconductor

Electric and system noise

When a CCD image is taken, noise will appear as well as the main CCD image. Noise is an unwanted signal. There exist mainly two different sources of noise in the CCD detector: detector intrinsic noise and electronic noise. The basic reasons for the detector intrinsic noise are mainly metal contamination in the silicon or imperfections in the silicon lattice. This detector intrinsic noise can be generally described by the Fano factor:

$$< \sigma^2_{Fano} >= F \cdot \frac{E}{\varepsilon}, \tag{4.4}$$

where F is about 0.12 for Si and the mean energy for electron-hole pair creations is $\varepsilon = 3.65$ eV. With typical absorbed energy for Mn-K_α of 5.9 keV the intrinsic Fano noise is about 14 eV. The electronics of the CCD will also create noise signals. The main electric noise components are thermal noise, leakage current noise of the read-out anode, and low frequency noise. Thermal noise occurs by thermal fluctuations of electrons without any application of external power. The leakage current noise is caused by all currents flowing to the electronics input. The largest noise contribution arises from the read-out chip CAMEX. The low frequency noise arises mostly by electrical devices e.g. amplifiers or ADCs. Most of the noise is essentially random, so that it cannot be completely removed from the image. However, the noise could be reduced by cooling the detector. By the summation of the Fano noise and the electronic noise, the total detector noise can be approximated

$$\sigma_{noise} = \sqrt{\sigma^2_{Fano} + \sigma^2_{CAMEX} + \sigma^2_{ADC}} \approx 24\text{eV}. \tag{4.5}$$

A detailed noise calculation is given in Refs. [97, 98].

Dark current

Another important effect is an offset. Even when the detector is not illuminated, a small current is generated thermally in the CCD itself and will contribute to the measured signal. This current is called the dark current which is strongly affected by the temperature of the chip. All CCDs have a dark current which can cause each pixel to fill with electrons in only a few seconds at room temperature even in the absence of the light. Main contributions to dark current are thermally generated electrons within the bulk silicon and in the deep depletion region. By cooling the CCD to about -120°C, the dark current signals as well as all potential sources of noise are usually minimized to negligible levels [98].

Partial events

Partial events are events caused by photons detected in the CCD close to the surface, whereby part of the charge is lost. X-ray photons with low energies between 100 eV and 500 eV have a low penetration depth, so that these photons will be absorbed close to the entrance region and thus lose part of their charges in the surface layer. The partial events have an energy dependent effect but play a role at the few percent level. The effect is known and predicted and can be recombined and signalized.

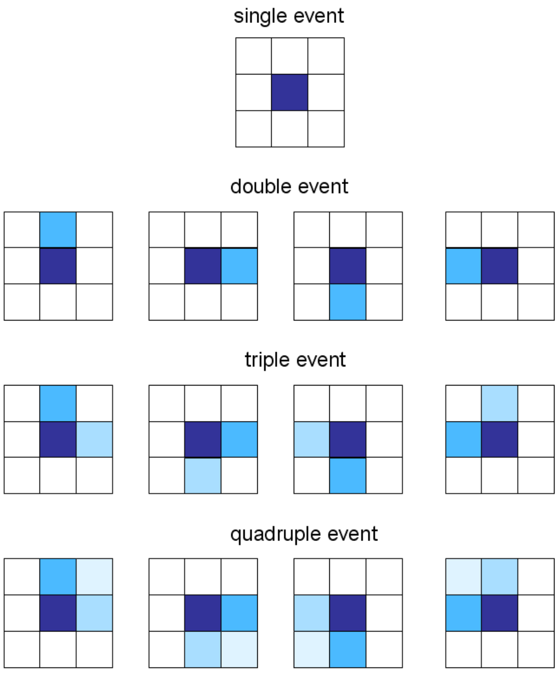

Figure 4.16: An example of single, double, triple, and quadruple events. The dark blue pixels represent the pixel with the most charge content.

Split events

During the electron signals generated by an X-ray photon drift to the potential minimum, the charge carriers spread out due to diffusion or mutual repulsion. Thus the electron signals are collected in a single pixel or spread over up to four pixels. As shown in Fig. 4.16 the different signal patterns are single, double, triple, and quadruple events which are dependent on the position of the X-ray photon relative to the pixel border. The smaller the pixel size of the CCD the higher the probability for event splitting. Table 4.2 shows the probability of split events; single events are the most frequent type as compared to split events.

Single events	70%
Double events	28%
Triple events	1.6%
Quadruple events	0.4%

Table 4.2: Probability of split events for a pixel size (150 μm)^2.

Pile-up events

Pile-up events occur on the CCD when two or more photons are detected in one pixel during one accumulation period. In that case they are counted as one and the apparent energy is approximately the sum of their energies. One method which can avoid pile-up effects is by reducing the CCD exposure time. By shortening the exposure time, the probability of pile-up events reduces. In addition, the fraction of pile-up events can be estimated with sophisticated pile-up models to reach a better precision of the spectrum.

Out-of-Time events

Photons are detected not only during the actual integration time but also during the read-out time of the CCD. These Out-of-Time (OoT) events are recorded with an incorrect row in the CCD. Since charges shift along a column towards the read-out anode, these events are distributed along each read-out channel. The fraction of out-of-time events is given by the ratio of the read-out and integration time. The signal transfer and read-out takes 6.06 ms for the entire CCD with 200 rows. The CCD is exposed to the X-rays during the whole cycle time which is 71.7705 ms in the standard full frame mode. Hence the fraction of out-of-time events becomes to 6.06 ms / 65.7105 ms = 9.2 %.

Charge transfer efficiency

The charge transfer efficiency (CTE) is an extremely important parameter of the CCD, because the charge has to be transfered to many pixels before arriving at the read-out node. The transfer of charges along the channels to the anodes causes a signal charge loss due to the capture of single electrons in traps within the silicon lattice. The CTE less than 1 describes the fraction of electrons which are successfully transferred from one pixel to the next pixel during read-out and is given by

$$CTE = \frac{Q_{i+1}}{Q_i}, \tag{4.6}$$

where Q_{i+1} and Q_i are the charges of the $(i+1)$th and ith pixels, respectively. The charge transfer of the CCD is good with the order of a few % signal loss from the last to the first pixel over a distance of 3 cm charge transfer [99].

Bad pixel

Some of the pixels may be faulty and return signals which are grossly inaccurate. Those pixels that having a higher than average dark current are often referred to as hot or bad pixels. Since such pixels arise from the CCD manufacturing process, each hot pixel location will remain fixed and can therefore be excluded.

4.2.5 Quantum efficiency

The quantum efficiency (QE) of the CCD detector is defined as the percentage of the generated electric charges by the incoming photons. This efficiency is usually determined by material properties, production, and its design structure. In order to determine the quantum efficiency of the CCD, measurements were performed at the synchrotron radiation facilities in Berlin.

Figure 4.17 shows the measured quantum efficiency of the CCD in the spectral range between 150 eV and 15 keV. At 538 eV a 5% drop can be seen from the absorption at the oxygene edge in SiO_2 layers. The same happens at the silicon K absorption edge at 1840 eV (see inset of Fig. 4.17). For all energies the quantum efficiency is well represented by a model using the photon absorption coefficients from the atomic data tables. A detailed description of the quantum efficiency measurements can be found in Ref. [100]. Over the entire energy range between 300 eV and 10 keV, the quantum efficiency is higher than 90%, showing small drops at the oxygen and silicon K edges caused by the covering silicon dioxide layer.

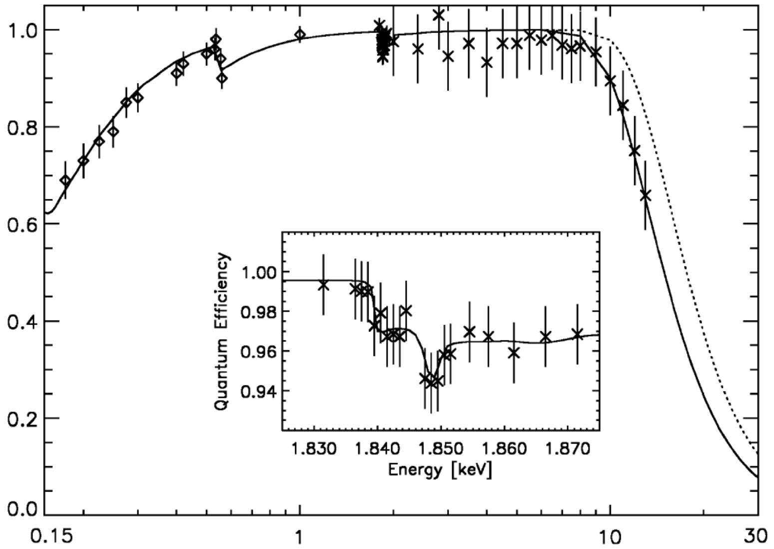

Figure 4.17: Quantum efficiency of the CCD detector. The drops at 538 eV and 1840 eV are due to absorption losses from oxygen and silicon K edges in the 30 nm SiO_2 layer. The solid line represents a 300 μm thick sensitive volume and the dotted line 500 μm [100].

4.3 Commissioning of the detector

4.3.1 Gain

Before the CCD detector was mounted to the CAST magnet, the detector was calibrated with an X-ray fluorescence generator at the X-ray test facility PUMA in Munich in order to optimize the performance of the detector. Continuous X-rays from the X-ray generator shine the target in the chamber. The targets are on a platform that can be rotated to select the target. The measurements mainly concentrated on the gain calibration which represents the scale factor of the conversion from electrons (e^-) detected to Analog Digital Unit (ADU) assigned in the read-out image. A large gain allows for a high range of linear detectability on the chip, but causes higher digitization noise.

As shown in Fig. 4.18 the gain was determined as 4.6 eV/ADU with a straight line fit to the measured data and the detector gain of the CCD is almost perfectly linear over the full energy range of 0.2 - 10 keV.

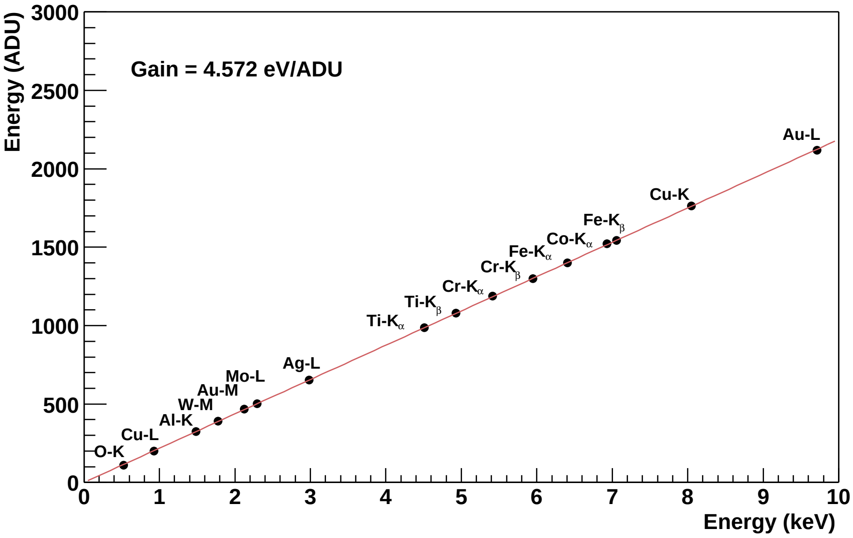

Figure 4.18: Gain calibration of the CCD detector. The solid circles represent the data points from each X-ray source.

4.3.2 Energy resolution

The achievable energy resolution [86] of a silicon detector can be as good as

$$\Delta E_{FWHM} = 2.355 w \sqrt{ENC^2 + \frac{FE}{w}}. \tag{4.7}$$

F is the Fano factor, E the total X-ray energy, w the pair creation energy, ENC (Equivalent Noise Charge) the rms fluctuation of the read-out noise, and 2.355 the conversion factor between the standard deviation σ (rms) of a Gaussian and the FWHM. With F = 0.12, w = 3.65 eV, for E = 5.9 keV and a read-out noise of 10 electrons, the best achievable energy resolution is about 150 eV FWHM.

In general, the ^{55}Fe X-ray source is a standard in measuring characteristics for the CCD. An ^{55}Fe atom is inherently unstable and decays into a manganese (Mn) atom by electron capture with a half-life of 2.7 years. An X-ray is generated when an electron drops from either the L- or M-shell to fill the empty K-shell. This action in turn produces either a K_α or K_β lines (X-ray), respectively. The measured energy spectrum with a ^{55}Fe X-ray source is shown in Fig. 4.19. Two well separated peaks correspond to the Mn-K_α (5.9 keV) and Mn-K_β (6.5 keV) in the electron capture decay of the ^{55}Fe source. The spectrum gives an energy resolution of about 160 eV FWHM for the K_α line.

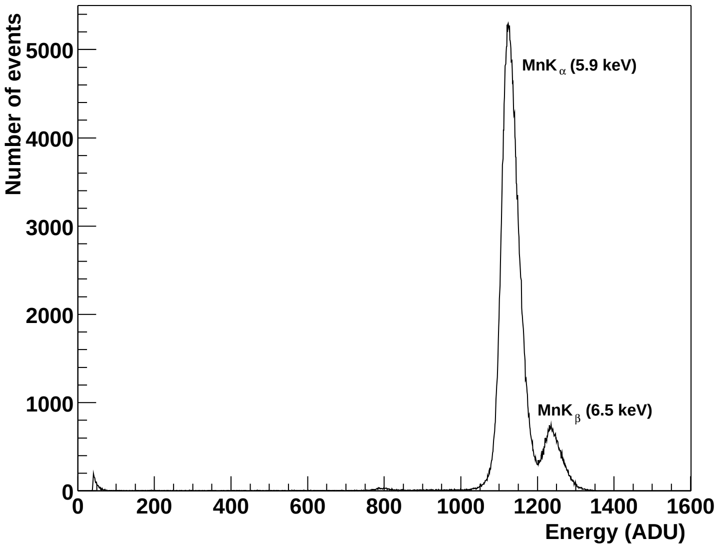

Figure 4.19: Energy spectrum for a ^{55}Fe source measured with the CCD detector. The energy resolution is about 160 eV (FWHM) at -130°C.

4.3.3 First background measurements

In autumn 2002 the CCD was installed on the telescope at CERN after it has been aligned. First operation tests and background measurements [101] were done to verify the performance of the detector. As shown in the left of Fig. 4.21 these data show a low energy background component which originates from fluorescent emission induced by electrons emitted by a pressure gauge and photons originating from the ^{55}Fe calibration source. Both components could be eliminated by improving the shielding of the ^{55}Fe source and by adding a filter mesh in front of the pressure gauge.

Detector shielding

In order to reduce the detector background, a copper shield made of 1 cm thick low activity Cu was put inside the vacuum chamber of the CCD detector and encloses the CCD chip (see right Fig. 4.20). Towards the telescope an aperture hole limits the field of view of the CCD to the field of view of the X-ray telescope. The copper shield has improved the background level to 2×10^{-4} counts cm^{-2} sec^{-1} keV^{-1} (see bottom Fig. 4.21). The background is almost flat in the energy range up to 10 keV. The only significant Cu peak close to 8 keV is due to the copper shielding and cooling mask enclosing the CCD. The background has been reduced further with an additional shielding (Section 6.2.1).

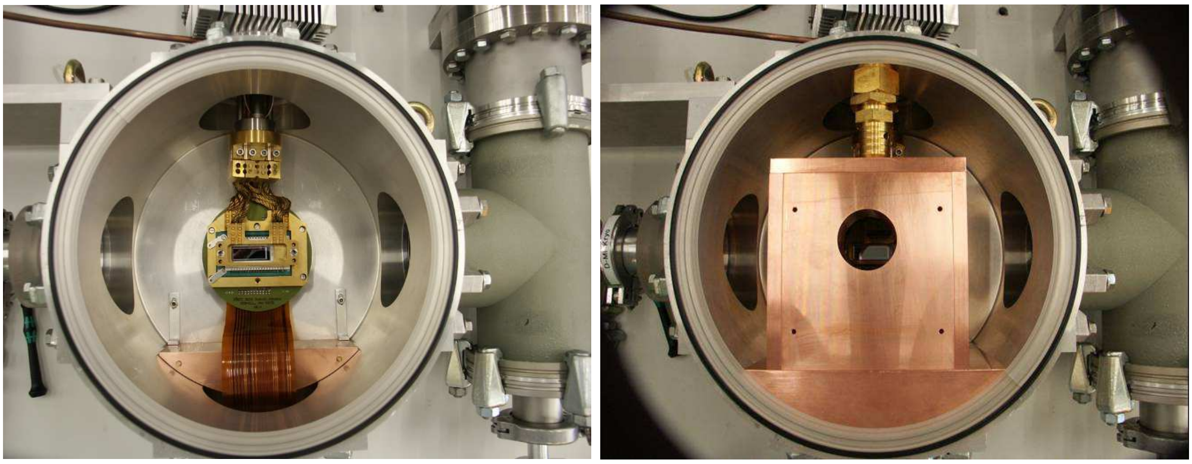

Figure 4.20: Left: Front view of the CCD detector. The black region in the center is the active area of the CCD chip. The CCD chip is surrounded by a gold plated copper cooling mask. At the bottom the flexible electronic connections to the outside are visible. Right: Inside view of the CCD with the copper shielding. The hole in the center is the aperture to the telescope.

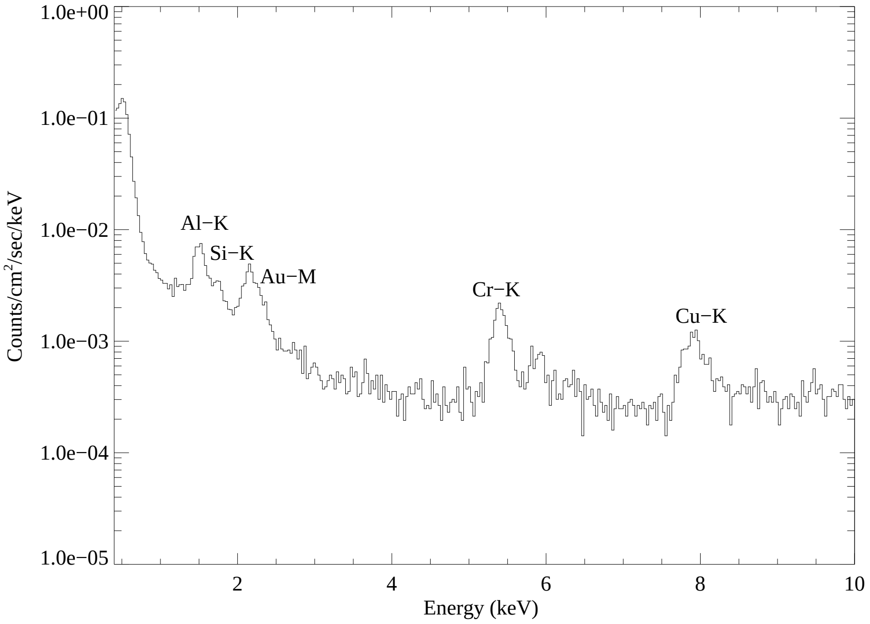

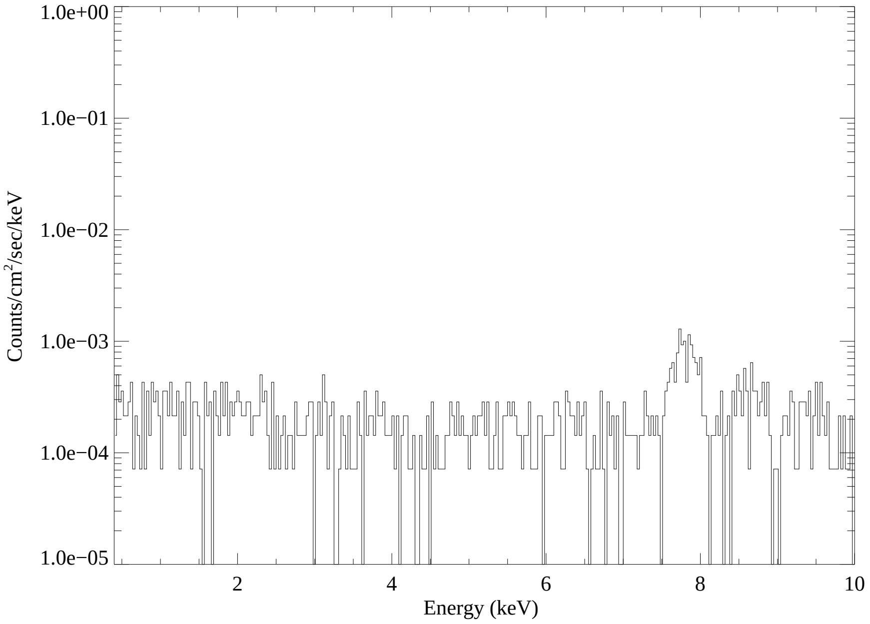

Figure 4.21: Background spectra of the CCD detector. Top: First background spectrum taken in the CAST experiment in autumn 2002. The fluorescence lines (Al and Si) appear to come from within the detector itself. The Au and Cu peaks are from a gold plated copper cooling mask. Bottom: Background spectrum in spring 2003 after installing a Cu shield, a new shielding of the ^{55}Fe calibration source, and a filter for the pressure gauge.

Chapter 5

Analysis of the 2003 Data

All CAST detectors operated stably for about 6 months in 2003. In this Chapter the analysis of the data acquired with the CCD detector will be presented in detail. The 2003 data taking and how the data was processed are given in the first Section. In order to identify the background, studies of background are discussed in Section 5.2. The main goal of the data analysis is to determine an upper limit on the coupling constant of axions to photons, $g_{a\gamma}$. In Section 5.3 and 5.4 the upper limit on $g_{a\gamma}$ will be determined with various statistical methods.

5.1 Data collection

Data collection of the CCD started on May 1st in 2003. In the beginning of the data taking periods a mechanical problem in the magnet lifting system appeared and the magnet movement was fully stopped on May 31st. In order to resume the data taking some mechanical play was added into the lifting system as well as the lubrication system was improved. Due to these modifications on the magnet moving system data taking was restarted after 6 weeks and ended on November 13th in 2003.

During the data taking periods of CAST, the CCD detector was operated continuously for 24 hours. Each morning before tracking a calibration measurement had to be done. The calibration measurement consists of a dark run[1] (200 frames of about 30 seconds) and a calibration run (2000 frames of about 2.5 minutes) for the dark run with the ^{55}Fe source. After the calibration is finished a continuous data taking run (12570 frames of 15 minutes) will start automatically and be running untill the next morning.

Data taken when the magnet is pointing to the sun during sunrise is defined as solar tracking data which is equivalent to signal plus background. All other measurements are considered as background data.

---

[1] A dark run is a part of the calibration run without a ^{55}Fe source.

5.1.1 Data processing

Raw data files are generally supplied in compact unformatted binary files for speedy access and efficient storage. In order to port the data into software packages that manipulate images and data structures, the Flexible Image Transport System (FITS) format, which allows easy export of data, is used. The FITS is a standardized data format which was originally created by NASA[2] and is widely used in astronomy. FITS files can be used to store ASCII or binary tabulated data, in addition to spectra and images. Detailed information can be obtained in Ref. [102]. A FITS file consists of one or more Header and Data Units (HDUs). A header is composed of ASCII images that is usually read into a string array variable in the Interactive Data Language (IDL) software. The header describes the content of the associated data unit, which might be a spectrum, an image, or tabular data in ASCII or binary format.

An important feature of the data processing is a pattern recognition. In order to separate real events from the cosmic ray events, pattern recognition is used to identify tracks of cosmic rays. This is done by separating allowed pattern geometries from not allowed pattern geometries which means patterns that can not result from mere photon interaction with the detector. As mentioned in Section 4.2.4, when a charge cloud is generated by interaction of a photon with the detector close to one pixel edge, the resulting charge can be split over several pixels. Generally four kinds of valid patterns are possible: single, double, triple, and quadruple patterns. Moreover the valid patterns can be classified into different pattern geometries (see Fig. 4.16). Note that charge splitting over the diagonal of pixels is not possible. All other pattern are classified as invalid during data processing and are removed during the analysis. The resulting patterns depend on the location of the charge cloud in the pixel. In addition the charge cloud depends on the energy of the initial photon.

5.1.2 Data selection

For the CCD data analysis, the first step is that the processed data has to be selected with respect to the data quality. Therefore, the Good Time Interval (GTI) was used. It is a common filtering method involved with selecting rows which have a time value. The time intervals are defined in a separate FITS table extension which contains the start and stop times of each good interval. These time intervals indicate the periods of the observation times and are further taken into account during the analysis. In order to extract solar tracking and background data, the parameters from the Slow Control data have been taken into account and the following data selection criteria (Table 5.1) are used for the analysis of the 2003 data:

---

[2] National Aeronautics and Space Administration

- **MAGB** The magnetic field strength as read by the Slow Control (SC) software. The value of the magnetic field is 9.0 Tesla which corresponds to 13300 A.

- **HMOTV** Supply voltage of the horizontal motor. Together with the **TRACK** this information can be used to identify solar tracking periods. For background data it equals zero.

- **VT4OPEN** Status of the gate valve between the magnet and the X-ray telescope. 1 indicates that the valve is open and 0 indicates that the valve is closed.

- **TRACK** This means that the solar tracking switch in the tracking software is turned on. For real tracking it can be used in combination with **HMOTV**. The cut **TRACK = 0** is applied for background data.

- **QUENCH** It indicates the time of a quench of the magnet.

- **TIME** In order to separate the morning tracking run from the evening run, the time information in the SC data is used.

- **LIGHT** It summarizes all information of anomalies found in the data (Appendix A.1). The following cases are possible:

  0 It is the default value for good data that can be used for the analysis.

  1 While a TPC shield was not installed, optical light illuminating the magnet bore on the TPC end illuminated the aperture of the X-ray telescope and are focused onto the CCD. This can modify the background and the performance of the CCD.

  2 Change of the detector noise over long time periods like days or weeks. So far there was not influence on the data.

  3 It summarizes all kinds of unknown problems that are not covered by the others. Most are sudden increases of detector noise of one file.

  4 One or more columns show a sudden increase in noise.

  5 One or more lines show a sudden increase in noise.

Finally, the selected data from FITS files was transformed into ASCII files and the transfered data was then analyzed with a software program based on ROOT and C^{++}.

	Tracking	Background
MAGB	> 8.9 T	> 8.9 T
HMOTV	> 10 V	= 0 V
VT4OPEN	1	1
TRACK	1	0
QUENCH	0	0

Table 5.1: Cuts for tracking and background data sets used for the analysis of the 2003 data.

5.1.3 Summary of the 2003 data

As mentioned above, to extract the tracking and background data the Good Time Interval (GTI) cuts have been applied to all data taken in 2003. In total the CCD detector has accumulated 121.3 hours for good tracking data and 1233.5 hours for background data in 2003. Table 5.2 summarizes the resulting exposure time and counts rates for tracking and background data taking into account all valid patterns, i.e. single, double, triple, and quadruple patterns. Here the background used all data taken under the same conditions as the tracking data. Detailed systematic studies of the background will be discussed in the next Section. An important feature of the data is that the background is measured with about 10 times longer exposure time during the nonaligned periods, so that the time ratio between tracking and background data is 10.08.

	Tracking	Background
Exposure time	121.3 h	1233.5 h
Counts	848	8441
Count rate (10^{-4} counts s^{-1})	19.42 ± 0.67	19.01 ± 0.21

Table 5.2: Summary of the 2003 data for the energy range between 1 and 7 keV.

Fig. 5.1 represents the CCD images consisting of 64 columns and 200 lines for solar tracking and background data. The events are homogeneously distributed over the whole CCD area. The corresponding energy spectra are given in Fig. 5.2. Both tracking and background spectra are normalized to the area of the magnet bore (14.5 cm^2), each exposure time, and the energy. The spectra are binned with a bin size of 0.3 keV, which is approximately twice the energy resolution of the detector. Systematic errors are not taken into account so far. The most noticeable peaks are the emission lines of Cu-K_α and Cu-K_β at 8.0 keV and at 8.9 keV, respectively, due to the copper shielding inside the detector. The peak at 9.7 keV is Au-L_α because the cooling mask of the CCD is made from gold. The escape peak of copper

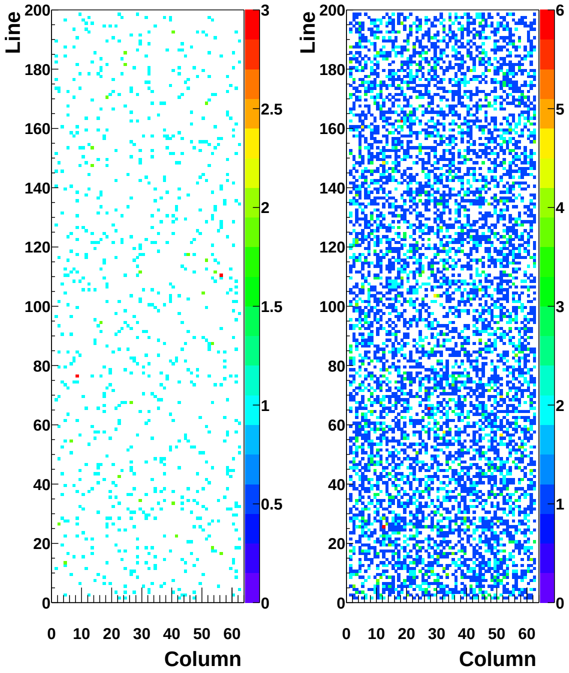

Figure 5.1: CCD images for solar tracking (left) and background (right) data. Both plots are shown for the energy range 1 - 10 keV.

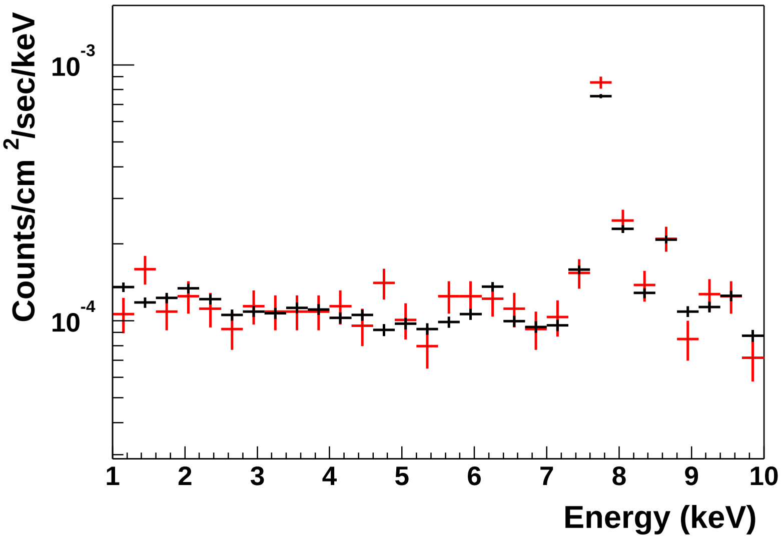

Figure 5.2: Normalized energy spectrum of the solar tracking (red) with the background data (black).

around 6 keV can be seen as well. The shape of both distributions is almost the same, so that the tracking data seems to be consistent with background. Due to the copper lines, the flat energy range between 1 and 7 keV was used for further analysis, i.e. the determination of the coupling constant.

5.2 Background studies

The goal of the background studies is to characterize all backgrounds in order to develop an analysis method to subtract the background from the data, which will allow us to extract an upper limit on the axion coupling constant from the data.

5.2.1 Sources of background

Most contributions to the background come from cosmic rays. Moreover, electronic noise and dark current could also be a source of the background. But they do not contribute to the energy spectrum in the sensitive energy range of axions, since the electric noise is below the energy threshold ($E < 0.5$ keV) and the dark current is subtracted during data processing.

The background can contain the natural radioactive contamination of the materials, e.g. of CCD itself, the shielding with copper and lead, and of the electronics. All the materials close to the CCD and the CCD itself were measured to have background. The natural radioactivity of the CCD made of silicon is negligible. There is some measurable contribution coming from the CCD socket and the CCD ceramics. Electrons emitted by the pressure gauge can influence the low energy background ($E < 3$ keV) and can induce fluorescent X-rays depending on the material close to the gauge.

In addition, X-rays produced in the magnet or telescope walls which could have a natural radioactive contamination cannot be distinguished from X-rays produced by axions. However, this source is negligible as the solid angle is rather small for an X-ray to be emitted exactly parallel to the telescope and walls of the magnet. Ref. [103] gives further details of the detector background.

5.2.2 Time variation

First of all, the temporal variation of the 2003 data can be seen in Fig. 5.3. All events are in the energy range from 1 to 7 keV of the full CCD area. The tracking data seems to be more or less stable over all data taking periods as well as the background does not depend significantly on time.

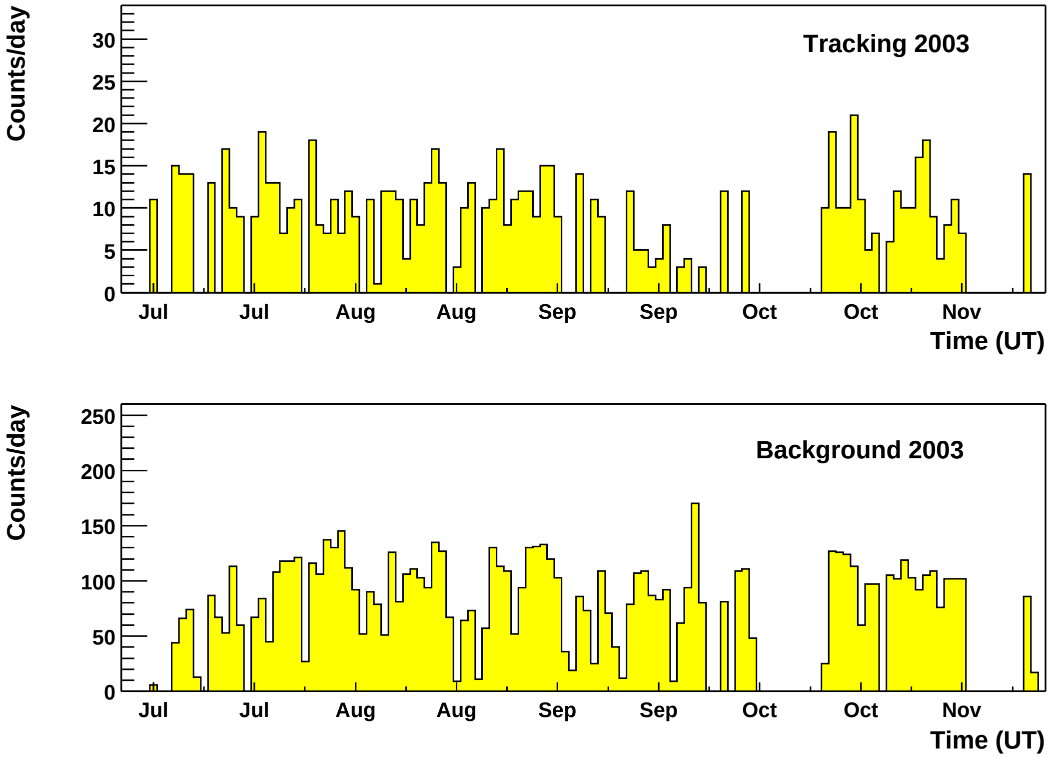

Figure 5.3: Time variation of tracking (top) and background (bottom) as a function of the exposure time for the whole data taking periods in 2003. The binning of the time is one day.

5.2.3 Line and column distributions

The background can be characterized by using the data taken in a region of the CCD with distributions of 200 lines and 64 columns. In the line distribution of the background data of Fig. 5.4, it is observed that slightly more charge is collected at the bottom of the CCD. Fig. 5.4 shows also that the count rate is lower for the upper lines and columns in case of background data, but this effect is not so obvious for tracking data. To check the significance of this effect a linear fit was done. The result of the fit shows, that this effect is not statistically significant, so it might be just a matter of statistics. Both distributions of tracking and background spectra are consistent with each other.

5.2.4 Operating condition

One of the background characterizations is to check the background dependence on the experimental conditions. Basically, the background data is defined by the data taken under the same experimental conditions as the solar tracking data. The data was collected when the

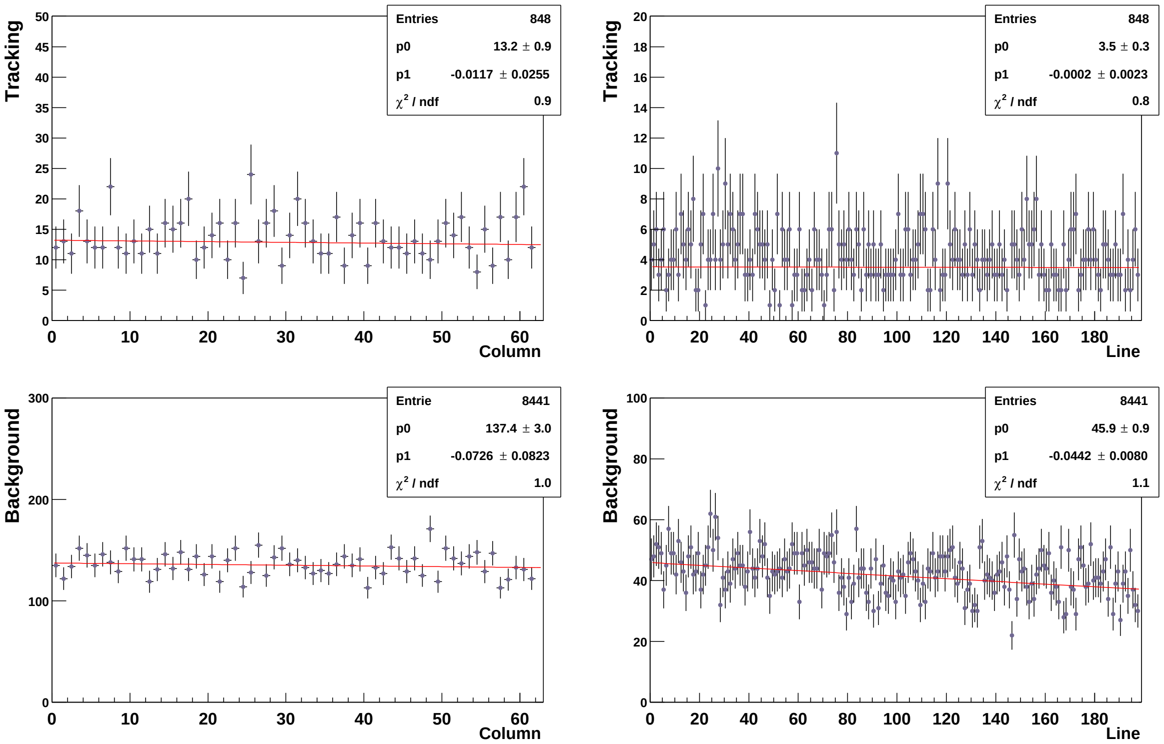

Figure 5.4: Distribution of events as a function of lines and columns on the CCD with a linear fit for both tracking (upper) and background (lower) data. Error bars are the square root of the bin contents.

magnetic field $\vec{B}$ inside the magnet should be on and the valve VT4 between the magnet and the X-ray telescope should be opened. Here the background was studied with four combinations of two important operating parameters. Fig. 5.5 shows the normalized background to the exposure time for the following four cases:

- $\vec{B}$ **on and VT4 open**
  The upper left plot in Fig. 5.5 is the case of the magnetic field on and the valve open. This is the standard condition for the background in order to determine the coupling constant of axion to photon.

- $\vec{B}$ **on and VT4 close**
  The upper right plot is the background when the magnetic field was on but the valve was closed. Due to the small statistics the data have large error bars. However, the shape of the background distribution seems to be compatible with the standard case.

- $\vec{B}$ **off and VT4 open**
  The background when there was no magnetic field in the magnet bore and the valve

was opened, is shown in the lower left plot. In particular, an unusual peak around 6 keV was observed, but the origin of the peak is not understood so far.

- **$\vec{B}$ off and VT4 close**
  The lower right plot is the background when the magnetic field was off as well as the valve was closed. In this case the background shape agrees quite well with (a).

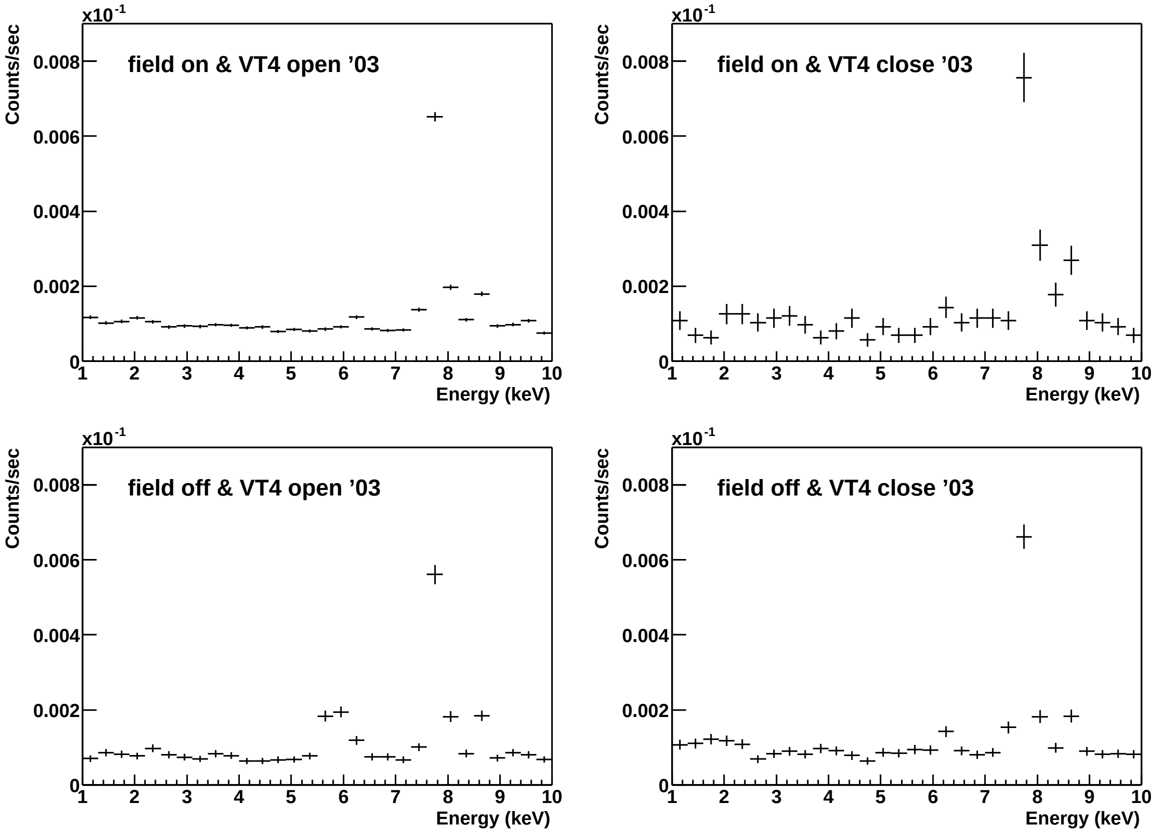

Figure 5.5: Background dependence on the experimental conditions: (a) magnetic field on and VT4 opened, (b) magnetic field on and VT4 closed, (c) magnetic field off and VT4 opened, and (d) magnetic field off and VT4 closed.

The mean count rates of the background for all cases are summarized in Table 5.3. They are consistent with each other within the 1 σ error bar and prove that there is no significant influence of the different experimental conditions on the background.

	$\vec{B}$ on	$\vec{B}$ off
VT4 open	$(1.008 \pm 0.009) \times 10^{-4}$ cts/s	$(0.858 \pm 0.018) \times 10^{-4}$ cts/s
VT4 close	$(1.001 \pm 0.044) \times 10^{-4}$ cts/s	$(0.973 \pm 0.022) \times 10^{-4}$ cts/s

Table 5.3: Summary of the mean background rate for four different operating conditions.

5.2.5 Angular dependence

An important systematic study of the background is to check the dependence of the background on the magnet position. Most of the solar tracking data are collected in a certain area of the experimental hall, while the background data are taken in all locations. Thus it is possible that there might be an angular dependence. In fact a significant dependence of the TPC background on the magnet position has been observed. In order to check the position dependence, the background was divided by a binning of 2 degrees vertically and 10 degrees azimuthally. Fig. 5.6 shows the background rate and the exposure time in each position of the magnet. In the top left and right plots in Fig. 5.6 several significant regions with higher count rates compared to other regions are just because of the longer exposure time. The bottom plots show, however, that the count rates of the background are randomly distributed around an average value for all angles. Thus, the background is proven to be independent of the position of the magnet and compatible with statistical fluctuations.

From the above background studies no significant dependence of the background data on the different magnet position or experimental conditions was found. Therefore, all background data which were taken at the same condition as solar tracking data was used in order to extract a signal.

5.3 Determination of the upper limit on $g_{a\gamma}$

5.3.1 Background selection methods

In order to extract the coupling constant of the axion to photon from the observed data, the analysis is classified in two categories, namely the analysis of the full CCD area and the restricted area. The analysis of the limited area is based on two different kinds of methods, which depend on the background definition. Actually, there are several possibilities to define regions on the CCD that are considered as background, if the background is equally distributed over the all CCD area. If this is not the case, the background has to be chosen more carefully.

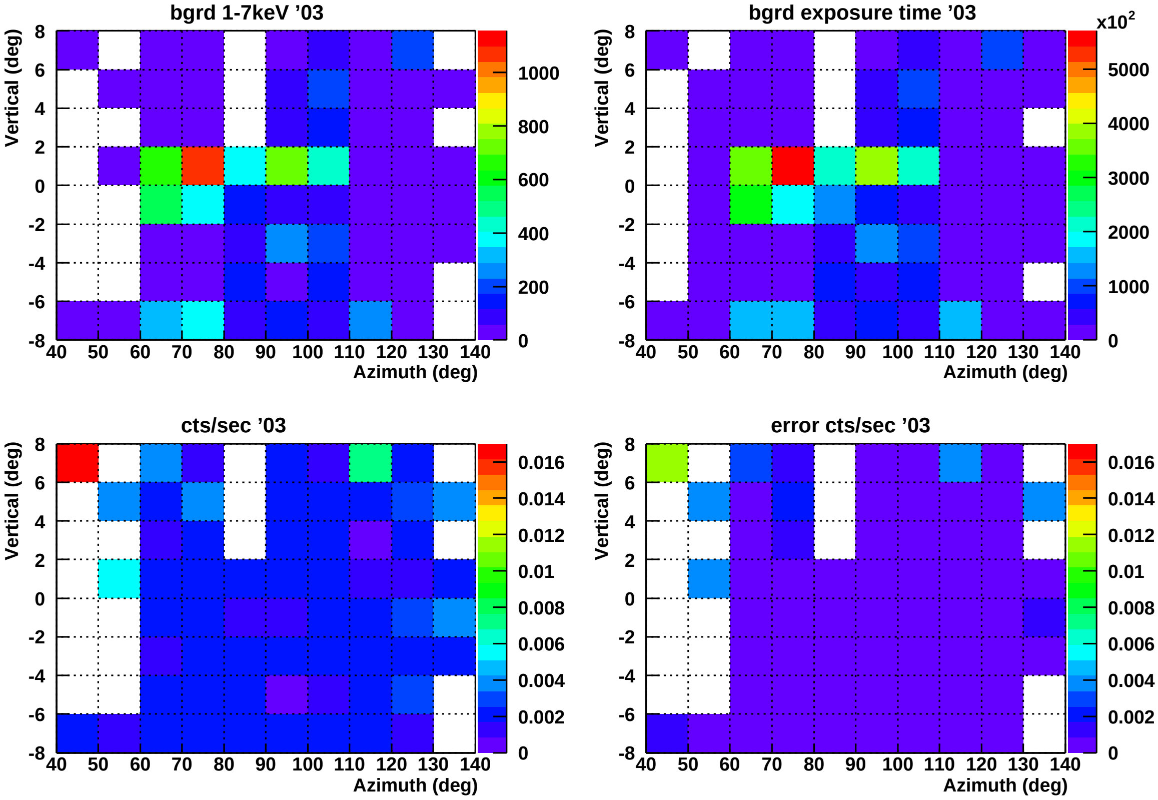

Figure 5.6: Angular dependence of the background: the counts of the background collected within the energy between 1 and 7 keV (top left), the exposure time (top right), the normalized background rate to the exposure time (bottom left), and its corresponding statistical errors (bottom right). The range of solar tracking is roughly from 40° to 100° for the CCD detector.

During the data taking period of 2003 a continuous monitoring of the pointing stability of the X-ray telescope was not possible, so that the analysis had to allow for a larger signal area than the size of the spot. Since it is not known where exactly the spot is located inside the CCD area and whether the spot position was stable over the data collection periods, the analysis is restricted to a small area on the CCD where the axion signal is expected after the focusing of the X-ray telescope. Taking into account all uncertainties of the telescope alignment, the size of the area containing the signal was conservatively estimated to be 34×71 pixels (54.32 mm^2) with the following pixel coordinates: $30 \leq$ column ≤ 63 and $70 \leq$ line ≤ 140, as shown in the top plots of Fig. 5.7.

Method I

Both tracking and background data were used for method I. The signal is taken from the potential signal area of the tracking data and the background is defined by the data taken from the same area during the non tracking periods. The selected area can be seen in the top plots of Fig. 5.7. The total number of events in the signal area is then 155 counts from the tracking data, while the background is 1524 counts from the background data. The total exposure time for tracking and background are 121.3 and 1233.5 hours, respectively. The bottom plot of Fig. 5.7 shows its corresponding energy spectrum for both signal and background.

Method II

Alternatively, the background in the signal area was also determined by determining the background measured during the tracking periods in those parts of the CCD not containing the sun spot. Therefore, only the solar tracking data was taken into account for method II. As shown in the upper right plot of Fig. 5.8, events in the area excluding the potential signal area were defined as background. The background area is thus 233.69 mm^2 and the area ratio of the background to the signal is 4.3. In total 155 tracking counts (same as the first method) and 693 background counts in the non signal area during same exposure time have been measured.

Shape of the background spectrum

In a first step, straight line fits were applied to check whether the background spectra for different selected areas are consistent with a flat distribution. This was done for three different cases of the background: the full CCD area from the background data, the potential signal area (54.32 mm^2) from the background data for method I, and the background from the non signal area (233.69 mm^2) from the tracking data for method II. Linear fits to the background energy spectra are shown in Fig. 5.9. As a fit result the shape of all three background selections agrees with each other.

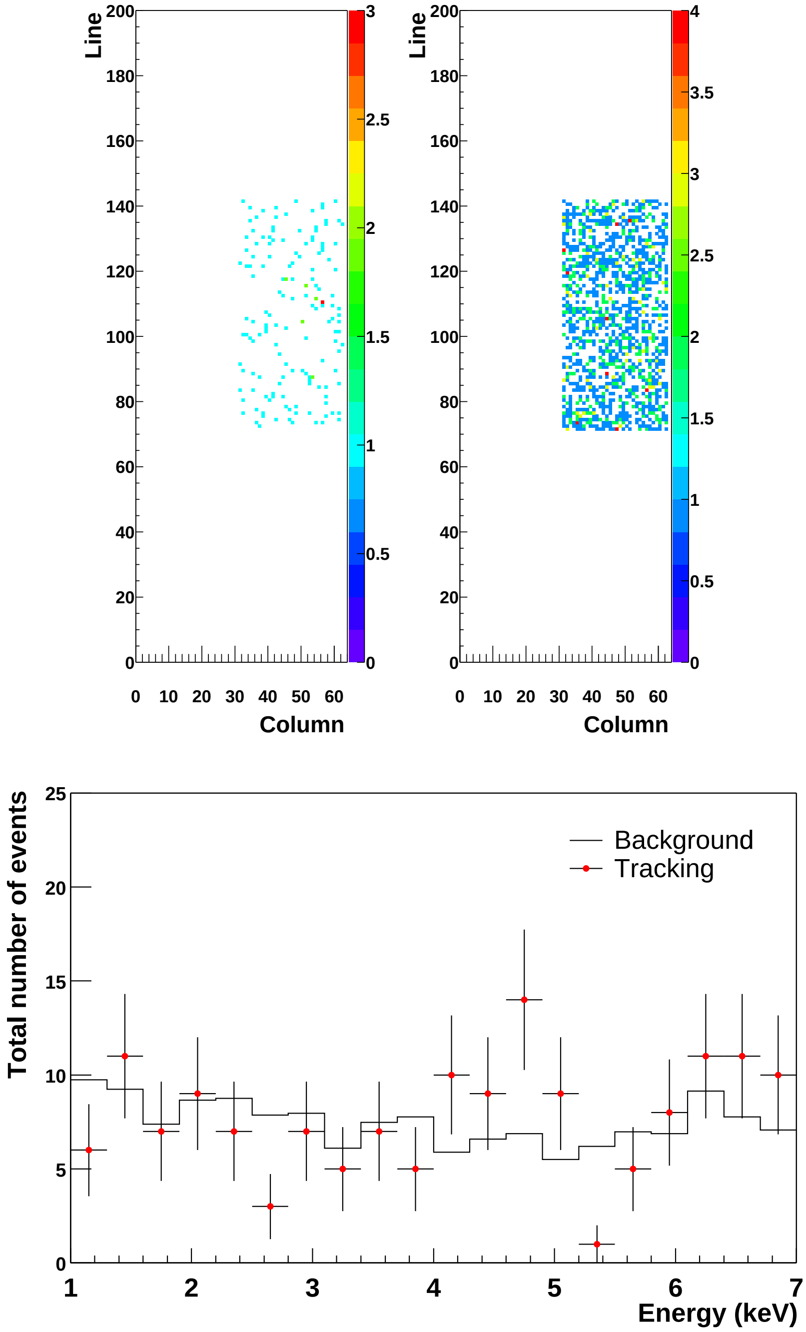

Figure 5.7: Top: CCD images of the signal from the tracking data (left) and of the background (right) from the background data for method I. The z axis is in units of counts. Bottom: Energy spectrum of the tracking data (dots with error bars) and the background (solid line) normalized by the time ratio between tracking and background.

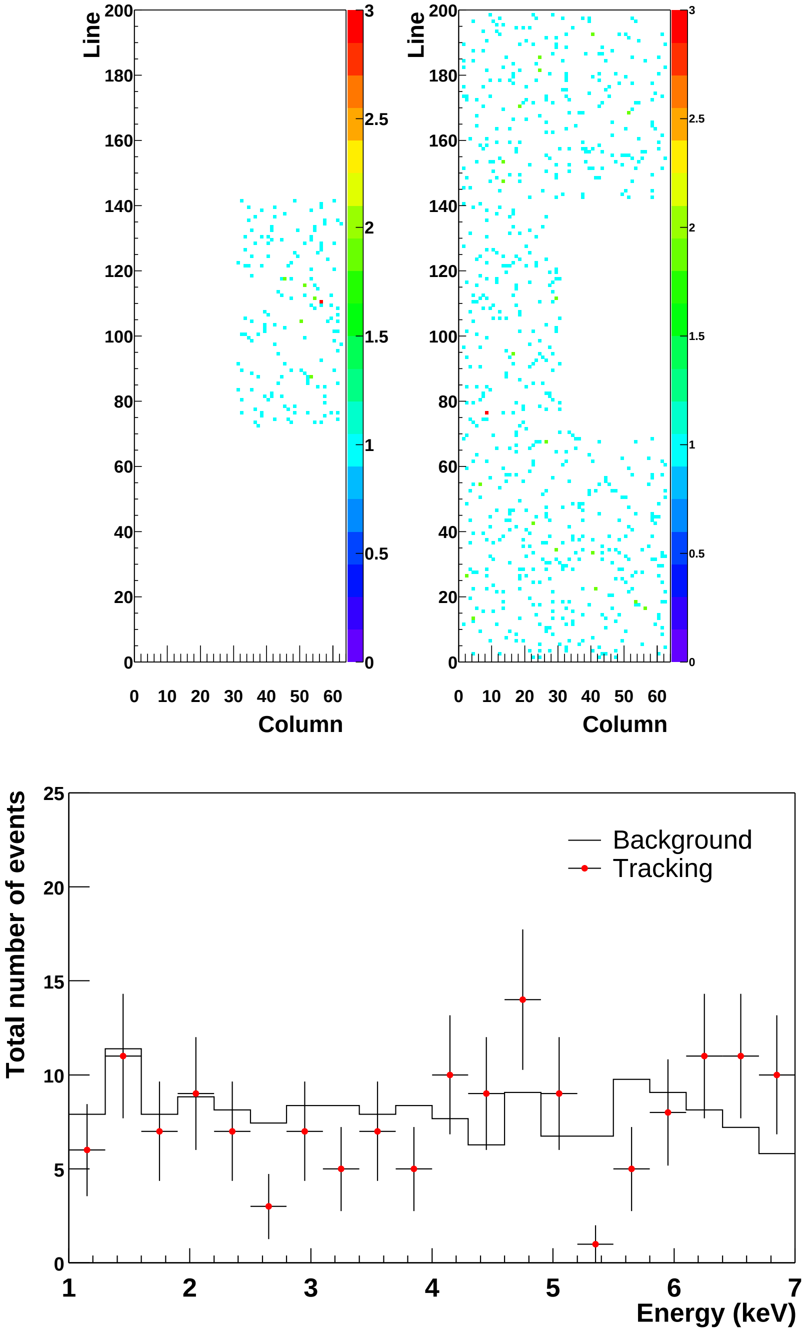

Figure 5.8: Top: CCD images of the signal (left) and of the background (right) from the tracking data for method II. The z axis is in units of counts. Bottom: Energy spectrum of the tracking (dots with error bars) data over the background (solid line) normalized by the area ratio between tracking and background.

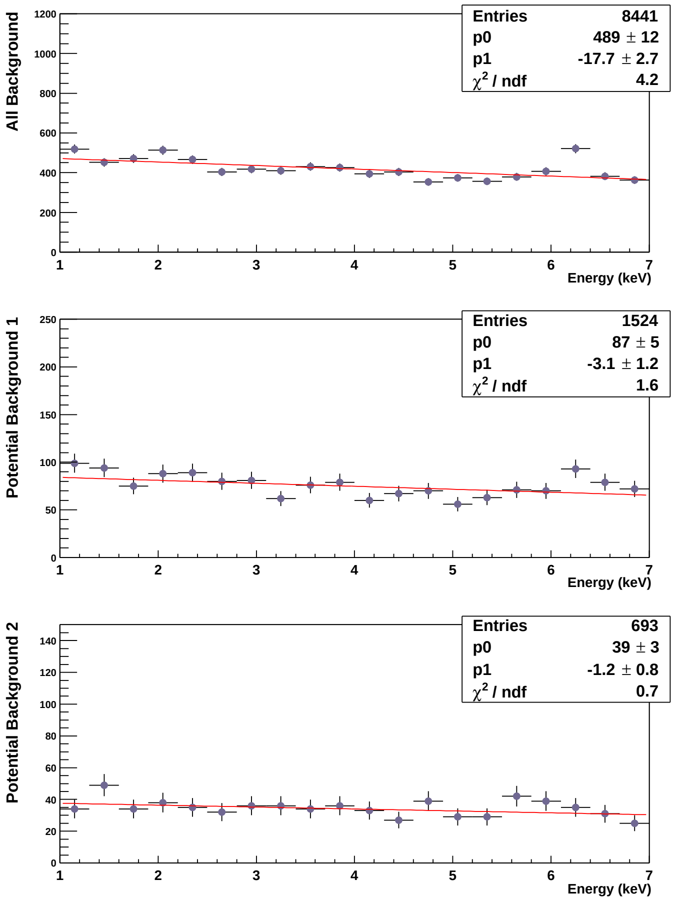

Figure 5.9: Background spectra with a linear fit: all background data taking the full CCD chip into account (top), background data from the potential signal area (center), and background from the non signal area from tracking data (bottom).

5.3.2 The χ^2 minimization

As the background turned out to be flat, the normalized background can be directly subtracted from the tracking data normalized by the area of the magnet bore, the exposure time, and the energy. With the subtracted data the coupling constant of the axion to the photon $g_{a\gamma}$ was determined by minimizing with the χ^2 method. The estimation of the upper limit on $g_{a\gamma}$ consists of three parts: (1) a null hypothesis test, (2) a best fit, and (3) an extraction of the upper limit on $g_{a\gamma}$.

In practice, if no signals are observed, the subtracted spectrum should be compatible with zero within statistical fluctuations. Hence a null hypothesis test was firstly performed with the subtracted data. From the null hypothesis test it turned out that no positive signal over the background was detected. Then a χ^2 fit is performed on the subtracted data. After that an upper limit of the coupling constant was derived by the extraction of the confidence interval.

χ^2 method

The χ^2 distribution function is defined as

$$\chi^2 = \sum_{i=1}^{20} \frac{(\mathrm{S}_i - f(\mathrm{E}_i))^2}{\sigma_i^2} \tag{5.1}$$

with

$$f(\mathrm{E}_i) = \frac{\mathrm{d}\Phi_a}{\mathrm{dE}} \times \mathrm{P}_{a\to\gamma} \times \varepsilon(\mathrm{E}_i), \tag{5.2}$$

where i = 1,...,20 is the number of spectral bins, S_i are the experimentally observed data points, i.e. the background subtracted data from the tracking data, and σ_i are their statistical errors. The fit function $f(\mathrm{E}_i)$ corresponds to the theoretically expected spectrum of axion induced photons. The expected spectrum has been calculated and multiplied by the axion flux on earth, the conversion probability of the axion to the photon inside the magnet, and the complete efficiency of the CCD detector and the X-ray telescope $\varepsilon(\mathrm{E}_i)$ at each energy bin. The quantum efficiency of the CCD is over 95% in the sensitive range of the axion energies between 1 keV and 7 keV which is used for fitting. The total efficiency of the X-ray telescope is 36% in the same energy range as shown in Section 4.

Axion fit function

Based on Eq. (3.7) the differential flux of the solar axion on earth [63] is given by

$$\frac{\mathrm{d}\Phi_a}{\mathrm{dE}} = 4.02 \times 10^{10}\mathrm{cm}^{-2}\mathrm{s}^{-1}\mathrm{keV}^{-1} \times \left(\frac{\mathrm{g}_{a\gamma}}{10^{-10}\mathrm{GeV}^{-1}}\right)^2 \times \frac{(\mathrm{E}/1\mathrm{keV})^3}{e^{\mathrm{E}/1.08\mathrm{keV}} - 1} \tag{5.3}$$

with $\mathrm{g}_{a\gamma}$ the axion to photon coupling constant. The conversion probability of axion to photon in the magnetic field can be calculated by Eq. (3.19) and is given by

$$\mathrm{P}_{a\to\gamma} = 1.736 \times 10^{-17} \times \left(\left[\frac{\mathrm{B}}{9.0\mathrm{T}}\right]^2 \cdot \left[\frac{\mathrm{L}}{9.26\mathrm{m}}\right]^2 \cdot \left[\frac{10^{-10}\mathrm{GeV}^{-1}}{\mathrm{g}_{a\gamma}}\right]^2\right) \tag{5.4}$$

for a magnetic field strength B = 9.0 Tesla and an effective length of the magnetic field L = 9.26 m. The differential axion flux is proportional to $\mathrm{g}_{a\gamma}^2$ and the conversion probability is also proportional to $\mathrm{g}_{a\gamma}^2$, i.e. the fit function is proportional to the $\mathrm{g}_{a\gamma}^4$. Therefore the $\mathrm{g}_{a\gamma}^4$ was taken as a fit parameter instead of $\mathrm{g}_{a\gamma}$. For the subtracted data, the fitting is performed by standard χ^2 minimization.

Confidence level and upper limit

After it turns out that the data are compatible with the absence of any signals from the null hypothesis, the extraction of an upper limit on $g_{a\gamma}$ is performed. In general, when a parameter is experimentally determined, the result is usually expressed by quoting some sort of confidence interval or upper limit for its value which reflects the statistical precision of the measurement. In the simplest case, this can be given by the estimated value of the parameter plus or minus an estimate of the standard deviation of the parameter. However, if there are physical boundaries on the possible values of the parameter or if the probability distribution function of the estimator is not Gaussian, then the Bayesian approach can usually be used. The more sensible method would seem to be set a 95% confidence level upper limit on $g^4_{a\gamma}$ at a value such that

$$A_{95\%}/A_{\text{total}} = 0.95, \tag{5.5}$$

where $A_{95\%}$ is the area of the probability distribution up to 95% confidence estimate within the physical region for $g^4_{a\gamma}$ and A_{total} is the corresponding area within the whole physical region. Such a procedure would also be relevant even for $(g^4_{a\gamma})_{\text{min}}$ being zero or slightly positive [104]. To find the upper limit on $g_{a\gamma}$ for 95% confidence level, an integration method of a Bayesian probability was used. The Bayesian probability is given by

$$P = \int_0^{95\%} e^{-\chi^2/2} dg^4_{a\gamma}. \tag{5.6}$$

The exponential term represents the Likelihood distribution with respect to the variable $g^4_{a\gamma}$ where the χ^2 distribution is a function of $g^4_{a\gamma}$. Applying the χ^2 distribution to Eq. (5.6) the Bayesian probability can be obtained for the data. The minimum value of the χ^2 can be located in the negative region, which is the unphysical region, so that only the physically allowed part (i.e. positive signals) were taken into account. Eventually the upper limit of $g^4_{a\gamma}$ for 95% confidence level was calculated at the value given by Eq. (5.5) for $g^4_{a\gamma} \geq 0$. Generally, a confidence level describes the uncertainty in an estimated result and there is a lot of choice about the confidence level. In practice 90 and 95% (or 2σ) limits are commonly used and thus the upper limit of $g_{a\gamma}$ will here be estimated as a 95% confidence level.

5.3.3 Results from the χ^2 analysis

Full CCD area

At first, all data from the full CCD area, which is 2.88 cm^2, was analyzed. The normalized background was directly subtracted from the tracking data bin by bin. The residual rate over the full CCD data is $(1.48 \pm 7.95) \times 10^{-7}$ cm^{-2} s^{-1} keV^{-1} in the energy range of

1 - 7 keV. All errors are only statistic errors and the systematic errors were not taken into account for the fit. From the χ^2 fitting an upper limit on the coupling constant of axions to photons we obtain by $g_{a\gamma} < 1.46 \times 10^{-10}$ GeV^{-1} at χ^2 / ndf = 23.3 / 19 with 95% confidence level, respectively. Fig. 5.10 shows the energy spectrum of the full CCD analysis after the background is subtracted from the solar tracking data where the red line is the theoretical axion curve with $g_{a\gamma}$ at 95% CL.

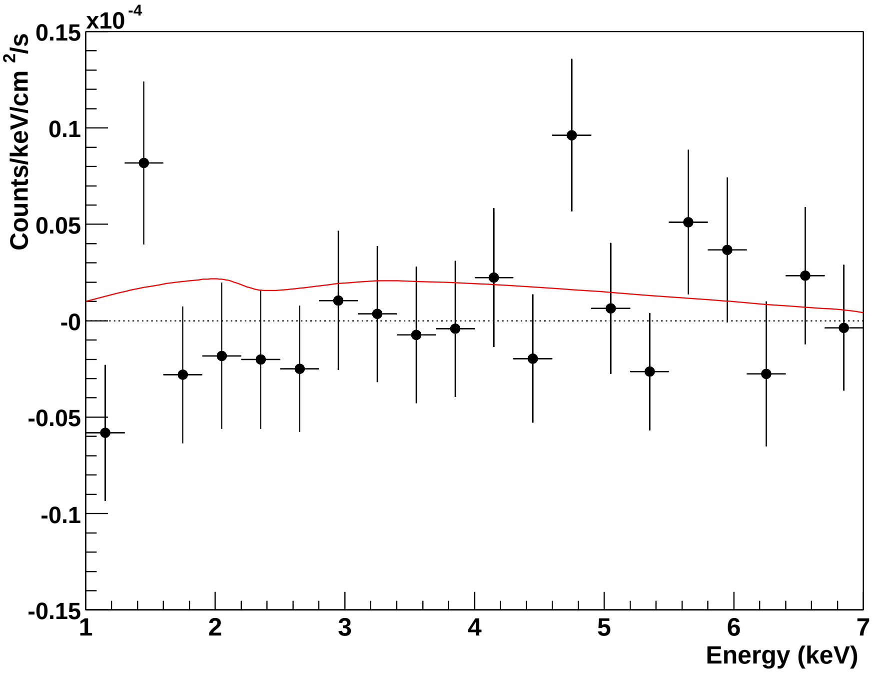

Figure 5.10: The background subtracted spectrum from the tracking data. The red curve is the theoretically expected axion curve with $g_{a\gamma}$ at 95% CL from the full CCD analysis.

Method I

The tracking and background data only from the potential area (54.32 mm^2) were used for method I. The ratio of the full CCD area to the potential area is 5.3 and it will give a better upper limit on the coupling constant by factor of the 4th root of 5.3, i.e. 1.5. The same analysis procedure was applied to determine the upper limit of the axion coupling. The mean rate of the subtraction data is (-7.07 ± 3.04) × 10^{-7} cm^{-2} s^{-1} keV^{-1} in Fig. 5.11. The upper limit from method I analysis is $g_{a\gamma} < 0.96 \times 10^{-10}$ GeV^{-1} at χ^2 / ndf = 42.5 / 19 with 95% confidence level.

Method II

In method II only the solar tracking data was considered. The tracking data surrounding the signal area was regarded as the background. The background area is 233.69 mm^2, so the ratio of the background and signal area is 4.3. After the background subtraction from tracking the mean rate is (-8.12 ± 3.36) × 10^{-7} cm^{-2} s^{-1} keV^{-1} in Fig. 5.12. The result from methode II analysis is $g_{a\gamma} < 0.96 \times 10^{-10}$ GeV^{-1} at χ^2 / ndf = 36.5 / 19 with 95% confidence level.

Conclusion of the χ^2 analysis

From the χ^2 methods the excluded values of the coupling constant $g_{a\gamma}$ for a 95% confidence level are summarized in Table 5.4. Both results of method I and method II for the upper limit of the axion coupling agree with each other and improve the result obtained by considering the full CCD area by exactly the expected factor of $5.3^{1/4}$. However, the χ^2 value is large due to a few low statistics bins as we can see in the subtracted plot in Figs. 5.11 and 5.12. Actually, the χ^2 method can be applied to the directly measured data points having more than approximately 5 counts per bin before normalization. Therefore, a maximum Likelihood fit is performed.

	$g_{a\gamma}$ (95%C.L.) (10^{-10}GeV^{-1})	χ^2 / ndf
full CCD	1.458	23.3/19
method I	0.956	42.5/19
method II	0.963	36.5/19

Table 5.4: Results of three different methods from the χ^2 minimization.

5.3.4 Maximum Log Likelihood Fit

The χ^2 method is not applicable to fit very low numbers of events from the small area on the CCD plane where the signal is expected by focusing effect of the telescope. Therefore, the low counting statistics of the restricted area in the CCD requires the use of a Likelihood function in the minimization procedure, rather than a χ^2 analysis [105].

Likelihood method

The maximum Likelihood function based on a Poissonian distribution is defined as

$$L = \prod_i^{20} e^{-\mu_i} \frac{\mu_i^{n_i}}{n_i} / \prod_i^{20} e^{-n_i} \frac{n_i^{n_i}}{n_i} \tag{5.7}$$

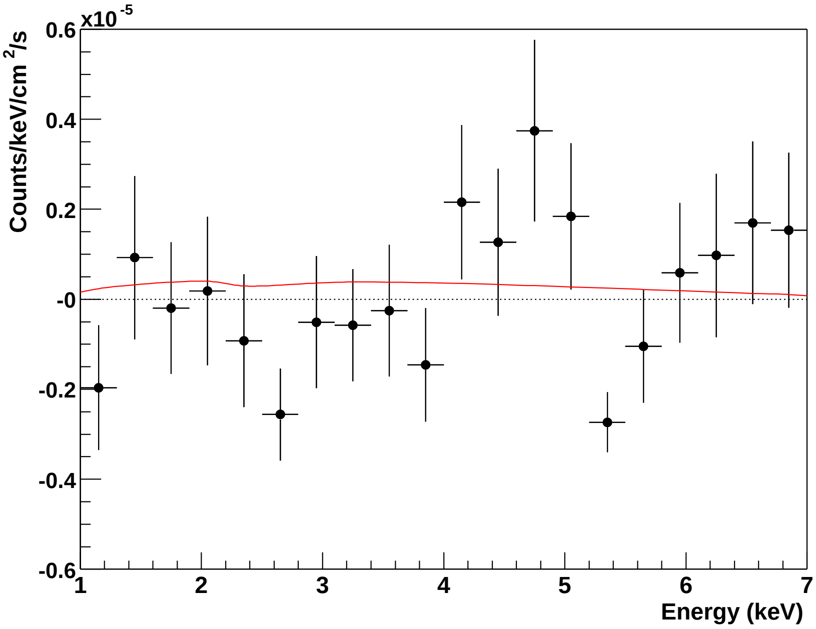

Figure 5.11: The background subtracted spectrum from the tracking data for method I together with the theoretically expected axion curve with $g_{a\gamma}$ at 95% CL.

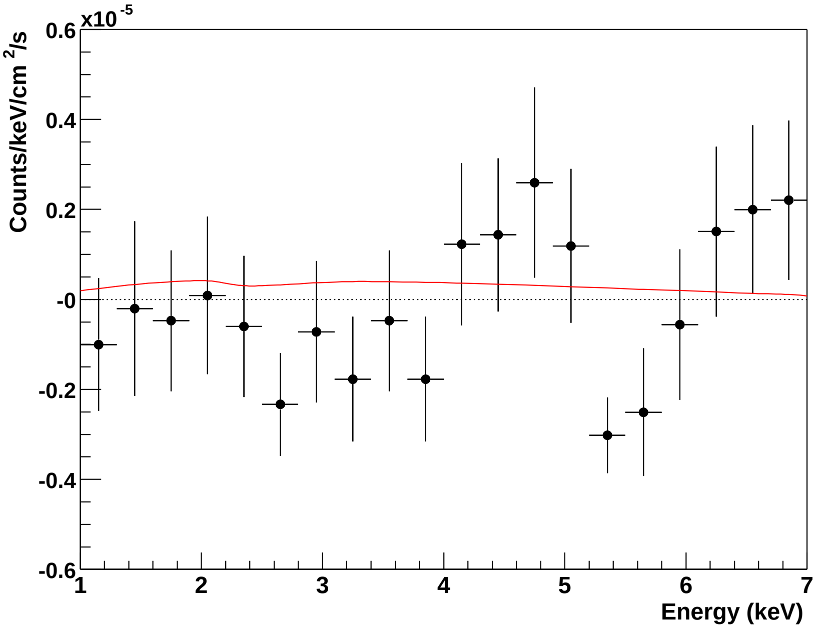

Figure 5.12: The background subtracted spectrum from the tracking data for method II with the theoretically expected axion curve at 95% CL.

with the fit function

$$\mu_i = b_i/\alpha + a(\mathrm{E}_i), \tag{5.8}$$

where n_i is the tracking data over 20 bins which have a 0.3 keV bin size between 1 and 7 keV energy range, μ_i is the fit function, b_i is the measured background data, α is the ratio of background over tracking time 10.2 for method I, and the ratio of background over tracking area for method II. The theoretically expected axion spectrum $a(\mathrm{E}_i)$, which is proportional to $\mathrm{g}^4_{a\gamma}$, is given by

$$a(\mathrm{E}_i) = \frac{\mathrm{d}\Phi_a}{\mathrm{dE}} \times \mathrm{P}_{a\rightarrow\gamma} \times 436716.87\mathrm{s} \times 14.522\mathrm{cm}^2 \times 0.3\mathrm{keV} \times \varepsilon(\mathrm{E}_i), \tag{5.9}$$

where the exposure time is 436716.87 s, the magnet bore area is 14.522 cm^2, the bin size is 0.3 keV, and ε is the total efficiency of the CCD detector and X-ray telescope at each energy bin. Thus it becomes

$$a(\mathrm{E}_i) = 1.2353 \times {\mathrm{g}_{a\gamma}}^4 \times \frac{(\mathrm{E}_i/\mathrm{keV})^3}{e^{\mathrm{E}_i/1.103\mathrm{keV}} - 1} \times \varepsilon(\mathrm{E}_i). \tag{5.10}$$

The differential flux of the solar axion on earth is

$$\frac{\mathrm{d}\Phi_a}{\mathrm{dE}} = 3.821 \times 10^{10}\mathrm{cm}^{-2}\mathrm{s}^{-1}\mathrm{keV}^{-1} \times \left(\frac{\mathrm{g}_{a\gamma}}{10^{-10}\mathrm{GeV}^{-1}}\right)^2 \times \frac{(\mathrm{E}/1\mathrm{keV})^3}{e^{\mathrm{E}/1.103\mathrm{keV}} - 1}. \tag{5.11}$$

This axion flux is calculated newly by considering a new solar model [66]. The conversion probability is

$$\mathrm{P}_{a\rightarrow\gamma} = 1.7018 \times 10^{-17} \times \left(\left[\frac{\mathrm{B}}{9.0\mathrm{T}}\right]^2 \cdot \left[\frac{\mathrm{L}}{9.26\mathrm{m}}\right]^2 \cdot \left[\frac{10^{-10}\mathrm{GeV}^{-1}}{\mathrm{g}_{a\gamma}}\right]^2\right), \tag{5.12}$$

using the conversion factor of B/T = 0.990 GeV/m from the natural to the SI unit [106].

In order to estimate the upper limit of the coupling constant the same procedure as in the χ^2 analysis was used. The fit function is proportional to the $\mathrm{g}^4_{a\gamma}$, so that $\mathrm{g}^4_{a\gamma}$ was taken as a fit parameter instead of $\mathrm{g}_{a\gamma}$. After the Likelihood fit the upper limit on $\mathrm{g}_{a\gamma\gamma}$ for a 95% confidence level was determined by integrating the Bayesian probability, namely that a χ^2 distributed magnitude can be defined from the Likelihood:

$$-2\ln L \equiv \chi^2, \tag{5.13}$$

where only the physically allowed region of $\mathrm{g}^4_{a\gamma}$ was taken into account.

Method I

In method I the restricted area, which is the potential signal area (54.32 mm^2) shown in Fig. 5.7, is used both for tracking and background data. The null hypothesis yielded

$$\chi^2_{\mathrm{null}}/\mathrm{ndf} = 28.6/20.$$

It can be seen clearly that the data is compatible with the absence of a signal. From the Likelihood fitting the best fit value of $g^4_{a\gamma}$ with its 1 σ error is

$$(0.352 \pm 0.990) \times 10^{-40}\mathrm{GeV}^{-4}.$$

As shown in Fig. 5.13 the 1 σ statistical error was determined from the condition that χ^2 as a function of a $g^4_{a\gamma}$ increases from χ^2_{min} to χ^2_{min} + 1 [107]:

$$\chi^2_{1\sigma} = \chi^2_{\mathrm{min}} + 1.$$

In the top plot of Fig. 5.13 the χ^2 distribution seems to be almost parabolic and the minimum gives the best fit value of $g^4_{a\gamma}$. The width of the parabola determines the statistical error assuming to be symmetric. Thus upper limit on the axion-photon coupling constant is

$$g_{a\gamma} < 1.228 \times 10^{-10}\mathrm{GeV}^{-1}$$

with 95% confidence level and its corresponding χ^2_{min} value is

$$\chi^2_{\mathrm{min}}/\mathrm{ndf} = 28.5/19.$$

The top plot of Fig. 5.14 shows both the tracking (solid circles) and normalized background (dashed line) spectrum with an expected axion spectrum (solid line), which is the normalized background plus the 95% signal with $g_{a\gamma}$ at 95% C.L. for the analysis of method I.

Method II

In the method II only the solar tracking data were used. The data in the restricted area was regarded as the tracking data and the data surrounding the potential signal area was taken as the background (233.69 mm^2) shown in Fig. 5.8. The null hypothesis yields

$$\chi^2_{\mathrm{null}}/\mathrm{ndf} = 28.1/20.$$

The best fit value of $g^4_{a\gamma}$ from the Likelihood fit is slightly negative:

$$(-0.785 \pm 0.994) \times 10^{-40}\mathrm{GeV}^{-4}.$$

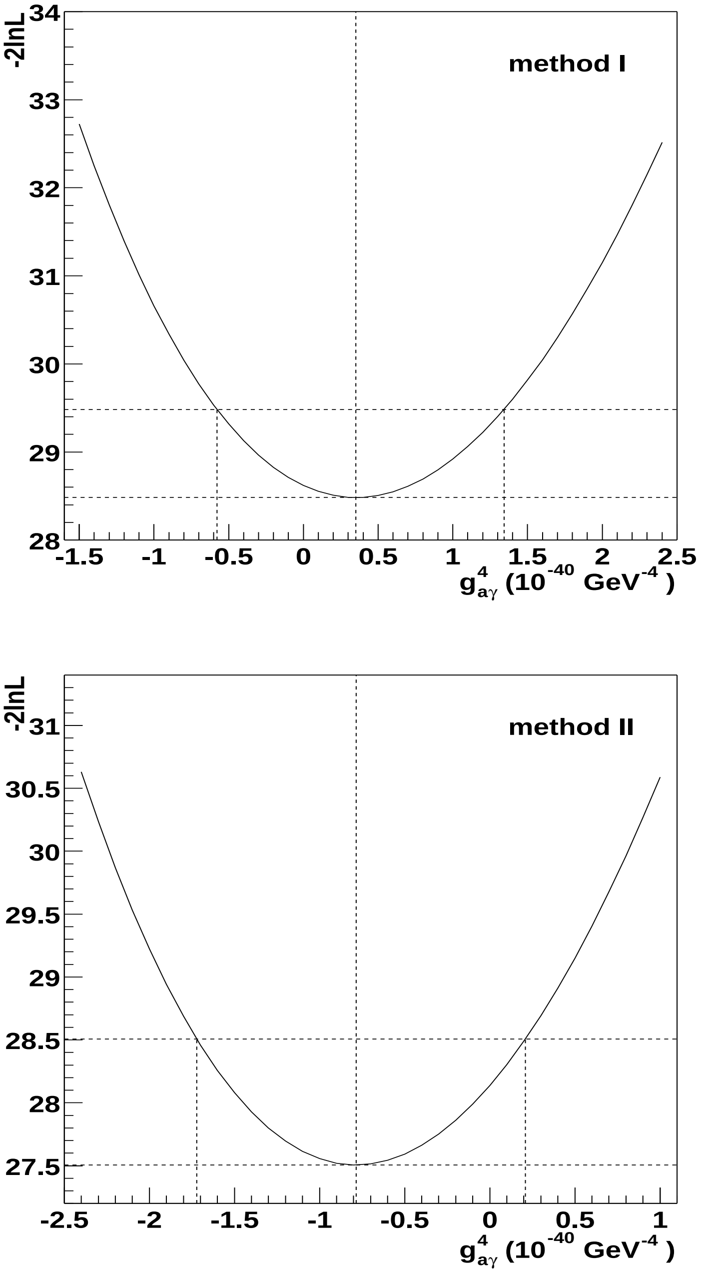

Figure 5.13: χ^2 distributions as a function of $g^4_{a\gamma}$ for method I (top) and method II (bottom). The best fit value corresponds to the minimum of $g^4_{a\gamma}$, and the width of the parabola at -2ln$L_{\min}$ + 1 gives the statistical error (upper dashed line).

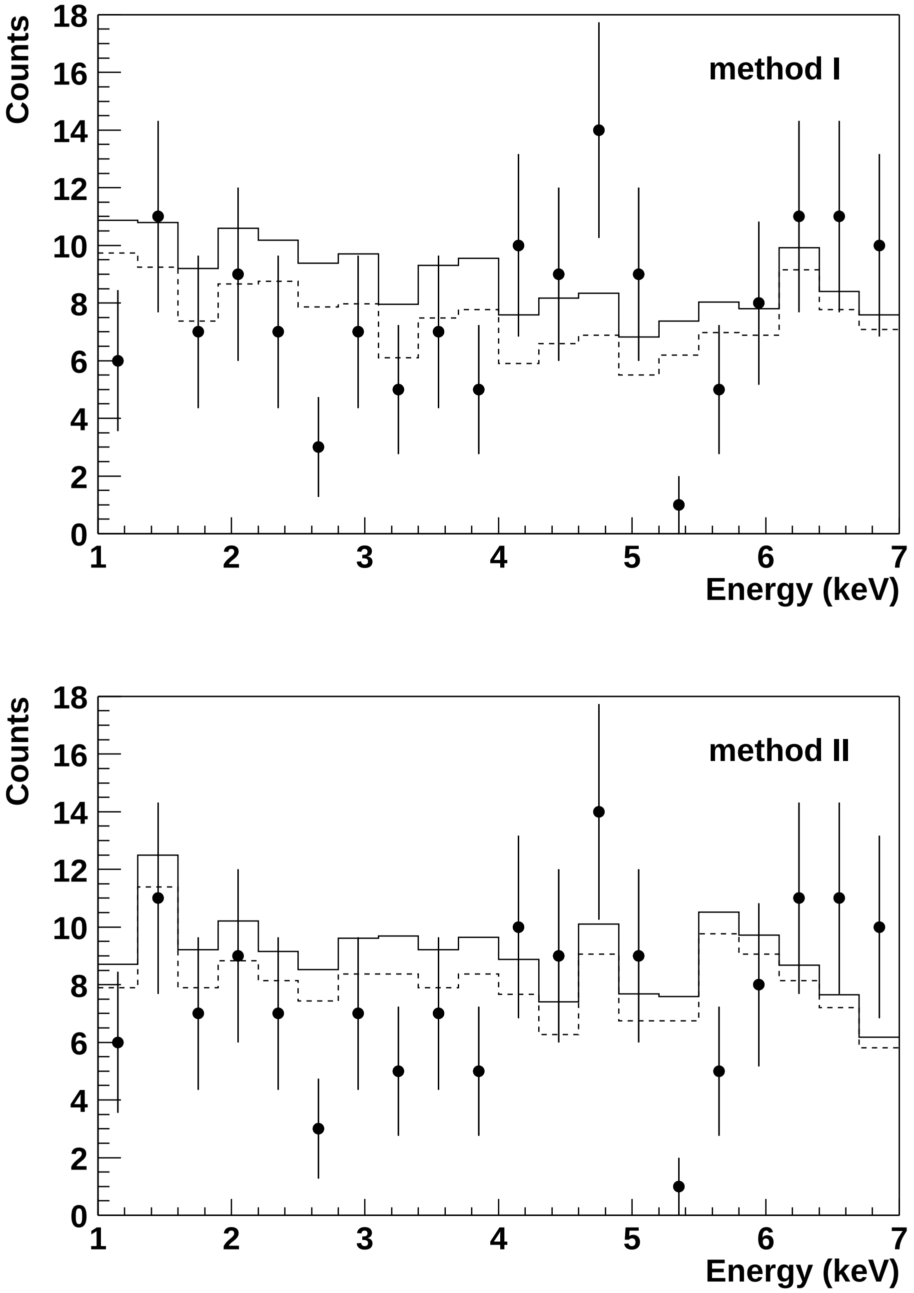

Figure 5.14: The tracking and background spectra with the expected theoretical spectrum for the analysis of method I (top) and method II (bottom). The solid circles are tracking data with statistical error bars, the dashed line is the normalized background spectrum by the time ratio of the signal area to background for method I and the area ratio for method II, respectively, and the solid line is the background plus the expected signal at 95% confidence level.

Its 1 σ error was determined from the width of parabolic χ^2 distribution as can be seen in the bottom plot of Fig. 5.13. The result of the analysis of method II is

$$g_{a\gamma} < 1.129 \times 10^{-10}\mathrm{GeV}^{-1}$$

with a 95% confidence level and the corresponding χ^2_{min} value is

$$\chi^2_{\mathrm{min}}/\mathrm{ndf} = 27.5/19.$$

The bottom plot of Fig. 5.14 represents also both the tracking (solid circles with statistical error bars) and the normalized background (dashed line) spectrum with the expected axion spectrum (solid line), which is the normalized background plus the 95% signal from the analysis of method II.

5.4 First result on $g_{a\gamma}$

Due to small statistics in the CCD a Likelihood analysis was required. Both methods of background selection led to the same final upper limit in the coupling constant $g_{a\gamma}$ with a reasonable χ^2 value. The analysis of the restricted area improves the result obtained by considering the full CCD area by the expected factor of $5.3^{1/4}$. Since the best fit value of $g^4_{a\gamma}$ from the method II analysis is negative which is physically not allowed, the result of method I was taken as the final result [58]:

$$g_{a\gamma} < 1.23 \times 10^{-10}\ \mathrm{GeV}^{-1}\ (95\%\ \mathrm{C.L.}).$$

Systematic effects Method II is a good check for systematic uncertainties and further checks have been performed in order to exclude any possible systematic effects. They were based on rebinning the data, varying the fitting window, and verifying the null hypothesis test in energy windows of the detector where no signal is expected. In general, the systematic uncertainties are estimated to have an effect of less than about 10 % on the final upper limits.

5.4.1 Combined result of CAST 2003

All three detectors, which were operated independently, obtained compatible results. In fact, the CCD result is the most restrictive of all results, because the analysis was restricted to within the small area of the X-ray telescope. The 95% C.L. limits on $g_{a\gamma}$ for each of the data sets of the three detectors were statistically combined by multiplying the Bayesian probability distributions and repeating the fit over the physically allowed region, in order to obtain the combined result for the 2003 CAST data:

$$g_{a\gamma} < 1.16 \times 10^{-10}\ \mathrm{GeV}^{-1}\ (95\%\ \mathrm{C.L.}).$$

This result is limited to the axion mass range $m_a < 0.02$ eV where the expected signal is independent of the mass, since the axion to photon oscillation length far exceeds the length of the magnet. For higher masses, the number of expected signal counts decreases rapidly and the shape of the spectral curve differs. This analysis procedure was repeated for different values of axion masses to derive the whole exclusion line for 95% C.L. as shown in Fig. 5.15.

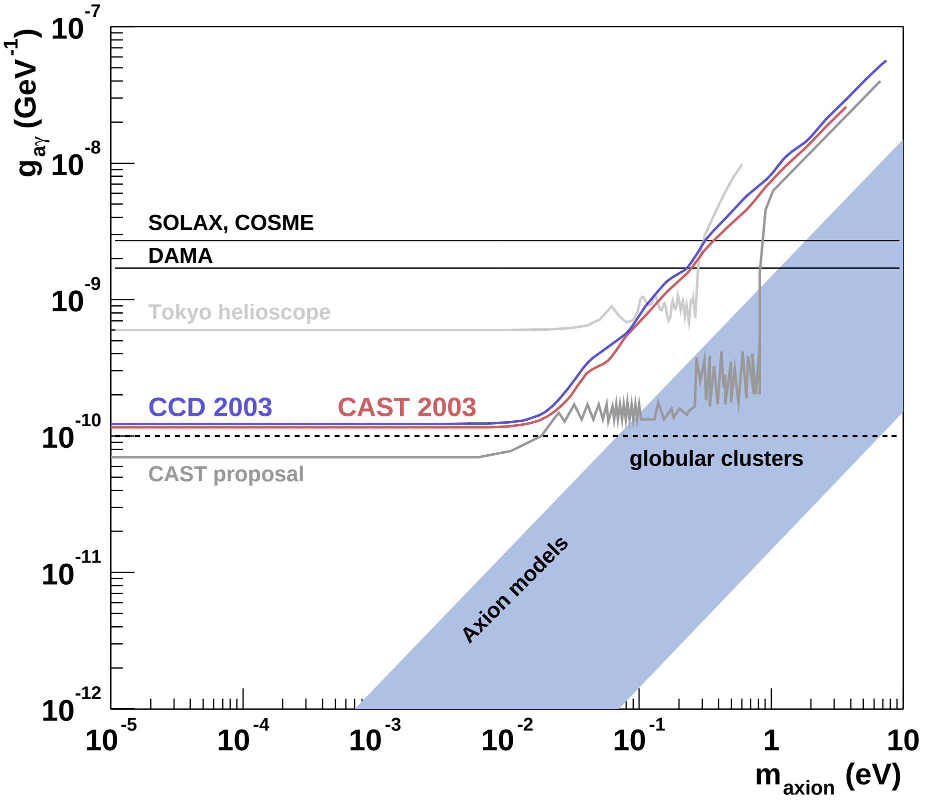

Figure 5.15: Exclusion limits at 95% C.L. from the CCD 2003 data (blue line) and from the combined result of the CAST 2003 data (red line) compared with constraints from other experiments. The shaded region represents theoretical models.

No signal above background was observed in the CCD 2003 data as well as the full CAST 2003 data. However, this exclusion limit improves the best previous constraints on $g_{a\gamma}$ by a factor 5 in the axion mass range $m_a < 0.02$ eV, where the coherence region is. Moreover it is comparable to astrophysical constraints discussed in Chapter 2. Finally, a higher sensitivity is expected from the 2004 data with the spot of the X-ray telescope on the CCD better known.

Chapter 6

Analysis of the 2004 Data

In 2004 the CCD detector was operated with an extra shield inside the detector chamber and it was working almost throughout all data collection periods. A very important point is that it was possible to monitor the location of the focus of the X-ray telescope with alignment measurements. In this Chapter the analysis of the 2004 CCD data and their results are explained. First of all the alignment measurements are reviewed in Section 6.1. The detector improvement in 2004 and the background studies are discussed in the next Section. After that an upper limit on the axion-photon coupling constant $g_{a\gamma}$ will be determined in Section 6.3. In Section 6.4 the systematic studies are discussed as well as the systematic error of $g_{a\gamma}$ is evaluated. Finally, the combined result of the 2003 and 2004 CCD data is presented in Section 6.5.

6.1 Telescope alignment

Using a parallel laser beam which is focused by the X-ray mirror system on the CCD detector, the position of the expected axion signal on the CCD can be determined. In addition an external X-ray source is used to verify the stability of the alignment of the telescope and correspondingly to monitor the solar spot on the CCD during the 2004 data collection periods.

6.1.1 Laser measurement

To define the location of the spot of the expected axion signal on the CCD a parallel laser beam was used. A theodolite[1] and an attached laser system is installed on a support fixed to the concrete wall on one corner of the experimental area. It is then leveled vertically at the same height as the center of the magnet. The laser system is installed to the theodolite, after the internal alignment of the laser to the optical axis of the theodolite has been checked. Here

---

[1] A theodolite is an instrument for measuring both horizontal and vertical angles with high precision.

the optical axis is defined by the line going through the center of the bore on each end of the magnet tube. This line is horizontal with an accuracy of ± 0.2 mm and is the theoretical axis used as a reference line during the alignment. The misalignment of the laser relative to the optical axis of the theodolite was better than 0.2 mm / 15 m. The laser beam is focused on the target of the telescope aperture and the location of the laser spot is visually estimated by aid of a cross hair on the telescope target. The laser is collimated with a prism in order to provide a parallel beam. The collimated laser beam is dimmed using polarization filters in order to reduce the intensity so that the focal spot can be observed with the CCD detector. After collimating the parallel laser beam, the laser spot is observed on the CCD and the position of the spot on the CCD is determined.

Figure 6.1 shows the intensity distribution of the laser measurement. The position of the laser spot on the CCD was calculated by fitting a Gaussian to the observed intensity distributions. The barycenter of the laser spot was determined to x = 30.8 pixels (column) and y = 109.6 pixels (line).

6.1.2 X-ray finger measurement

The monitoring of the location of the focus by the X-ray telescope as well as a check of the stability of the alignment were possible with a newly installed parallel X-ray beam through the magnet bore. Measurements with the X-ray source were performed regularly during the 2004 data taking periods. The X-ray source is mounted on a manipulator at the TPC end of the CAST magnet 12 m away from the telescope focal plane. The source illuminates the telescope aperture with an X-ray beam. Since the source is extended and the distance between the telescope and the source is finite, the image of the X-ray source on the CCD will be not in the center of the CCD chip as it was the case for the parallel laser beam. The beam is produced by a commercial miniature X-ray generator (AMPTEK COOL-X) based on a pyroelectric crystal producing a peak activity of 100 MBq when thermally cycled. A computer controlled manipulator is used to move the source into or out of the field of view of the X-ray telescope with an accuracy of the order of a few μm. During the alignment measurement the X-ray source was on the optical axis of the magnet and the X-ray telescope.

The intensity image of the X-ray measurement can be seen in Fig. 6.2. Since the source is not at an infinite distance to the mirror system, the observable X-ray image is larger than the focal spot of the X-ray beam. The emission strength depending on the angle of the X-ray beam is non-uniform and thus the observed intensity distribution in the focal spot is not uniform. The center of the X-ray spot from the X-ray measurements was calculated to x = 43.3 pixels and y = 107.3 pixels from all measurements depending on the magnet position. These measurements demonstrate that the position of the expected axion image of the sun has been stable within one pixel diameter of the CCD ($\approx$ 20 arcsec = 0.006 degrees) at

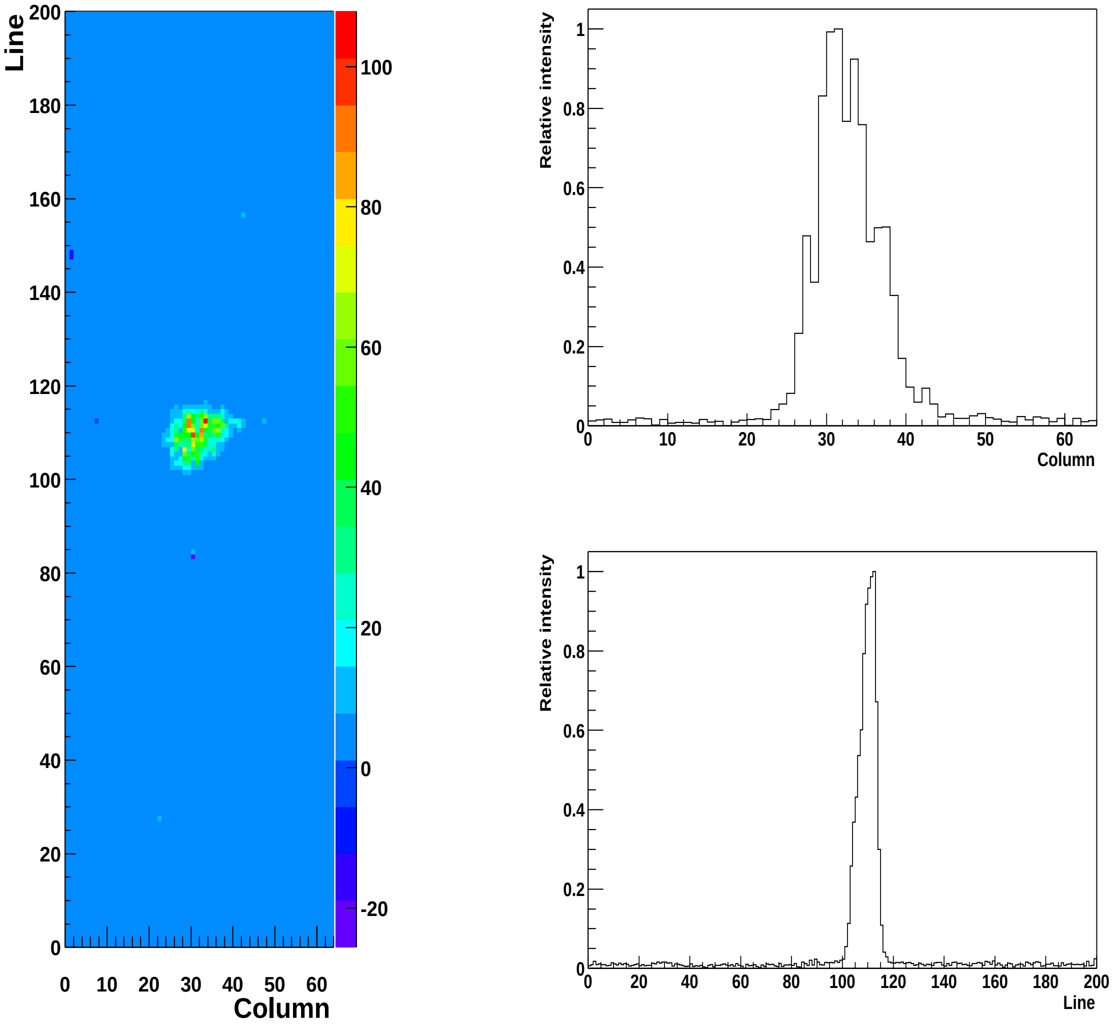

Figure 6.1: Left: One of the intensity images from the laser measurments in April 2004. Right: Corresponding projection plots onto *x* (top) and *y* (bottom) axis.

different magnet positions. Compared to the intensity image of the X-ray measurement (Fig. 6.2), the laser spot is offset to the left relative to the center of the region given by the X-ray distribution. Therefore, from both results of the laser and X-ray measurement the center of the spot is determined in the following Section.

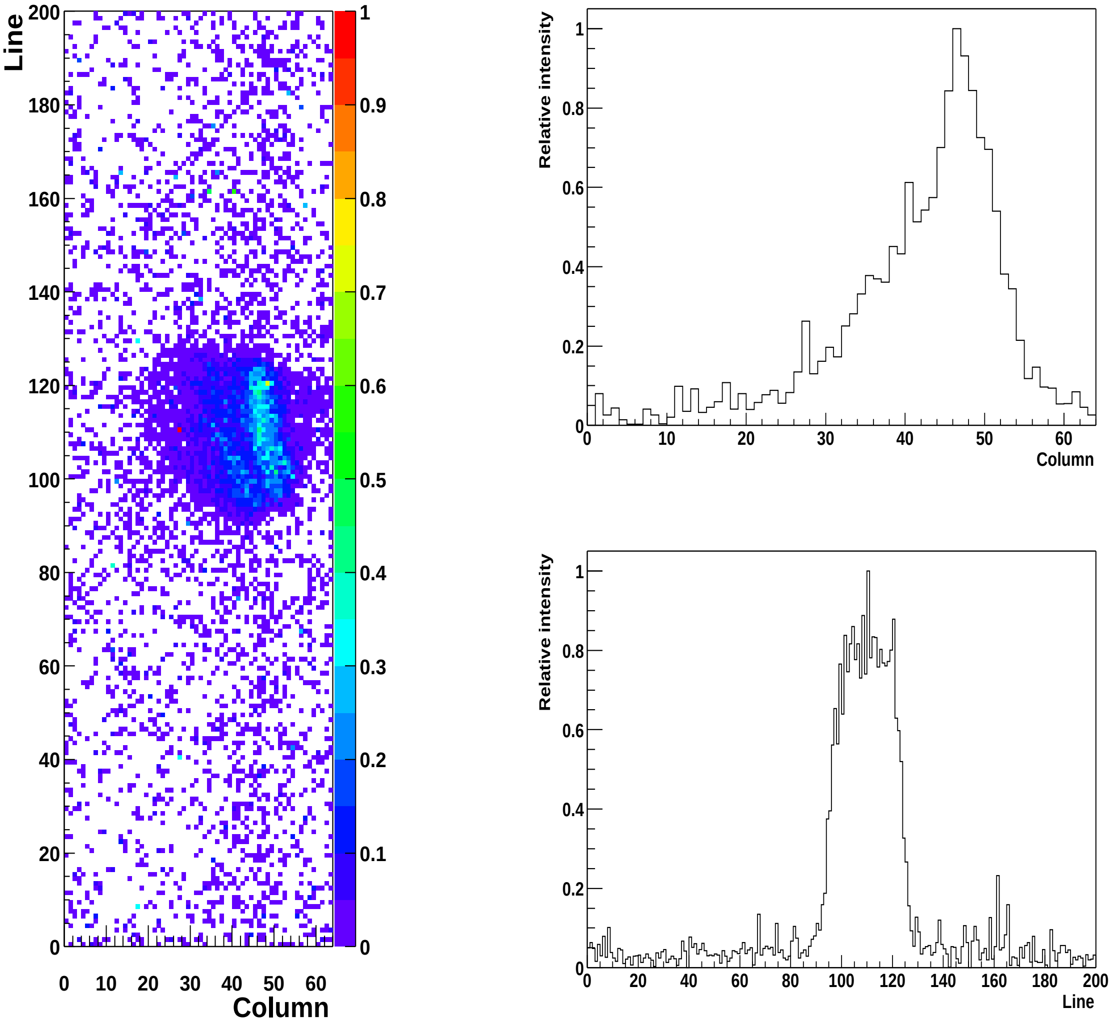

Figure 6.2: Left: One of the intensity images from the X-ray measurments. Due to the finite distance between the telescope and the extended source the X-ray image is not in the center of the CCD and also larger focal spot compared with the laser spot. Right: Corresponding projection plots onto *x* (top) and *y* (bottom) axis.

6.1.3 Determination of the spot position

Figure 6.3 shows the laser and X-ray intensity distribution by overlapping the normalized projected x and y intensity distribution of the laser and X-ray spot. If one assumes that the X-ray intensity distribution is limited to a circular region (Fig. 6.2), then the center of this circle should coincide with the center of the laser spot. To determine the coordinates of the center of the circle, the projected distribution into x and y direction was used. The diameter of the circle was defined as the position on the CCD where the intensity dropps to 7% of the maximum intensity in the X-ray spot. These points are marked by the two outermost vertical lines in Fig. 6.3 and the central line represents the center of the circle. From the regularly performed laser and X-ray measurements the center of the spot was determined to be at x = 40 pixels and y = 108 pixels with a radius of 19 pixels and it was shown to be stable within one pixel (150 μm)^2 diameter of the CCD.

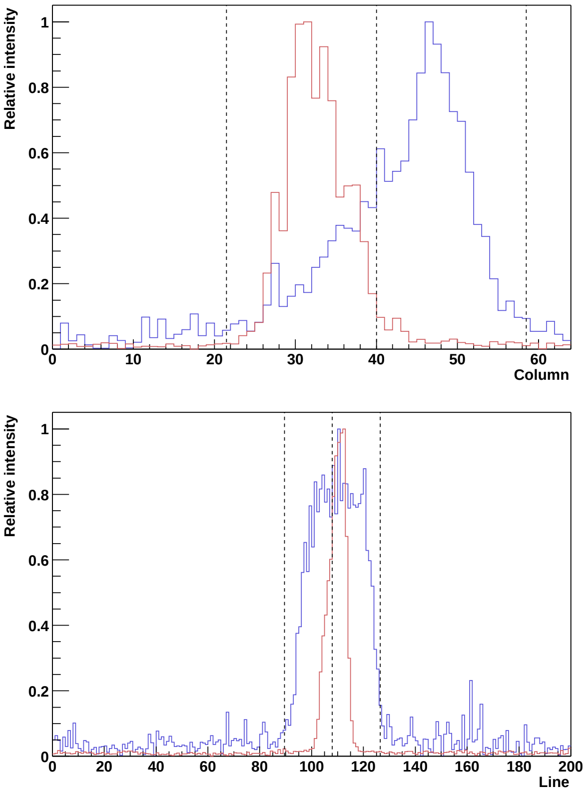

Figure 6.3: Projected intensity distribution in column (top) and line (bottom) direction of the laser and the X-ray spot for 2004 alignment measurements. The red and blue histogram correspond to the laser and X-ray measurements, respectively. The two outermost lines mark the position where the X-ray intensity dropps to 7% of the maximum intensity.

6.2 The 2004 data collection

6.2.1 Detector improvement in 2004

In 2004 the CCD detector was operated with an extra shielding inside the detector. The detector shield was enlarged by adding a 17 to 25 mm thick layer of low activity ancient lead on the outside of the copper shielding used during the 2003 data taking period. The lead shield inside the CCD chamber is encapsulated in sealed boxes made of high purity copper. The additional shielding has reduced the background level by a factor of 1.5 compared to the previous setup. The differential mean background rate is about 7.5×10^{-5} counts cm^{-2} s^{-1} keV^{-1} with a flat distribution over the 1 to 7 keV energy range.

In addition, during the winter shutdown 2003/2004 an intensive test was done to reduce the irregular electronic noise of the CCD detector. The source for the high electronic noise or a correlation to electronic equipment could unfortunately not be found in the CAST experimental area, nor in the laboratory in Munich. Due to this reason the energy range of the CCD is restricted to energies above 0.75 keV, whereas when the detector is operated in Munich, the noise level is about 250 eV.

6.2.2 Data taking and selection

The CCD detector has taken data quite stably with improved conditions from 20th of May to 14th of November in 2004. During the whole 2004 data collection period the X-ray telescope was aligned parallel to the magnet. The procedures for data processing and data selection are almost the same as before in 2003 analysis. As usual the CCD detector acquired data during 1.5 hours per day when the magnet was pointing to the sun. Background measurements where taken during non alignments periods and have about a 10 fold exposure time. All background data were selected with the same conditions as the solar tracking data, i.e. the magnetic field was on, and the valve VT4 between the magnet and the telescope was open. For the analysis the data from 11th to 28th of June were not included since the integration time of the CCD was set incorrectly during this period. It is about 9% of the total exposure time. In addition all bad runs that contain a few columns or lines with higher noise than others were skipped after the detector noise check. A list of bad runs can be found in Appendix A.2. But it is less than 1% of all data.

After applying the same cuts as in 2003 (Table 5.1) the total exposure time is 179.4 hours for the tracking data and 1723.1 hours for the background data. The 2004 measurement yielded a roughly 50% longer exposure time compared to the 2003 measurements. The resulting exposure time and count rates are summarized in Table 6.1.

	Tracking	Background
Exposure time	179.4 h	1723.1 h
Counts	861	8178
Count rate (10^{-4} counts s^{-1})	13.33 ± 0.45	13.18 ± 0.15

Table 6.1: Exposure time and counts rate of the 2004 data for the energy range between 1 keV and 7 keV.

6.2.3 Stability

The stability of the 2004 data taking can be seen in Fig. 6.4. Events are in the energy range between 1 and 7 keV for both tracking and background data. The interval between 11th and 28th of June is skipped because of the wrong integration time. The background seems to be quite stable over all data taking periods as can be seen in the bottom plot of Fig. 6.4. However in the solar tracking data there is a slight slope between July and September.

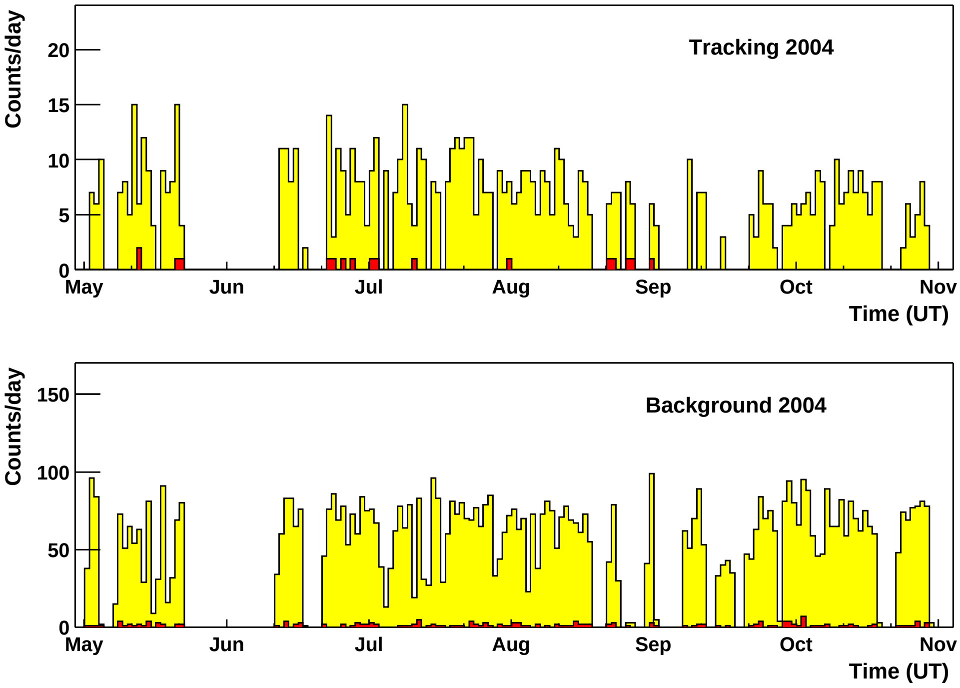

Figure 6.4: Time variation for the tracking data (top) and for the background data (bottom). Counts are from the full CCD area in the energy range 1 - 7 keV. Red histogram represents only the counts from the area of the expected solar spot.

6.2.4 Full CCD

Figure 6.5 represents the CCD images consisting of 64 columns and 200 lines for tracking and background data. It appears that the events are distributed uniformly over the whole CCD plane. The corresponding energy spectra are given in Fig. 6.6. It shows the tracking data and the background data normalized by the time ratio of the tracking to the background data (9.5). The peaks at 8.0 keV and at 8.9 keV are the Cu-K_α and Cu-K_β lines due to the Cu shielding inside of the CCD detector chamber. Because of the cooling mask of the CCD made by Au, the Au-L_α line at 9.7 keV appears. The peak near 6.3 keV is the Cu escape peak. The tracking data seems to be consistent with background. Furthermore, the interesting energy range between 1 and 7 keV is quite flat.

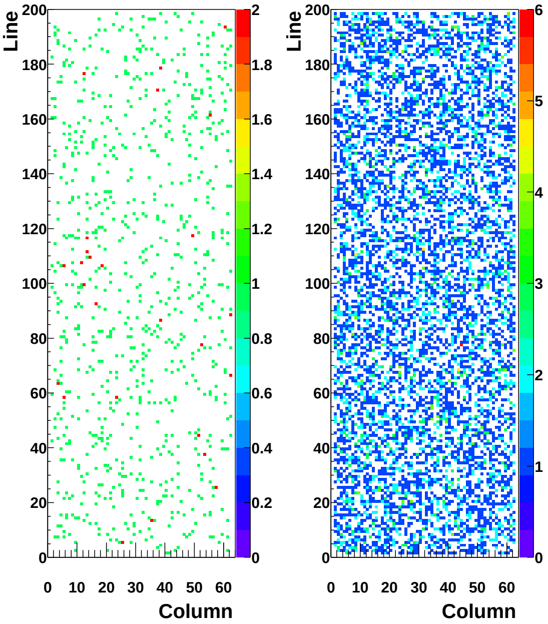

Figure 6.5: 2D plots of CCD images for the tracking (left) and background (right) data. Counts (z axis) are in the energy range 1 to 10 keV.

The residual plot (see Fig. 6.7) shows the difference between the signal and the background, i.e. the normalized background was directly subtracted from the tracking data bin by bin. Generally from the residual plot it can be seen whether the average of the residuals is zero or whether the residuals have a trend. To check that, a straight line fit was done to the subtracted data. It turned out from the fitting that the regression line for the residual plot coincides with zero and the subtracted data is apparently compatible with zero. In other words, no signal above background was observed.

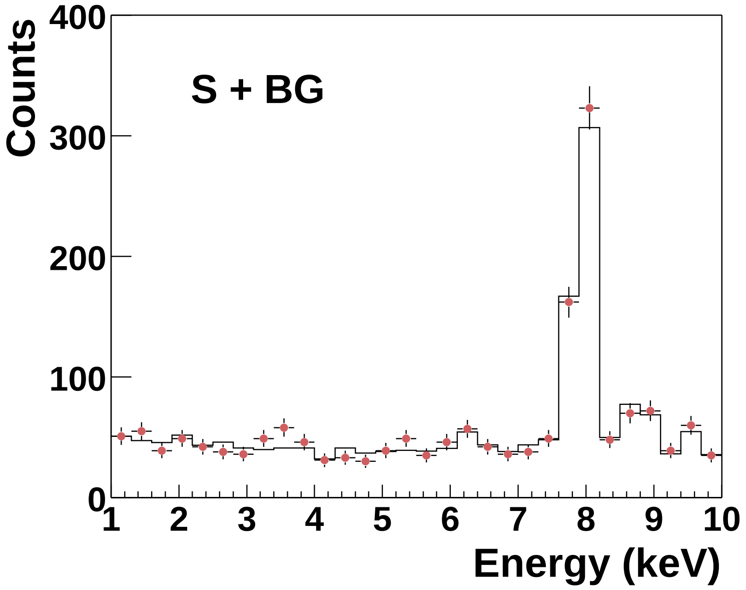

Figure 6.6: Energy spectrum of the tracking data (red circles) with statistical error bars and the normalized background data by the ratio 9.61 between tracking and background time (histogram).

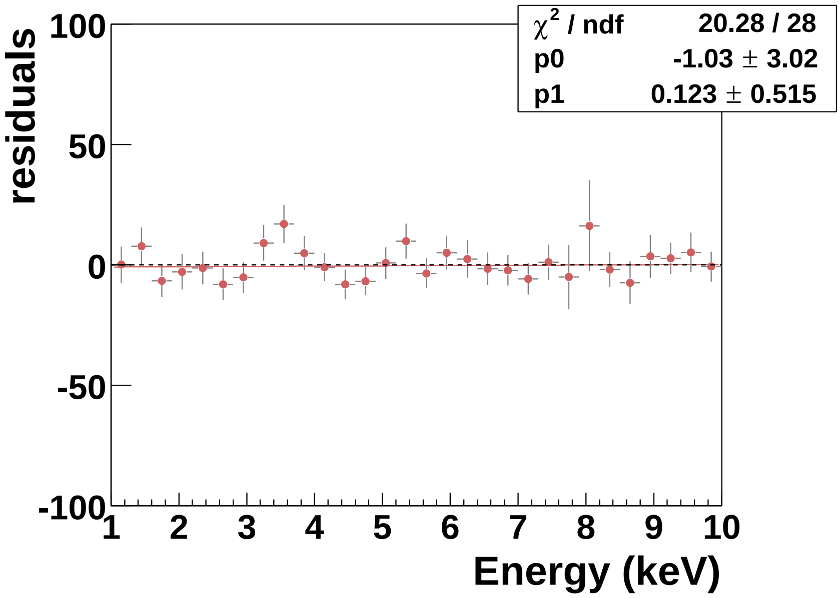

Figure 6.7: Residual plot with a linear fit. Error bars represent statistical errors only.

6.3 Background studies

In order to characterize the background, studies of the background were carried out in the same way as before in the analysis of 2003 data. Thus the background was studied under different experimental conditions and different azimuthal and horizontal positions of the magnet.

6.3.1 Column and line distributions

A test of a straight line fit for the line and column distribution shows whether the events are distributed equally over the CCD plane. Figure 6.8 shows the distribution of events as a function of lines and columns on the CCD plane. Counts are after energy cut (1 - 7 keV) in all histograms. The counts in the first and last columns and lines were not taken into account because those events are not allowed by the pattern recognition during data processing. From the fit results it turns out that the events are distributed quite uniformly over all the CCD. Moreover both tracking and background distributions are consistent with each other within statistical fluctuations if one takes into account the different exposure times.

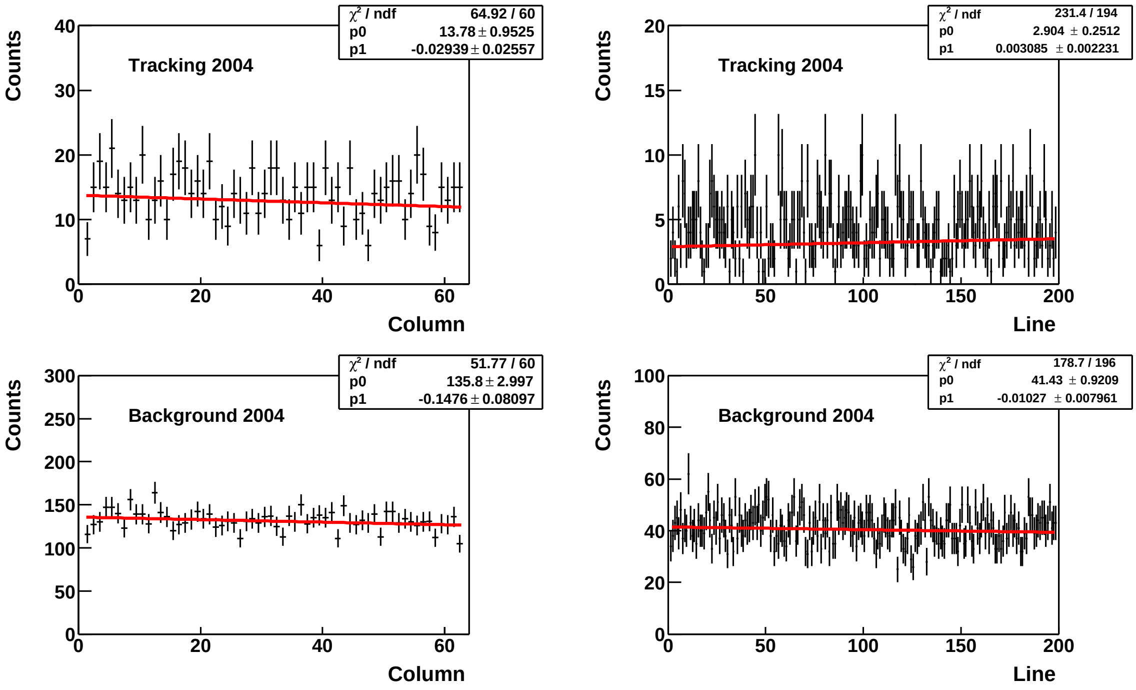

Figure 6.8: Distributions of 64 columns and 200 lines of the CCD with a linear fit (red line). The upper plots are the tracking data and the bottom plots are the background data. Statistical error bars are given as well.

6.3.2 Experimental conditions

The dependence of the background on different experimental conditions was examined. In fact the background taken under the same conditions as the solar tracking data was used for the determination of the coupling constant $g_{a\gamma}$. Figure 6.9 shows the normalized background by the exposure time with respect to four combinations of two important operating parameters, i.e. the magnetic field $\vec{B}$ and the valve VT4 between the magnet and the X-ray telescope. The case of the $\vec{B}$ field on and the VT4 open (upper left in Fig. 6.9) is the standard condition for the background. In the upper right plot, the large error bars are because of the small statistics for the configuration with VT4 closed and field on. When the magnetic field was off and VT4 was closed, more counts were observed in the lower energy range below 2 keV. However, as shown in Table 6.2, the mean count rates of the background for all cases are compatible with each other within the 1 σ error. As a result, significant effects on the background by changing the experimental conditions could not be found.

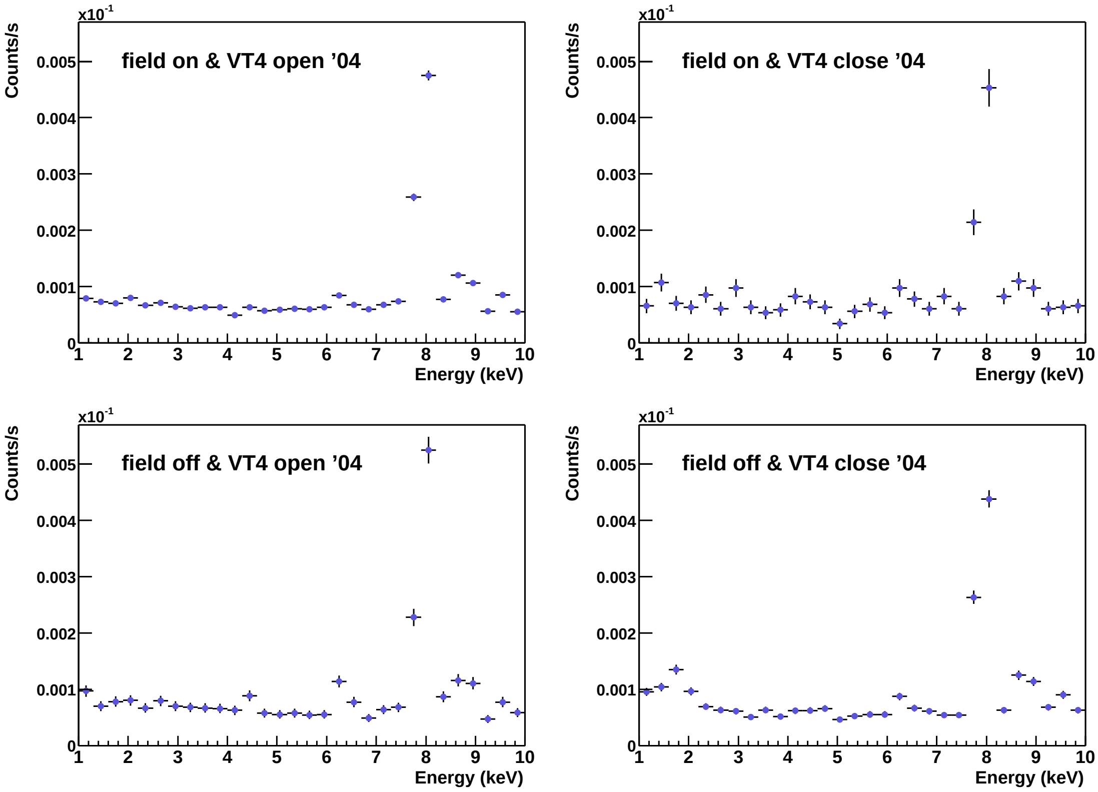

Figure 6.9: Background under the different operation conditions: $\vec{B}$ field on and VT4 open (top left), $\vec{B}$ field on and VT4 close (top right), $\vec{B}$ field off and VT4 open (bottom left), and $\vec{B}$ field off and VT4 close (bottom right).

	$\vec{B}$ on	$\vec{B}$ off
VT4 open	$(7.173 \pm 0.067) \times 10^{-5}$ cts/s	$(7.247 \pm 0.160) \times 10^{-5}$ cts/s
VT4 close	$(7.142 \pm 0.241) \times 10^{-5}$ cts/s	$(7.059 \pm 0.113) \times 10^{-5}$ cts/s

Table 6.2: Mean count rates of 2004 background under different operating conditions.

6.3.3 Position dependence

The background dependence on the various azimuthal and horizontal positions of the magnet was also investigated. As mentioned in Section 5.2.5 the background data were taken in all areas of the experimental hall, on the other hand the solar tracking data were collected in a certain location. This means that there could be a position dependence of the background.

The background counts distributed with a binning of 10° azimuthally and 2° vertically are shown in Fig. 6.10. The count rates normalized by the exposure time can be seen in the left plot. The background seems to be almost equally distributed over all areas. The projection of the vertical and azimuthal distributions is plotted in Fig. 6.11. The mean count rate of the background is about $(1.33 \pm 0.02) \times 10^{-3}$ counts s^{-1} in both cases. A significant tendency of the background distribution on the vertical angle was not observed as well as the distribution on the azimuthal angle is fairly stable within statistical errors. The solar tracking data were gathered roughly in the range from 40° to 100° azimuthally.

In summary, the background study was carefully performed with all possible factors. It turned out that no remarkable dependence under changing experimental conditions or in different positions of the magnet have been found. Therefore all background data taken under the same conditions as the tracking data was used for further analysis.

6.4 Determination of the upper limit on $g_{a\gamma}$

As mentioned already in Section 6.1 a very important point in the determination of $g_{a\gamma}$ is that the size and the position of the CCD image are determined using a laser beam. The observed focus is well within the solar image of 6.4 mm^2. The spot stability of the telescope was observed continuously by an X-ray source during data taking time. Therefore the analysis of a smaller area was possible for 2004 data than in 2003. To determine the upper limit on the coupling constant of the axion to photon, a Likelihood method was used due to the low counting statistics on the spot of the CCD.

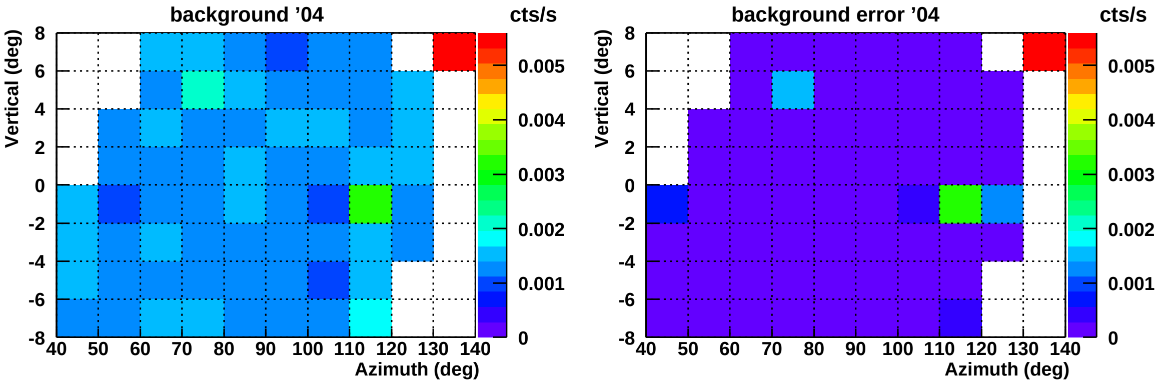

Figure 6.10: Background dependence on the magnet position. Background rates normalized by the exposure time (left) and its corresponding statistical errors (right).

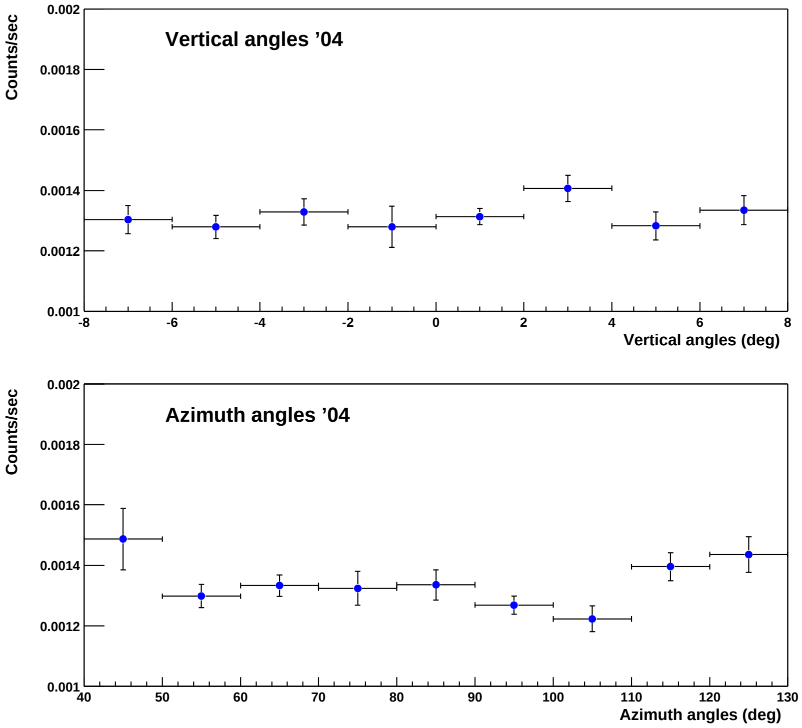

Figure 6.11: Count rates of the background projected onto the vertical (top) and azimuthal (bottom) plane.

Spot extraction

It is known from the alignment measurements that the center of the spot with 19 pixels diameter is located in the 40th line and 108th column of CCD plane as can be seen in the top plot of Fig. 6.12. The data in the spot area is selected by using the following circle cut

$$\sqrt{(x-a)^2+(y-b)^2} \leq r \,,$$

where the spot radius r is 9.5 pixels and the numbers of the spot center on the line a and column b are 40.5 and 108.5, respectively. The effective area of the spot with 19 pixels diameter is 6.38 mm^2 for both signal and background data. Here signals are counts in the spot area from tracking data, and background are defined as the data in the same area from background data. After the position cut only 18 counts as signal and 194 counts for background were obtained for 179.4 hours tracking time and 1723.1 hours background time, where the time ratio between tracking and background data is 9.61.

The analysis procedures of 2004 data are mostly done in the same way as in 2003. A few differences between the 2003 and the 2004 analyses are summarized below:

- The telescope was slightly tilted to the axis of the magnet bore during the data taking period in 2004. Because of this small misalignment between the X-ray telescope and the magnet, the total efficiency of the CCD and the telescope has decreased by about 10% compared to 2003. The efficiency curve given by the mirror reflectivity of the telescope multiplied by the quantum efficiency of the CCD has been already mentioned in Section 4.1.2 (see Fig. 4.8). The total detection efficiency is about 32% in the energy range of 1 - 7 keV.

- Out-of-Time events were corrected for in the 2004 analysis. As was discussed in Section 4.2.4 the CCD detector is at all times exposed to incoming radiation. Trying to prevent pile-up events, the CCD is read out frequently. During readout, photons can still be received, i.e. they hit pixels while their charges are being transferred to the readout nodes. Those events hitting them during readout are Out-of-Time (OoT) events. One cannot correct for this effect in individual cases but only account for them statistically. This effect scales with the ratio of readout time and integration time so that the fraction of the OoT events was multiplied with the fit function.

- The magnetic field was not set to the same value during the whole of the 2004 data taking period. From August 16th to September 15th in 2004 the applied current in the magnet was 13330 Amperes corresponding to 9.0 Tesla and in the other periods as 13000 Amperes which corresponds to 8.79 Tesla, i.e. 19.86% of total exposure time was with 9.0 Tesla and 80.14% with 8.79 Tesla. Therefore the weighted mean of the magnetic field is 8.832 Tesla, which is used in the data analysis.

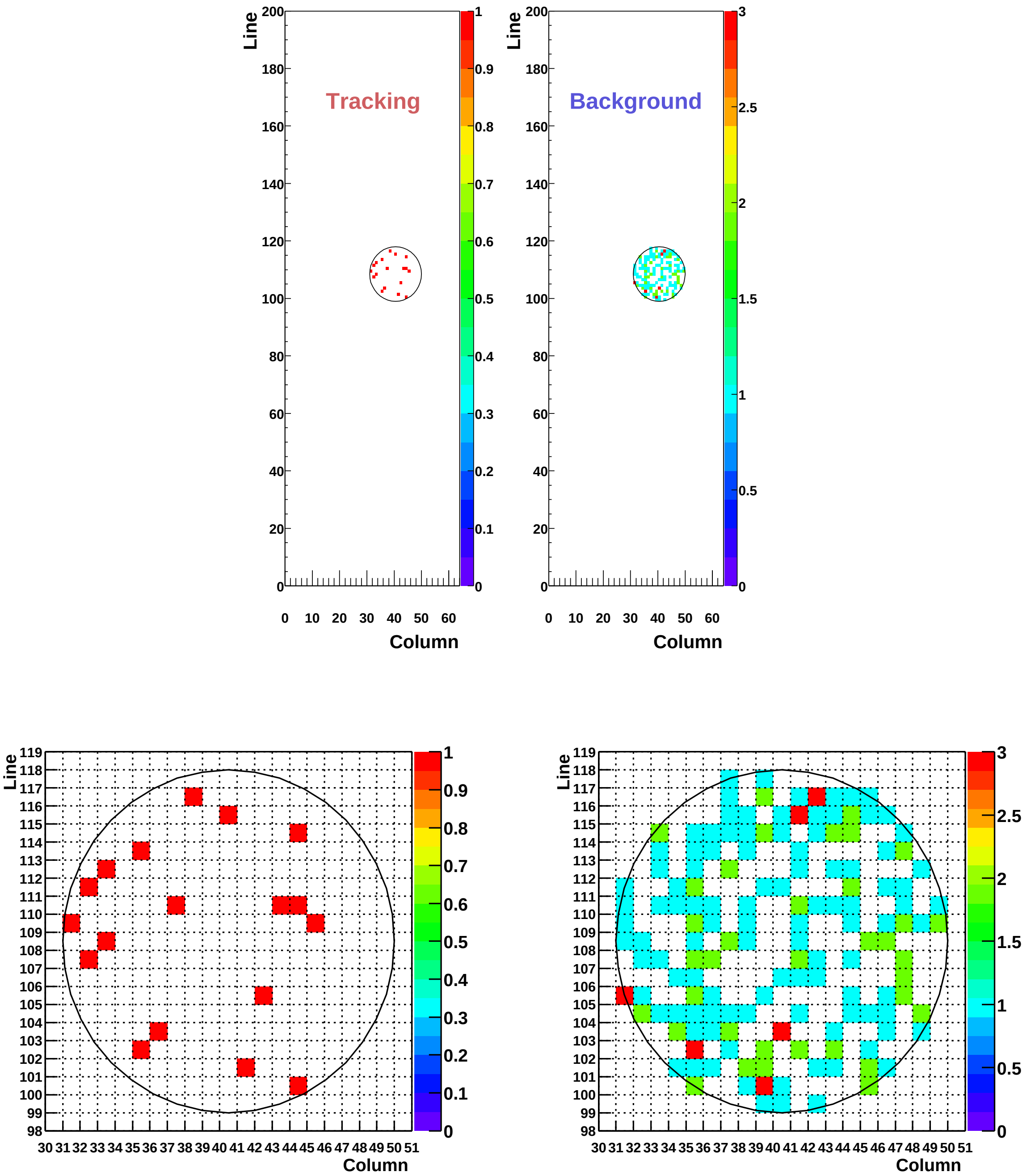

Figure 6.12: Top: CCD images of the signal (left) from the tracking data and of the background (right) from the background data. Units of the z axis are counts per pixel. Bottom: Equivalent zoom plot. The spot position is located in the center of the 40th line and the 108th column of the CCD plane.

- The effective length of the magnet is 9.26 m and the effective area of the magnet bore is 14.52 mm^2 with a 43 mm diameter of the magnet bore.
- In the energy spectrum, there is a detector noise peak below 1 keV and a Cu peak at 8 keV due to the Cu shielding. Thus the comparative flat range of the energy between 1 and 7 keV with a bin size of 0.3 keV was used for fitting as before in 2003 analysis.

Maximum Likelihood fit

The maximum Likelihood function is defined by the same Eq. (5.9) with the fit function $\mu_i = b_i/\alpha + a(\mathrm{E}_i)$, where b_i is the measured background data over 20 bins and α = 9.61 is the time ratio of the tracking to the background data. The theoretically expected axion spectrum $a(\mathrm{E}_i)$ is given by

$$a(\mathrm{E}_i) = \frac{\mathrm{d}\Phi_a}{\mathrm{dE}} \times \mathrm{P}_{a\to\gamma} \times 645784.21\mathrm{s} \times 14.522\mathrm{cm}^2 \times 0.3\mathrm{keV} \times \varepsilon(\mathrm{E}_i) \times (1 - f_{\mathrm{OoT}}) \tag{6.1}$$

with the tracking exposure time of 645784.21 s, the magnet bore area of 14.522 cm^2, the bin size of 0.3 keV, the total efficiency $\varepsilon(\mathrm{E}_i)$ of the telescope and the CCD, and the fraction of the OoT events (1-f_{OoT}) of 0.917. The spectrum, which is proportional to $\mathrm{g}^4_{a\gamma}$, is directly used as the fit function. A newly estimated flux of the solar axion based on the most recent 2004 solar model was used for the 2004 analysis. The differential form of the solar axion flux can be found in Eq. (3.11). The conversion probability from axion to photon in the magnetic field is given by

$$\mathrm{P}_{a\to\gamma} = 1.6388 \times 10^{-17} \times \left(\left[\frac{\mathrm{B}}{8.83\mathrm{T}}\right]^2 \cdot \left[\frac{\mathrm{L}}{9.26\mathrm{m}}\right]^2 \cdot \left[\frac{10^{-10}\mathrm{GeV}^{-1}}{\mathrm{g}_{a\gamma}}\right]^2 \right). \tag{6.2}$$

It was slightly reduced in comparison to 2003 due to the small changes of the magnetic field strength.

As can be seen in the residual plot (see Fig. 6.7) the 2004 data is consistent with the absence of a signal so that a 95% confidence limit has been extracted. After the Likelihood fit, the upper limit of the coupling constant $\mathrm{g}_{a\gamma}$ was determined by integrating the Bayesian probability distribution only over the physically allowed region, i.e. positive signals, using Eq. (5.7) as described in Section 5.3.2.

Results

To check whether the data is compatible with the absence of the signal, a null hypothesis test was done at first and yielded

$$\chi^2_{\mathrm{null}}/\mathrm{ndf} = 12.0/20\ .$$

After that, the Likelihood fit yields a best fit value of $g^4_{\text{best fit}}$ of

$$g^4_{\text{best fit}} \pm 1\sigma \text{ error} = (-0.1041 \pm 0.2848) \times 10^{-40}\ \text{GeV}^{-4}\ ,$$

which is slightly negative. Its 1 σ statistical error is obtained from the width of $\chi^2(g^4_{a\gamma})$ when the χ^2 value increases by one unit. The χ^2 distribution as a function of $g^4_{a\gamma}$ can be seen in the top plot of Fig. 6.13. For the 2004 data an upper limit on the coupling constant of the axion to photon is constrained by

$$g_{a\gamma} < 0.875 \times 10^{-10}\ \text{GeV}^{-1}$$

with 95% confidence level and the corresponding χ^2_{min} value is

$$\chi^2_{\text{min}}/\text{ndf} = 11.9/19\ .$$

This upper limit is more restrictive by a factor of 1.4 than the one obtained from the 2003 data. This can be explained by several reasons: In 2004 there was more statistics collected than in 2003 by a factor of 1.5 and the background level was reduced as well as by a factor of 1.5. The most important reason is that for the 2004 data the analysis could be restricted to a smaller spot on the CCD since the stability of the X-ray telescope was regularly monitored. Fig. 6.13 shows the tracking data (solid circles) with statistical error bars and the normalized background (dashed line), together with the expected axion spectrum, that is the normalized background plus the expected signal with the $g_{a\gamma}$ at 95% C.L. from the analysis.

6.5 Systematic studies

In order to check how big the systematic uncertainty of the final result might actually be, several systematic studies were carried out. The systematic studies were performed by varying many possible sources of errors. In fact, it was already known that there was not a significant tendency in the background behavior from the systematic studies of the background, like e.g. the position dependence and the different experimental conditions. Therefore the remaining possible systematic effects are carefully studied. After that the systematic uncertainties on the final result are estimated in this Section. These systematic studies have been performed with the 2004 data only.

6.5.1 Variation of the background

The largest systematic effect on $g_{a\gamma}$ comes from the definition of the background. In a first step the background was defined in many different ways, using the tracking data. Moreover the influence of the spot size on the result was investigated.

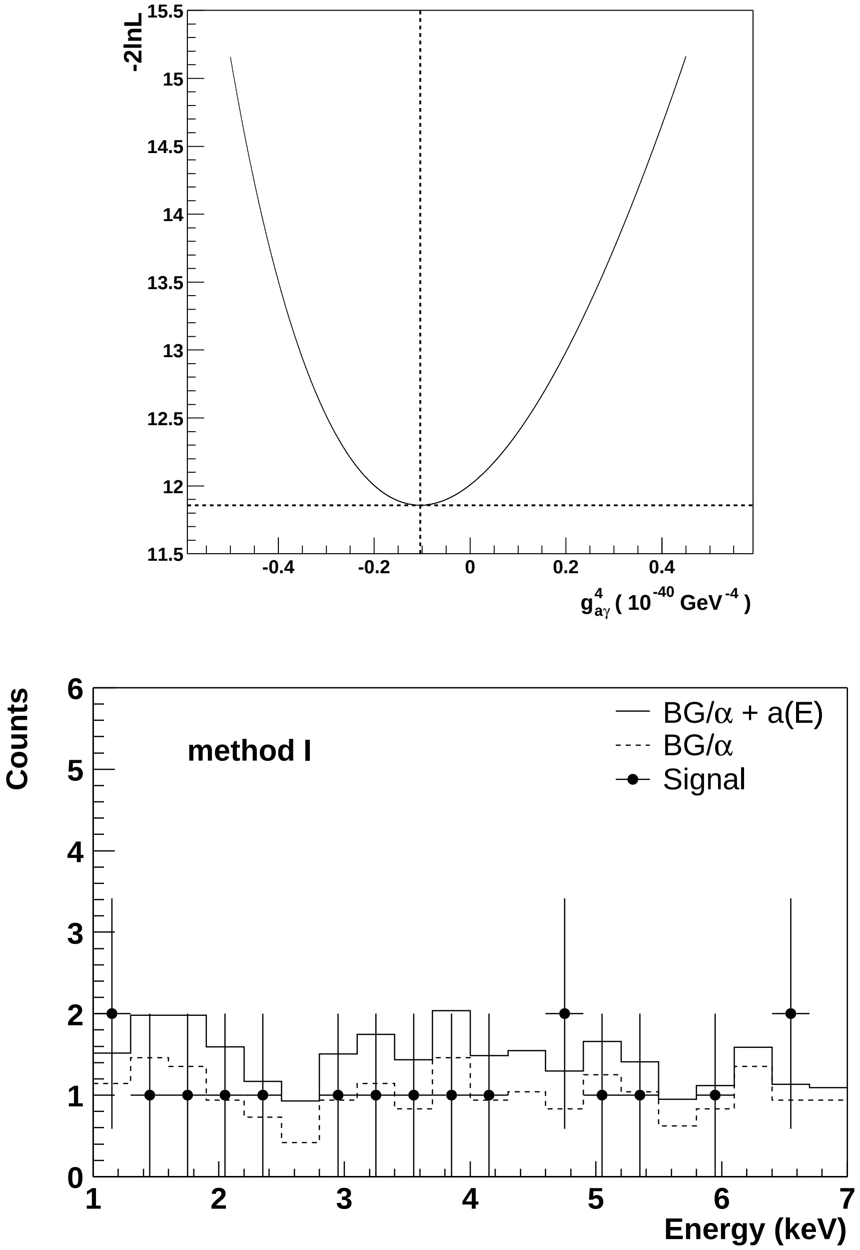

Figure 6.13: Top: χ^2 distribution as a function of $g^4_{a\gamma}$. The best fit value corresponds to the minimum of $g^4_{a\gamma}$ (dashed line). Bottom: The tracking and background spectra with the expected theoretical axion spectrum. The solid circles are tracking data with statistical error bars, the dashed line is the background spectrum normalized by the time ratio of the signal to background and the solid line is the normalized background plus the expected signal with $g_{a\gamma}$ at 95% confidence level.

Method II

In the standard way to determine the coupling constant $g_{a\gamma}$, the background was defined as the same area as the signal but from the background data taken during the non tracking time. Thus the idea for method II is to use only the tracking data for both signal and background. So the data from the area surrounding the spot (59.4 mm^2) from the tracking data is regarded as background, and the signal (6.38 mm^2) is the same as in the standard method. Images after the geometric cut are illustrated in the two-dimensional plot of Fig. 6.14. The outer circle of the background is bound by the circle of maximum area in the region of 64 columns. A total 18 counts and 192 counts were obtained for signal and background, respectively. In this case the background was normalized by the area ratio of 9.31 since both signal and background use the same tracking data, where the area ratio is defined as the area of the background divided by the area of the signal.

Method III

In method III the data of all surrounding area except for the spot from the tracking data was defined as background, while the signal is the same as in the standard method. Shown in Fig. 6.15 is the area of the background 276.19 mm^2, so that the ratio of the signal area to the background area is 42.29, which is used for the normalization of the background. The total number of events from the background region is 843 counts.

Method IV

Since there could be a signal in the region between the signal area and the background area, the data in this region from the tracking data were excluded for the background definition of method IV, as demonstrated in Fig. 6.16. The background yields a total of 785 counts in an area of 249.31 mm^2 and is normalized by the area ratio of 39.08 between the tracking and the background data.

Method V

In principle the size of the solar spot on the CCD has a diameter of 19 pixels with an uncertainty of one pixel diameter. Thus the effects of changing the spot size were checked. At first, the spot size with one pixel bigger radius, i.e. 21 pixels diameter, was used for method V. Like the standard method the signal and background are defined as the counts from tracking and background data, respectively. As can be seen in Fig. 6.17 the area for both signal and background is 7.79 mm^2. In this area the signal has one more count than the usual one and the background has total 232 counts. Due to the same area for signal and background, the time ratio of the tracking to the background data was used for the background normalization. In fact when the spot size varies slightly the efficiency of the X-ray telescope should be corrected for the determination of $g_{a\gamma}$. However, as described in Section 4.1.1, the efficiency for the spot with the diameter of 19 pixels is valid for a spot size of 21 pixels diameter. Thus the same efficiency was taken.

Method VI

A reduced spot size of 17 pixels diameter was also checked. The spot images with an area of 5.11 mm^2 are demonstrated in Fig. 6.18. Due to this small area of the spot, only 14 counts for signal and 154 counts for background were gathered. The time ratio was used as the normalization factor for background, as well as the same efficiency as method V was used here.

To determine the upper limit on the axion-photon coupling constant $g_{a\gamma}$ the same procedures as the standard method were applied for all cases. The results from the Likelihood fit are summarized in Table 6.3. Values of $\Delta g^4_{\text{best fit}}$ and $\Delta g_{a\gamma}$ are calculated by comparing the standard result of method I with each result. The best fit value of $g^4_{a\gamma}$ varies from 5% to 14% depending on the different definition of the background as shown in Fig. 6.19. The largest change on the result for both $g^4_{\text{best fit}}$ as well as $g_{a\gamma}$ comes from the method V with the spot size of 21 pixels diameter. However all values of $g^4_{\text{best fit}}$ are stable within 1 σ standard deviation. Furthermore as can be seen in the last column of Table 6.3 all final results of $g_{a\gamma}$ lie apparently within 1 - 2% deviation. It seems that all values are in good agreement with each other. In summary, this study demonstrates that the systematic effect of the different background definition does not much affect the final result. The value for the maximum deviation on $g^4_{\text{best fit}}$ from the method V was taken into account for the determination of the systematic error on $g^4_{\text{best fit}}$.

method	$g^4_{\text{best fit}} \pm 1\,\sigma$ error (10^{-40} GeV^{-4})	$\Delta g^4_{\text{best fit}}$	χ^2_{null} / ndf	χ^2_{min} / ndf	$g_{a\gamma}$ (95% C.L.) (10^{-10} GeV^{-1})	$\Delta g_{a\gamma}$
I	- 0.104 ± 0.285	0	12.0/20	11.9/19	0.875	0
II	0.019 ± 0.273	+ 0.123	14.0/20	14.0/19	0.892	+ 0.017
III	- 0.042 ± 0.284	+ 0.062	12.9/20	12.9/19	0.886	+ 0.011
IV	- 0.053 ± 0.284	+ 0.051	13.1/20	13.1/19	0.884	+ 0.009
V	- 0.243 ± 0.288	- 0.139	13.5/20	12.8/19	0.854	- 0.021
VI	- 0.040 ± 0.259	+ 0.065	17.3/20	17.3/19	0.868	- 0.007

Table 6.3: Summary of the results for different background definitions.

6.5.2 Extended energy range

The next step is to check the effect of the energy range on the fitting of the final result. The normal fit is performed in the energy range between 1 and 7 keV. As explained in Section 5.1.3, the reason is that there is a detector noise peak in the energy range below 1 keV and

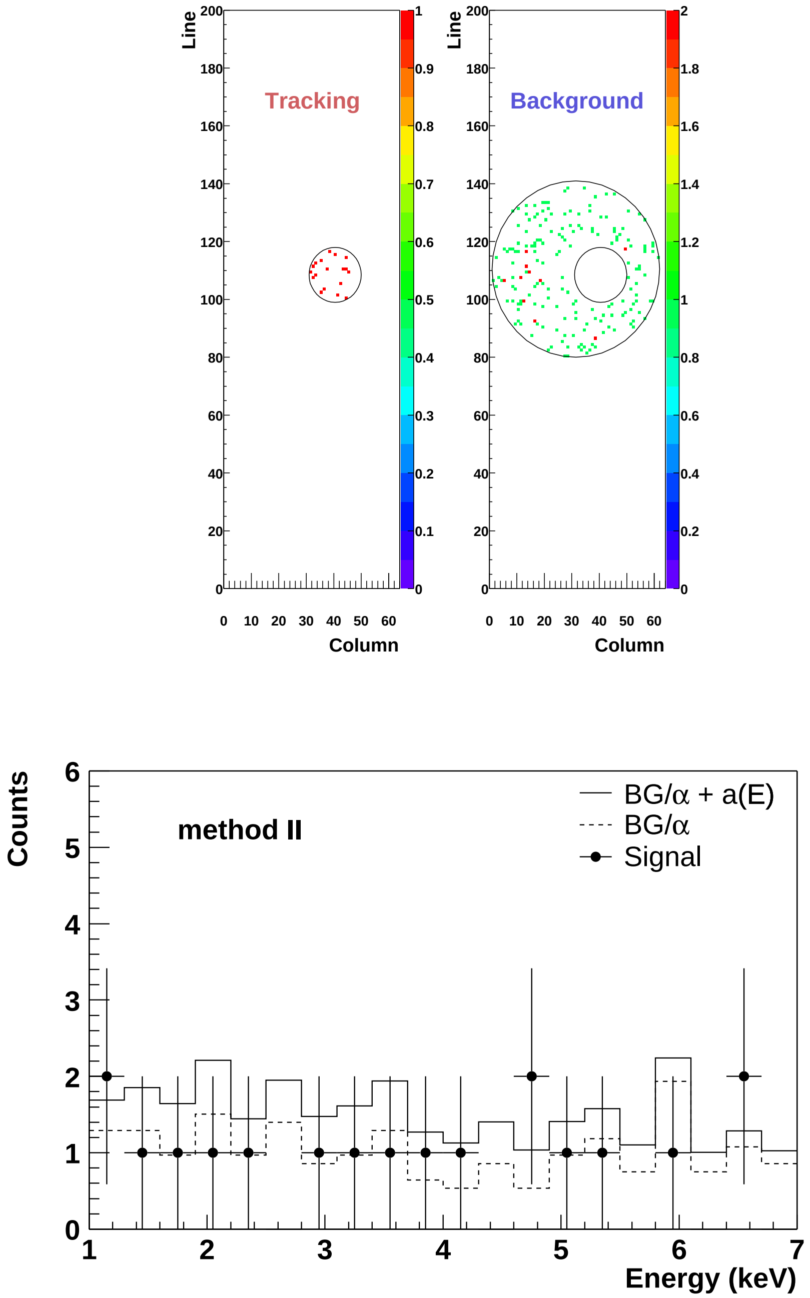

Figure 6.14: Top: Images of the signal (left) and background (right) from tracking data for method II. Units of the z axis are counts per pixel. Bottom: The tracking and background spectra with the expected theoretical axion spectrum. The solid circles are tracking data with statistical error bars, the dashed line is the background spectrum normalized by the area ratio of the signal to the background and the solid line is the normalized background plus the expected signal with $g_{a\gamma}$ at 95% confidence level for method II.

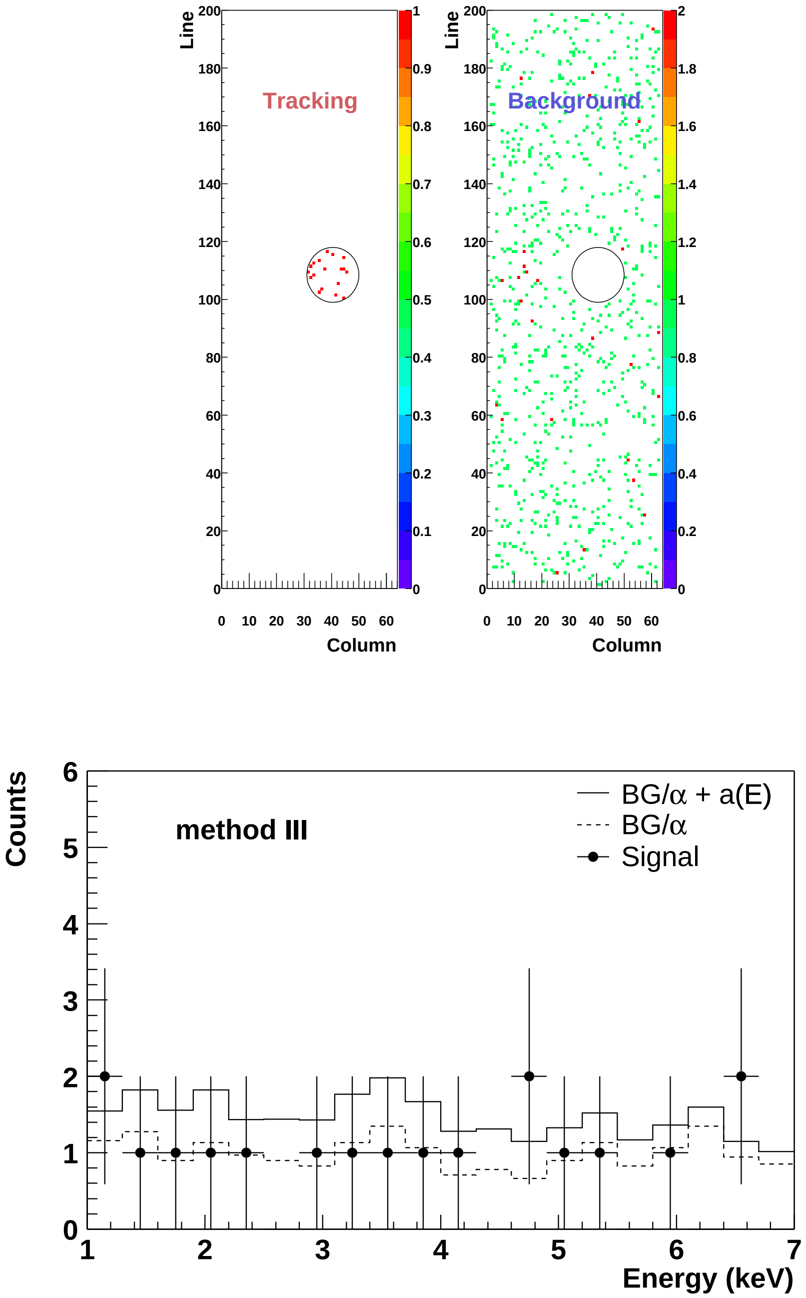

Figure 6.15: Top: Images of the signal (left) and background (right) from tracking data for method III. Bottom: The tracking and background spectra with the expected theoretical axion spectrum. Tracking data (solid circles) with statistical error bars, the background (dashed line) normalized with the area ratio of $\alpha = 42.29$, and the normalized background plus the 95% expected signal with $g_{a\gamma}$ (solid line) are represented for method III.

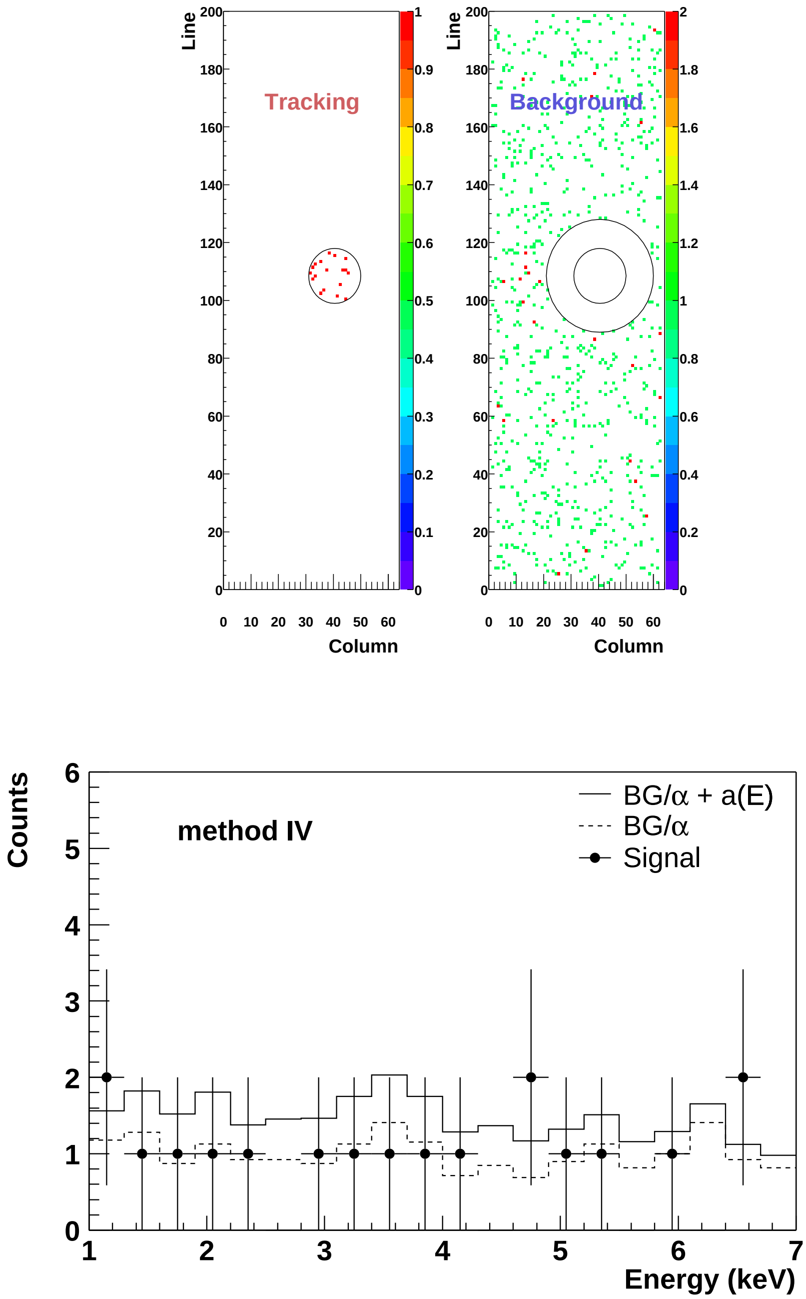

Figure 6.16: Top: Two-dimensional plots of the signal (left) and background (right) from tracking data for method IV. Bottom: The tracking and background spectra with the expected theoretical axion spectrum for method IV.

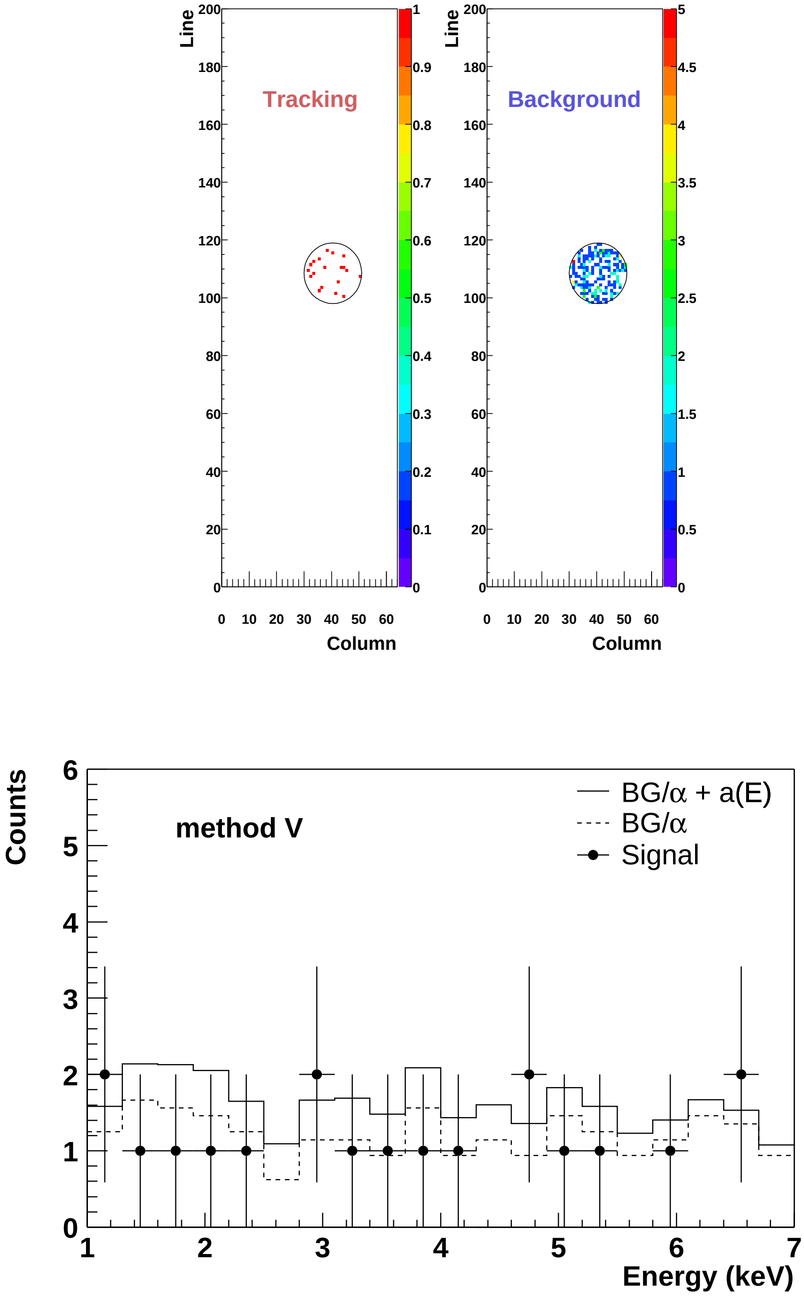

Figure 6.17: Top: Images of the signal (left) from tracking data and background (right) from background data with the spot size of 21 pixels diameter for method V. Bottom: The tracking and background spectra, together with the expected theoretical axion spectrum for method V.

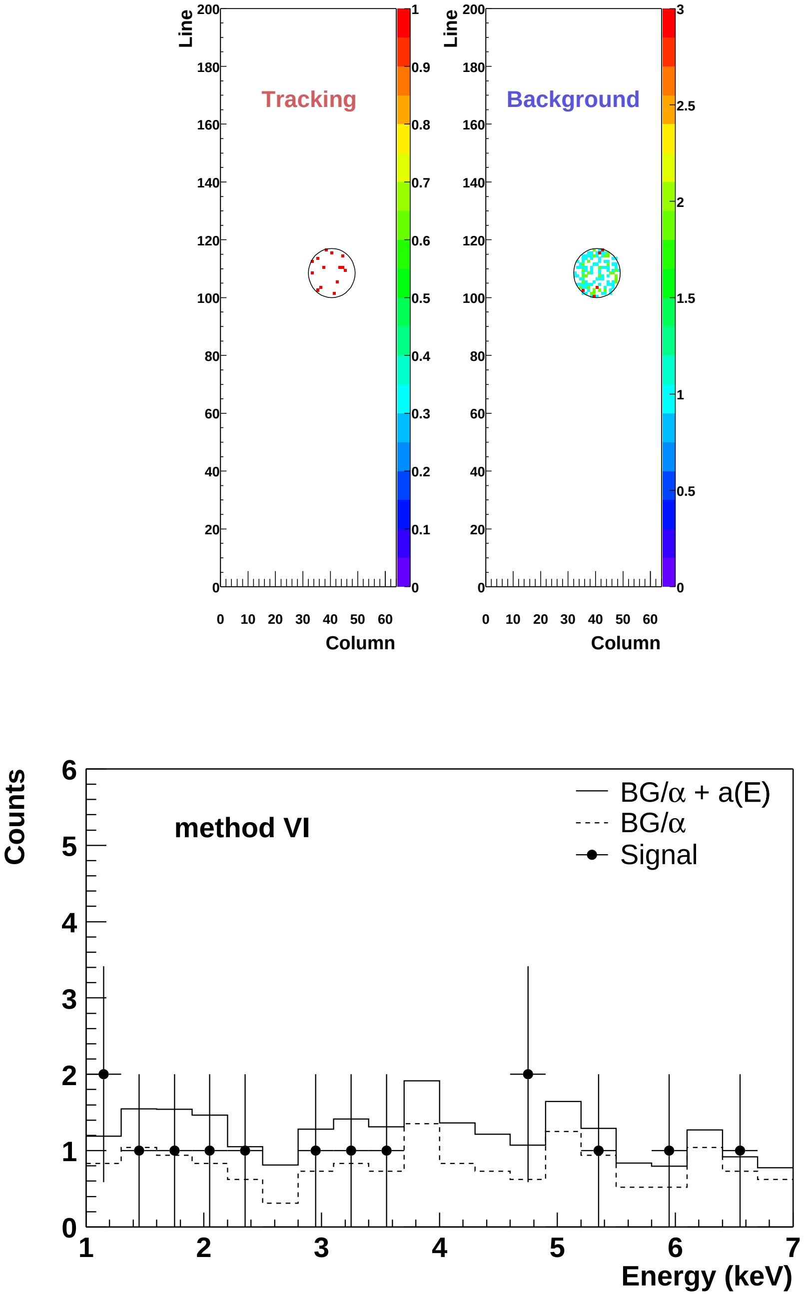

Figure 6.18: Top: Two-dimensional plots of the signal (left) from tracking data and background (right) from background data with the spot size of 17 pixels diameter for method VI. Bottom: The tracking and background spectra, together with the expected theoretical axion spectrum for method VI.

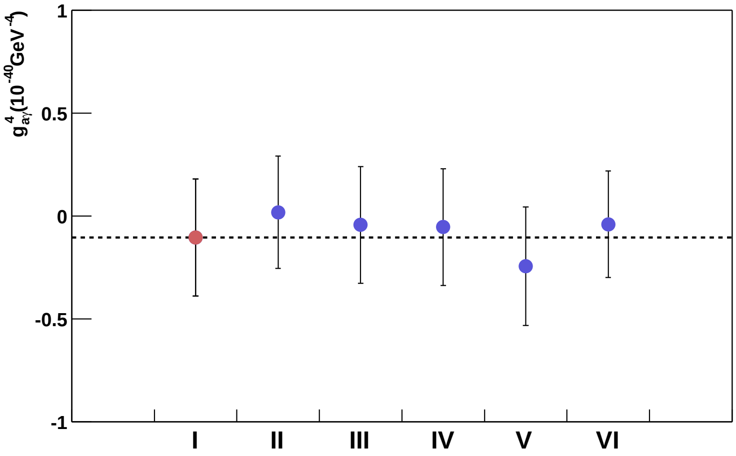

Figure 6.19: The best fit value of $g^4_{a\gamma}$ as a function of methods. Error bars are the statistical errors of $g^4_{a\gamma}$. The dashed line represents the standard value of method I.

a copper peak above 7 keV due to the Cu shielding inside the CCD chamber, so that the flat distribution range of 1 - 7 keV was decided to be used for the fitting. Due to too small counting rates it is impossible to reduce the fit range and thus the fit range was extended up to 10 keV, including the copper lines around 8 keV. This is the maximal range of the energy for the determination of $g_{a\gamma}$ since efficiency data of the X-ray telescope exit only up to 10 keV.

By applying the standard method, a total 39 counts for the signal and 390 counts for the background are obtained in the range of 1 - 10 keV, where the signal and background come from the tracking and background data, respectively. The corresponding energy spectrum is demonstrated in Fig. 6.20 and the results from the Likelihood fit are shown in Table 6.4.

energy range	$g^4_{\text{best fit}} \pm 1\,\sigma$ error (10^{-40} GeV^{-4})	χ^2_{null} / ndf	χ^2_{min} / ndf	$g_{a\gamma}$ (95% C.L.) (10^{-10} GeV^{-1})
1 - 10 keV	- 0.076 ± 0.291	20.8 / 30	20.7 / 29	0.884

Table 6.4: Fit results for the extension of the energy range.

The best fit value of $g^4_{a\gamma}$ is still slightly negative and its difference is 2.8 % in the positive direction compared to the result with an energy range of up to 7 keV. But only 1% was changed in the final result of $g_{a\gamma}$ with a reasonable χ^2 value. Thus the result indicates that the value of $g_{a\gamma}$ is fairly stable under variation of the energy range. Moreover, as can be seen clearly in Fig. 6.20, the expected axion spectrum (solid line) is almost the same as the background spectrum in the energy range above 7 keV.

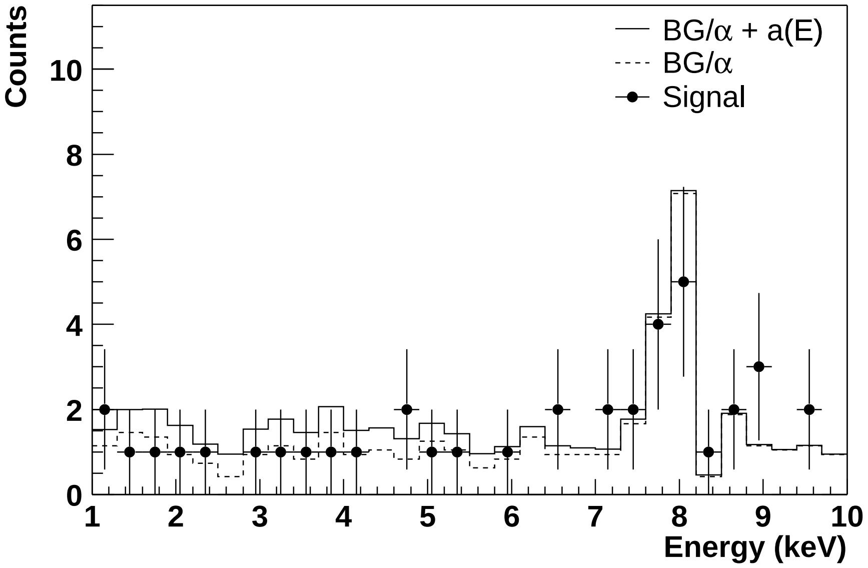

Figure 6.20: Tracking (solid circles) and normalized background (dashed line) spectra together with the expected axion signal (solid line) with $g_{a\gamma}$ at 95% confidence level.

6.5.3 Fit parameters

Lastly the effects of varying the fit parameters has been checked. The fit function is proportional to the square of the magnetic fields times the magnetic length so that the most important input parameters are the magnetic length and its field strength. The effective magnetic length of the CAST magnet is 9.26 m since the magnetic field strength becomes zero at 150 to 200 mm from the end of the magnet bore. By changing the magnetic length with an uncertainty of ± 0.05 m the coupling constant $g_{a\gamma}$ was estimated while the magnetic field stays at fixed 8.83 T. Analogous to the case of the magnetic length, $g_{a\gamma}$ is also calculated by varying the magnetic field with an uncertainty of ± 0.1 T where the length is fixed. Because of the proportionality of the magnetic fields and length to the fit function, the results would be expected to be only proportional to varying those parameters. The fit results for all cases are summarized in Table 6.5. No influence of the fit parameters on the final result has been observed. As expected, all results change proportionally with less than 1%.

6.5.4 Estimation of systematic error on $g^4_{\text{best fit}}$

The systematic studies were divided into several categories and carried out, as shown before. Using the maximum variation of each category from those systematic studies, the systematic error of $g^4_{\text{best fit}}$ value is determined at first. The following Table 6.6 summarises the results

	$g^4_{\text{best fit}} \pm 1\,\sigma$ error (10^{-40} GeV^{-4})	$\Delta g^4_{\text{best fit}}$	χ^2_{null} / ndf	χ^2_{min} / ndf	$g_{a\gamma}$ (95% C.L.) (10^{-10} GeV^{-1})	$\Delta g_{a\gamma}$
L=9.31m	- 0.103 ± 0.282	+ 0.001	12.0/20	11.9/19	0.872	- 0.003
L=9.21m	- 0.105 ± 0.288	- 0.001	12.0/20	11.9/19	0.877	+ 0.002
B=8.93T	- 0.102 ± 0.278	+ 0.002	12.0/20	11.9/19	0.870	- 0.005
B=8.73T	- 0.107 ± 0.291	- 0.002	12.0/20	11.9/19	0.880	+ 0.005

Table 6.5: Results for the varying of the fit parameter.

of the previous Sections 6.5.1 - 6.5.3. The largest contribution to the systematic error for the best fit value of $g^4_{a\gamma}$ arises from the different definitions of the background. The error contributions from other categories are small enough to be neglected.

category	$\Delta g^4_{\text{best fit}}$ (10^{-40} GeV^{-4})
background definition	- 0.139
energy range	+ 0.028
magnetic length	+ 0.001
magnetic field	+ 0.002

Table 6.6: Summary for the maximum variation of $g^4_{\text{best fit}}$ from the systematic studies.

To estimate the total systematic error on the best fit value of $g^4_{a\gamma}$ the largest differences shown in Table 6.6 between $g^4_{\text{best fit}}$ of each study and $g^4_{\text{best fit}}$ used for the $g_{a\gamma}$ extraction are added quadratically:

$$\begin{aligned}\Delta g^4_{\text{best fit}} &= \sqrt{0.139^2 + 0.028^2 + 0.001^2 + 0.002^2} \\ &= 0.142 \times 10^{-40}\text{GeV}^{-4}.\end{aligned}$$

Consequently, the result for the best fit value of $g^4_{a\gamma}$ obtained in Section 6.4 and the systematic error estimated in the last Section lead to the following result for the best fit value of $g^4_{a\gamma}$:

$$g^4_{\text{best fit}} = (-0.104 \pm 0.285(\text{stat.}) \pm 0.142(\text{syst.})) \times 10^{-40}\text{GeV}^{-4}.$$

6.5.5 Upper limit on $g_{a\gamma}$ with systematic errors

In Section 6.4 the upper limit on the coupling constant of the axion to photon has been determined. However the result did not take the systematic error into consideration yet and hence the upper limit on the coupling constant with systematic errors will be evaluated here.

In principle, if the experimentally obtained Likelihood distribution is Gaussian, the mean value and the standard deviation of the Gaussian distribution will correspond to the minimum value of $g_{a\gamma}^4$ and its statistical error, respectively. The result given by integrating this Gaussian distribution over the physically allowed region up to 95% would therefore give the upper limit on $g_{a\gamma}$. Using this idea, the upper limit on $g_{a\gamma}^4$, which includes the systematic error, can be estimated by replacing the statistical error with the total (i.e. statistical plus systematic) error in the Gaussian distribution.

Strictly speaking, the Likelihood distribution illustrated as red curve in Fig. 6.21 is not perfectly Gaussian, as well as the log Likelihood is not a parabola (see Fig. 6.13). But nevertheless the above method can be applied, assuming that the Likelihood distribution is almost Gaussian, especially in the physically allowed region. The solid curve in Fig. 6.21 represents a probability distribution:

$$e^{-(x-\mu)^2/2\sigma_{stat}^2}$$

with the mean μ = - 0.104 ($g_{\text{best fit}}^4$) and standard deviation σ_{stat} = 0.285 (statistical error of $g_{\text{best fit}}^4$). By integrating up to 95% of the physically allowed part of the probability distribution, the upper limit of $g_{a\gamma}$ with only 1 σ statistical error is found:

$$g_{a\gamma}(95\%\,\text{C.L.}) \quad < \quad 0.838 \times 10^{-10}\text{GeV}^{-1}.$$

To consider the systematic error in this result, the statistical error would be then replaced with the total error:

$$e^{-(x-\mu)^2/2\sigma_{total}^2}.$$

Here the total error can be calculated by quadratically adding each statistical and systematic error:

$$\sigma_{total} = \sqrt{\sigma_{stat}^2 + \sigma_{syst}^2} = 0.318.$$

With regards to the total error, the width of the probability distribution becomes broader, demonstrated as the dashed curve in Fig. 6.21. Now the same integration method can be applied to the calculation of the upper limit on $g_{a\gamma}$ and it gives then

$$g_{a\gamma}(95\%\text{C.L.}) \quad < \quad 0.865 \times 10^{-10}\text{GeV}^{-1},$$

including statistical and systematic errors. This result is 3.2% worse than the one obtained with the statistical error only, i.e. the difference between the result with only statistical error and the result with the total error is 0.027.

As a result, the upper limit at 95% C.L. of $g_{a\gamma}$ which is obtained experimentally (see Section 6.4) can be expected to change by the difference if the systematic error is taken into account. Therefore including the statistic and systematic errors leads to the final result for the upper limit on the coupling constant $g_{a\gamma}$:

$$g_{a\gamma} \quad < \quad 0.902 \times 10^{-10} \mathrm{GeV}^{-1}$$

with 95% confidence level for the 2004 CCD data.

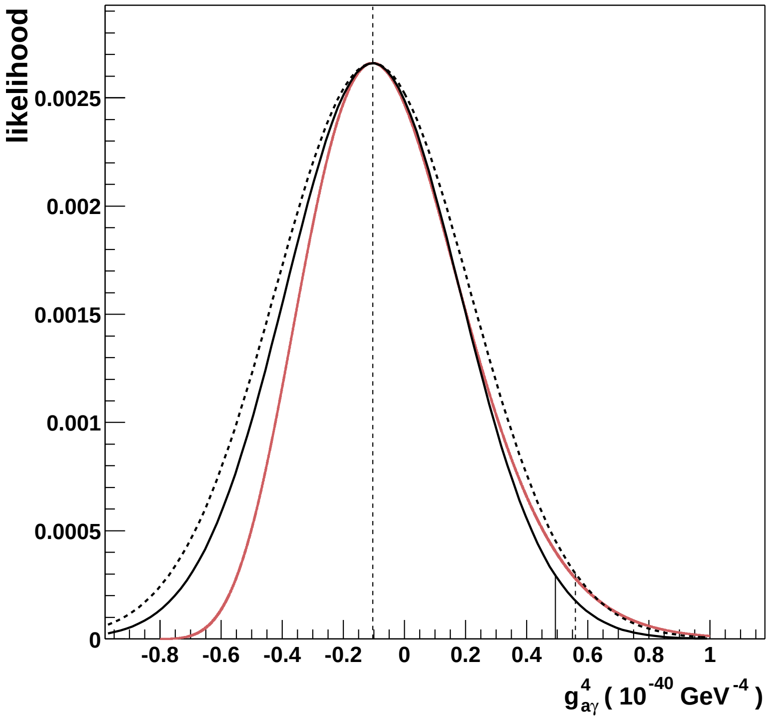

Figure 6.21: Distribution of the normalized Likelihood function (red curve) obtained experimentally. The solid and dashed curves are probability distributions with standard deviation $\sigma_{stat} = 0.285$ and $\sigma_{total} = 0.318$, respectively. Both distributions are appropriately normalized. The two vertical lines represent 95% upper limits.

6.6 Further studies: Scanning

In practice, the position of the solar spot on the CCD has been determined by the alignment measurements of the X-ray telescope in Section 6.1 and it was used for the estimation of the coupling constant $g_{a\gamma}$ in Section 6.4. Nevertheless it was further checked how well the spot position is known and this can be investigated by further systematic studies. Therefore a scanning over the whole CCD area is performed, i.e. the coupling constant $g_{a\gamma}$ is calculated by varying the spot position on the CCD plane in this Section.

For the scanning the full CCD is divided into three parts of columns (x) where each column is divided into ten parts of lines (y) as shown in the two-dimensional plots of Fig. 6.22. The x-coordinates of the spot center are at x = 13, 32 and 51 and the y-coordinates are at y = 16, 35, 54, 73, 92, 111, 130, 149, 168 and 187 for each column. The corresponding energy spectra for all cases can be found in the Appendix B.1. To determine the upper limit of the coupling constant $g_{a\gamma}$ the standard method I was applied, i.e. signal and background are defined as the counts in the same area from the tracking and the background data, respectively. Table 6.7 shows the fit results from the Likelihood fit for all these cases. In case of centers at (13,54), (13,73), (32,92), (51,73), (51,139) and (51,147) the values of the signal minus the background normalized by the time ratio of 9.61 are negative, though the best fit values of those cases are positive. But this can happen in the fitting procedure. On the contrary, there is no case when positive values of the signal minus the normalized background lead to a negative result for $g^4_{\text{best fit}}$. Overall, it seems to be quite correct statistically. The distribution of 30 values for $g^4_{\text{best fit}}$ is compatible with zero: 4 cases of minus 1-2 sigma, 7 cases of minus 0-1 sigma, 12 cases of 0-1 sigma, 5 cases of 1-2 sigma and 2 cases of 2-3 sigma. In addition the scanning around the spot can be found in Appendix B.2.

Eventually, all results from the scanning over the CCD are not strongly dependent on different positions of the spot. In other words, the study of changing spot positions proved that a variation of the spot position does not affect significantly the final result. To sum up, from all above systematic studies it was shown that the final result of the upper limit on $g_{a\gamma}$ obtained in Section 6.4 will remain almost unchanged, even though some experimental conditions and fit parameters as well as the size and position of the spot were slightly varied.

6.7 Combination of 2003 and 2004 results

The 95% confidence level limits on $g_{a\gamma}$ for the 2003 and 2004 CCD data were obtained in Section 5.4 and 6.4, respectively. Both results can be statistically combined by multiplying the Bayesian probability functions:

$$\mathrm{P}(95\%\mathrm{C.L.}) = \int_0^{95\%} e^{-\chi^2/2} \times e^{-\chi^2/2} \mathrm{d}g^4_{a\gamma} \tag{6.3}$$

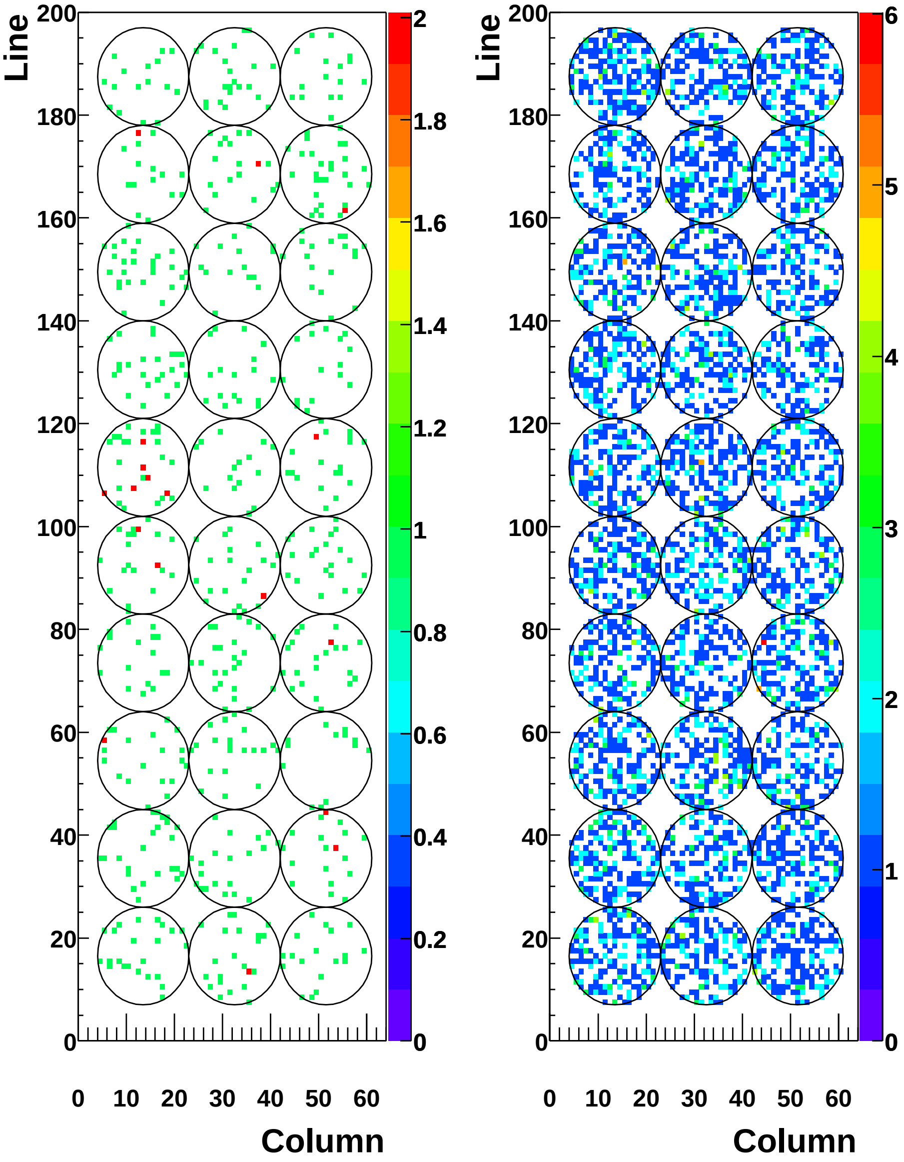

Figure 6.22: Two-dimensional plot of signal (left) and background (right) for 30 different spot positions. Signal and background are defined as the same area data from tracking and background date, respectively. The center of x-coordinates are 13, 32, and 51st column and of y-coordinates are 16, 35, 54, 73, 92, 111, 130, 149, 168 and 187th line for each column.

spot center	S	B	$g^4_{\text{best fit}} \pm 1\,\sigma$ error (10^{-40} GeV^{-4})	χ^2_{min} / ndf	χ^2_{null} / ndf	$g_{a\gamma}$ (95%) (10^{-10} GeV^{-1})
(13,16)	23	220	0.189 ± 0.327	18.4/19	18.9/20	0.962
(13,35)	26	223	0.154 ± 0.340	22.6/19	22.9/20	0.962
(13,54)	21	206	0.070 ± 0.312	20.5/19	20.6/20	0.928
(13,73)	17	188	0.117 ± 0.286	27.0/19	27.2/20	0.922
(13,92)	22	201	0.167 ± 0.319	19.9/19	20.3/20	0.953
(13,111)	33	193	0.897 ± 0.399	15.3/19	24.4/20	1.131
(13,139)	24	197	0.400 ± 0.342	17.1/19	19.0/20	1.014
(13,147)	27	196	0.534 ± 0.364	13.2/19	16.5/20	1.051
(13,168)	16	169	- 0.032 ± 0.278	33.6/19	33.6/20	0.886
(13,187)	16	229	- 0.338 ± 0.280	27.3/19	28.7/20	0.837
(32,16)	23	196	0.475 ± 0.329	40.7/19	44.1/20	1.025
(32,35)	20	181	0.215 ± 0.317	16.1/19	16.8/20	0.961
(32,54)	20	216	- 0.067 ± 0.292	21.6/19	21.7/20	0.892
(32,73)	24	166	0.437 ± 0.332	23.4/19	26.2/20	1.019
(32,92)	22	213	0.039 ± 0.323	20.3/19	20.3/20	0.928
(32,111)	15	196	- 0.262 ± 0.248	19.2/19	20.3/20	0.828
(32,139)	17	184	- 0.112 ± 0.275	21.9/19	22.1/20	0.871
(32,147)	15	200	- 0.198 ± 0.277	23.8/19	24.4/20	0.855
(32,168)	19	205	- 0.102 ± 0.299	20.7/19	20.8/20	0.887
(32,187)	22	185	0.360 ± 0.327	24.6/19	26.4/20	0.999
(51,16)	18	197	- 0.104 ± 0.284	14.4/19	14.5/20	0.877
(51,35)	20	188	0.118 ± 0.312	16.4/19	16.5/20	0.938
(51,54)	13	185	- 0.425 ± 0.249	22.3/19	24.9/20	0.805
(51,73)	22	217	0.222 ± 0.323	22.3/19	22.9/20	0.966
(51,92)	21	192	0.040 ± 0.306	23.1/19	23.1/20	0.920
(51,111)	20	193	- 0.260 ± 0.319	21.6/19	22.3/20	0.874
(51,139)	16	172	0.116 ± 0.268	26.3/19	26.6/20	0.913
(51,147)	18	173	0.266 ± 0.293	27.1/19	28.4/20	0.962
(51,168)	30	197	0.851 ± 0.387	22.5/19	30.7/20	1.119
(51,187)	16	205	- 0.431 ± 0.245	25.7/19	28.4/20	0.809

Table 6.7: Results from the Likelihood fit for the first (upper), second (middle) and third (lower) column scanning. S and B denote signal and background.

The previous integration process has been repeated to find the combined result at 95% confidence level, yielding finally,

$$g_{a\gamma} \quad < \quad 0.872 \times 10^{-10}\text{GeV}^{-1}(95\%\text{C.L.})$$

for axion masses $m_a < 0.02$ eV. In this case systematic errors have been neglected. This analysis procedure was repeated for different values of the axion masses to derive the whole exclusion line for 95% confidence level as shown in Fig. 6.23 which shows the coupling constant $g_{a\gamma}$ as a function of the axion mass m_a.

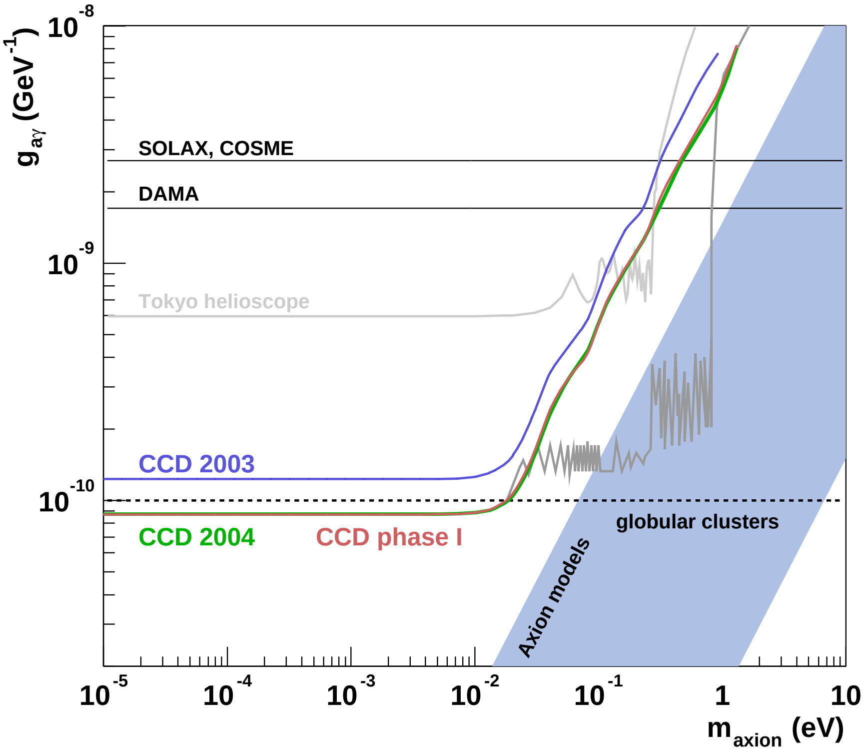

Figure 6.23: Exclusion limits (95% C.L.) from the 2003 (blue) and 2004 (green) CCD data compared with other constraints. The red curve reprsents the combined result of both 2003 and 2004 results. The blue shaded band shows typical theoretical models. The future CAST sensitivity for Phase II is shown as well.

In the sensitivity plot of Fig. 6.23, the 2004 result (green curve) is more restrictive than the one from the 2003 data (blue curve) roughly by a factor of 1.5 mainly due to a smaller spot on the CCD. This final result improves previous constraints given by other previous experiments by a factor of 7. It is the first time that an experimental limit is stronger than the astrophysical limit from globular clusters shown as the dashed line. In fact the astrophysical limit from horizontal branch stars in globular cluster is 0.6×10^{-10} GeV^{-1} and its uncertainty is estimated as a factor of 2. Thus a constraint of 1.0×10^{-10} GeV^{-1} is generally mentioned as the globular cluster limit where this limit is mass independent up to the axion mass of 10 keV. The combined CCD result for the first phase of the experiment is also shown as the red curve. The combined preliminary result including the results of the other two detectors for the 2004 CAST data can also be found in Ref. [108].

All results are limited to an axion mass range $m_a < 0.02$ eV and thus the exclusion curves are flat below the axion mass of 0.02 eV. This means that the expected signal is independent from the axion mass up to this range since the oscillation length of axion-photon is larger than the length of the magnet, as mentioned once in Chapter 5. For higher m_a, the number of expected signal counts decreases due to the loss of coherence between axions and photons, so that the shape of the spectral curve looks differently. The blue area represents the region of theoretical axion models discussed in Chapter 2. The axion-photon coupling constant $g_{a\gamma}$ is theoretically proportional to the axion mass m_a, which both are inversely proportional to an unknown spontaeous symmetry breaking scale. Hence this proportionality between $g_{a\gamma}$ and m_a is limited by this symmetry breaking scale which is bigger than the scale of electroweak symmetry and smaller than the Planck scale.

Finally, in order to restore the coherence for axion masses above 0.02 eV, data taking started at the end of 2005 by introducing a buffer gas with various pressures in the magnet pipes. The extended sensitivity to higher masses will allow to enter into the region of theoretical axion models, shown in Fig. 6.23.

Chapter 7

Summary and Outlook

The CERN Axion Search Telescope (CAST) experiment at CERN searching for elusive axions with energies in the keV range has been detailed in this thesis. In particular, axion theories have been introduced in the first part of this thesis. After that, a general description of the CAST experiment has been given. An X-ray mirror telescope with a Charge Coupled Device (CCD) as a focal plane detector, which is the most sensitive detector system of the CAST experiment, was discussed. This thesis is devoted to the determination of an upper limit on the axion-photon coupling constant $g_{a\gamma}$. The analysis is based on the data taken by the CCD detector in the CAST experiment during the years 2003 and 2004.

In 2003 the CCD detector has accumulated tracking data with good quality during 121.3 hours when the magnet was pointing to the sun. Background measurements taken during non-alignment periods have an exposure time of 1233.5 hours. During the 2003 data taking period, a monitoring of the focusing stability of the X-ray telescope was not continuously possible, and hence a signal area larger than the expected size of the sun spot had to be considered. Taking into account all uncertainties of the telescope alignment, the size of the area containing the signal was estimated to be 34×71 pixels ($54.3\ \mathrm{mm}^2$). The background was defined by the data taken from the same area during the nontracking periods. From the background studies a significant dependence of the background data on different experimental conditions was not observed. The null hypothesis test showed that the data is compatible with the absence of a signal and therefore an upper limit on the coupling constant $g_{a\gamma}$ has been extracted from the observed data. Due to low counting statistics in the CCD the use of a likelihood function in the minimization procedure was required. The 95% confidence limit for the 2003 CCD data was determined by integrating the Bayesian probability function over the physically allowed region, i.e. positive signals:

$$g_{a\gamma} < 1.23 \times 10^{-10}\ \mathrm{GeV}^{-1}\ (95\%\ \mathrm{C.L.}).$$

To check systematic uncertainties, the background in the signal area was also determined by extrapolating the background measured during tracking periods in that part of the CCD not containing the sun spot. Both methods of background selection led to the same final upper limit on the coupling constant $g_{a\gamma}$. In order to find the combined result for the 2003 CAST data, the CCD result was statistically combined with the results of the other two detectors of the experiment:

$$g_{a\gamma} < 1.16 \times 10^{-10}\ \mathrm{GeV}^{-1}\ (95\%\ \mathrm{C.L.}).$$

Both results are limited to an axion mass range $m_a < 0.02$ eV where the expected signal is independent of mass because the axion photon oscillation length by far exceeds the length of the magnet. This limit improves the best previous laboratory constraints on $g_{a\gamma}$ by a factor of 5 in the coherence region $m_a < 0.02$ eV.

In 2004 the CCD detector was operated with an extra shield inside the detector chamber. This additional shielding has reduced the background level by a factor of 1.5 as compared to 2003. Very important for the CCD setup is the monitoring of the position of the solar spot on the CCD. From the regularly performed alignment measurements with a parallel laser beam and an X-ray source, the center of the expected solar spot on the CCD was determined to be at $x = 40$ pixels and $y = 108$ pixels with a radius of 19 pixels and it was shown to be stable within one pixel diameter of the CCD. Therefore, for the CCD data collected in 2004 the analysis could be restricted to a smaller spot on the CCD since the telescope stability was continuously monitored. For the 2004 data taking period CCD data were collected during 179.4 hours for solar tracking and 1723.1 hours for background. The data analysis procedures were mostly conducted in the same way as the one in 2003. The 95% exclusion limit for the 2004 CCD data yielded

$$g_{a\gamma} < 0.88 \times 10^{-10}\ \mathrm{GeV}^{-1}\ (95\%\ \mathrm{C.L.}).$$

Here systematic uncertainties were not taken into account. By multiplying the Bayesian probability distributions, the combined result of the 2003 and 2004 data for the upper limit on the axion-photon coupling constant $g_{a\gamma}$ is

$$g_{a\gamma} < 0.87 \times 10^{-10}\ \mathrm{GeV}^{-1}\ (95\%\ \mathrm{C.L.})$$

for axion masses $m_a < 0.02$ eV. Including the systematic error of $g^4_{a\gamma}$, the 95% confidence limit on the couplings $g_{a\gamma}$ has been determined to

$$g_{a\gamma} < 0.90 \times 10^{-10}\ \mathrm{GeV}^{-1}\ (95\%\ \mathrm{C.L.}).$$

The CCD detector at CAST experiment has been operated successfully since May 2003 and during 2004 it was taking data in upgraded versions with higher sensitivity. Unfortunately, no signal above background was observed in any of the data taken so far. The result of the 2004 data improved the previous constraints from other experiments by a factor of 7. For the first time, the experimental result is below the astrophysical limit from globular clusters. So far the CAST experiment has been operated with an evacuated magnet bore and thus was restricted to axion masses below 0.02 eV. During 2005 a major modification to the magnet pipe system was undertaken. At the end of 2005 CAST started with measurements for its second phase. The magnet pipes were filled with a low Z buffer gas (starting with ^{4}He and in the future ^{3}He) of various pressures in order to restore coherence for higher axion masses m_a > 0.02 eV. The extended sensitivity will allow CAST to reach masses up to 0.8 eV and thus reach into the region of the theoretical axion models.

Appendix A

Detector noise check

A.1 Problematic files of the 2003 CCD data

Data files	Start Time (UT)	End Time (UT)	Comment
C09_07_10_030714_02042 - 02050	14.07.2003 12:59:00	14.07.2003 15:14:00	
C09_07_10_030718_02014	18.07.2003 06:06:00	18.07.2003 06:21:00	
C09_07_10_030718_02030	18.07.2003 10:07:00	18.07.2003 10:22:00	
C09_07_10_030718_02046	18.07.2003 14:07:00	18.07.2003 14:22:00	bad column
C09_07_10_030721_04003 - 04005	21.07.2003 03:51:00	21.07.2003 04:36:00	
C09_07_10_030724_02018	24.07.2003 07:38:00	24.07.2003 07:53:00	bad line
C09_07_10_030724_02023	24.07.2003 08:54:00	24.07.2003 09:09:00	
C09_07_10_030727_02013	27.07.2003 06:34:23	27.07.2003 06:43:00	bad column
C09_07_10_030727_03004	27.07.2003 10:29:00	27.07.2003 10:44:00	
C09_07_10_030729_02031	29.07.2003 10:43:00	29.07.2003 10:58:00	
C09_07_10_030729_02065	29.07.2003 19:14:00	29.07.2003 19:29:00	bad column
C09_07_10_030731_02058	31.07.2003 17:44:00	31.07.2003 17:59:00	bad column
C09_07_10_030731_02065	31.07.2003 19:30:00	31.07.2003 19:45:00	bad column
C09_07_10_030804_02067	04.08.2003 20:07:00	04.08.2003 20:22:00	bad column
C09_07_10_030806_02009	06.08.2003 05:50:00	06.08.2003 06:05:00	
C09_07_10_030808_02006 - 02007	08.08.2003 04:49:00	08.08.2003 05:19:00	
C09_07_10_030810_02007	10.08.2003 05:12:00	10.08.2003 05:27:00	
C09_07_10_030814_02014	14.08.2003 06:42:00	14.08.2003 06:57:00	bad line
C09_07_10_030815_02005	15.08.2003 04:31:00	15.08.2003 04:46:00	
C09_07_10_030815_02046	15.08.2003 14:47:00	15.08.2003 15:02:00	
C09_07_10_030817_02053 - 02054	17.08.2003 16:42:00	17.08.2003 17:04:00	
C09_07_10_030819_02049	19.08.2003 15:46:00	19.08.2003 16:01:00	bad line
C09_07_10_030821_02059	21.08.2003 18:05:00	21.08.2003 18:20:00	bad line
C09_07_10_030825_02021 - 02025	25.08.2003 07:24:00	25.08.2003 08:29:00	

C09_07_10_030828_09008 - 09010	28.08.2003 20:55:53	28.08.2003 21:41:00	
C09_07_10_030828_09025	29.08.2003 01:12:53	29.08.2003 01:28:00	
C09_07_10_030829_05020 - 05021	29.08.2003 11:33:00	29.08.2003 12:03:00	
C09_07_10_030830_02008	30.08.2003 06:14:00	30.08.2003 06:29:00	bad column
C09_07_10_030830_02022	30.08.2003 09:45:00	30.08.2003 10:00:00	bad line
C09_07_10_030908_02006	08.09.2003 20:33:00	08.09.2003 20:48:00	bad column
C09_07_10_030910_02006	10.09.2003 05:47:00	10.09.2003 06:02:00	
C09_07_10_030911_02030 - 02031	11.09.2003 11:53:00	11.09.2003 12:24:00	bad column
C09_07_10_030911_02061	11.09.2003 19:41:00	11.09.2003 19:56:00	bad line
C09_07_10_030912_02008 - 02009	12.09.2003 06:22:00	12.09.2003 06:52:00	
C09_07_10_030912_02053 - 02055	12.09.2003 17:40:00	12.09.2003 18:20:00	
C09_07_10_030912_02057	12.09.2003 18:40:00	12.09.2003 18:55:00	
C09_07_10_030913_02003 - 02009	13.09.2003 05:09:00	13.09.2003 06:54:00	
C09_07_10_030914_02012 - 02015	14.09.2003 07:19:00	14.09.2003 08:19:00	
C09_07_10_030915_02015 - 02021	15.09.2003 08:27:00	15.09.2003 10:12:00	
C09_07_10_030915_02023	15.09.2003 10:27:00	15.09.2003 10:42:00	
C09_07_10_030915_02033 - 02035	15.09.2003 12:58:00	15.09.2003 13:43:00	
C09_07_10_030915_05016	15.09.2003 20:15:50	15.09.2003 20:16:00	
C09_07_10_030915_05047	16.09.2003 04:01:22	16.09.2003 04:05:00	end file
C09_07_10_030917_03042	17.09.2003 04:27:47	17.09.2003 04:28:00	end file
C09_07_10_030926_02033	26.09.2003 12:38:00	26.09.2003 12:53:00	bad column
C09_07_10_030926_02059	26.09.2003 19:09:00	26.09.2003 19:24:00	bad column
C09_07_10_030927_02082	28.09.2003 00:45:00	28.09.2003 01:00:00	bad column
C09_07_10_031001_02010	01.10.2003 18:35:00	01.10.2003 18:50:00	bad column
C09_07_10_031010_02100	11.10.2003 11:11:56	11.10.2003 11:20:00	bad column
C09_07_10_031010_02133	11.10.2003 19:29:00	11.10.2003 19:44:00	bad line
C09_07_10_031010_02166	12.10.2003 03:45:00	12.10.2003 04:00:00	bad column
C09_07_10_031020_03040 - 03041	21.10.2003 04:46:00	21.10.2003 05:01:00	bad column
C09_07_10_031024_02030 - 02037	24.10.2003 17:42:00	24.10.2003 19:43:00	
C09_07_10_031025_03046	25.10.2003 19:32:00	25.10.2003 19:47:00	bad line
C09_07_10_031026_02004	26.10.2003 05:50:00	26.10.2003 06:05:00	bad column
C09_07_10_031026_02062	26.10.2003 20:22:00	26.10.2003 20:37:00	bad line
C09_07_10_031027_02013	27.10.2003 08:25:00	27.10.2003 08:40:00	bad column
C09_07_10_031027_02054	27.10.2003 18:41:00	27.10.2003 18:56:00	bad column
C09_07_10_031104_02031 - 02047	04.11.2003 13:08:00	04.11.2003 17:24:00	
C09_07_10_031106_02000 - 02015	06.11.2003 13:02:00	06.11.2003 15:02:00	
C09_07_10_031106_02081	07.11.2003 09:20:00	07.11.2003 09:35:00	
C09_07_10_031112_02000 - 02004	12.11.2003 15:34:26	12.11.2003 16:55:00	
C09_07_10_031114_02004	14.11.2003 12:31:00	14.11.2003 12:46:00	bad column
C09_07_10_031114_02013	14.11.2003 14:46:00	14.11.2003 15:01:00	bad line
C09_07_10_031117_02009 - 02017	17.11.2003 16:01:00	17.11.2003 18:16:00	
C09_07_10_031117_02074 - 02075	18.11.2003 08:19:00	18.11.2003 08:49:00	

Table A.1: Problematic files of the 2003 CCD data after the detector noise check. If there is no comment, this indicates that the noise level was unusual high, or otherwise corrupted due to unknown reasons.

A.2 Problematic files of the 2004 CCD data

Data files	Start Time (UT)	End Time (UT)	Comment
C09_07_10_040331_20046	2004.04.01 06:38:20	2004.04.01 06:53:00	
C09_07_10_040505_09002	2004.05.05 14:03:21	2004.05.05 14:18:23	
C09_07_10_040511_02000 - 02003	no time info		no data
C09_07_10_040523_02004	2004.05.23 04:02:27	2004.05.23 04:17:29	bad column
C09_07_10_040604_05063	2004.06.05 01:33:10	2004.06.05 01:34:09	end file
C09_07_10_040610_02045 - 02085	2004.06.10 14:04:36	2004.06.11 00:22:58	fuse burned
C09_07_10_040613_02000 - 02088	no time info		fuse burned
C09_07_10_040617_05044	2004.06.18 02:23:17	2004.06.18 02:23:35	end file
C09_07_10_040622_02053	2004.06.22 16:15:20	2004.06.22 16:30:22	bad column
C09_07_10_040623_02048	2004.06.23 19:57:49	2004.06.23 20:12:51	bad column
C09_07_10_040714_02061	2004.07.14 18:11:57	2004.07.14 18:26:59	bad column
C09_07_10_040716_02039	2004.07.16 12:29:46	2004.07.16 12:44:48	bad column
C09_07_10_040717_02021	2004.07.17 08:11:56	2004.07.17 08:26:58	bad column
C09_07_10_040718_02005	2004.07.18 04:10:42	2004.07.18 04:25:44	bad column
C09_07_10_040721_05070	2004.07.22 02:38:38	2004.07.22 02:38:38	end file
C09_07_10_040819_02058	2004.08.19 18:15:46	2004.08.19 18:30:48	bad column
C09_07_10_040829_02045	2004.08.29 14:47:13	2004.08.29 15:02:15	bad column
C09_07_10_040830_02039	2004.08.30 13:35:05	2004.08.30 13:50:07	bad column
C09_07_10_040910_02008	2004.09.10 10:49:28	2004.09.10 11:04:30	bad column
C09_07_10_040910_02074	2004.09.11 03:22:08	2004.09.11 03:22:09	end file
C09_07_10_040914_02025	2004.09.15 00:14:56	2004.09.15 00:29:58	bad column
C09_07_10_040925_02008	2004.09.25 12:48:54	2004.09.25 13:03:56	bad column
C09_07_10_040930_02027	2004.09.30 11:55:43	2004.09.30 12:10:44	bad column
C09_07_10_041011_02044	2004.10.11 15:27:23	2004.10.11 15:42:25	bad column
C09_07_10_041014_02031	2004.10.14 12:33:33	2004.10.14 12:48:35	bad line
C09_07_10_041019_02010	2004.10.19 07:09:23	2004.10.19 07:24:25	bad column

Table A.2: Problematic files of the 2004 CCD data after the detector noise check.

A.3 Time variation of the detector noise for the 2004 data

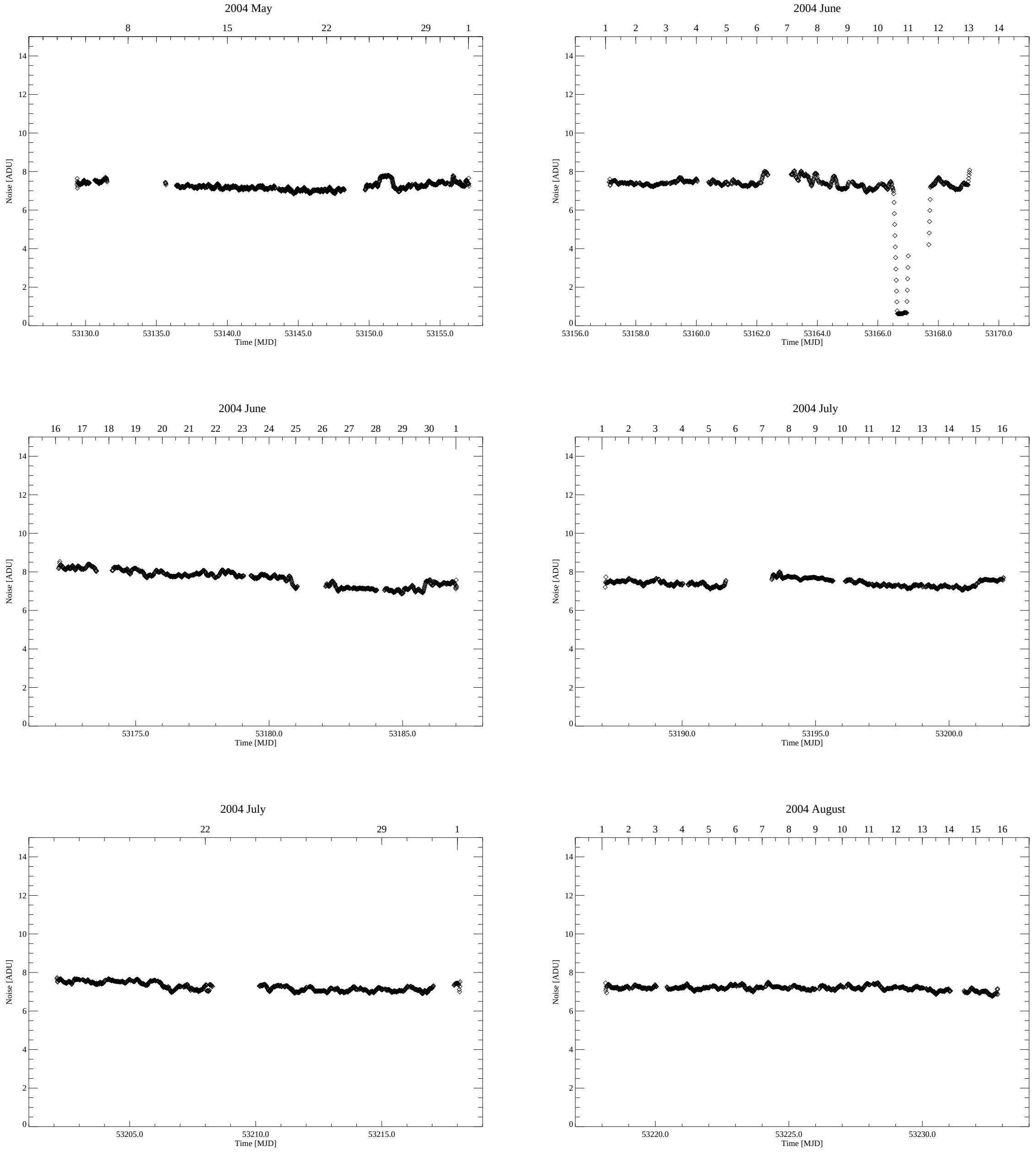

Figure A.1: The mean noise of the detector as a function of time from May to 15th of August in 2004 for all data.

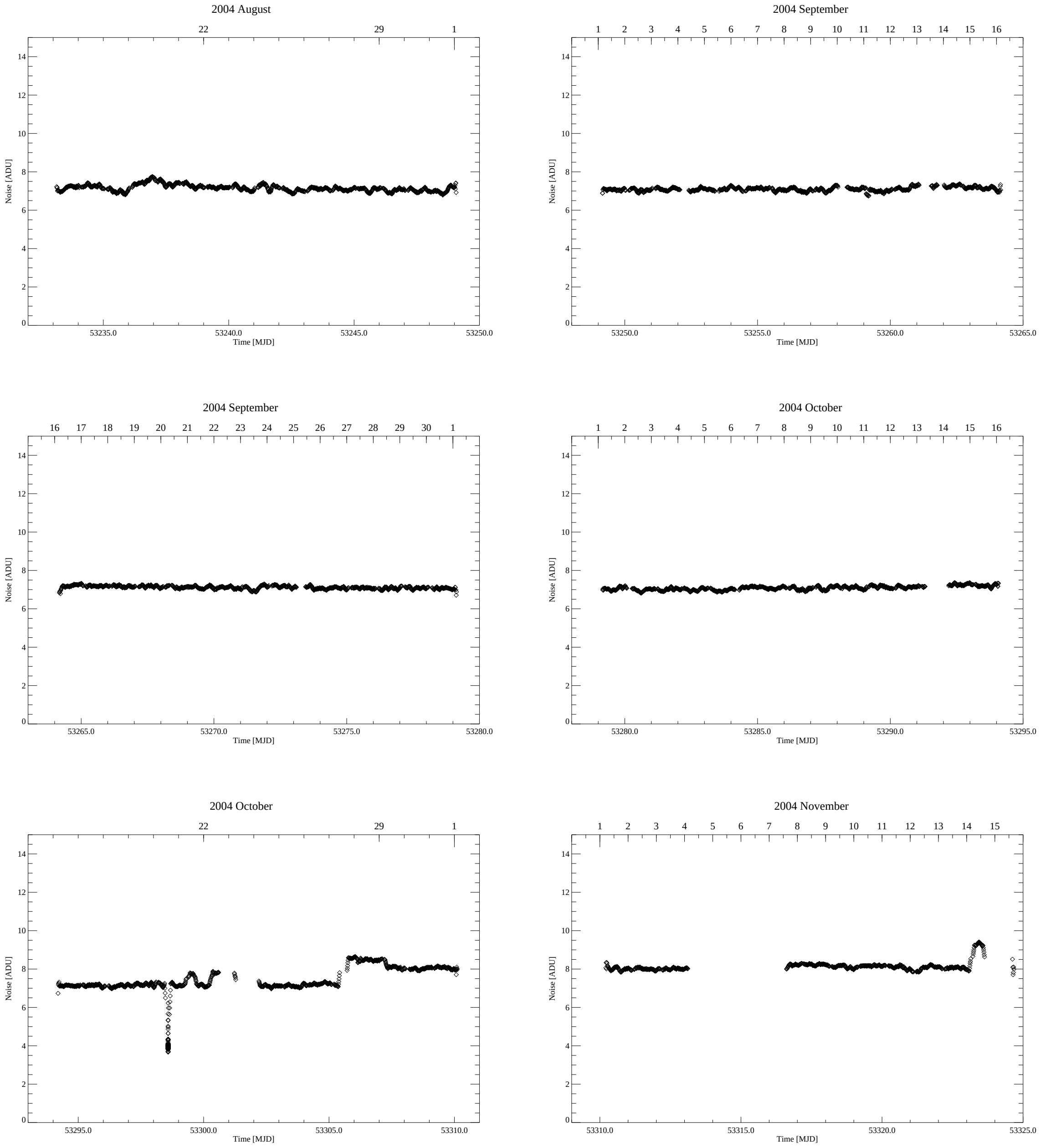

Figure A.2: The mean noise of the detector as a function of time from 16th of August to November in 2004 for all data.

Appendix B

Scanning

B.1 Energy spectra for the scanning of the CCD

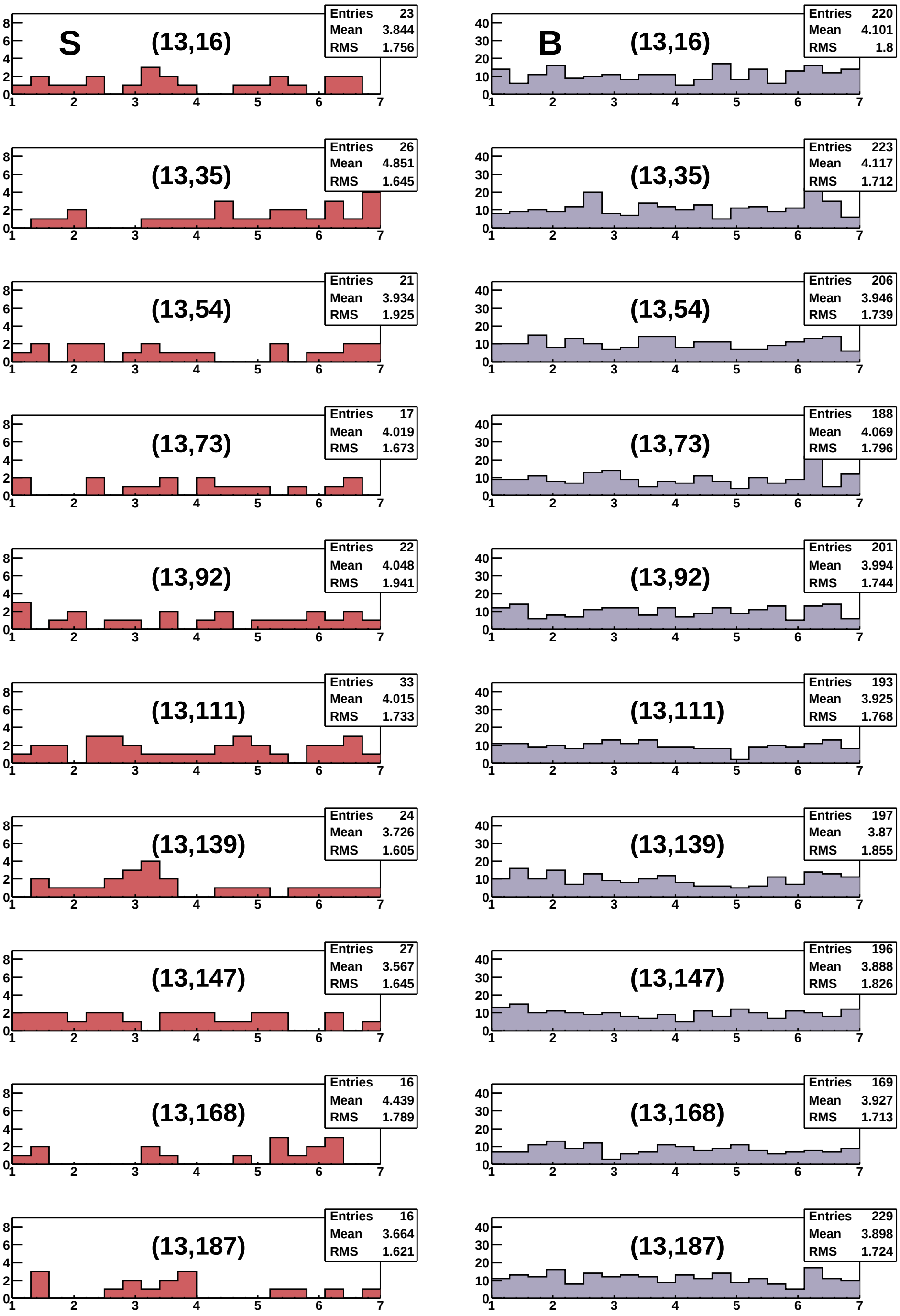

Figure B.1: Energy spectra of the first column (x=13) scanning. S and B denote signal and background, respectively.

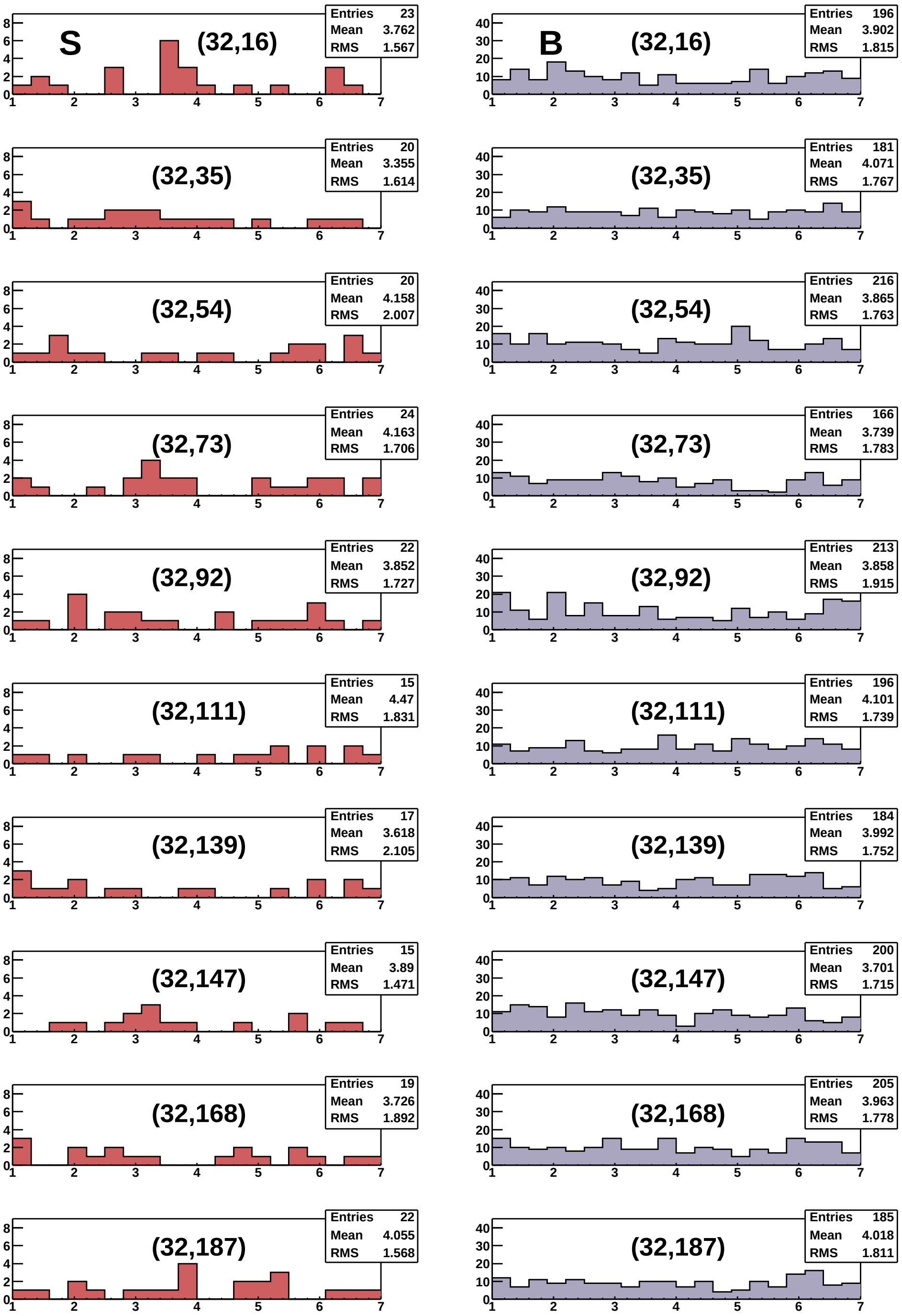

Figure B.2: Energy spectra of the second column (x=32) scanning.

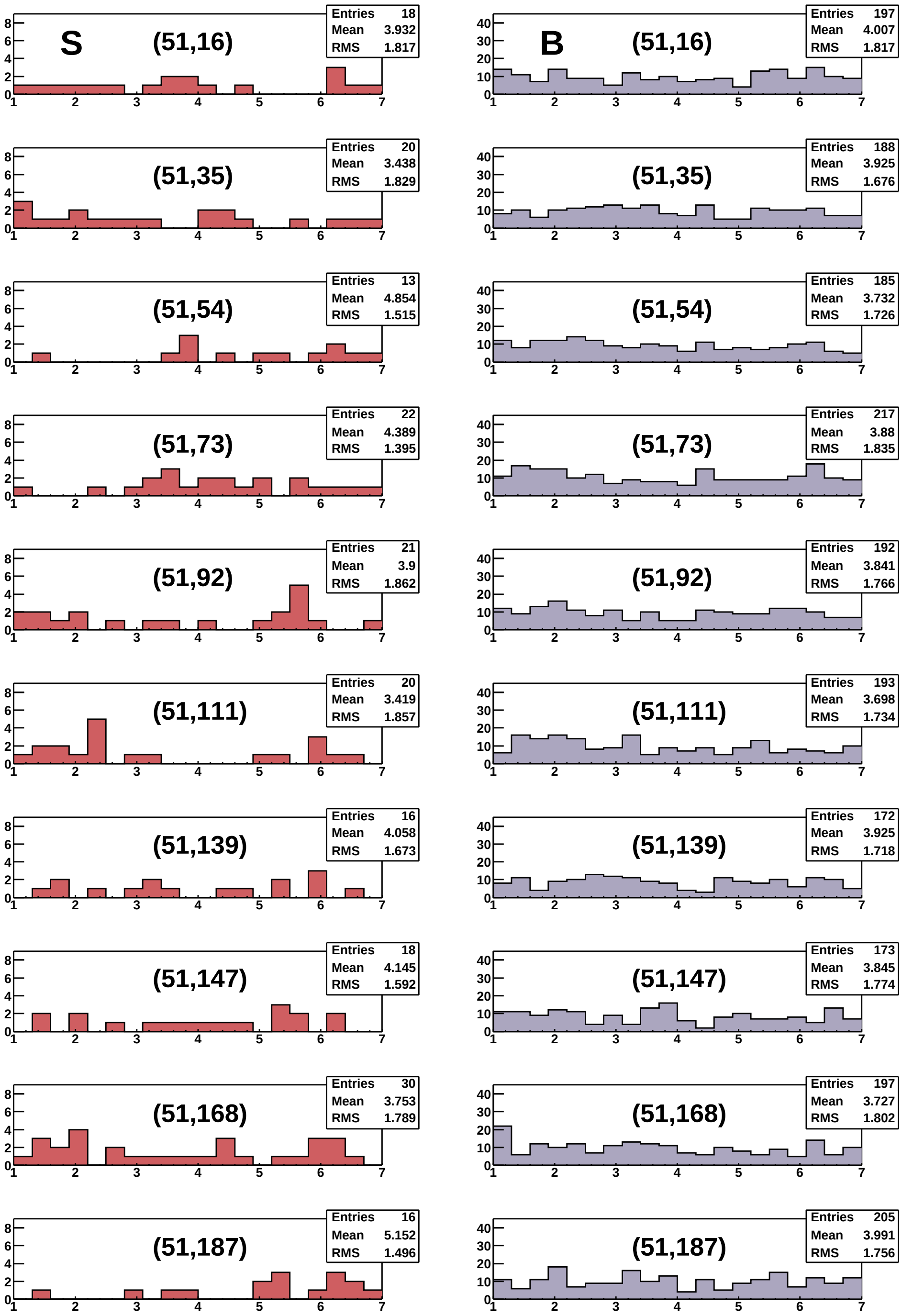

Figure B.3: Energy spectra of the third column (x=52) scanning.

B.2 Scanning around the spot

In addition to the Section 6.6 the coupling constant $g_{a\gamma}$ is calculated by moving the spot position vertically and/or horizontally around the spot with two pixels. The results from the likelihood fit is summarized in Table B.1 and the corresponding energy spectra can be found in Figs. B.4 - B.8. The maximum difference from the final result is 4.5%.

spot center	S	B	$g^4_{\text{best fit}} \pm 1\,\sigma$ error (10^{-40} GeV^{-4})	χ^2_{min} / ndf	χ^2_{null} / ndf	$g_{a\gamma}$ (95%) (10^{-10} GeV^{-1})
(38,106)	16	206	-0.294 ± 0.268	9.5/19	10.7/20	0.832
(39,106)	17	197	-0.176 ± 0.278	9.2/19	9.6/20	0.858
(40,106)	19	195	-0.068 ± 0.294	9.5/19	9.5/20	0.887
(41,106)	16	196	-0.212 ± 0.268	12.0/19	12.6/20	0.844
(42,106)	16	202	-0.225 ± 0.269	14.2/19	14.9/20	0.843
(38,107)	17	201	-0.176 ± 0.277	11.6/19	12.0/20	0.856
(39,107)	18	202	-0.170 ± 0.284	11.2/19	11.6/20	0.863
(40,107)	18	197	-0.143 ± 0.284	11.0/19	11.3/20	0.867
(41,107)	18	198	-0.041 ± 0.288	11.4/19	13.4/20	0.888
(42,107)	16	203	-0.302 ± 0.265	9.6/19	10.9/20	0.830
(38,108)	17	199	-0.159 ± 0.275	15.2/19	15.5/20	0.858
(39,108)	18	194	-0.120 ± 0.285	11.4/19	11.6/20	0.872
(40,108)	18	194	-0.104 ± 0.285	11.9/19	12.0/20	0.875
(41,108)	17	193	-0.124 ± 0.280	13.6/19	13.8/20	0.867
(42,108)	16	195	-0.218 ± 0.265	12.6/19	13.3/20	0.842
(38,109)	17	199	-0.150 ± 0.274	15.0/19	15.3/20	0.859
(39,109)	17	195	-0.129 ± 0.275	15.1/19	15.4/20	0.863
(40,109)	17	193	-0.118 ± 0.275	15.0/19	15.2/20	0.865
(41,109)	18	192	-0.048 ± 0.284	12.4/19	12.5/20	0.885
(42,109)	16	187	-0.080 ± 0.265	14.1/19	14.2/20	0.866
(38,110)	17	195	-0.077 ± 0.270	15.7/19	15.8/20	0.870
(39,110)	17	191	-0.067 ± 0.271	15.6/19	15.7/20	0.873
(40,110)	17	192	-0.041 ± 0.269	16.1/19	16.2/20	0.877
(41,110)	17	190	-0.025 ± 0.273	16.0/19	16.0/20	0.882
(42,110)	15	183	-0.071 ± 0.259	19.7/19	19.7/20	0.862

Table B.1: Results from the likelihood fit for the scanning around the spot

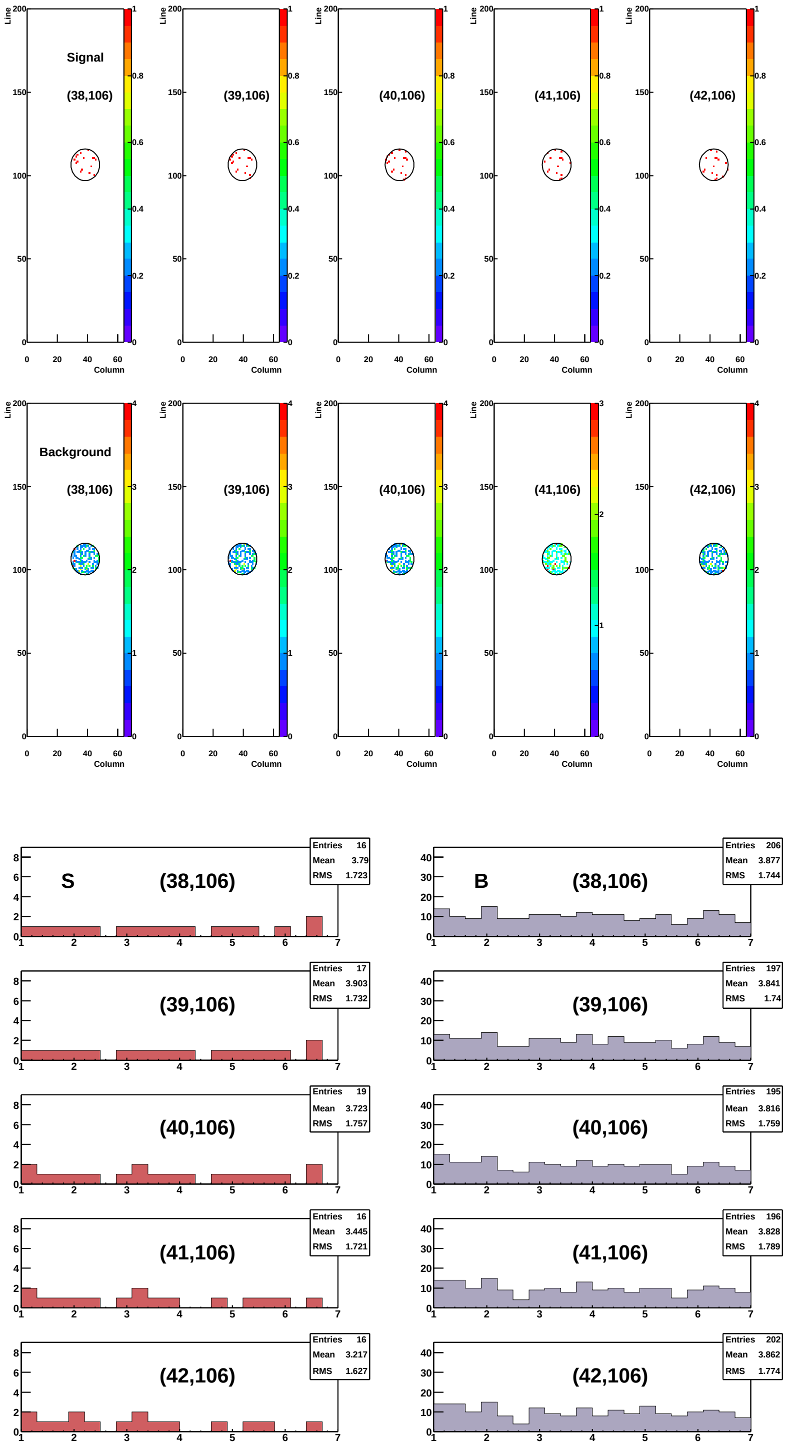

Figure B.4: Top: Two-dimensional plots for the signal and background. Bottom: Corresponding energy spectra. S and B denote signal and background, respectively.

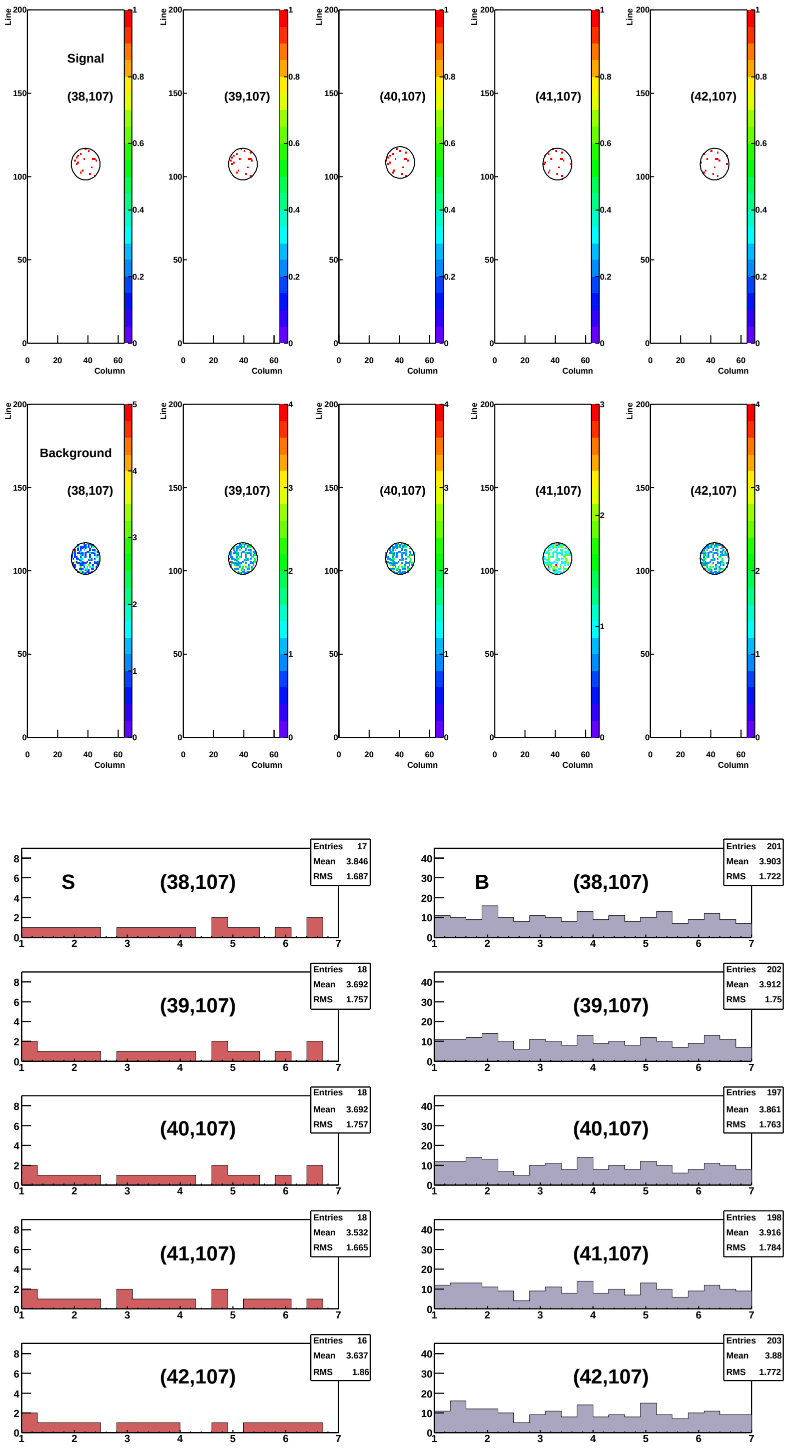

Figure B.5: Top: Two-dimensional plots for the signal and background. Bottom: Corresponding energy spectra.

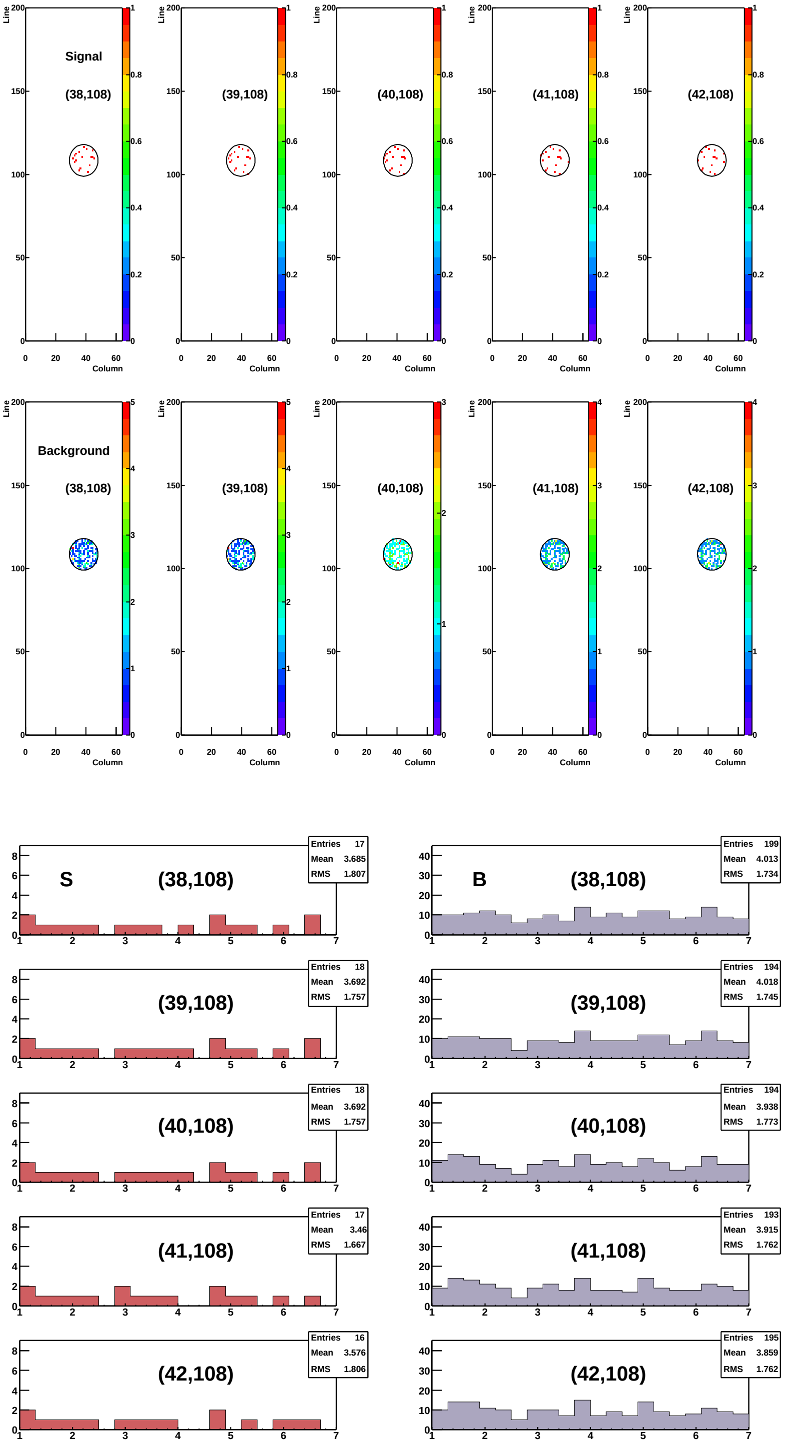

Figure B.6: Top: Two-dimensional plots for the signal and background. Bottom: Corresponding energy spectra.

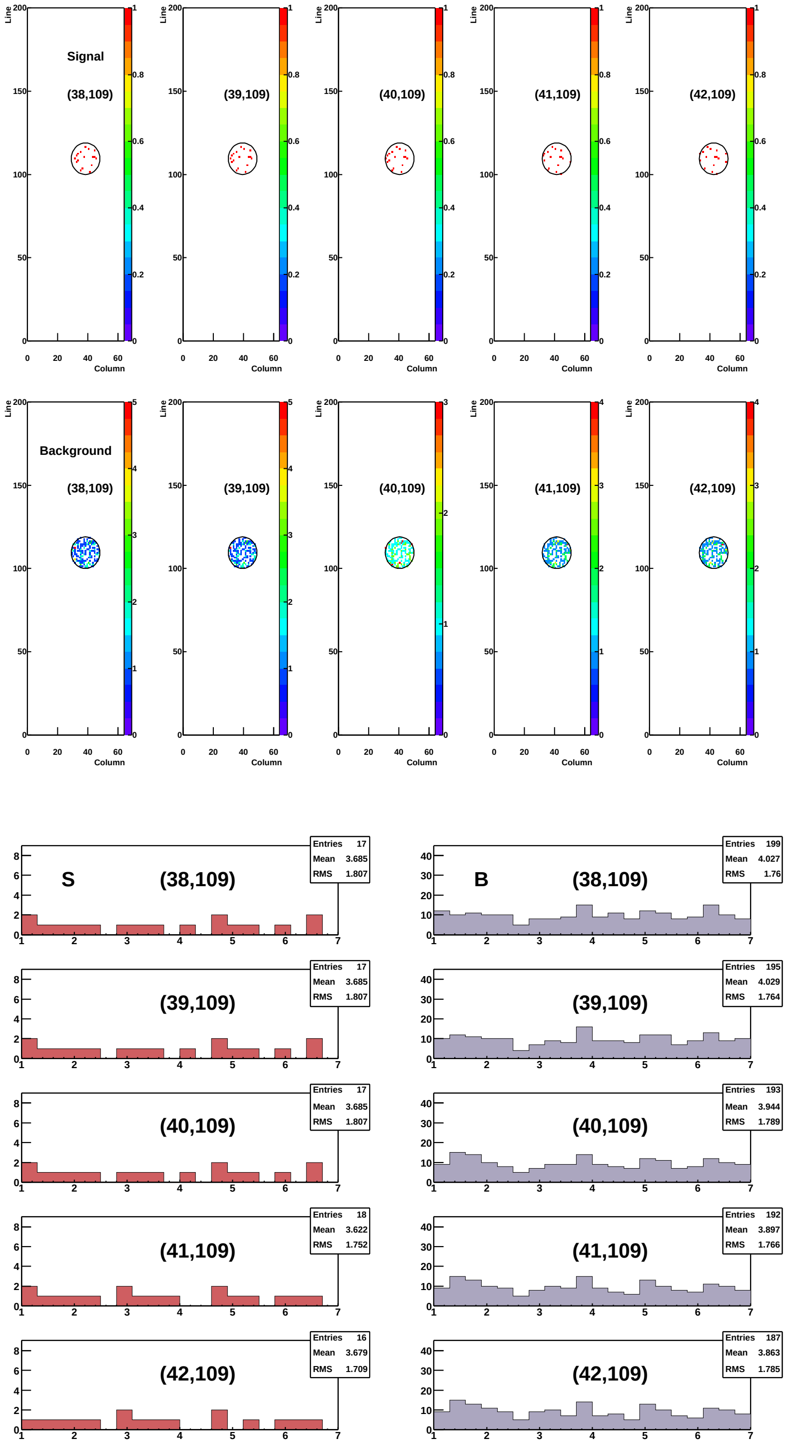

Figure B.7: Top: Two-dimensional plots for the signal and background. Bottom: Corresponding energy spectra.

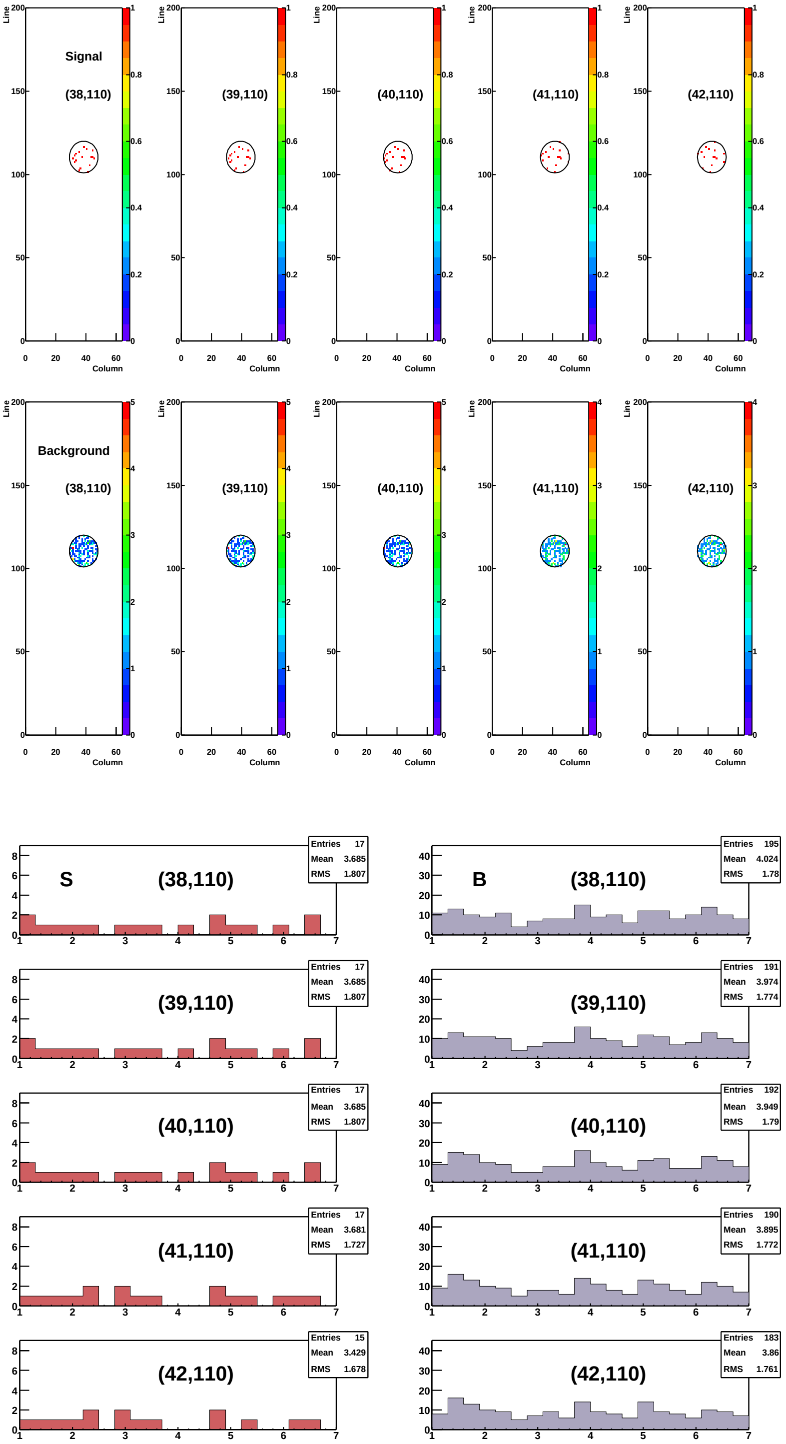

Figure B.8: Top: Two-dimensional plots for the signal and background. Bottom: Corresponding energy spectra.

Bibliography

[1] F. Halzen and A. D. Martin, Quarks and Leptons (Wiley 1983)

[2] C. Quigg, Gauge Theories of the Strong, Weak and Electromagnetic Interactions (Addison-Wesley 1983)

[3] B. Povh, K. Rith, C. Scholz and F. Zetsche, Particles and Nuclei (Springer 1995)

[4] S. Weinberg, The U(1) problem, Phys. Rev. **D11** (1975) 3583

[5] G. 't Hooft, Symmetry Breaking through Bell-Jackiw Anomalies, Phys. Rev. Lett. **37** (1976) 8

[6] S. L. Adler, Axial-Vector Vertex in Spinor Electrodynamics, Phys. Rev. **177** (1969) 2426

[7] J. D. Jackson, Classical Electrodynamics 3rd Edition (Wiley 1998)

[8] C. Callan, R. Dashen and D. Gross, The Structure of the Gauge Theory Vacuum, Phys. Lett. **B63** (1976) 334

[9] R. Jackiw and C. Rebbi, Vacuum Periodicity in a Yang-Mills Quantum Theory, Phys. Rev. Lett. **37** (1976) 172

[10] V. Baluni, CP-nonconserving effects in quantum chromodynamics, Phys. Rev. **D19** (1979) 2227

[11] W. B. Dress et al., Search for an electric dipole moment of the neutron, Phys. Rev. **D15** (1977) 9

[12] C. A. Baker et al., Improved Experimental Limit on the Electric Dipole Moment of the Neutron, Phys. Rev. Lett. **97** (2006) 131801; P. G. Harris et al., New Experimental Limit on the Electric Dipole Moment of the Neutron, Phys. Rev. Lett. **82** (1999) 904

[13] R. D. Peccei and H. R. Quinn, CP Conservation in the Presence of Pseudoparticles, Phys. Rev. Lett. **38** (1977) 1440

[14] R. D. Peccei and H. R. Quinn, Constraints imposed by CP conservation in the presence of pseudoparticles, Phys. Rev. **D16** (1977) 1791

[15] J. E. Kim, Light Pseudoscalars, Particle Physics and Cosmology, Phys. Rep. **150** (1987)

[16] S. Weinberg, A New Light Boson?, Phys. Rev. Lett. **40** (1978) 223

[17] T. W. Donnelly et al., Do axions exist?, Phys. Rev. **D18** (1978) 1607

[18] W. A. Bardeen and S. -H. H. Tye, Current Algebra Applied to Properties of the Light Higgs Boson, Phys. Lett. **B74** (1978) 229

[19] C. Edwards et al., Upper Limit for $J/\psi \to \gamma +$ Axion, Phys. Rev. Lett. **48** (1982) 903

[20] F. C. Porter and K. C. Königsmann, Unambiguous test for the axion, Phys. Rev. **D25** (1982) 1993

[21] G. G. Raffelt, Stars as Laboratories for Fundamental Physics (Chicago University Press 1996)

[22] M. A. Shifman, A. I. Vainshtein and V. I. Zakharov, Can confinement ensure natural CP invariance of the strong interactions?, Nucl. Phys.**B166** (1980) 493

[23] M. Dine, W. Fischler and M. Srednicki, A simple solution to the strong CP problem with a harmless axion, Phys. Lett. **B104** (1981) 199

[24] G. G. Raffelt, Astrophysical methods to constrain axions and other novel particle phenomena, Phys. Rep. **198** (1990)

[25] H. Leutwyler, The ratios of the light quark masses, Phys. Lett. **B378** (1996) 313

[26] M. S. Turner, Windows on the axion, FERMILAB-Conf. 89/104-A (1989)

[27] M. Srednicki, Axion couplings to matter, Nucl. Phys. **B260** (1985) 689

[28] D. B. Kaplan, Opening the axion window, Nucl. Phys. **B260** (1985) 215

[29] W. Keil et al., Fresh look at axions and SN 1987A, Phys. Rev. **D56** (1997) 2419

[30] E. W. Kolb and M. S. Turner, The Early Universe (Westview Press 1990)

[31] H. V. Klapdor-Kleingrothaus and K. Zuber, Teilchenastrophysik (Teubner 1997)

[32] D. Perkins, Particle Astrophysics (Oxford 2003)

[33] H. Primakoff, Photo-Production of Neutral Mesons in Nuclear Electric Fields and the Mean Life of the Neutral Meson, Phys. Rev. **81** (1951) 899

[34] G. G. Raffelt, Astrophysical axion bounds diminished by screening effects, Phys. Rev. **D33** (1986) 897

[35] H. Schlattl et al., Helioseismological constraint on solar axion emission, Astro. Phys. **10** (1999) 353

[36] M. S. Turner, Coherent scalar-field oscillations in an expanding universe, Phys. Rev. **D28** (1983) 1243

[37] M. S. Turner, Cosmic and local mass density of “invisible” axions, Phys. Rev. **D33** (1986) 889

[38] Particle Data Group, Phys. Lett. **B592** (2004) 392

[39] P. Sikivie, Experimental Tests of the “Invisible” Axion, Phys. Rev. Lett. **51** (1983) 1415

[40] C. Hagmann et al., Results from a High-Sensitivity Search For Cosmic Axions, Phys. Rev. Lett. **80** (1998) 2043

[41] W. U. Wuensch et al., Results of a laboratory search for cosmic axions and other weakly coupled light particles, Phys. Rev. **D40** (1989) 3153

[42] C. Hagmann et al., Results from a search for cosmic axions, Phys. Rev. **D42** (1990) 1297

[43] S. J. Asztalos et al., Improved rf cavity search for halo axions, Phys. Rev. **D69** (2004) 011101

[44] K. Yamamoto et al., The Rydberg-Atom-Cavity Axion Search, hep-ph/0101200

[45] M. T. Ressell, Limits to the radioactive decay of the axion, Phys. Rev. **D44** (1991) 3001

[46] M. A. Bershady et al., Telescope Search for a 3 eV to 8 eV Axion, Phys. Rev. Lett. **66** (1991) 1398

[47] B. D. Blout et al., A Radio Telescope Search for Axions, Astrophys. J. **546** (2001) 825

[48] D. M. Lazarus et al., Search for Solar Axions, Phys. Rev. Lett. **69** (1992) 2333

[49] S. Moriyama et al., Direct search for solar axions by using strong magnetic field and X-ray detectors, Phys. Lett. **B434** (1998) 147

[50] E. A. Paschos and K. Zioutas, A proposal for solar axion detection via Bragg scattering, Phys. Lett. **B323** (1994) 367

[51] F. T. Avignone et al., Experimental Search for Solar Axions via Coherent Primakoff Conversion in a Germanium Spectrometer, Phys. Rev. Lett. **81** (1998) 5068

[52] A. Morales et al., Particle Dark Matter and Solar Axion Searches with a small germanium detector at the Canfranc Underground Laboratory, Astropart. Phys. **16** (2002) 325

[53] R. Bernabei et al., Search for solar axions by Primakoff effect in NaI crystals, Phys. Lett. **B515** (2001) 6

[54] K. van Bibber et al., Proposal Experiment to Produce and Detect Light Pseudoscalars, Phys. Rev. Lett. **59** (1987) 759

[55] R. Cameron et al., Search for nearly massless, weakly coupled particles by optical techniques, Phys. Rev. **D47** (1993) 3707

[56] Y. Semertzidis et al., Limits on the Production of Light Scalar and Pseudoscalar Particles, Phys. Rev. Lett. **64** (1990) 2988

[57] E. Zavattini et al., Experimental Observation of Optical Rotation Generated in Vacuum by a Magnetic Field, Phys. Rev. Lett. **96** (2006) 110406

[58] K. Zioutas et al., [CAST Collaboration], First Results from the CERN Axion Solar Telescope, Phys. Rev. Lett. **94** (2005) 121301

[59] A. Ringwald, Production and detection of very light bosons in the HERA tunnel, Phys. Lett. **B569** (2003) 51; A. Ringwald, Axion interpretation of the PVLAS data?, hep-ph/0511184

[60] G. G. Raffelt, Plasmon decay into low-mass bosons in stars, Phys. Rev. **D37** (1988) 1356

[61] L. Di Lella et al., Search for solar Kaluza-Klein axions in theories of low-scale quantum gravity, Phys. Rev. **D62** 125011 (2000)

[62] J. Bahcall et al., Standard solar models and the uncertainties in predicted capture rates of solar neutrinos, Rev. Mod. Phys. **54** (1982) 767

[63] K. van Bibber et al., Design for a practical laboratory detector for solar axions, Phys. Rev. **D39** (1989) 2089

[64] L. Di Lella and K. Zioutas, Observational evidence for gravitationally trapped massive axion(-like) particles, Astropart. Phys. **19** (2003) 145

[65] J. Bahcall and M. H. Pinsonneault, What Do We (Not) Know Theoretically about Solar Neutrino Fluxes?, Phys. Rev. Lett. **92** (2004) 12

[66] P. D. Serpico and G. G. Raffelt, New Calculation of Solar Axion Flux, CAST Internal Report, January 2005

[67] G. G. Raffelt and L. Stodolsky, Mixing of the photon with low-mass particles, Phys. Rev. **D37** (1988) 1237

[68] Figure courtesy of Dr. Biljana Lakić

[69] K. Zioutas et al., A solar axion search using a decommissioned LHC test magnet, Nucl. Instrum. Methods **A425** (1999) 480

[70] M. Bona et al., Performance of the First CERN-INFN 10 m Long Superconducting Dipole Prototype for the LHC, Proc. 4th Europ. Particle Accelerator Conf., London, June 1994

[71] http://doc.cern.ch//archive/electronic/cern/others/PHO/photo-di/

[72] K. Barth et al., Cryogenics for the CERN Solar Axion Telescope (CAST) using a LHC Dipole Prototype Magnet, Divisional Report, CERN LHC/2002-17 (ACR/ECR/MTA)

[73] K. Barth et al., Commissioning and First Operation of the Cryogenics for the CERN Axion Solar Telescope (CAST), Departmental Report, CERN/AT 2004-1 (ECR)

[74] CAST shift documentation, Version 1.1 August 2003

[75] 5th CAST collaboration meeting, CERN, March 2001

[76] http://aa.usno.navy.mil/software/

[77] 12th CAST collaboration meeting, Greece, September 2002

[78] 11th CAST collaboration meeting, CERN, July 2002

[79] J. Vogel, The Precision of the Tracking System in Search of Solar Axions, Diploma Thesis, Universität Freiburg (2005)

[80] Status report of the CAST experiment, CERN-SPSC-2005-022, June 2005

[81] B. Beltrán, A TPC (Time Projection Chamber) for axion searches in the CAST experiment at CERN, Ph.D. Thesis, Universidad de Zaragoza (2006)

[82] Y. Giomataris et al., MICROMEGAS: a high-granularity position-sensitive gaseous detector for high particle-flux environments, Nucl. Instrum. Methods **A376** (1996) 29

[83] S. Andriamonje et al., A Micromegas detector for the CAST experiment, Nucl. Instrum. Methods **A518** (2004) 252

[84] Th. Dafni, A Search for Solar axions with the MICROMEGAS Detector in CAST, Ph.D. Thesis, Technischen Universität Darmstadt (2005)

[85] J. Altmann et al., Mirror system for the German X-ray satellite ABRIXAS: I. Flight mirror fabrication, integration, and testing, Proc. SPIE Vol. 3444 (1998) 350

[86] L. Strüder, High-resolution imaging X-ray spectrometers, Nucl. Instrum. Methods **A454** (2000) 73

[87] R. Kotthaus, H. Bräuninger, P. Friedrich, R. Hartmann, D. Kang, M. Kuster, G. Lutz and L. Strüder, The X-ray Telescope of the CAST Experiment, astro-ph/0511390 (2005)

[88] M. Kuster, H. Bräuninger, J. Englhauser, P. Friedrich, R. Hartmann, R. Kotthaus, G. Lutz, W. Serber, L. Strüder, D. Kang, J. Franz and J. Morales, The X-ray Mirror Telescope and the pn-CCD Detector of CAST, Proc. SPIE Vol. 5500 (2004) 139

[89] Data courtesy of Dr. Peter Friedrich

[90] L. Strüder et al., The European Photon Imaging Camera on XMM-Newton: The pn-CCD camera, Astronomy & Astrophysics Vol. 365 (2001) L18

[91] W. R. Leo, Techniques for Nuclear and Particle Physics Experiments (Springer 1987)

[92] U. Fano, Ionization Yield of Radiations. II. The Fluctuations of the Number of Ions, Phys. Rev. **72** (1947) 26

[93] L. Strüder et al., First tests with fully depleted pn-CCD's, IEEE Trans. Nuc. Sci. Vol. 35 (1988) 372

[94] H. Bräuninger et al., PN-CCDs for the XMM Satellite Mission, Proc. SPIE Vol. 1344 (1990) 404

[95] G. Lutz, Semiconductor Radiation Detectors (Springer 1999)

[96] L. Strüder et al., The MPI/AIT X-ray Imager (MAXI) - High Speed pn CCDs for X-ray Detection, Nucl. Instrum. Methods **A288** (1990) 227

[97] E. Pinotti et al., The pn-CCD on-chip electronics, Nucl. Instrum. Methods **A326** (1993) 85

[98] J. R. Janesick, Scientific Charge-Coupled Devices (SPIE Press 2000)

[99] J. Pal et al., The influence of optical light on the charge transfer efficiency of the XMM EPIC pn-CCD camera, Proc. SPIE Vol. 3765 (1999) 683

[100] R. Hartmann et al., The Quantum Efficiency of the XMM pn-CCD camera, Proc. SPIE Vol. 3765 (1999) 703

[101] G. Lutz, H. Bräuninger, J. Englhauser, R. Hartmann, D. Kang, R. Kotthaus, M. Kuster, W. Serber and L. Strüder, An application of space technology to the terrestrial search for axions: the X-ray mirror telescope at CAST, Nucl. Instrum. Methods **A518** (2004) 201

[102] http://fits.gsfc.nasa.gov/

[103] M. Kuster, S. Cebrian, A. Rodriquez, R. Kotthaus, H. Bräuninger, J. Franz, P. Friedrich, R. Hartmann, D. Kang, G. Lutz and L. Strüder, pn-CCDs in a Low Background Environment: Detector Background of the CAST X-ray Telescope, Proc. SPIE Vol. 5898 (2005) 236

[104] L. Lyons, Statistics for nuclear and particle physicists (Cambridge University Press 1986)

[105] M. D. Hannam and W. J. Thompson, Estimating small signals by using maximum likelihood and Poisson statistic, Nucl. Instrum. Methods **A431** (1999) 239

[106] J. Franz, CAST Internal Report (Normalization) 2004

[107] R. J. Barlow, Statistics (John Wiley & Sons 1989)

[108] D. Kang et al., [CAST Collaboration], The search for solar axions in the CAST experiment, hep-ex/0605049

List of Figures

List of Tables

Acknowledgements

First of all, I would like to thank my supervisor Prof. Dr. Kay Königsmann for giving me the opportunity to do my Ph.D. at the University of Freiburg in Germany and to work on the CAST experiment at CERN. I sincerely appreciate for his continuous supports, helps on my research, and for trusting me during the past few years. I also would like to express great thanks to Dr. Jürgen Franz for his continuous guidance and helping me throughout this doctorate research. Many thanks and appreciations go to Dr. Horst Fischer, Dr. Fritz-Herbert Heinsius and Dr. Christian Schill for their valuable comments and helpful suggestions.

I am thankful for all members of Freiburg group, Prof. Dr. Hans Schmitt, Dr. Sonja Hedicke, Anna Danasino, Dr. Thomas Schmidt, Dr. Andreas Grünemaier, Dr. Eric Weise, Dominik Setter, Dr. Frank Nerling, Dr. Andreas Mutter, Florain Hermann, Anselm Vossen, Heiner Wollny, Roland Hagemann, Jasmin Kiefer, Konrad Wenzl, Wolfgang Käfer, Khalil Rehmani, Rainer Fastner and Gisela Mössner for giving me such a warm and very friendly atmosphere that made my research possible. Specially, many thanks to my CAST buddies Julia Vogel and Chiara Spáno for working together and sharing good times in the same office.

I would like to express sincere thanks to the members of CCD group, particularly, Dr. Rainer Kotthaus and Dr. Markus Kuster for fruitful discussions and their help getting started. Also thanks to Dr. Jakob Engelhauser, Dr. Peter Friedrich and Prof. Dr. Gehart Lutz. In addition, I give my thanks many people in the CAST Collaboration, especially, Prof. Dr. Konstantin Zioutas and Dr. Martyn Davenport who always try to run this great experiment. Many thanks go to Dr. Berta Beltrán, Dr. Theopisti Dafni, David Miller, Dr. Igor Irastorza, Thomas Papaevangelou, Dr. Biljana Lakić, Dr. Esther Ferrer Ribas and Jaime Ruz for their help, suggestions and good friendship. Also thanks to all the people during many shifts. Many thanks to all who read carefully my thesis and commented on improvements, especially, Prof. Dr. Georg Raffelt.

I am very grateful to my parents for encouraging me always to follow my chosen path and for their continued love and support and faith in me. I also thank my lovely younger sister Dong-Hee Kang and her fiance Jang-Woo Seo for making me feel better whenever I get frustrated. Many thanks to Donghee's parents, all my relatives and all my friends for their encouragements and their steadfast love.

Finally, I am indebted to my life's companion Donghee Kang for his endless love and devotion and for helping me as always. Without him this work would not have been possible.